"New physics probes through loop computation in effective theories"

Vasquez Tocora, Andres

ABSTRACT

Given the current situation, where no new particles or direct signs for Beyond the Standard Model (BSM) physics have been found, we consider the indirect signs that such states would leave on measurement at LHC and foreseen collider energies. The Standard Model Effective Field Theory (SMEFT) is a powerful framework useful in the search of such deviations. Higher-order SM predictions allow to correctly establish a deviation, while higher-order SMEFT predictions allow to enhance sensitivity by correctly describing correlations, by accounting for new dependencies and allow to precisely interpret deviations (towards the correct family of UV models). It is for this reasons that one-loop contributions should be taken into consideration when making predictions in the SMEFT. Given the fact that the top quark is the heaviest elementary particle known to date, BSM particles are often expected to have sizable couplings to the top. Moreover, studies in the top sector are motivated by the fact that the top is the least known particle from the strong sector and the LHC is a top factory. The top sector is thus of interest in the search of new physics signals. This thesis aims at presenting several theoretical and phenomenological aspects of the SMEFT. We discuss the challenges and subtleties appearing in the computation of the top-pair production in the SMEFT at one-loop in QCD, and the corresponding sensitivity of this process to new physics. As a result, we provide bounds on four-heavy-quark operators from the top-pair production data, which are complementary to other bounds found in ...

CITE THIS VERSION

New physics probes through loop computation in effective theories

Doctoral dissertation presented by

Andres Vasquez

in fulfillment of the requirements for the degree of Doctor in Sciences.

Thesis Jury

Prof. Fabio Maltoni	President	Université catholique de Louvain
Prof. Céline Degrande	Supervisor	Université catholique de Louvain
Prof. Rogerio Rosenfeld	Supervisor	Universidade Estadual Paulista
Prof. Giacomo Bruno	Secretary	Université catholique de Louvain
Prof. Oscar Éboli		Universidade de São Paulo
Dr. Gauthier Durieux		CERN

December, 2022

Acknowledgements

This thesis could have not been completed without my supervisors Céline Degrande and Rogerio Rosenfeld, who patiently accompanied me along the doctoral formation, going beyond their duties to give me support. It has been an honor and a pleasure to develop myself as a researcher under their guidance. For this and all of their trust I would like to thank them. I express special gratitude to Fabio Maltoni for giving me the life-changing opportunity of joining CP3.

Warm thanks to the members of my thesis committee Gauthier Durieux, Oscar Éboli, Fabio Maltoni and Giacomo Bruno for their enlightening questions and their meticulous comments which improved the quality of the manuscript.

I would like to thank Olivier Mattelaer for his continuous support when it was about bugs and developments in MadGraph. Additionally, I thank Ambresh Shivaji, Eleni Vryonidou, Ken Mimasu and Luca Mantani, who kept my research ongoing in difficult moments.

To my friends during the PhD: Luis, Samip, Julien, Matteo, Jan and Xiaoran, thanks from the bottom of my heart for all the help and, more importantly, the funny moments. To the Football group, thanks for the ultra high-level games. In general, I am grateful to all CP3 members who always make of it a place with an ideal atmosphere. I owe special thanks to the excellent work carried on by Carinne on the administrative support, Andres and Jerome for the IT support and to the secretary team at UNESP for their prompt solutions.

I am deeply grateful to Belinda for being by my side me when things were not going well, always bringing hope to my life in many ways. She has being the anchor that I needed in this turbulent time. Similarly, I owe gratitude to my parents and siblings, who despite the distance have encouraged me countless times. Finally, I would like to dedicate this thesis to my family and, in particular, to my newborn daughter.

Abstract

Given the current situation, where no new particles or direct signs for Beyond the Standard Model (BSM) physics have been found, we consider the indirect signs that such states would leave on measurement at LHC and foreseen collider energies. The Standard Model Effective Field Theory (SMEFT) is a powerful framework useful in the search of such deviations. Higher-order SM predictions allow to correctly establish a deviation, while higher-order SMEFT predictions allow to enhance sensitivity by correctly describing correlations, by accounting for new dependencies and allow to precisely interpret deviations (towards the correct family of UV models). It is for this reasons that one-loop contributions should be taken into consideration when making predictions in the SMEFT. Given the fact that the top quark is the heaviest elementary particle known to date, BSM particles are often expected to have sizable couplings to the top. Moreover, studies in the top sector are motivated by the fact that the top is the least known particle from the strong sector and the LHC is a top factory. The top sector is thus of interest in the search of new physics signals. This thesis aims at presenting several theoretical and phenomenological aspects of the SMEFT. We discuss the challenges and subtleties appearing in the computation of the top-pair production in the SMEFT at one-loop in QCD, and the corresponding sensitivity of this process to new physics. As a result, we provide bounds on four-heavy-quark operators from the top-pair production data, which are complementary to other bounds found in the literature.

The effects of BSM physics coupling to the top can also be studied in processes without tops in the final state. Because of the large Yukawa coupling of the top, the one-loop induced double Higgs production in e^+e^- colliders offers the possibility of studying such couplings. We perform a sensitivity study for several benchmark values of energy and integrated luminosity foreseen for future lepton colliders such as CLIC, ILC and FCC-ee.

While the SMEFT focuses on BSM effects via deviations at high energy we also investigate near-threshold effects through the Sommerfeld enhancement. As a matter of fact, light mediators from hidden sectors could couple to final state particles, leading to the origin of resonances due to non-perturbative effects. Experimentally, the near-threshold-energy regions of several production

processes are not yet well measured, such as the top-pair and double Higgs production. On the theoretical side, an identification in terms of UV divergences in the relativistic QFT of the divergences of the calculation of P-wave Sommerfeld enhancement in processes with unstable particles in the final state was missing in the literature. To obtain a finite result, we implement a renormalization procedure, showing that these divergences can be removed by adding proper counterterms. This procedure offers the advantage of not having the arbitrariness of introducing a cutoff and thus is safe of spoiling the physical significance of the enhancement.

Associated Publications:

Andres Vasquez, Céline Degrande, Alberto Tonero, and Rogerio Rosen-feld, "New physics in double higgs production at future e^+e^--colliders", *Journal of High Energy Physics*, vol. 2019, no. 5, 2019.

Carlos Henrique de Lima, Alberto Tonero, Andres Vasquez, and Rogerio Rosenfeld, "The role of renormalization in sommerfeld enhancement with unstable particles", *arXiv:hep-th/2208.13309*, 2022.

Thesis Jury

Prof. Fabio Maltoni	President	Université catholique de Louvain
Prof. Celine Degrande	Supervisor	Université catholique de Louvain
Prof. Rogerio Rosenfeld	Supervisor	Universidade Estadual Paulista
Prof. Giacomo Bruno	Secretary	Université catholique de Louvain
Prof. Oscar Éboli		Universidade de São Paulo
Dr. Gauthier Durieux		CERN

Contents

Chapter 1

Introduction

In 1922, one hundred years ago, Niels Bohr received the Nobel Prize for *«his services in the investigation of the structure of atoms and of the radiation emanating from them»*. Since then, our conception of the fundamental building blocks of nature has gone far beyond what was imagined at that time. The advent of Quantum Field Theories (QFT), successfully gathering the small and the fast, provided a consistent framework on which many theories could be formulated. Amongst which the Standard Model of particle physics (SM) stands out as the pinnacle of fundamental contemporary physics.

More than a model, the SM is the most successful theory that answers the question of the composition of matter at the most elementary level. Ten years have passed since the discovery of the Higgs, whose properties have since been measured to an ever increasing precision, and the SM remains undefeated in high energy experiments. As a result of those experiments, we know the best measured quantities defining the electroweak input parameters at the accuracy of 1 part-per-trillion for the magnetic moment of the electron from which the fine-structure constant (α) is extracted, 0.23 parts-per-million for the mass of the Z boson and 510 parts-per-billion for the Fermi constant. Agreement between the SM predictions and the experiments is assessed by a broad range of measurements. Among the most recent, we find the interactions of the Higgs boson to electroweak bosons which are measured at the 6-8% level of accuracy [3]. Hence, the SM has been established as the most precise theory of Nature. Nevertheless indirect observations such as matter-antimatter asymmetry and the dark matter content of the universe reveal the weaknesses of the SM and hint towards a more complete theory.

Collecting the most beautiful ideas in particle physics of the 60's and 70's, in general terms, the SM incorporates the theory of Electroweak interactions (EW) of Glashow, Weinberg and Salam [4–6] (GWS theory), and the theory of Quantum Chromodynamics (QCD) [7]. The former gives a consistent unification of the weak and electromagnetic interactions between quark and leptons, complemented with the Brout–Englert–Higgs mechanism (BEH) [8–10]. QCD describes the strong interaction between gluons and quarks. The QCD sector historically appeared as a fundamental description to the organizational models accommodating the large amount of hadrons discovered in the 60's (Eightfold way), getting its theoretical structure from the works of Gell-Mann, Fritzsch, and Leutwyler [7], additionally complemented by the crucial property of asymptotic freedom postulated by Gross, Wilczek and Politzer [11, 12]. The renormalizability of the theory was proven in 1972 by 't Hooft and Veltman [13] allowing for consistent computations of finite corrections.

All these ingredients have received great experimental confirmations, from the prediction of neutral currents and the baryon and meson spectrum, up to the last discovered particle in 2012 at the LHC: the Higgs boson [14, 15]. Even though it is known to be incomplete, the SM is the best description for the physics of particle accelerators, where the gravitational interactions are negligible.

The SM, as a quantum field theory, is determined by the degrees of freedom, *i.e.* the particle content, and the gauge symmetry. The fermionic part of the particle spectrum of the theory is given by six quark types coming in three colors each and six lepton types. The bosonic part is given by the spin-1 mediating particles, from which photons (long-range Coulomb interaction) and gluons (confined due to strong interaction and thus a short-range interaction with range of order 1-3 fm) are massless, while the weak bosons are heavy particles (at a typical scale of 100 GeV) leading to the short-range nature of weak interactions. Additionally, we have the Higgs boson, the only spin-0 scalar field without known substructure up to this date.

It is observed that the quark masses span the range $\{10^{-3} - 10^2\}\,\text{GeV}$. As it is well known, the measure of such quark masses is intricate due to the confinement phenomenon. Thus, instead of existing as free particles, the final manifestation of quarks is through bound states, such as pions. The characteristic energy at which such bound states appear is set by the QCD scale at $\Lambda_{\text{QCD}} \sim 200\,\text{MeV}$. Furthermore, in the fermionic sector, we have the hierarchical span of the charged leptons masses and the particular lightness of the neutrinos. In fact, the absolute scale of the neutrino masses remains unknown

due to the fact that only differences between masses can be measured through neutrino oscillations. Hence, we have scenarios where the three neutrinos are massive as well as there exists the possibility in which just two of the three neutrinos are massive. This is one of the unanswered questions of the SM.

The gauge symmetry that the Lagrangian of the SM manifests is given by the non semi-simple group $SU(3)_c \otimes SU(2)_L \otimes U(1)_Y$. Therefore, the covariant derivative is

$$D_\mu = \partial_\mu + ig_s G_\mu^a T^a + ig_2 W_\mu^a \tau^a + ig_1 \frac{Y}{2} B_\mu, \qquad (1.1)$$

where the G_μ^a corresponds to the eight gauge fields of the $SU(3)_c$, *i.e.* the eight colored gluons of the strong interaction, the W_μ^a are the three gauge fields of the $SU(2)_L$ and B_μ is the gauge field of the $U(1)_Y$. The force carrier particles are known once the gauge group is set. The quantities g_s, g_2 and g_1 are the gauge couplings, with the first one corresponding to the strong force and with the other two leading to strength of the electroweak interactions.

The field tensors of the vector bosons can be obtained from the relationship $[D_\mu, D_\nu] = igF_{\mu\nu}^a t^a$, leading to

$$G_{\mu\nu}^a = \partial_\mu G_\nu^a - \partial_\nu G_\mu^a + g_s f^{abc} G_\mu^b G_\nu^c, \qquad (1.2)$$

$$W_{\mu\nu}^i = \partial_\mu W_\nu^i - \partial_\nu W_\mu^i + g_2 \epsilon^{ijk} W_\mu^j W_\nu^k, \qquad (1.3)$$

$$B_{\mu\nu} = \partial_\mu B_\nu - \partial_\nu B_\mu, \qquad (1.4)$$

where f^{abc} and ϵ^{ijk} are the structure constant of the $SU(3)_c$ and $SU(2)_L$ groups, respectively. The generators of the gauge transformation satisfy

$$[T^a, T^b] = if^{abc} T^c, \qquad [\tau^i, \tau^j] = i\epsilon^{ijk} \tau^k, \qquad (1.5)$$

with τ^i ($i = 1, 2, 3$) the generators of the $SU(2)_L$ group, *i.e.* proportional to the Pauli matrices, and T^a ($a = 1, ..., 8$) the generators of the $SU(3)_c$ group, *i.e.* proportional to the the Gell-Mann matrices. The generators satisfy the relations $\text{tr}[T^a T^b] = \frac{1}{2}\delta^{ab}$ and $\text{tr}[\tau^a \tau^b] = \frac{1}{2}\delta^{ab}$, which fixes their normalization.

With this, the Yang-Mills Lagrangian for the gauge fields can be written as

$$\mathcal{L}^{\text{YM}} = -\frac{1}{4} G_{\mu\nu}^a G^{a\mu\nu} - \frac{1}{4} W_{\mu\nu}^i W^{i\mu\nu} - \frac{1}{4} B_{\mu\nu} B^{\mu\nu}. \qquad (1.6)$$

The bosons described by this Lagrangian are massless particles due to gauge symmetry. The W_μ^i and B_μ fields cannot be identified with the physical massive bosons mediating the weak interactions. This task brings the challenge of introducing longitudinal modes for the massive bosons while preserving uni-

tarity. The simplest and most elegant way to preserve gauge invariance is via the BEH mechanism. This mechanism introduces the Higgs field as a complex scalar φ that transforms as a singlet of $SU(3)_c$, a doublet of $SU(2)_L$ and with an hypercharge of $+1$ under $U(1)_Y$. The spontaneous symmetry breaking (SSB) pattern of the theory must be specified, through which the Higgs field endows with mass the particles of the SM. While the $SU(2)_L \otimes U(1)_Y$ part of the gauge symmetry should be broken, this breaking should be partially realized giving masses to the W and Z boson, and so that a sector of this symmetry remains unbroken to account for the gauge invariance of electromagnetism and the associated massless boson. Explicitly, we must have

$$SU(2)_L \otimes U(1)_Y \xrightarrow{SSB} U(1)_{EM},\tag{1.7}$$

from which we see that three of the four generators of $SU(2)_L \otimes U(1)_Y$ are broken through the SSB. Therefore, the Higgs field (φ) should have at least three real scalars to play the role of the Nambu-Goldstone bosons (NGB), which are *eaten* by the three weak gauge fields, becoming the longitudinal degrees of freedom of the new massive bosons. From this symmetry breaking pattern, a massless vectorial boson associated to an unbroken generator and a real physical scalar field remain, recognized respectively as the photon and the Higgs boson.

The Lagrangian leading to the SSB is expressed as

$$\mathcal{L}^{\text{Higgs}} = (D_\mu\varphi)^\dagger (D^\mu\varphi) - V(\varphi),\tag{1.8}$$

with the potential

$$V(\varphi) = \lambda\left(\varphi^\dagger\varphi - \frac{1}{2}v^2\right)^2,\tag{1.9}$$

where $v > 0$ and $\lambda > 0$. This potential has a minimum at a non-trivial vacuum expectation value (VEV), $\langle\varphi\rangle$. The arbitrary VEV can be rotated by applying $SU(2)_L$ transformations such that

$$\langle\varphi\rangle = \begin{pmatrix} 0 \\ v/\sqrt{2} \end{pmatrix}.\tag{1.10}$$

The origin of the spontaneous symmetry breaking comes from the fact that despite the Lagrangian in Eq. (1.8) is invariant under the $SU(2)_L \otimes U(1)_Y$ symmetry, the VEV in Eq. (1.10) is not.

	ℓ_L	ℓ_R	ν_L	u_L	d_L	u_R	d_R	φ^+	h
τ^3	$-\frac{1}{2}$	0	$\frac{1}{2}$	$\frac{1}{2}$	$-\frac{1}{2}$	0	0	$\frac{1}{2}$	$-\frac{1}{2}$
Y	-1	-2	-1	$\frac{1}{3}$	$\frac{1}{3}$	$\frac{4}{3}$	$-\frac{2}{3}$	1	1
Q	-1	-1	0	$\frac{2}{3}$	$-\frac{1}{3}$	$\frac{2}{3}$	$-\frac{1}{3}$	1	0

Table 1.1: Quantum numbers Q, τ^3 and Y for the fermion and Higgs field.

The Higgs field can be parametrized around its minimum by

$$\varphi \;=\; \frac{1}{\sqrt{2}} e^{-i\chi^i \tau^i} \begin{pmatrix} 0 \\ v+h \end{pmatrix}, \tag{1.11}$$

where the χ^a are the NGB's and the radial mode h is the Higgs boson. After spontaneous symmetry breaking, we have that the potential of the scalar sector is

$$V(\varphi) \;=\; \tfrac{1}{2} m_h h^2 + \lambda v h^3 + \tfrac{\lambda}{4} h^4, \tag{1.12}$$

where the Higgs mass is $m_h^2 = 2\lambda v^2$. As a result in the SM, the cubic and quartic self coupling interactions of the Higgs are fixed by its mass and the vacuum expectation value.

By applying the Goldstone theorem, we realize that the only unbroken symmetry arises from transformations along the linear combination of generators $Q = \tau^3 + \frac{Y}{2}\mathbb{1}_{2\times 2}$, where Q is identified as the electric charge generator and $Y = 1$ for the Higgs boson (See Table 1.1 for the values of the isospin, hypercharge and electric charge of the matter fields and the Higgs boson). The physical electroweak bosons can also be identified with the mass eigentstates, and their interactions with the Higgs boson are completely fixed by the kinetic term of the Higgs doublet. Thus, rotation of the gauge fields leaves the electromagnetic field massless and with the corresponding the unbroken generator Q. We notice that by defining $\tau^\pm = \tau^1 \pm i\tau^2$, the commutation relations

$$\left[Q, \tau^\pm\right] \;=\; \left[\tau^3, \tau^\pm\right] = \pm\tau^\pm \tag{1.13}$$

are obtained, suggesting that the gauge bosons corresponding to τ^+ and τ^- are electrically positive and negative charged, respectively. We can rotate the

gauge fields by doing

$$W_\mu^\pm = \frac{1}{\sqrt{2}} \left(W_\mu^1 \mp i W_\mu^2 \right), \tag{1.14}$$

$$Z_\mu = c_W W_\mu^3 - s_W B_\mu, \tag{1.15}$$

$$A_\mu = s_W W_\mu^3 + c_W B_\mu, \tag{1.16}$$

where the rotation angle is defined as $s_W \equiv \sin\theta_W = g_1/\sqrt{g_1^2 + g_2^2}$. The electromagnetic constant is identified to be $e = g_2 \, s_W = g_1 c_W$. This defines the physical vector bosons of the electroweak sector. Under these field re-definitions and by choosing a gauge in which the Higgs field is written as

$$\varphi = \frac{1}{\sqrt{2}} \begin{pmatrix} 0 \\ v + h \end{pmatrix}, \tag{1.17}$$

corresponding to the Unitary gauge, the kinetic term of the Higgs fields is written as

$$|D_\mu \varphi|^2 = \frac{1}{2} \partial_\mu h \partial^\mu h + M_W^2 W_\mu^+ W^{-\mu} + \frac{1}{2} M_Z^2 Z_\mu Z^\mu \\ + \frac{1}{8} \left(2vh + h^2 \right) \left(2g^2 W_\mu^+ W^{-\mu} + g_Z^2 Z_\mu Z^\mu \right), \tag{1.18}$$

where it has been identified $M_Z = \frac{1}{2} v \sqrt{g_1^2 + g_2^2}$ and $M_W = \frac{1}{2} g_2 v$. Hence, the BEH mechanism provides the mass of the bosons $W_\mu^\pm$ and Z_μ. In this particular gauge, the Goldstone bosons do not appear as propagating fields, nevertheless they provide the missing degrees of freedom to make the weak bosons massive. Moreover, the couplings of the W and Z bosons to the Higgs are entirely fixed by their masses and the VEV.

Sometimes it is convenient to work in different gauges. We introduce a generalization of the class of Lorenz gauges: the renormalizability, or R_ξ, gauges. Let's use the following parametrization for the Higgs field:

$$\varphi = \begin{pmatrix} \varphi^+ \\ (v + h + i\varphi_Z)/\sqrt{2} \end{pmatrix}, \quad \widetilde{\varphi} = i\sigma_2 \varphi^* = \begin{pmatrix} (v + h - i\varphi_Z)/\sqrt{2} \\ -\varphi^- \end{pmatrix}, \tag{1.19}$$

with $\varphi^\pm = \chi^1 \pm \chi^2$ and $\varphi_Z = \chi^3$. The gauge-fixing Lagrangian has the form

$$\mathcal{L}^{R_\xi} = -\frac{1}{2\xi} F_G^2 - \frac{1}{2\xi} F_A^2 - \frac{1}{2\xi} F_Z^2 - \frac{1}{\xi} F_- F_+, \tag{1.20}$$

with

$$F_G^a = \partial^\mu G_\mu^a, \qquad F_A = \partial^\mu A_\mu, \qquad F_Z = \partial^\mu Z_\mu - \xi M_Z \varphi_Z, \quad (1.21)$$

$$F_+ = \partial^\mu W_\mu^+ - i\xi M_W \varphi^+, \quad (1.22)$$

$$F_- = \partial^\mu W_\mu^- + i\xi M_W \varphi^-. \quad (1.23)$$

The Unitary gauge corresponds to $\xi \to \infty$. Most loop computations are simpler in the Feynman–'t Hooft gauge, in which $\xi = 1$.

In order to have a consistent QFT, we must specify the Lagrangian for the ghosts. Although unphysical particles, ghosts preserve unitarity during the quantization process of non-Abelian theories. With the Faddeev-Popov technique, we have

$$\mathcal{L}^{\text{Ghost}} = \sum_{i=1}^{4} \left[\bar{c}_+ \frac{\partial (\delta F_+)}{\partial \alpha^i} + \bar{c}_- \frac{\partial (\delta F_+)}{\partial \alpha^i} + \bar{c}_Z \frac{\partial (\delta F_Z)}{\partial \alpha^i} + \bar{c}_A \frac{\partial (\delta F_A)}{\partial \alpha^i} \right] c_i$$

$$+ \sum_{a,b=1}^{8} \bar{\omega}^a \frac{\partial (\delta F_G^a)}{\partial \beta^b} \omega^b, \quad (1.24)$$

where the ghosts related to the QCD sector are denoted with ω^a and the ghosts associated to the electroweak sector are denoted with $c_\pm$, c_A, c_Z. To be more explicit, we redefine the parameters of the electroweak sector as

$$\alpha^\pm = \frac{\alpha^1 \mp \alpha^2}{\sqrt{2}}, \alpha_Z = \alpha^3 \cos\theta_W + \alpha^4 \sin\theta_W, \alpha_A = -\alpha^3 \sin\theta_W + \alpha^4 \cos\theta_W.$$

$$(1.25)$$

Then, we have the set of transformations

$$\delta F_G^a = -\partial_\mu \beta^a + g_s f^{abc} \beta^b G_\mu^c, \quad (1.26)$$

$$\delta F_A = -\partial_\mu \alpha_A, \quad (1.27)$$

$$\delta F_Z = \partial_\mu (\delta Z^\mu) - M_Z \delta\varphi_Z, \quad (1.28)$$

$$\delta F_+ = \partial_\mu (\delta W_\mu^+) - iM_W \delta\varphi^+, \quad (1.29)$$

$$\delta F_- = \partial_\mu (\delta W_\mu^-) - iM_W \delta\varphi^-, \quad (1.30)$$

where, for the electroweak bosons,

$$\delta Z_\mu = -\partial_\mu \alpha_Z + igc_W \left(W_\mu^+ \alpha^- - W_\mu^- \alpha^+ \right), \quad (1.31)$$

$$\delta W_\mu^\pm = -\partial_\mu \alpha^\pm \pm ig \left[\alpha^\pm \left(Z_\mu c_W - A_\mu s_W \right) - \left(\alpha_Z c_W - \alpha_A s_W \right) W_\mu^\pm \right], \quad (1.32)$$

while, for the unphysical scalars,

$$\delta\varphi_Z = -\frac{1}{2}g\left(\alpha^-\varphi^+ + \alpha^+\varphi^-\right) + \frac{g}{2c_W}\alpha_Z\left(v+h\right), \tag{1.33}$$

$$\delta\varphi^\pm = \mp i\frac{g}{2}\left(v+h\pm i\varphi_Z\right)\alpha^\pm \mp i\frac{gc_{2W}}{2c_W}\varphi^\pm\alpha_Z \pm ie\varphi^+\alpha_A. \tag{1.34}$$

Now that we have a consistent construction for the interactions, all we need is to include the matter content of the SM. The GWS theory is known to be a chiral gauge theory, *i.e.* left- and right-handed components of the fermions can have different quantum numbers under the gauge group. Specifically, just the left-handed components of the fermions are sensitive to the weak interaction, while the right-handed are not. The sensitive components to $SU(2)_L$ transform in the fundamental representation, therefore we define the quark and lepton doublets as

$$q_p = \left\{\begin{pmatrix} u_L \\ d_L \end{pmatrix}, \begin{pmatrix} c_L \\ s_L \end{pmatrix}, \begin{pmatrix} t_L \\ b_L \end{pmatrix}\right\}, \quad \ell_p = \left\{\begin{pmatrix} \nu_{e_L} \\ e_L \end{pmatrix}, \begin{pmatrix} \nu_{\mu_L} \\ \mu_L \end{pmatrix}, \begin{pmatrix} \nu_{\tau_L} \\ \tau_L \end{pmatrix}\right\}. \tag{1.35}$$

The right-handed components are then $SU(2)_L$-singlets: $u_p = \{u_R, c_R, t_R\}$, $d_p = \{d_R, s_R, b_R\}$, $e_p = \{e_R, \mu_R, \tau_R\}$. With these definitions, we can specify the couplings of fermions to the gauge bosons of the electroweak sector. The Lagrangian of the kinetic terms of the fermions has the form

$$\mathcal{L}^{\text{Fermion}} = i\bar{q}_p\slashed{D}q_p + i\bar{u}_p\slashed{D}u_p + i\bar{d}_p\slashed{D}d_p + i\bar{\ell}_p\slashed{D}\ell_p + i\bar{e}_p\slashed{D}e_p, \tag{1.36}$$

where a sum over the generation index p is implicit. Here, we must note that the hypercharges of the two components of any doublet are the same, because of the commutation relations between $SU(2)_L$ and $U(1)_Y$, or equivalently because the symmetry can be written as the direct product of the two groups.

A fundamental difference can be noticed between leptons and quarks: the former are singlets of the $SU(3)_C$ while the latter are in the fundamental representation. Thus, the covariant derivatives used for the quarks in this section must include the term with the gluon fields that appears in Eq. (1.1). The Lagrangian in Eq. (1.36) encodes the kinetic terms, the strong and the electroweak interactions of the fermions, $\mathcal{L}^{\text{Fermion}} = \mathcal{L}^{\text{Fermion}}_{\text{Kin.}} + \mathcal{L}^{\text{Fermion}}_{\text{QCD}} +$

$\mathcal{L}_{\text{EW}}^{\text{Fermion}}$. Explicitly, the kinematic and interaction terms in Eq. (1.36) are

$$\mathcal{L}_{\text{Kin.}}^{\text{Fermion}} = i\bar{q}_p\slashed{\partial}\, q_p + i\bar{u}_p\slashed{\partial}\, u_p + i\bar{d}_p\slashed{\partial}\, d_p + i\bar{\ell}_p\slashed{\partial}\, \ell_p + i\bar{e}_p\slashed{\partial}\, e_p, \qquad (1.37)$$

$$\mathcal{L}_{\text{QCD}}^{\text{Fermion}} = -g_s G_\mu J_s^\mu, \qquad (1.38)$$

$$\mathcal{L}_{\text{EW}}^{\text{Fermion}} = -\frac{g}{\sqrt{2}} W_\mu^+ J^{\mu+} - \frac{g}{\sqrt{2}} W_\mu^- J^{\mu-} - e A_\mu J_Q^\mu - \frac{e}{s_W c_W} Z_\mu J_Z^\mu, \qquad (1.39)$$

with the Noether currents given by

$$J_s^\mu = \bar{q}_p\gamma^\mu q_p + \bar{u}_p\gamma^\mu u_p + \bar{d}_p\gamma^\mu d_p, \qquad (1.40)$$

$$J^{\mu+} = \bar{u}_{p,L}\gamma^\mu d_{p,L} + \bar{\nu}_{p,L}\gamma^\mu e_{p,L}, \qquad (1.41)$$

$$J^{\mu-} = \bar{d}_{p,L}\gamma^\mu u_{p,L} + \bar{e}_{p,L}\gamma^\mu \nu_{p,L}, \qquad (1.42)$$

$$J_Q^\mu = \frac{2}{3}\bar{q}_1\gamma^\mu q_1 - \frac{1}{3}\bar{q}_2\gamma^\mu q_2 + \frac{2}{3}\bar{u}_p\gamma^\mu u_p - \frac{1}{3}\bar{d}_p\gamma^\mu d_p - \bar{e}_p\gamma^\mu e_p, \qquad (1.43)$$

$$\begin{aligned}
J_Z^\mu &= \bar{u}_{p,L}\left(\frac{1}{2} - \frac{2}{3}s_W^2\right)\gamma^\mu u_{p,L} + \bar{d}_{p,L}\left(-\frac{1}{2} + \frac{1}{3}s_W^2\right)\gamma^\mu d_{p,L} \\
&\quad + \bar{u}_{p,R}\left(-\frac{2}{3}s_W^2\right)\gamma^\mu u_{p,R} + \bar{d}_{p,R}\left(\frac{1}{3}s_W^2\right)\gamma^\mu d_{p,R} \\
&\quad + \bar{e}_{p,L}\left(s_W^2 - \frac{1}{2}\right)\gamma^\mu e_{p,L} + \bar{e}_{p,R}\left(s_W^2\right)\gamma^\mu e_{p,R} \\
&\quad + \bar{\nu}_{p,L}\left(\frac{1}{2}\right)\gamma^\mu \nu_{p,L}.
\end{aligned} \qquad (1.44)$$

Last but not least, we introduce mass terms for the fermions. The usual mass terms $m\bar{\psi}\psi$ spoil the $SU(2)_L \otimes U(1)_Y$ symmetry because fermions of different chiralities have different gauge transformations. In the SM, the fermions get their masses through BEH mechanism through Yukawa couplings with the Higgs field. We write

$$\mathcal{L}^{\text{Yukawa}} = -(y_u)_{pr}\bar{q}_p\widetilde{\varphi}u_r - (y_d)_{pr}\bar{q}_p\varphi d_r - (y_e)_{pr}\bar{\ell}_p\varphi e_r + \text{h.c.} \qquad (1.45)$$

The fermion-mass matrices $M^u = v y_u/\sqrt{2}$, $M^d = v y_d/\sqrt{2}$ and $M^e = v y_e/\sqrt{2}$ are obtained from the VEV of the Higgs field, which can be readily seen in the Unitary gauge. The fermionic field basis can be rotated such that these matrices are diagonalized, with the eigenvalues corresponding to

real and positive masses m_f. Therefore

$$\mathcal{L}^{\text{Yukawa}} = \left(1 + \frac{h}{v}\right)\left(m_u\bar{u}u + m_c\bar{c}c + m_t\bar{t}t + m_d\bar{d}d + m_u\bar{s}s + m_b\bar{b}b\right.$$
$$\left. m_e\bar{e}e + m_\mu\bar{\mu}\mu + m_\tau\bar{\tau}\tau\right). \tag{1.46}$$

The Yukawa interactions between the Higgs and a fermion is therefore proportional to the mass of the considered fermion. Consequently, the strongest coupling to the Higgs boson is the top quark Yukawa coupling.

The interaction terms appearing in the Lagrangian of Eq. (1.39) are manifestly modified by the field-basis change used to diagonalize the mass matrices. Since the change of the field basis is $u'_L = L_u u_L$ and $d'_L = L_d d_L$, $\bar{u}_L\gamma^\mu d_L = \bar{u}'_L L_u\gamma^\mu L_{d\dagger}d'_L = \bar{u}'_L\gamma^\mu V_{CKM}d'_L$, where $V_{CKM} \equiv L^u L^{d\dagger}$ is the Cabibbo-Kobayashi-Maskawa (CKM) mixing matrix. The CKM matrix is parametrized by three angles and one complex phase that takes into account CP violation. There are two kinds of electroweak interactions involving fermions in the weak sector: the flavor-changing charged currents, generated by the $W^\pm$ bosons, and the flavor-preserving neutral currents, mediated by the Z and the A bosons.

The full Lagrangian of the SM is then given by adding up the different sectors presented above:

$$\mathcal{L}^{\text{SM}} = \mathcal{L}^{\text{YM}} + \mathcal{L}^{\text{Higgs}} + \mathcal{L}^{R_\xi} + \mathcal{L}^{\text{Ghost}} + \mathcal{L}^{\text{Fermion}} + \mathcal{L}^{\text{Yukawa}}. \tag{1.47}$$

The fermionic fields and Higgs boson appearing in this Lagrangian transform under $SU(3)_c \otimes SU(2)_L \otimes U(1)_Y$ as

$$q_p \sim \left(3, 2, \frac{1}{3}\right), \quad u_p \sim \left(3, 1, \frac{4}{3}\right), \quad d_p \sim \left(3, 1, -\frac{2}{3}\right), \tag{1.48}$$

$$\ell_p \sim (1, 2, -1), \quad e_p \sim (1, 1, -2), \quad \varphi \sim (1, 2, 1). \tag{1.49}$$

The Standard Model is determined by a total of 18 parameters: there are 3 gauge couplings, 2 constants from the Higgs potential, 3 lepton masses, 6 quark masses and 4 CKM parameters. As a result, we must choose the best 18 measured quantities that allow us to determine the full set of parameters to make predictions as accurate as possible. In addition to the parameters counted above, there is one extra parameters to be determined corresponding to the vacuum angle θ of QCD. The θ parameter is allowed by gauge symmetry and associated to CP-violating contributions, but it is not included here because is much smaller than one.

Currently, all the fermion masses have been directly measured, as well as the CKM parameters, obtained from flavor physics experiments.

The best measured quantities in the SM are the magnetic moment of the electron (g_e), the muon lifetime (τ_μ) and the pole mass of the Z-boson:

$$\frac{g_e - 2}{2} = (1159.65218091 \pm 0.00000026) \cdot 10^{-6}, \qquad (1.50)$$

$$\tau_\mu^{-1} = 2.99588(1) \times 10^{-19} \text{ GeV}, \qquad (1.51)$$

$$M_Z = 91.1876 \pm 0.0021 \text{ GeV}. \qquad (1.52)$$

The first two quantities are measured in the rest-frame. The Z pole mass is measured at the electroweak scale ($\sqrt{s} \sim M_Z$). The electric magnetic moment gives the fine-structure constant through the 1-loop relation $g_e - 2 = \frac{\alpha(0)}{\pi}$, so that $\alpha^{-1}(0) = 137.035999139(31)$. The muon lifetime enables the determination of the Fermi constant (G_F) by noticing that the width of the muon at tree-level is

$$\Gamma_\mu = \frac{G_F^2 m_\mu^5}{192\pi^3}, \qquad (1.53)$$

which yields $G_F = 1.1663787(6) \cdot 10^{-5}$ GeV^{-2}. Furthermore, the last result provides the value of the VEV since $G_F/\sqrt{2} = g_2^2/8M_W^2 = 1/2v^2$, hence $v = 246$ GeV. Once those SM parameters are known, we can make predictions for all the other parameters. For example, the weak mixing angle can be predicted as a combination of $\{\alpha, G_F, M_Z\}$ and is measured through asymmetries in processes, such as the forward-backward asymmetry in $e^+e^- \to \mu^+\mu^-$, leading to $s_W^2 = 0.23129(5)$ at $\sqrt{s} = M_Z$. In the case of the mass of the W-boson, if the relation $e = g_2 s_W$ is used in the definition of M_W, we can predict through the formula $M_W = ev/2s_W$ that at tree-level $M_W = 79.794$ GeV. This prediction is close to the measured value and can be improved by including radiative corrections. This motivates the high precision program of electroweak observables [16].

Furthermore, the Higgs mass finally determines the scalar potential of the SM. A direct measurement of the triple and quartic Higgs interactions is yet to be performed, but it will test the SM. Production of Higgs bosons via the single, double and triple Higgs are expected to provide constraints on the Higgs self-interactions, but they are not expected to be accessible in the near future. Some hints point at a scenario where the full story about the Higgs sector is not completely told. The Higgs boson acquires its mass from the VEV, but it receives quadratically divergent contributions through loop corrections. These

divergent terms cancel out by the addition of the counter-terms when using dimensional regularization. The problem arises when we consider the fact the SM is not the ultimate theory for nature, but the low-energy limit of a given theory beyond the SM. Because of this, the Higgs mass parameter is sensitive to UV parameters via loop corrections. In this context, it is suitable to use cutoff regularization to estimate the corrections to the Higgs mass arising at the UV scale, so that

$$\delta m_h^2 = \left(\frac{3\lambda_t^2}{4\pi^2} - \frac{9g_2^2}{32\pi^2} - \frac{3g_1^2}{32\pi^2} - \frac{3\lambda}{8\pi^2} + \ldots \right) \Lambda^2, \qquad (1.54)$$

where Λ stands as the UV scale. The corrections in Eq. (1.54) can be much larger than the measured value of m_h^2, therefore fine-tuning is required to have them under control. In this case, the Higgs mass seems to be an oddly small parameter without any symmetry protecting it. This motivates several models proposing new physics in which symmetries protect the Higgs mass.

As it stands, the Higgs potential of the SM is the minimal possible realization of the BEH mechanism in agreement with the experimental data even though it remains partially unexplored. The complete Higgs sector may not be the simplest one proposed in the SM but may contain multiple isospin multiplets. Models including extended Higgs sectors are motivated by electroweak baryogenesis aiming to solve the matter-antimatter problem. Although the study of BSM extensions is beyond the goal of this thesis, below we outline some ideas that attempt to explain some of the phenomena that escape the reach of the SM

- **Supersymmetric models** (SUSY), in which the Poincaré algebra is extended by introducing anti-commuting spinor generators. Supersymmetric models predict many new particles with the same masses as the SM particles unless SUSY is broken. Representative models are the minimal- and next-to minimal- supersymmetric Standard Model (MSSM and NMSSM, respectively) [17–20]. One of the challenges of these theories is to present a satisfactory breaking mechanism of the supersymmetry.

- **Non-linear realizations** of the SSB describes the Higgs boson as a composite state and not a fundamental particle. The Higgs boson is proposed to be the Goldstone boson from a new spontaneously broken global symmetry [21–25].

- the **Singlet extension** [26, 27], **two Higgs doublet model (2HDM)** [28, 29] and the **Georgi-Machacek model** [30, 31], which are examples of proposals where new scalars are introduced without the need of new symmetries. In certain cases, this kind of models can be seen as sectors of the models mentioned above. Just like the SM, this kind of models do not address the hierarcy problem, but open the possibility for stronger first-order phase-transitions, hence of relevance in baryogenesis.

- **Extra dimensions** appear as the main ingredient in several models. When expanding the fields in higher dimensions, the SM particles are recovered and new additional Kaluza-Klein modes corresponding to new particles are predicted. The mass hierarchy is understood thanks to the localization of the field on the different branes.

- **Technicolor theories** propose that there are no elementary scalars in nature. Instead of using the Higgs mechanism to provide masses to the SM particles they introduce new particles that break the electroweak group in analogy to the case of the lightest mesons in QCD.

New physics is believed to couple to the Higgs boson, for which the largest known coupling is the Yukawa interaction with the top quark. In fact, the top quark is the only SM particle with a coupling of order one. The top sector presents potential for the search for new physics, has been broadly analyzed in collider experiments and is actively being probed at the LHC.

Chapter 2

The Standard Model Effective Field Theory

The proposed SM extensions discussed in the end of the previous chapter introduce new particles coupled to the SM fields. Such particles have been extensively searched in collider experiments without success, which strongly motivates the precision program to search for new physics. This is where the idea of Effective Field Theories (EFT) comes at hand. The aim of the EFTs is to parametrize the deviations from the SM by the introduction of new interactions between the SM fields induced by heavy new physics.

There are multiple contexts where EFTs are useful. From QCD, many effective theories can be constructed depending on the set up. Decays and production near the threshold energy of heavy quarkonium are well described by the Non-Relativistic QCD (NRQCD), valid in the limit low velocities (v) $m_Q \gg m_Q v, m_Q v^2, \Lambda_{\text{QCD}}$ [32]. The physics of heavy quark systems (c,b and t quarks) is well captured by an expansion in the the parameter Λ_{QCD}/m_Q in the Heavy Quark Effective Theory (HQET) [33]. Developed in the 1960s [34–36], Chiral Perturbation Theory (χPT) allows the analysis of the QCD dynamics at low energies, with a cutoff at around $\Lambda_\chi \sim 1$ GeV. χPT is an interesting example of an EFT for which the fields at low energies are totally different from the ones in the full theory and for which is not possible to compute the matching analytically [37].

In general, EFTs are suitable in situations with scale separations. As experiments indicate, the long-searched BSM physics seems to be at higher scales than the electroweak scale, making the use of the SMEFT suitable for the study of the physics within the energy range of the current accelerators. The goal of

this chapter is to provide an introduction to the main concepts in the application of EFTs to particle physics.

2.1   Fermi theory

The example *par excellence* of EFTs in particle physics is the Fermi theory, precursor of the SM. Pauli's proposal for the existence of the neutrino lead to Fermi's formulation of the β decay assuming that the missing energy in the experiments had escaped our means to detect it. The β decay and the muon decay can be described by the effective Lagrangian containing the product of axial and vector currents

$$\mathcal{L}^{\text{Fermi}} = -\frac{G^{(\beta)}}{\sqrt{2}}(\bar{p}\gamma^\alpha(1-a\gamma_5)n)(\bar{e}\gamma_\alpha(1-\gamma_5)\nu_e)$$
$$-\frac{G^{(\mu)}}{\sqrt{2}}(\bar{\nu}_\mu\gamma^\alpha(1-\gamma_5)\mu)(\bar{e}\gamma_\alpha(1-\gamma_5)\nu_e), \qquad (2.1)$$

where $G^{(\beta)} \simeq G^{(\mu)} \equiv G_F$ comes to be the effective coupling of the theory. The muon decay, $\mu^-(p_1) \rightarrow e^-(p_2)\bar{\nu}_e(p_3)\nu_\mu(p_4)$, can be computed from this Lagrangian. The amplitude for the process shown in Fig. 2.1b is written as

$$\mathcal{M} = -i\frac{G_F}{\sqrt{2}}\bar{u}(p_2)\gamma^\alpha(1-\gamma_5)v(p_3)\bar{u}(p_4)\gamma_\alpha(1-\gamma_5)u(p_1). \qquad (2.2)$$

Therefore, after squaring and properly dealing with the helicities we obtain

$$|\mathcal{M}(\mu^- \rightarrow e^-\bar{\nu}_e\nu_\mu)|^2 = 4G_F^2\text{Tr}[\not{p}_2\gamma^\alpha P_L\not{p}_3\gamma^\beta P_L]\,\text{Tr}[\not{p}_4\gamma_\alpha P_L(\not{p}_1 + m_\mu)\gamma_\beta P_L]$$
$$= 4G_F^2\,(p_1 \cdot p_3)(p_2 \cdot p_4), \qquad (2.3)$$

where the electron is considered massless. In the rest frame of the muon, the scalar products above are found to be

$$p_1 \cdot p_3 = m_\mu E_3, \qquad p_2 \cdot p_4 = \frac{1}{2}m_\mu\,(m_\mu - 2E_3)\,, \qquad (2.4)$$

with E_3 as the energy of the electron neutrino.

$$|\mathcal{M}(\mu^- \rightarrow e^-\bar{\nu}_e\nu_\mu)|^2 = 32m_\mu^2 G_F^2\,(\mu - 2E_3)E_3. \qquad (2.5)$$
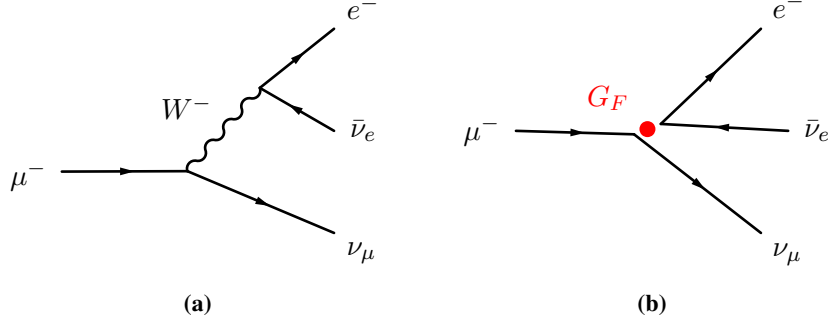
Figure 2.1: Feynman diagram of the most common decay of muon $\mu^- \to e^- \bar{\nu}_e \nu_\mu$ in (a) the SM and (b) the Fermi theory.

Finally, we perform the integral over E_3, yielding

$$\Gamma\left(\mu^- \to e^- \bar{\nu}_e \nu_\mu\right) = \frac{m_\mu^2 G_F^2}{4\pi^3} \int_0^{\frac{1}{2}m_\mu} dE_2 \, E_2^2 \left(1 - \frac{4}{3}\frac{E_2}{m_\mu}\right)$$

$$= \frac{m_\mu^5 G_F^2}{192\pi^3}. \tag{2.6}$$

This is the result already not computed in Eq. (1.53). The computation in the SM renders the same result, but as it can be seen, there was no need to know the nature of the underlying UV completion of the EFT. In the bottom-up approach, to know the decay rate, only the measurement of the new parameter G_F is required.

When the UV origin of the Fermi constant was unknown, unitarity can shed light on the scale of its UV-completion. To see this, we recall that amplitudes can be expanded in partial waves by means of the Legendre polynomials $P_\ell(\cos\theta)$ as

$$\mathcal{M}(s,t) = 16\pi \sum_\ell (2\ell + 1) a_\ell(s) P_\ell(\cos\theta), \tag{2.7}$$

with s and t the Mandelstam variables of the process. The functions a_ℓ are the partial-wave amplitudes, which can be computed as

$$a_\ell(s) = \frac{1}{32\pi} \int_{-1}^{1} d\cos\theta \, P_\ell(\cos\theta) \mathcal{M}(s,t). \tag{2.8}$$

From the optical theorem, it is known that the partial wave amplitudes satisfy the bounds

$$|a_\ell(s)| \leq 1, \quad \text{and} \quad \operatorname{Re} a_0 < \frac{1}{2}, \tag{2.9}$$

which is required by the unitarity of the scattering matrix.

Now, let us turn our attention on the reaction

$$e^-(p_1)\nu_\mu(p_2) \to \mu^-(p_3)\nu_e(p_4), \tag{2.10}$$

with the corresponding amplitude

$$\mathcal{M} = -\frac{G_F}{\sqrt{2}}\bar{u}(p_4)\gamma^\alpha(1-\gamma_5)u(p_1)\,\bar{u}(p_3)\gamma_\alpha(1-\gamma_5)u(p_2). \tag{2.11}$$

which, in the massless limit, leads to

$$|\mathcal{M}(e^-\nu_\mu \to \mu^-\nu_e)|^2 = \frac{G_F^2}{2}\text{Tr}[\slashed{p}_1\gamma^\alpha P_L\slashed{p}_4\gamma^\beta P_L]\,\text{Tr}[\slashed{p}_2\gamma_\alpha P_L\slashed{p}_3\gamma_\beta P_L]$$

$$= 32G_F^2\,s^2, \tag{2.12}$$

where sum over polarization has been taken. Since there is no dependence on $\cos\theta$, this process occurs purely as an s-wave. The corresponding partial wave is computed from the Eq. (2.8):

$$|a_0(s)| = \frac{G_F s}{2\sqrt{2}\pi}. \tag{2.13}$$

Hence, unitarity is violated at an energy

$$\sqrt{s} = \left(\frac{2\sqrt{2}\pi}{G_F}\right)^{1/2} \simeq 875\,\text{GeV}. \tag{2.14}$$

It is interesting to see that this unitarity violation does not occur at the W mass due to weak nature of the couplings. In the unitary gauge, the amplitude for the same process in the SM is

$$\mathcal{M} = -i\frac{g^2}{2}\bar{u}(p_4)\gamma^\alpha P_L u(p_1)\,\frac{-g_{\alpha\beta} + q_\alpha q_\beta/M_W^2}{q^2 - M_W^2}\bar{u}(p_3)\gamma^\beta P_L u(p_2). \tag{2.15}$$

with $q^\alpha = p_1^\alpha - p_4^\alpha$. The momentum dependence in the numerator of the propagator vanishes when the Dirac equation is used in the massless limit. The following steps are just like in the previous computation using the Fermi Lagrangian. In this case, the squared unpolarized amplitude turns out to be

$$|\mathcal{M}(e^-\nu_\mu \to \mu^-\nu_e)|^2 = \frac{g^4 s^2}{(t - M_W^2)^2}. \tag{2.16}$$
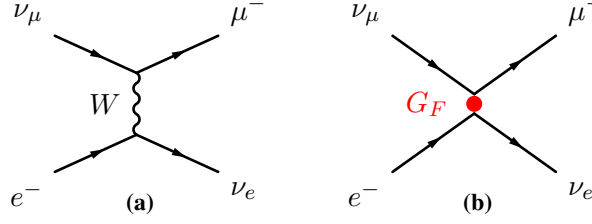
Figure 2.2: Feynman diagrams of the $e^-\nu_\mu \to \mu^-\nu_e$ scattering in (a) the SM and (b) the Fermi theory.

For the total cross-section we obtain

$$\sigma = \frac{g^4}{64\pi M_W^2} \frac{s}{s + M_W^2}.$$ (2.17)

The linear growth obtained in the EFT gets damped by the UV propagator, and the total cross-sections start to deviate from the EFT values significantly at $\sqrt{s} \sim M_W$. In the low energy limit, with $s \ll M_W^2$, the expression in Eq. (2.16) can be approximated thanks to

$$\frac{1}{t - M_W^2} \approx \frac{1}{M_W^2}\left(1 + \frac{t}{M_W^2} + \dots\right),$$ (2.18)

in such a way that when compared to the amplitude in Eq. (2.12) arising from the EFT, the relationship

$$\frac{G_F}{\sqrt{2}} = \frac{g^2}{8M_W^2},$$ (2.19)

is recovered. The Eq. (2.19) shown the relation between the effective couplings and the parameters from the UV completion is known as matching. We notice that a numerical value on the effective constant G_F does not provide the value for the masses of the heavy states, instead, it gives information about the ratio between the coupling g and the mass M_W. This is a general feature of EFTs.

In the introduction, we presented the muon lifetime at leading-order which can be derived from the SM. Back in the days when the mechanism of the decay of unstable nuclei was unknown, non-renormalizable theories were instrumental in the computation of lifetimes. Hence, non-renormalizable theories, although non-fundamental, pragmatically laid the foundations for the SM.

2.2 Formal approach to EFT

The procedure of integrating out degrees of freedom is formally treated in the path integral formulation. For simplicity we consider a theory of a scalar field, φ. The starting point is the Lagrangian for the UV theory, $\mathcal{L}(\varphi)$, being a full description of the physics of the field φ. The modes of the field can be separated into hard (φ_{h}) and soft (φ_{l}) modes as $\varphi = \varphi_{\mathrm{h}} + \varphi_{\mathrm{l}}$. In the regime of low energies the hard modes cannot be accessed as external states, thus the physics at such energies is described by the interactions of φ_{l}. The UV theory is defined by the partition function

$$Z_{\mathrm{UV}}[J_{\mathrm{l}}, J_{\mathrm{h}}] = \int \mathcal{D}\varphi_{\mathrm{l}} \mathcal{D}\varphi_{\mathrm{h}} \exp\left\{\left(i \int d^4x \left(\mathcal{L}_{\mathrm{UV}}(\varphi_{\mathrm{l}}, \varphi_{\mathrm{h}}) + J_{\mathrm{l}}\varphi_{\mathrm{l}} + J_{\mathrm{h}}\varphi_{\mathrm{h}}\right)\right)\right\}$$

(2.20)

The n-point amplitudes are generated by functional derivatives of Z_{UV} with respect to the currents J_{h} and J_{l}. In the low-energy regime, $E \ll \Lambda$, we can set the external current $J_{\mathrm{h}} = 0$, additionally, the action of the effective theory is defined as

$$\exp\{(iS_{\mathrm{EFT}}(\varphi_{\mathrm{l}}))\} \equiv \int \mathcal{D}\varphi_{\mathrm{h}} \exp\left\{\left(i \int d^4x \, \mathcal{L}_{\mathrm{UV}}(\varphi_{\mathrm{l}}, \varphi_{\mathrm{h}})\right)\right\}, \quad (2.21)$$

which is understood as the integration of hard degrees of freedom and with the associated Lagrangian $\mathcal{L}_{\mathrm{EFT}}$. Then the amplitudes from the EFT are computed from the partition function

$$Z_{\mathrm{EFT}}[J_{\mathrm{l}}] = \int \mathcal{D}\varphi_{\mathrm{l}} \exp\left\{\left(i \int d^4x \left(\mathcal{L}_{\mathrm{EFT}}(\varphi_{\mathrm{l}}) + J_{\mathrm{l}}\varphi_{\mathrm{l}}\right)\right)\right\}. \quad (2.22)$$

The process above generates a Lagrangian that, in general, contains non-local terms. As an example of such non-local terms we consider the theory where a heavy field with mass M is integrated out, leading to

$$\mathcal{L}_{\mathrm{EFT}} \supset \varphi^2(\Box + M^2)^{-1}\varphi^2. \quad (2.23)$$

In this case the non-locality is of order $r \sim 1/M$. This Lagrangian can be approximated by a local Lagrangian when an expansion around $r = 0$ is possible. Hence, in the limit of heavy masses compared to the momentum of the heavy state

$$(\Box + M^2)^{-1} \approx \frac{1}{M^2} - \frac{\Box}{M^4} + \frac{\Box^2}{M^6} + \dots, \quad (2.24)$$

which provides an infinite series of local operators with contact interactions in the field φ. In the end, the effects at low-energies of the hard modes and physics above the scale Λ is fully encoded in the local operators. In terms of the light modes, the effective Lagrangian has the form

$$\mathcal{L}_{\text{EFT}}(\varphi_l) = \sum_i g_i(\Lambda)\mathcal{O}_i(\varphi_l). \tag{2.25}$$

The coefficients $g_i(\Lambda)$ are normally written as the ratio of the cutoff Λ and the so called Wilson coefficients.

2.3 Power counting

The infinite tower of operators composing the Lagrangian of the effective theory can be systematically categorized, making possible the computation of predictions. This procedure allows us to identify the leading contributing terms. In the context of QFT, typically operators have the generic form

$$\mathcal{O} = (D_\mu)^{d_D}(\bar{\psi}\psi)^{d_\psi}(F^{\mu\nu})^{d_F}(\varphi)^{d_\varphi}, \tag{2.26}$$

where the operators are built respecting the symmetries of the theory. With this, the mass dimension (d) of a given operator is

$$d = d_D + 3d_\psi + 2d_F + d_\varphi. \tag{2.27}$$

In natural units and for theories in 4-dimensions the action is dimensionless, thus the Lagrangian density has mass dimensions $[\mathcal{L}] = 4$. In order to write terms of mass dimension 4 the operators in Eq. (2.25) must be divided by powers of Λ. Explicitly, an operator of dimension d is divided by a factor Λ^n with $n = d - 4$. Let us consider for convenience the 2-to-2 amplitude of a process ocurring at an energy E which by dimensional analysis is dimensionless. Such operator $\mathcal{O}$ leads to a contribution of order

$$\mathcal{M} \sim \left(\frac{E}{\Lambda}\right)^n \tag{2.28}$$

by dimensional analysis when no other scales like the VEV or masses are considered. From this, it follows that in the EFT validity region, $E \ll \Lambda$, the operators with $d > 4$ are suppressed. Thus, it is natural to classify the terms in the Lagrangian as *relevant* for $d < 4$, *marginal* for $d = 4$ and *irrelevant* for $d > 4$, where the names are given due to historical reasons.

The set of operators for $d \leq 4$ that can be built following the symmetries of the theory is finite. On the contrary, the number of irrelevant operators that we can write grows with their dimension [38]. The cutoff Λ provides a starting way to organize our computations, in which the leading contribution is given by the relevant and marginal terms. The leading-order corrections in E/Λ are given by irrelevant operators with $d = 5$, $(E/\Lambda)^2$ corrections are composed by $d = 6$ operators and double insertions of $d = 5$, and so on. The aim is to compute observables to a fixed value of n in Eq. (2.28).

This dimensional analysis allows us to have a first understanding of the renormalizability of an EFT. A Lagrangian built with relevant and marginal terms can be renormalizable, which is guaranteed by its gauge symmetry, but irrelevant operators lead to a non-renormalizable theory. As an heuristic argument, we consider the case where $d = 5$ operators of order E/Λ have a finite coefficient while the coefficients of $d = 6$ operators of order $(E/\Lambda)^2$ are set to zero. Divergent loop corrections arising from the effective interactions might contain double insertions of $d = 5$ operators can be of order $(E/\Lambda)^2$. Therefore, even though at first dimension 6 operators were not included, counter-terms of higher dimensions than 5 have to be included. Nothing can stop us at two insertions of effective operators, thus, in general, an infinite set of counter-terms is required to absorb all of the divergences.

From this, we can see that renormalizable theories are special cases where $\Lambda \rightarrow \infty$. In this cases, all the terms in the Lagrangian have dimension at the most the dimension of the time-space where it is built. On the other hand, non-renormalizable (EFTs) theories are defined as the cases where an infinite set of higher dimensional operators are needed to provide the required counter-terms. Nevertheless, in practice, we are concerned with corrections of a fixed value n, thus requiring a finite number of counter-terms. In this senses, EFTs are known to be renormalizable order by order.

2.4   The precision program for new physics

The absence of resonances beyond the SM observed at colliders suggests that we are in a similar situation to that of particle physics almost one century ago when Fermi proposed his theory for the β-decay. A possibility is that those resonances are beyond the energy reach of colliders, just like the electroweak bosons W and Z eluded the direct searches. This situation is sketched in Fig. 2.3. Instead of looking for new states, the precision program for new physics consists of indirect searches for new interactions leading to deviations from the
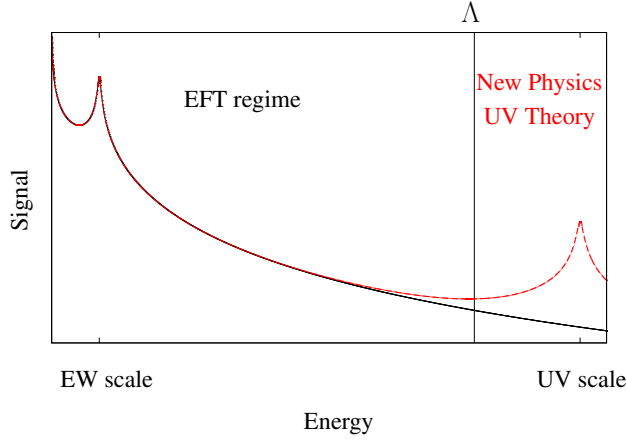
Figure 2.3: Schematic graph representing the EFT approach in the search for new physics.

SM predictions. As shown in Fig. 2.3, such deviations are stronger in the tails of distributions. Additionally, with the imminent start of the Run 3 and with the upgrade to reach high luminosities, the LHC is entering a precision era, hence making precise theoretical predictions necessary to match the experimental progresses. The Lagrangian which parametrizes the new physics effects is built as

$$\mathcal{L}_{\text{EFT}} = \mathcal{L}_{\text{SM}} + \sum_i \frac{c_i^{(n)}}{\Lambda^{n-4}} \mathcal{O}_i^{(n)} + \dots, \tag{2.29}$$

where Λ is the cutoff scale of the EFT and the coefficients c_i are the so-called Wilson coefficients. It is important to clarify that the scale Λ does not set the energy at which new states start to appear, as it is pointed out graphically in Fig. 2.3, and they are not measured separately, *i.e.* only the combinations $c_i^{(n)}/\Lambda^{n-4}$ are measured. The cutoff is a combination of parameters of the UV theory. The ratio between the Wilson coefficients, energy of the process and the cutoff scale ($c_i^{(n)} E^{n-4}/\Lambda^{n-4}$) are very small, and so is the strength of the new interactions that can be mediated by very heavy particles. In the parameter space, EFT extensions are slight deformations of the SM. The effective operators $\mathcal{O}^{(n)}$ are classified according to their dimension n. The effective operators are built depending on the assumptions and the purpose of the EFT.

The deformations given by the effective operators in Eq. (2.29) allows the parametrization of new physics for a given observable O_n

$$\Delta\mathrm{O}_n = \mathrm{O}_n^{\mathrm{Exp}} - \mathrm{O}_n^{\mathrm{SM}}$$
$$= \sum_i \frac{a_{n,i}^{(6)}(\mu)c_i^{(6)}(\mu)}{\Lambda^2} + \sum_{ij} \frac{b_{n,ij}^{(6)}(\mu)c_i^{(6)}(\mu)c_j^{(6)}(\mu)}{\Lambda^4} + \sum_i \frac{a_{n,i}^{(8)}(\mu)c_i^{(8)}(\mu)}{\Lambda^4} + \dots,$$

$$(2.30)$$

where $\mathrm{O}_n^{\mathrm{SM}}$ and the coefficients a_n and b_n depend on the renormalization scale μ and are computed through standard perturbative techniques. For the physics in which we are interested in, only even-dimensions operators are of relevance, as we will see later. The formula above shows that, if we want trustful deviations indicating new physics, we want our experiments and our theoretical predictions from the SM to be performed with a high accuracy. In addition, the parametrization of such deviations must be also accurate and consistent. Hence, to enhance our sensitivity to new physics, we can also improve the predictions from the EFT by going at next to leading orders.

2.5 EFTs for New Physics

There are several realizations of EFTs that can accomplish the task of parametrizing NP effects. A first approach is to assume that the SM describes fully the physics at collider energies. To construct our EFT basis we could require that the Lagrangian symmetries should contain the $SU(3)_c \otimes SU(2)_L \otimes U(1)_Y$ gauge symmetry and all the degrees of freedom of the SM are incorporated. In addition, the Lagrangian of the SM should be recovered when the cutoff is removed, *i.e.* in the limit $\Lambda \to \infty$. Consequently, all the possible operators satisfying the requirements above can be written. The resulting Lagrangian is known as the Standard Model Effective Field Theory (SMEFT) [39–41].

Alternatively, since the Higgs potential has not been measured, we could consider the situation in which the SM does not provide a complete description of the SSB. As a result, a more general approach would be to replace the Higgs doublet defined in Eq. (1.11) by a massive singlet scalar h which accounts for the Higgs boson detected at CERN [42–45]. This approach is known as the Higgs Effective Field Theory (HEFT). The scalar sector of the HEFT collects four scalar fields: the Higgs singlet h and the the Goldstones χ^i ($i = 1, 2, 3$) to be eaten by the W and Z bosons. The first consequence of this choice is that the coefficients of different terms in the scalar potential of the HEFT are

not related by any symmetry, in contrast to the potentials in the SM and the SMEFT. Similar situation is the couplings of EW bosons to the Higgs scalar.

The HEFT offers an advantage over the SMEFT when it comes to capture low energy effects from UV models in which the SSB is non-linearly realized. In this sense the HEFT is a more general approach than the SMEFT, but this generalization has the disadvantage of an increment the amount of free parameters. Moreover, measurements favor the hypothesis of the Higgs boson being part of an $SU(2)_L$ doublet, as can be seen on the constraints of the ρ-parameter associated to the custodial symmetry. For this reason the SMEFT is often the preferred framework for interpreting LHC data in terms of an EFT. The pattern of deviations from the SM could shed light on whether the SMEFT or the HEFT is the more suitable method. Deviations from the SMEFT expectation that follows from the exact $SU(2)_L$ doublet structure would have strong implications about the possible UV physics. To date, all of the measurements are in agreement with the SM and no hints disproving the SMEFT assumptions have been found, but future experimental analyses may shed further light on this issue.

Beyond these two options, different EFTs have been proposed. Some of these are motivated by their convenience at the computational level and by describing physics are other energy scales where even the EW bosons are integrated out [46–50]. Other EFTs aim to include more effects to which other options are not sensitive [51].

Finally, these EFTs can be seen as an upgrade of the well-known κ-framework [52], since the latest does not preserve the gauge symmetries. Moreover, the κ-framework is not a consistent QFT, breaking down due to divergences when radiative corrections are taken into account. This makes it not suitable for the precision program highlighted in the previous section. Nevertheless, sometimes this framework is useful to understand the effects of dimension 6 operators and makes evident the cancellations happening in the SM when we consider preservation of unitarity.

2.6   The SMEFT

From the of EFTs discussed in the previous section, we choose to work in the SMEFT for the rest of this thesis. In this section, we proceed to discuss the construction of its Lagrangian and to present thoroughly the basis conventionally used for SMEFT operators at dimension 6. This basis has been developed through several years, with a first proposal published by Büchmuller and

Wyler [39] finding its final form in the so called Warsaw basis [40]. The process of finding an independent set of operators starts by writing all the possible combination of operators that satisfy the symmetries of the SM. The resulting set has redundancies since many of the operators can be expressed as combinations of other operators up to total derivatives, field redefinitions, Fierz and other identities. This will be discussed further in the next section.

We start by considering the only operator that enters at dimension 5, the Weinberg operator [53]

$$Q_{\nu\nu}^{pr} = (\widetilde{\varphi}^\dagger \ell_p)^T C (\widetilde{\varphi} \ell_r), \tag{2.31}$$

where C indicates charge conjugation and its Hermitian conjugate is also included in the Lagrangian. The convention used above and in the following definitions is the one of the Introduction. This operator violates lepton number (L) conservation by two units $(\Delta L = 2)$ and, in the absence of right-handed neutrinos, it is the only term in the SMEFT that endows neutrinos with masses by generating Majorana mass terms in the broken phase. We notice that since p and r in $Q_{\nu\nu}$ are generation indices it is clear that this operator leads to mixing. This operator can be obtained from Seesaw models by integrating out the heavy right-handed neutrinos or scalars, depending on the type of the Seesaw model. The operator $Q_{\nu\nu}^{pr}$ will be irrelevant for the processes we study here as we will discuss later.

We turn now to the dimension 6 operators, which are listed in Table 2.1 up to generation index combinations. The generations of the matter fields are indicated by $\{p, r, s, t\}$. All of the operators at dimension 6 conserve Lepton number and operators violating Baryon number (B) are separated in a special group. The dual strength tensors are defined as

$$\widetilde{X}^{\mu\nu} = \frac{1}{2}\epsilon^{\mu\nu\rho\sigma} X_{\rho\sigma}, \qquad X_{\mu\nu} \in \{G_{\mu\nu}^A, W_{\mu\nu}^I, B_{\mu\nu}\}. \tag{2.32}$$

We also define the Hermitian derivative

$$\varphi^\dagger i \overleftrightarrow{D}_\mu \varphi = i\varphi^\dagger (D_\mu - \overleftarrow{D}_\mu)\varphi, \qquad \varphi^\dagger i \overleftrightarrow{D}_\mu^I \varphi = i\varphi^\dagger (\tau^I D_\mu - \overleftarrow{D}_\mu \tau^I)\varphi, \tag{2.33}$$

where the index $I = 1, 2, 3$ indicates isospin and D_μ meaning the covariant derivative as presented in chapter 1.

When we consider a fully general flavor structure, the Warsaw basis has 2499 operators [54]. These operators can be divided into the following categories

	X^3		φ^6 and $\varphi^4 D^2$		$\psi^2\varphi^3$
Q_G	$f^{ABC}G_\mu^{A\nu}G_\nu^{B\rho}G_\rho^{C\mu}$	Q_φ	$(\varphi^\dagger\varphi)^3$	$Q_{e\varphi}$	$(\varphi^\dagger\varphi)\,(\bar\ell_p e_r\varphi)$
$Q_{\widetilde{G}}$	$f^{ABC}\widetilde{G}_\mu^{A\nu}G_\nu^{B\rho}G_\rho^{C\mu}$	$Q_{\varphi\Box}$	$(\varphi^\dagger\varphi)\Box(\varphi^\dagger\varphi)$	$Q_{u\varphi}$	$(\varphi^\dagger\varphi)\,(\bar q_p u_r\widetilde{\varphi})$
Q_W	$\varepsilon^{IJK}W_\mu^{I\nu}W_\nu^{J\rho}W_\rho^{K\mu}$	$Q_{\varphi D}$	$(\varphi^\dagger D^\mu\varphi)^*(\varphi^\dagger D_\mu\varphi)$	$Q_{d\varphi}$	$(\varphi^\dagger\varphi)(\bar q_p d_r\varphi)$
$Q_{\widetilde{W}}$	$\varepsilon^{IJK}\widetilde{W}_\mu^{I\nu}W_\nu^{J\rho}W_\rho^{K\mu}$				

	$X^2\varphi^2$		$\psi^2 X\varphi$		$\psi^2\varphi^2 D$
$Q_{\varphi G}$	$\varphi^\dagger\varphi\, G_{\mu\nu}^A G^{A\mu\nu}$	Q_{eW}	$(\bar\ell_p\sigma^{\mu\nu}e_r)\tau^I\varphi W_{\mu\nu}^I$	$Q_{\varphi l}^{(1)}$	$(\varphi^\dagger i\overset{\leftrightarrow}{D}_\mu\varphi)(\bar\ell_p\gamma^\mu\ell_r)$
$Q_{\varphi\widetilde{G}}$	$\varphi^\dagger\varphi\,\widetilde{G}_{\mu\nu}^A G^{A\mu\nu}$	Q_{eB}	$(\bar\ell_p\sigma^{\mu\nu}e_r)\varphi B_{\mu\nu}$	$Q_{\varphi l}^{(3)}$	$(\varphi^\dagger i\overset{\leftrightarrow}{D}_\mu^I\varphi)(\bar\ell_p\tau^I\gamma^\mu\ell_r)$
$Q_{\varphi W}$	$\varphi^\dagger\varphi\, W_{\mu\nu}^I W^{I\mu\nu}$	Q_{uG}	$(\bar q_p\sigma^{\mu\nu}T^A u_r)\widetilde{\varphi}G_{\mu\nu}^A$	$q_{\varphi e}$	$(\varphi^\dagger i\overset{\leftrightarrow}{D}_\mu\varphi)(\bar e_p\gamma^\mu e_r)$
$Q_{\varphi\widetilde{W}}$	$\varphi^\dagger\varphi\,\widetilde{W}_{\mu\nu}^I W^{I\mu\nu}$	Q_{uW}	$(\bar q_p\sigma^{\mu\nu}u_r)\tau^I\widetilde{\varphi}W_{\mu\nu}^I$	$Q_{\varphi q}^{(1)}$	$(\varphi^\dagger i\overset{\leftrightarrow}{D}_\mu\varphi)(\bar q_p\gamma^\mu q_r)$
$Q_{\varphi B}$	$\varphi^\dagger\varphi\, B_{\mu\nu}B^{\mu\nu}$	Q_{uB}	$(\bar q_p\sigma^{\mu\nu}u_r)\widetilde{\varphi}B_{\mu\nu}$	$Q_{\varphi q}^{(3)}$	$(\varphi^\dagger i\overset{\leftrightarrow}{D}_\mu^I\varphi)(\bar q_p\tau^I\gamma^\mu q_r)$
$Q_{\varphi\widetilde{B}}$	$\varphi^\dagger\varphi\,\widetilde{B}_{\mu\nu}B^{\mu\nu}$	Q_{dG}	$(\bar q_p\sigma^{\mu\nu}T^A d_r)\varphi G_{\mu\nu}^A$	$Q_{\varphi u}$	$(\varphi^\dagger i\overset{\leftrightarrow}{D}_\mu\varphi)(\bar u_p\gamma^\mu u_r)$
$Q_{\varphi WB}$	$\varphi^\dagger\tau^I\varphi W_{\mu\nu}^I B^{\mu\nu}$	Q_{dW}	$(\bar q_p\sigma^{\mu\nu}d_r)\tau^I\varphi W_{\mu\nu}^I$	$Q_{\varphi d}$	$(\varphi^\dagger i\overset{\leftrightarrow}{D}_\mu\varphi)(\bar d_p\gamma^\mu d_r)$
$Q_{\varphi\widetilde{W}B}$	$\varphi^\dagger\tau^I\varphi\widetilde{W}_{\mu\nu}^I B^{\mu\nu}$	Q_{dB}	$(\bar q_p\sigma^{\mu\nu}d_r)\varphi B_{\mu\nu}$	$Q_{\varphi ud}$	$(\widetilde{\varphi}^\dagger D_\mu\varphi)(\bar u_p\gamma^\mu d_r)$

	$(\bar LL)\,(\bar LL)$		$(\bar RR)\,(\bar RR)$		$(\bar LL)\,(\bar RR)$
Q_{ll}	$(\bar\ell_p\gamma_\mu\ell_r)(\bar\ell_s\gamma^\mu\ell_t)$	Q_{ee}	$(\bar e_p\gamma_\mu e_r)(\bar e_s\gamma^\mu e_t)$	Q_{le}	$(\bar\ell_p\gamma_\mu\ell_r)(\bar e_s\gamma^\mu e_t)$
$Q_{qq}^{(1)}$	$(\bar q_p\gamma_\mu q_r)(\bar q_s\gamma^\mu q_t)$	Q_{uu}	$(\bar u_p\gamma_\mu u_r)(\bar u_s\gamma^\mu u_t)$	Q_{lu}	$(\bar\ell_p\gamma_\mu\ell_r)(\bar u_s\gamma^\mu u_t)$
$Q_{qq}^{(3)}$	$(\bar q_p\gamma_\mu\tau^I q_r)(\bar q_s\gamma^\mu\tau^I q_t)$	Q_{dd}	$(\bar d_p\gamma_\mu d_r)(\bar d_s\gamma^\mu d_t)$	Q_{ld}	$(\bar\ell_p\gamma_\mu\ell_r)(\bar d_s\gamma^\mu d_t)$
$Q_{lq}^{(1)}$	$(\bar\ell_p\gamma_\mu\ell_r)(\bar q_s\gamma^\mu q_t)$	Q_{eu}	$(\bar e_p\gamma_\mu e_r)(\bar u_s\gamma^\mu u_t)$	Q_{qe}	$(\bar q_p\gamma_\mu q_r)(\bar e_s\gamma^\mu e_t)$
$Q_{lq}^{(3)}$	$(\bar\ell_p\gamma_\mu\tau^I\ell_r)(\bar q_s\gamma^\mu\tau^I q_t)$	Q_{ed}	$(\bar e_p\gamma_\mu e_r)\,(\bar d_s\gamma^\mu d_t)$	$Q_{qu}^{(1)}$	$(\bar q_p\gamma_\mu q_r)\,(\bar u_s\gamma^\mu u_t)$
		$Q_{ud}^{(1)}$	$(\bar u_p\gamma_\mu u_r)(\bar d_s\gamma^\mu d_t)$	$Q_{qu}^{(8)}$	$(\bar q_p\gamma_\mu T^A q_r)(\bar u_s\gamma^\mu T^A u_t)$
		$Q_{ud}^{(8)}$	$(\bar u_p\gamma_\mu T^A u_r)(\bar d_s\gamma^\mu T^A d_t)$	$Q_{qd}^{(1)}$	$(\bar q_p\gamma_\mu q_r)(\bar d_s\gamma^\mu d_t)$
				$Q_{qd}^{(8)}$	$(\bar q_p\gamma_\mu T^A q_r)(\bar d_s\gamma^\mu T^A d_t)$

	$(\bar LR)\,(\bar RL)$ and $(\bar LR)\,(\bar LR)$		B-violating
Q_{ledq}	$(\bar\ell_p^j e_r)(\bar d_s q_t^j)$	Q_{duq}	$\varepsilon^{\alpha\beta\gamma}\varepsilon_{jk}\left[\left(d_p^\alpha\right)^T C u_r^\beta\right]\left[\left(q_s^{\gamma j}\right)^T C\ell_t^k\right]$
$Q_{quqd}^{(1)}$	$(\bar q_p^j u_r)\varepsilon_{jk}(\bar q_s^k d_t)$	Q_{qqu}	$\varepsilon^{\alpha\beta\gamma}\varepsilon_{jk}\left[\left(q_p^{\alpha j}\right)^T C q_r^{\beta k}\right]\left[(u_s^\gamma)^T C e_t\right]$
$Q_{quqd}^{(8)}$	$(\bar q_p^j T^A u_r)\varepsilon_{jk}(\bar q_s^k T^A d_t)$	Q_{qqq}	$\varepsilon^{\alpha\beta\gamma}\varepsilon_{jn}\varepsilon_{km}\left[\left(q_p^{\alpha j}\right)^T C q_r^{\beta k}\right]\left[(q_s^{\gamma m})^T C\ell_t^n\right]$
$Q_{lequ}^{(1)}$	$(\bar\ell_p^j e_r)\varepsilon_{jk}(\bar q_s^k u_t)$	Q_{duu}	$\varepsilon^{\alpha\beta\gamma}\left[\left(d_p^\alpha\right)^T C u_r^\beta\right]\left[(u_s^\gamma)^T C e_t\right]$
$Q_{lequ}^{(3)}$	$(\bar\ell_p^j\sigma_{\mu\nu}e_r)\varepsilon_{jk}(\bar q_s^k\sigma^{\mu\nu}u_t)$		

Table 2.1: Dimension-6 independent effective operators. The two tables at the top show 34 operators that take into account interactions involving bosons, while the two tables at the bottom present 29 operators describing four-fermion interactions. Without the four B-violating operators, there are 59 independent operators in total for one flavor as described in ref. [40]

- **X³**: These are operators involving products of three strength tensors. The operators $\mathcal{O}_{\widetilde{G}}$ and $\mathcal{O}_{\widetilde{W}}$ containing $\widetilde{X}$ lead to CP-odd terms. The $\mathcal{O}_G$ operator is present in processes involving jets. Interactions involving three to six bosons also arise from operators in this class, which are strongly constrained from di-boson production by considering triple anomalous couplings.

- **φ^6 and $\varphi^4 D^2$**: The operator $\mathcal{O}_\varphi$ modifies the self-interactions of the Higgs and add new ones. Moreover, the operators $\mathcal{O}_{\varphi\Box}$ and $\mathcal{O}_{\varphi D}$ modify the Higgs couplings to all particles, and in particular they contribute to Higgs associated production with EW bosons (VH), to vector boson fusion (VBF) and to the decays of the Higgs like $h \to \{VV, bb\}$.

- **$\psi^2 \varphi^3$**: These operators are built by taking the Yukawa interactions from the SM and multiply them by the factor $(\varphi^\dagger \varphi)$. The extra factor contains the term $v^2/2$ in the broken phase, leading to shifts in the Yukawa interactions. Even more, when all of the Higgs doublets are replaced by $v/\sqrt{2}$, we notice that these operators modify the relation between fermion masses and the Yukawa coupling, $m_f = y_f v/\sqrt{2}$. This relation can be maintained by defining these effective operators as the product of Yukawa terms and

$$\left(\varphi^\dagger \varphi - \frac{v^2}{2} \right). \tag{2.34}$$

- **$X^2 \varphi^2$**: Similar to operators involving only Higgs doublets, operators in this category couple the Higgs to gauge bosons with the difference that this time is through the gauge field strengths. Particular is the case of $\mathcal{O}_{\varphi G}$, which enters at tree-level in Higgs production via gluon boson fusion ($gg \to h$), while in the SM the leading order is at 1-loop.

- **$\psi^2 X \varphi$**: Elements of this category are known as dipole operators, since they lead to dipole interactions in the broken phase. Some dipole moments are measured to very high accuracy, thus operators from this category can be well constrained.

- **$\psi^2 \varphi^2 D$**: This kind of operators introduces modifications to the interactions between gauge bosons and fermions, and yields new interactions involving at the same time Higgs bosons, fermions and gauge bosons.

- ψ^4: These are operators with Fermi-like interactions. Four-fermion interactions constitute most of the dimension 6 operators listed in Table 2.1. Because of this, it is useful to subdivide operators into the different possible chirality combinations L and R.

Next orders in the SMEFT expansion have also been considered in the literature. We notice that similarly to the case of dimension 5, higher odd dimension operators break baryon and lepton number conservation. Because of this, odd-dimension operators are often considered as heavily suppressed. Complete basis for dimension 7 and 9 operators can be found in [55,56]. Additionally, efforts have been made in the construction of an independent basis of operators at dimension 8 [57, 58]. Thanks to group theory and Young tableau techniques, the writing of all possible Lorentz structures at higher dimensions can be done systematically.

To finish the introduction to the SMEFT, it is important to notice that the number of operators in Table 2.1 depends on the flavor assumptions. To see this, we remember that the SM presents a global symmetry under transformations of the flavor fields in the massless limit, *i.e.* with vanishing Yukawa couplings. Considering that we have three fermion flavor families, the unitary transformations are written explicitly as

$$q_p \to U_{pr}^q q_r, \quad \text{with} \quad U^q \in U(3)_q. \tag{2.35}$$

The $U(3)$ symmetry can be decomposed into the phase rotation given by $U(1)$ and the rotations in the flavor space generated by $SU(3)$. Then, taken into account the 5 multiplets l_p, e_p, q_p, u_p, d_p, we have the symmetry group

$$U(3)^5 \to SU(3)_l \otimes SU(3)_e \otimes SU(3)_q \otimes SU(3)_u \otimes SU(3)_d \otimes U(1)^5. \tag{2.36}$$

Imposing this symmetry eliminates operators that contract $SU(2)$ multiplets of different fermion type in Table 2.1. Furthermore, the symmetry imposes the corresponding Wilson coefficients to be diagonal and equal in flavor space.

The flavor assumptions in SMEFT analysis are chosen according to the scenarios that we want to analyse. For some scenarios it is customary for all of the quark operators to have Wilson coefficients independent of the flavor. In other scenarios, it is of interest to consider the third family of four-fermion operators different from those with the two lighter families, *i.e.* $p = 1, 2$.

2.7   Reduction of basis

In this section we present some of the tools used in Ref. [40] that make it possible to reduce a given set of operators to an independent one. We start by considering terms with more than one covariant derivative. By means of equations of motion (EOMs)

$$(D^\nu G_{\nu\mu})^A = g_s(\bar{q}\gamma_\mu T^A q + \bar{u}\gamma_\mu T^A u + \bar{d}\gamma_\mu T^A d) \qquad (2.37)$$

redundancies can be removed by field redefinitions. Operators that differ by EOMs are related to each other, and therefore are physically equivalent up to higher $1/\Lambda$ order corrections and provide the same matrix elements. We notice that contributions of $\mathcal{O}(\Lambda^{-1})$ and $\mathcal{O}(\Lambda^{-2})$ are discarded in EOMs as they lead to operators with dimension higher than 6. Momentum conservation is reflected in the fact that two actions differing only by total derivatives are equivalent. Thus, integration by parts sets the equivalency class

$$\mathcal{O}_i \cdot D_\mu \mathcal{O}_j \sim -D_\mu \mathcal{O}_i \cdot \mathcal{O}_j. \qquad (2.38)$$

The operators $\mathcal{O}_i$ and $\mathcal{O}_j$ are said to be equivalent up to a total derivative. As an example, let us consider the operator

$$\mathcal{O}_{\varphi^2 D^2} = (\varphi^\dagger \varphi) D_\mu \varphi^\dagger D^\mu \varphi, \qquad (2.39)$$

which in principle makes part of the $\varphi^4 D^2$ category but does not appear in Table 2.1. We find the following equivalence up to a total derivative

$$\mathcal{O}_{\varphi^2 D^2} \equiv \frac{1}{2}(\mathcal{O}_{\varphi\Box} - (\varphi^\dagger \varphi)(\varphi^\dagger \Box \varphi + \Box \varphi^\dagger \varphi)). \qquad (2.40)$$

The right-hand side of Eq. (2.40) can be written in terms of the operators in Table 2.1 by using the Higgs EOM

$$\Box \varphi^j = \lambda v^2 \varphi^j - 2\lambda(\varphi^\dagger \varphi)\varphi^j - (y_u)_{pr}\epsilon^{jk}\bar{q}_p^k u_r - (y_d)_{pr}\bar{q}_p d_r - (y_e)_{pr}\bar{\ell}_p e_r, \qquad (2.41)$$

with j and k being isospin indices. Hence, by substituting Eq. (2.41) into Eq. (2.40) yields the relation

$$\mathcal{O}_{\varphi^2 D^2} = \frac{1}{2}\mathcal{O}_{\varphi\Box} + 2\lambda\mathcal{O}_\varphi + \frac{1}{2}(\mathcal{O}_{u\varphi} + \mathcal{O}_{u\varphi} + \mathcal{O}_{u\varphi}) - \lambda v^2(\varphi^\dagger \varphi). \qquad (2.42)$$

This shows that the operator $\mathcal{O}_{\varphi^2 D^2}$ is redundant.

Products of fermion bilinears follow interchange relations coming from identities of Pauli matrices, and so equivalent from identities of γ-matrices. Known as Fierz identities, generically they can be written as

$$(\bar{\psi}_1 \Gamma^I \psi_2)(\bar{\psi}_3 \Gamma^J \psi_4) = \sum_{K,L} C_{KL}^{IJ} (\bar{\psi}_1 \Gamma^K \psi_4)(\bar{\psi}_3 \Gamma^L \psi_2), \qquad (2.43)$$

where $\Gamma^I = \{\mathbb{1}, \gamma^\mu, \gamma_5, \gamma^\mu \gamma_5, \sigma^{\mu\nu}\}$ indicates. The coefficients C_{KL}^{IJ} are computed using the completeness relation of a set of matrices Γ^I and the Lorentz algebra. Similarly, the $SU(2)_L$ and $SU(3)_c$ generators induce redundancies between operators that can be removed with the relations

$$\tau_{jk}^I \tau_{mn}^I = 2\delta_{jn}\delta_{mk} - \delta_{jk}\delta_{mn} \qquad \text{and} \qquad T_{\alpha\beta}^A T_{\kappa\lambda}^A = \frac{1}{2}\delta_{\alpha\lambda}\delta_{\kappa\beta} - \frac{1}{6}\delta_{\alpha\beta}\delta_{\kappa\lambda}, \tag{2.44}$$

To see the application of Fierz identities in the reduction of the basis, we study the case of the operator

$$\mathcal{O}_{uu}^{(8)} = (\bar{u}_p \gamma_\mu T^A u_r)(\bar{u}_s \gamma^\mu T^A u_t), \qquad (2.45)$$

which does not appear in Table 2.1. By using the identity on the right of Eq. (2.44) we obtain

$$\begin{aligned}\mathcal{O}_{uu}^{(8)} &= \frac{1}{2}(\bar{u}_p^\alpha \gamma_\mu T^A u_r^\beta)(\bar{u}_s^\beta \gamma^\mu T^A u_t^\alpha) - \frac{1}{6}(\bar{u}_p \gamma_\mu u_r)(\bar{u}_s \gamma^\mu u_t) \\ &= \frac{1}{2}Q_{uu}^{ptsr} - \frac{1}{6}Q_{uu}^{prst}. \end{aligned} \qquad (2.46)$$

Hence, the operator $\mathcal{O}_{uu}^{(8)}$ is redundant. Similarly can be done to show that the operator $\mathcal{O}_{dd}^{(8)}$ is also redundant.

We finish this section by remembering that the experimental measurements, like the cross-sections and differential distributions, are obtained from the S-matrix elements. With $\mathcal{S}$ being the scattering operator, then the S-matrix elements are given by

$$\langle \lambda_{\vec{p}}^{\mathrm{F}} | \mathcal{S} | \lambda_{\vec{p}}^{\mathrm{I}} \rangle = \langle \lambda_{\vec{p}}^{\mathrm{F}} | \lambda_{\vec{p}}^{\mathrm{I}} \rangle + 2\pi\delta(E_{\mathrm{F}} - E_{\mathrm{I}})\mathcal{A}, \qquad (2.47)$$

where $|\lambda_{\vec{p}}^{\mathrm{I}}\rangle$ and $|\lambda_{\vec{p}}^{\mathrm{F}}\rangle$ are the initial and final eigenstates of the full interacting Hamiltonian of the theory, respectively, and $\mathcal{A}$ is the corresponding scattering amplitude. The observable given by S-matrix elements in Eq (2.47) is obtained from the particle states and not from the fields, hence remains invari-

ant under field redefinitions. Therefore, different choices of the SMEFT basis parametrize the same new physics.

2.8 Fits of the SMEFT parameters

One of the goals of the EFT approach is to find a global fit on the 2499 independent Wilson coefficients at dimension 6, and the relevant operators at dimension 8, from the available LHC data and from other particle experiments. This is a cumbersome task, consequence of the ambitious goal of looking for new physics in a model-independent approach. To simplify such analysis, some Wilson coefficients are set to zero. Due to the renormalization group evolution (RGE) of the coefficients, the simplifications above are only valid at a fixed scale. Moreover, unless a symmetry is imposed, the setting of coefficients to zero should not be done arbitrarily as it might spoil the model and basis independence of the SMEFT.

Constraining a large number of Wilson coefficients requires a broad dataset. Therefore, a robust statistical analysis including all sources of uncertainties is required. Such an analysis relies on the fitting methodology. Let us see some of the relevant statistical concepts needed for this task. Constraints on the Wilson coefficients c_i can be obtained from their affinity to the observed data. First, we define the likelihood $\mathcal{L}(c_i, \theta | X)$ as the probability of the observed data X given the values of c_i and the nuisance parameter θ that can indicate uncertainties. Often analyses on constraining SMEFT parameters (including the ones presented in the results of this thesis) consider the Gaussian likelihood

$$\mathcal{L}(c_i, \theta | X) = N \exp \left(-\frac{1}{2} (x^{\mathrm{Exp}} - x(c_i, \theta))_k^T V_{kl}^{-1} (x^{\mathrm{Exp}} - x(c_i, \theta))_l \right),$$
$$(2.48)$$

where x_k^{Exp} stands for the k element of the dataset X, $x_k(c, \theta)$ is the corresponding theoretical prediction, V_{kl} is the covariance matrix and N is a normalization factor. Measurements are obtained from the detection of events organized in histograms composed of k bins, each of them with number of events n_b and $b = 1, \ldots, k$. The Gaussian likelihood assumes a large number of events n_b per bin. With the likelihood in Eq. (2.48), we define the test statistic $t(c_i)$ as

$$t(c_i) = -2 \log \frac{\mathcal{L}(c_i, \theta'' | X)}{\mathcal{L}(c_i', \theta' | X)},$$
$$(2.49)$$

so that the best fit values denoted by c_i' and θ' are the points where the likelihood is maximal. The best fit of θ at the fixed value of c_i is denoted by θ''. In the limit of large number of events n_b, the test statistics follows a χ^2-distribution with degrees of freedom determined by the number of Wilson coefficients considered in the fit and the number of data points. Now, we remember the expression of the χ^2-distribution

$$\chi^2(c_i, \theta) = (x^{\mathrm{Exp}} - x(c_i, \theta))_k^T V_{kl}^{-1}(x^{\mathrm{Exp}} - x(c_i, \theta))_l, \qquad (2.50)$$

so that the combination of Eq. (2.48) and (2.49) yields

$$t(c_i) = \chi^2(c_i, \theta'') - \chi^2(c_i', \theta'). \qquad (2.51)$$

The agreement between theoretical predictions and the observed measurements is then quantified by the p-value (probability value) computed from the test statistic as

$$p(t(c_i)) = \int_{t(c_i)}^{\infty} f(t(c_i')|c_i)dt(c_i') = 1 - F(t(c_i)|c_i), \qquad (2.52)$$

with $f(t(c_i')|c_i)$ the probability distribution function of $t(c_i')$ and $F(t(c_i)|c_i)$ the cumulative distribution function. The p-value corresponds to the probability of observing a measurement given the assumption of values c_i for the Wilson coefficients. Thus, values of the Wilson coefficients are excluded when the corresponding p-value is smaller than a specific significance level α. The constraints on the Wilson coefficients obtained in the results of the following chapters arise from computing confidence intervals at a significance of $\alpha = 0.05$ (95% Confidence Level) defined by the values that solve the equation

$$t(c_i)|_{c_i \in \mathrm{Boundary}} = F^{-1}(1 - \alpha), \qquad (2.53)$$

where we have inverted Eq. (2.52) after noticing that the boundary is given by $p(t(c_i)) = \alpha$ with $c_i \in \mathrm{Boundary}$. For the χ^2-distribution of one degree of freedom and $\alpha = 0.05$ we find that $F^{-1}(0.95) \approx 3.84$.

To obtain a rough estimate of the coefficients on a given coefficient, we set all the other coefficients to zero, thus the *individual* limit on the coefficient c_1 can be obtained by evaluating $t(c_1, 0, \ldots, 0)$. More realistic bounds are provided by allowing all of the coefficients to vary at the same time, often referred as *marginalized* limits. Comprehensive and complete reviews on the statistical concepts referred in this sections can be found in [59–62].

Chapter 3

The top quark at colliders
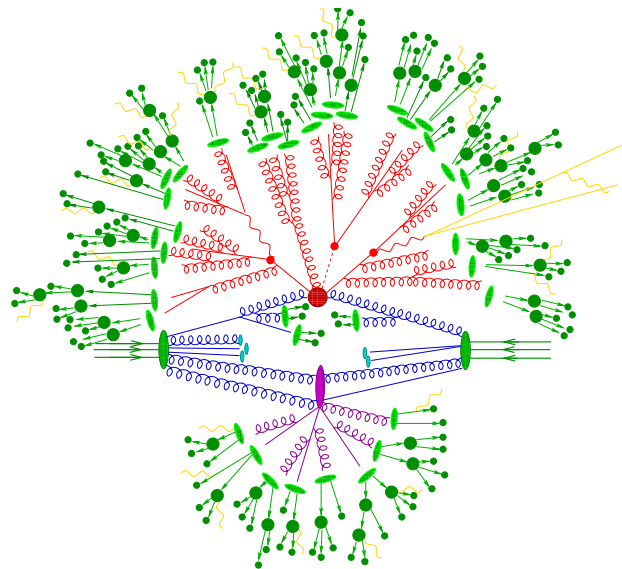
Figure 3.1: Ilustration of an event at hadron colliders [63]

In this chapter we will present the main facts to be taken into account when studying the top at colliders. Production processes of the top will be discussed as well as the possible SMEFT contributions to these processes.

3.1   Collider physics

Collider experiments range along a wide spectrum of options. They vary in size and shape. The design of colliders depends on the choice of the initial particles to be accelerated. Experiments with protons or electrons (and anti-particles)

are the most popular and realizable choice so far. In general, lepton colliders are known to present cleaner data with respect to those accelerating hadrons. In this section we will collect some of the fundamentals to be considered in the obtaining of predictions of hadronic collisions.

To reproduce the physics in high-energy hadron collisions, we need to include the structure of the hadrons and the fact that most of the heavy particles in which we are interested are short-lived. The objects that are finally detected are subproducts of such heavy particles. This is a complicated process that involves several challenges. In Fig. 3.1 a sketch of a typical process occurring at hadron colliders is shown. The red blob in the center represents the hard collision initiated by gluon scattering, where the gluons come from the protons drawn as the green ovals. The final results from the hard scattering decayed (Red) and the colored states (Blue) create a shower and end up transitioning into hadrons displayed in light green, which subsequently decay into light hadrons in dark green. Yellow lines indicate emissions of soft particles. Finally, secondary less hard events can also occur, like the multi-parton interaction indicated by the purple blob.

The stages described above happen at different energies and can be separated, which makes computations possible. In other words, the proton structure, the hard event, the showering, hadronization and decays can be obtained on their own. According to the parton model [64], the proton is composed by partons (gluons and quarks), which carry fractions (x_a) of its momentum. The scattering of hadrons h_1 and h_2 into the final state X can be computed as the sum of convoluted partonic cross-sections:

$$\sigma_{h_1 h_2 \to X} = \sum_{a,b \in \{q,g\}} \int dx_a \, dx_b f_a^{h_1}(x_a, \mu_F^2) f_b^{h_2}(x_b, \mu_F^2) \int d\Phi \frac{d\hat{\sigma}_{ab}(\Phi, \mu_F^2)}{d\Phi},$$

$$(3.1)$$

where f_1 and f_2 are the parton distribution functions (PDF) of the partons a, b and $\hat{\sigma}_{ab}$ is the partonic cross-section computed through perturbative methods. The phase-space of the subprocess $ab \to X$ is indicated by Φ. Finally, we note that the PDFs represent the probability of finding a parton a with momentum fraction x in the parent hadron h at the factorization scale μ_F. A process described by Eq. (3.1) in the parton model is diagramatically shown in Fig. 3.2.

The separation into different pieces in Eq. (3.1) already described above is possible due to the factorization theorem of QCD [65]. It is important to

point out that this factorization is not exact. In principle, there are further corrections of order $\mathcal{O}(\Lambda_{\mathrm{QCD}}/\mu_f^2)$. The factorization scale is often chosen to be at the order of the total mass of the final state.

The convolution in Eq. (3.1) introduces the dependence on the factorization scale μ_f. The parameter μ_f can be interpreted as delimiter between the non-perturbative structure of the proton and the hard process. The evolution of the PDFs with respect to the factorization scale provides information about the relation between the low energy PDF structure and the hard process. This evolution is given by the Dokshitzer–Gribov–Lipatov–Altarelli–Parisi (DGLAP) equations

$$\frac{df_a(x, \mu_f)}{d \log \mu_f^2} = \sum_{b \in \{q,g\}} \frac{\alpha_s}{2\pi} \int_x^1 \frac{dy}{y} f_b(y, \mu_f) P_{ba} \left(\frac{x}{y} \right), \qquad (3.2)$$

where P_{ba} are the splitting functions, which describe the collinear splitting of parton b into parton a. The Eq. (3.2) indicates that PDFs run with the scale μ_F, such that from a measurement at low energies, we can evolve them up to high energy scales. The DGLAP equations are widely used in determinations of parton distributions. Diagramatically, the evolution of PDFs can be seen as

The splitting functions are the computable part of the DGLAP equations and receive radiative corrections, which leads to LO, NLO and NNLO PDF sets that can be convoluted with partonic cross-sections of the corresponding order.

In Eq. (3.1), the effects of showering and hadronization are not written explicitly. These effects account for the transition of the parton level final state into the particles reaching the detector. Similarly to the PDFs, parton showers can be described in a universal and separated from the hard process procedure. Moreover, because showers are described as soft and collinear emissions of
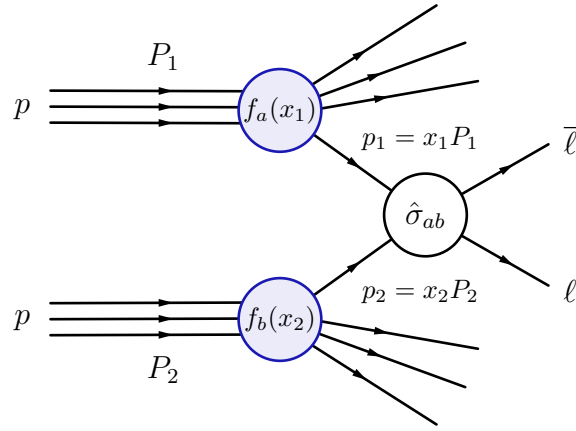
Figure 3.2: Diagram depicting the typical $pp \rightarrow \ell\bar{\ell}$ scattering at LHC colliders.

partons, they can be described by the splitting functions P_{ba}. Difficulties in the computation of showering arise when higher-order contributions are taken into account. Due to the fact that parton emissions are also included in radiative corrections, higher-order calculations in QCD run the risk of double counting of such emissions. The technique used to avoid these ambiguities is known as matching, mandatory in the merging of higher order QCD corrections with parton shower [66, 67].

Finally, in the practice, PDFs are determined from experimental data assuming that the SM is valid. Often, the PDFs fit takes into account the same processes that enter in the BSM analysis. As a consequence proton's PDFs obtained from the use of high-energy LHC measurements might include BSM effects. In the SMEFT framework the bounds on the Wilson coefficients get modifications if the fitting of the PDFs assumes a consistent BSM theory instead of the SM [68, 69].

3.2 The top quark

The top quark is the heaviest fundamental particle found to date. Together with the bottom quark, they were predicted in 1973 by Kobayashi and Maskawa to explain the observed CP violations in kaon decay [70]. Around 20 years later the top quark was discovered at Tevatron [71, 72]. Being the heaviest particle of the SM, with $m_t = 172.76 \pm 0.30$ GeV [73] (see Fig. 3.3) and as heavy as a gold atom, the top quark is one of the probes of new physics. In this
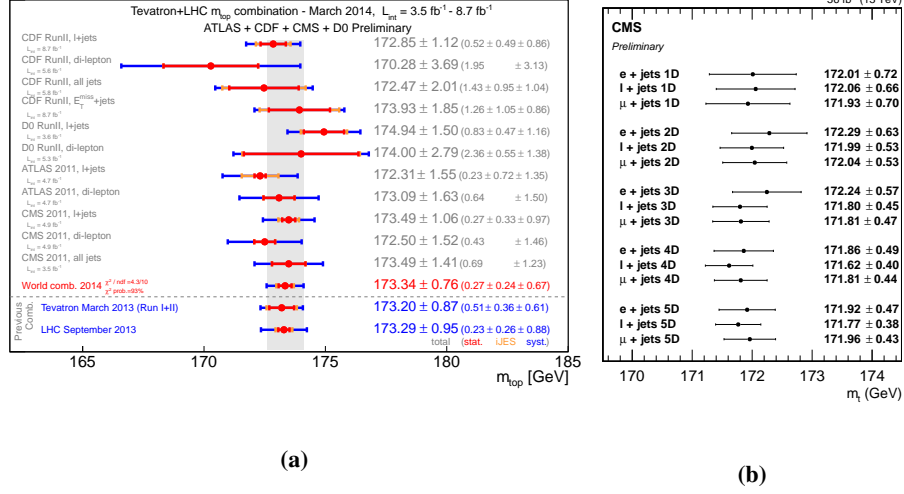
Figure 3.3: Top mass measurements (a) comparison between results of several collaborations [74] and (b) most recent reported measurement [75].

section we review some of its most fundamental aspects that will be useful in the following chapters.

Among the quarks, the top is the only particle that decays semi-weakly, in the sense that it decays into an on-shell W boson and a b quark in a proportion of almost 100%. When neglecting terms of order m_b^2/m_t^2, α_s^2 and $(\alpha_s/\pi)M_W^2/m_t^2$, the prediction from the SM at NLO is [76]

$$\Gamma_{t\to W^+b} = \frac{G_F m_t^3}{8\pi\sqrt{2}}|V_{tb}|^2 \left(1 - \frac{M_W^2}{m_t^2}\right)^2 \left(1 + 2\frac{M_W^2}{m_t^2}\right) \left(1 - \frac{2\alpha_s}{3\pi}\left(\frac{2\pi^2}{3} - \frac{5}{2}\right)\right),$$
(3.5)

with V_{tb} element of the CKM matrix. Similar formulas are obtained in the cases of the s and d quarks with the respective replacements of the CKM elements. Hence, the branching ratios are computed as proportional to, and so suppressed by, the mixing angles. By inserting the corresponding numbers we obtain [77]

$$\text{BR}(t \to W^+b) \simeq 0.998, \qquad \text{BR}(t \to W^+s) \simeq 1.9 \cdot 10^{-3},$$
$$\text{BR}(t \to W^+d) \simeq 10^{-4}.$$
(3.6)

Also, from Eq. (3.5), we find a decay width of $\Gamma_t \approx 1.5$ GeV, a value that in terms of lifetime corresponds to the small value of $\tau_t \approx 5 \cdot 10^{-25}$ s. We can compare this to the hadronization time, estimated from the QCD scale (Λ_{QCD})
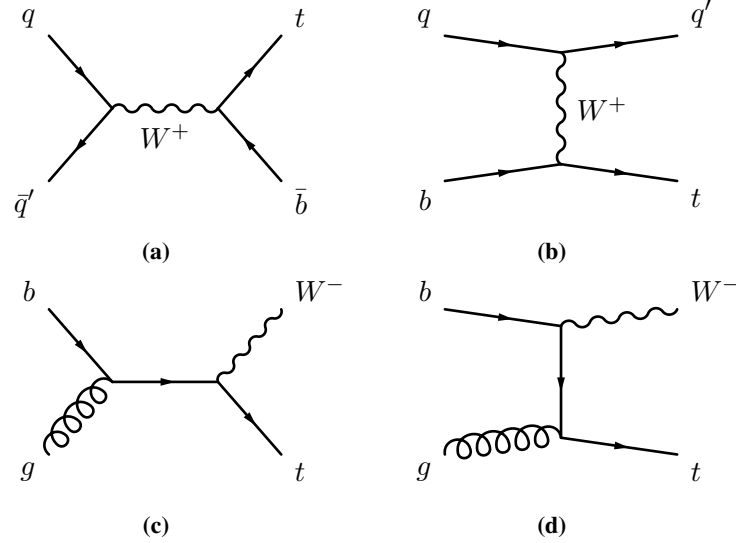
Figure 3.4: Feynman diagrams of top single production at LO in the SM for the (a) s-channel and (b) t-channel quark initiated, and (c-d) tW associated production. A cross diagram obtained from (d) also contributes.

to be $\tau_{\mathrm{had.}} \simeq 1/\Lambda_{\mathrm{QCD}} \approx 3 \cdot 10^{-24}$ s. This means that, because of its mass, the top quark decays before the strong interactions can act, in this sense the top is almost a free particle. Due to this, the spin information about the top is accessible through its decay products. Referred to as spin correlation, such information allows the study of the vertex structure in EW processes through the top decays.

It is interesting to notice that, even though the top quark does not hadronize, non-perturbative effects possibly contribute to the cross-section near threshold energy production of the $t\bar{t}$ process [78, 79], a regime where top quarks are produced with low velocities. Because of the size of the top width, bound states of a top pair does not appear as a sharp resonance but rather as smeared peak. This is of interest in a precise determination of the top mass, as non-relativistic effects can increase the uncertainties depending on the renormalization scheme [80]. In chapter 7, we will explore the possibilities that near-threshold effects offer in the search of new physics.

3.3 Production channels of the top quark

3.3.1 Single top production

The top quark can be produced in association with jets via the electroweak processes $q\bar{q}' \rightarrow t\bar{b}$ and $qb \rightarrow q't$ mediated by s- and t-channel W bosons, respectively (see Fig. 3.4a and 3.4b). Furthermore, a single top can also be produced in association with a W boson through the reaction $gb \rightarrow tW^-$ (see Fig. 3.4c and 3.4d). These processes are known to be relevant in the experimental determination of the mixing parameter $|V_{tb}|$.

The production of top+jets is affected by the weak coupling, however, the t-channel is favoured by the kinematics. Due to the quark initial state at Tevatron, the cross-sections of top and anti-top are the same, for which computations at approximate NNLO of the t-channel of the combined $t + \bar{t}$ are found in the literature [81]. Analogously, for all the available energies at the LHC, with the difference that top and anti-top cross-sections are not the same, computations have reached the NNLO accuracy for the t-channel [82, 83]. Results at approximate NNLO are also known in the s-channel case for the Tevatron and LHC for $\sqrt{s} = 7$ TeV [84]. On the other hand, associated production with W boson has a too small cross-section to be observed at the Tevatron. However, at the LHC sizable cross-sections have been computed at approximate NNLO [85]. All of these results are gathered in Table 3.1.

	cross-section [pb]		
	t-channel	s-channel	W associated
Tevatron, $\sqrt{s} = 1.6$ TeV	$2.06^{+0.13}_{-0.13}$	$1.03^{+0.05}_{-0.05}$	-
LHC, $\sqrt{s} = 7$ TeV	$64.0^{+0.77}_{-0.38}$	$4.5^{+0.2}_{-0.2}$	$15.5^{+1.2}_{-1.2}$
LHC, $\sqrt{s} = 13$ TeV	$215^{+2.1}_{-1.3}$	-	-
LHC, $\sqrt{s} = 14$ TeV	$245^{+2.7}_{-1.3}$	-	-

Table 3.1: SM predictions for the cross-sections of single top quark $(t + \bar{t})$ production at the Tevatron and LHC, where the quoted uncertainties are obtained from scale variations [73] .
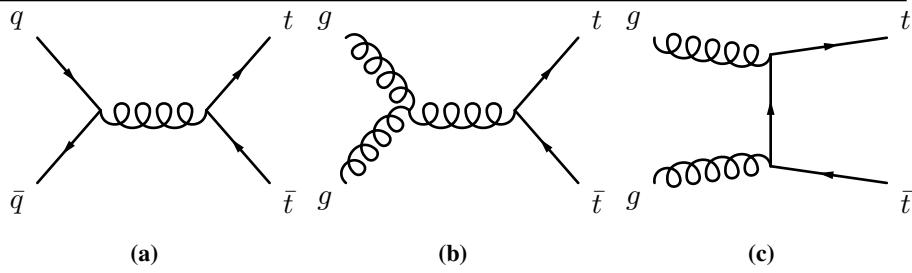
Figure 3.5: Feynman diagrams of top pair production at LO in the SM for the (a) quark initiated, (b) gluon initiated s-channel and (c) gluon initiated t-channel. A cross diagram obtained from (c) also contributes.

3.3.2 Top-pair production

At hadron colliders the top pair process is the dominant production channel of top quarks. In pp colliders, like the LHC, the gluon initiated subprocess ($gg \rightarrow t\bar{t}$) is the main channel with about 90% of the production at $\sqrt{s} = 14$ TeV. In $p\bar{p}$ colliders, like Tevatron, the production comes mostly from quark annihilation ($q\bar{q} \rightarrow t\bar{t}$), around 85% of the total cross-section at $\sqrt{s} = 1.96$ TeV. In Fig. 3.5 representative Feynman diagrams of the top pair production are shown for the (a) quark channel and (b-c) gluon channel. According to
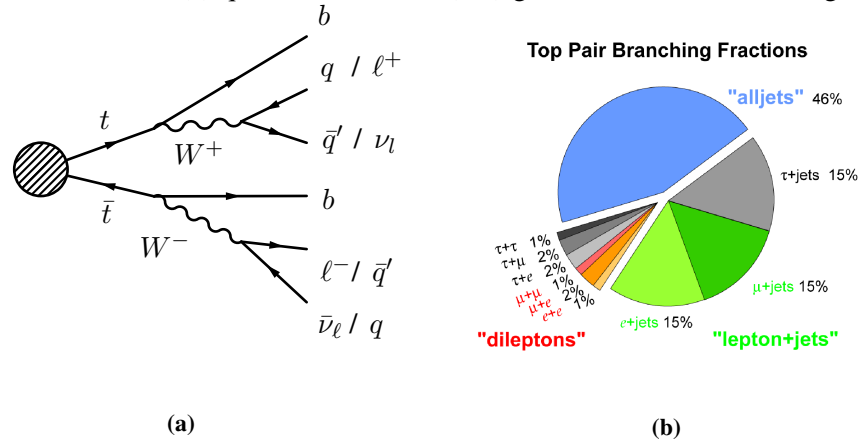
Figure 3.6: (a) Feynman diagram for the decay channels of the top pair final state and (b) corresponding branching ratios.

the discussion in the beginning of this section, the top pair final state present several possibilities of decay channels (see Fig. 3.6a). The signature of a $t\bar{t}$ decay mode is determined by the decay modes of the W boson. The so-called semi-leptonic channel (ℓ+jets) corresponds to events in which one W

boson decays into an electron or a muon and a neutrino and the other W boson decays into quark-antiquark pair. In some analysis the semi-leptonic channel might also include the W boson decay into a τ lepton that subsequently decays into an electron or a muon. Events where both W bosons decay into quark-antiquark pair are referred to as hadronic channel while events where both W boson decay into leptons are known as dileptons. The corresponding branching ratios of these decay channels are

$$\text{BR(hadronic)} \approx 0.46, \qquad \text{BR(semi} - \text{leptonic)} \approx 0.3,$$
$$\text{BR(dileptons)} \approx 0.05, \tag{3.7}$$

where we can see that the hadronic channel is the dominant decay. The other branching ratios are shown in Fig. 3.6b. The channels including leptons are often easier to identify in an experimental analysis than the hadronic channel and so are commonly found in the experimental reports. In particular, the ℓ+jets channel presents a low background signature and comes with high energy leptons, with the dominant background being W+jet. The dilepton channel is characterized by a large missing energy corresponding to the undetected neutrinos, the dominant background is Z +jet. The pure hadronic decay channel presents high momentum b-jets and the dominant background is multijets. In this context the technique of b-tagging is relevant, allowing to identify b-jets from displaced vertices.

Analytical and numerical results for the top pair production at NNLO in QCD in the quark channel have been computed for planar like diagrams [86–89]. Non-planar contributions subleading in the color expansion have been computed analytically recently [90], thus completing the full analytical NNLO computation of the quark channel. On the side of the subprocess $gg \rightarrow t\bar{t}$ partial computations have also been achieved at two-loop [91–94].

The leading top quark production mechanism at hadron colliders is the $t\bar{t}$ process. ATLAS and CMS have measured with Run-II the cross-section for this process in different decay channels. In particular, in the dilepton $e\mu$ channel it has been found $\sigma_{t\bar{t}} = 826.4 \pm 3.6 \, (\text{stat}) \pm 11.5 \, (\text{syst})$ pb at $\sqrt{s} = 13$ TeV [95–97]. At tree-level the partonic production of a top-pair is given by the

differential cross-sections

$$\frac{d\hat{\sigma}_{qq\to t\bar{t}}}{d\Omega} = \frac{\alpha_s^2\beta_t}{9\hat{s}^3}\left(2m_t^2\hat{s} + \left(\hat{t} - m_t^2\right)^2 + \left(\hat{u} - m_t^2\right)^2\right) \tag{3.8}$$

$$\frac{d\hat{\sigma}_{gg\to t\bar{t}}}{d\Omega} = \frac{\alpha_s^2\beta_t}{12\hat{s}^3}\frac{7\hat{s}^2 + 9(\hat{t}-\hat{u})^2}{\left(\hat{t} - m_t^2\right)^2\left(\hat{u} - m_t^2\right)^2}\big(m_t^4(3\hat{t}^2 + 14\hat{t}\hat{u} + 3\hat{u}^2)$$
$$- m_t^2(\hat{t} + \hat{u})(\hat{t}^2 + 6\hat{t}\hat{u} + \hat{u}^2) + \hat{t}\hat{u}(\hat{t}^2 + \hat{u}^2) - 6m_t^8), \tag{3.9}$$

with $\beta_t = \sqrt{1 - 4m_t^2/\hat{s}}$. The gluon channel gives around the 90% of the total production rate at the LHC, while at the Tevatron the quark channels were the dominant sub-processes. In the SM, the $t\bar{t}$ process is known numerically at NNLO-QCD + NLO-EW [98–102], fully differential at NNLO-QCD [103, 104] and approximate N^{3}LO-QCD [105]. Progress in analytical calculations has been achieved in the recent years, with the state-of-the-art being a full NNLO-QCD computation for the process $q\bar{q} \to t\bar{t}$ [87–90]. The NNLO-QCD analytical computation of the process $gg \to t\bar{t}$ is expected to be completed in the years to come [91–94] .

3.3.3   Four-top production

As discussed in previous sections, the top quark is the most massive elementary particle of the SM. As a result, when four tops are produced in a single event, they are the heaviest final state ever measured at the LHC. The four-top process is an extremely rare event at the LHC with a cross-section in proton-proton collisions predicted at NLO to be $\sigma(pp \to t\bar{t}t\bar{t}) = 12.0^{+20\%}_{-20\%}$ fb at $\sqrt{s} = 13$ TeV with the uncertainties obtained from scale variations [106]. Its cross-section is five orders of magnitude smaller than the production of the top-pair production.

The four-top production can occur through gg and $q\bar{q}$ initial states at tree-level. However, the gluon initiated subprocess largely dominates at 13 TeV. Representative Feynman diagrams for the $gg \to t\bar{t}t\bar{t}$ and $q\bar{q} \to t\bar{t}t\bar{t}$ subprocesses are shown in Fig. 3.7a-3.7d and Fig. 3.7e, respectively. We see that some of the diagrams present a sub-scattering of the form $t\bar{t} \to t\bar{t}$ with the exchange of a Higgs or Z, γ. Such diagrams can enter in the total rate through either their interference with QCD diagrams or through their squares. Although significant, those contributions come with opposite signs and end up partially cancelling each other. This motivates the inclusion of NLO corrections which can lift up those cancellations [106].
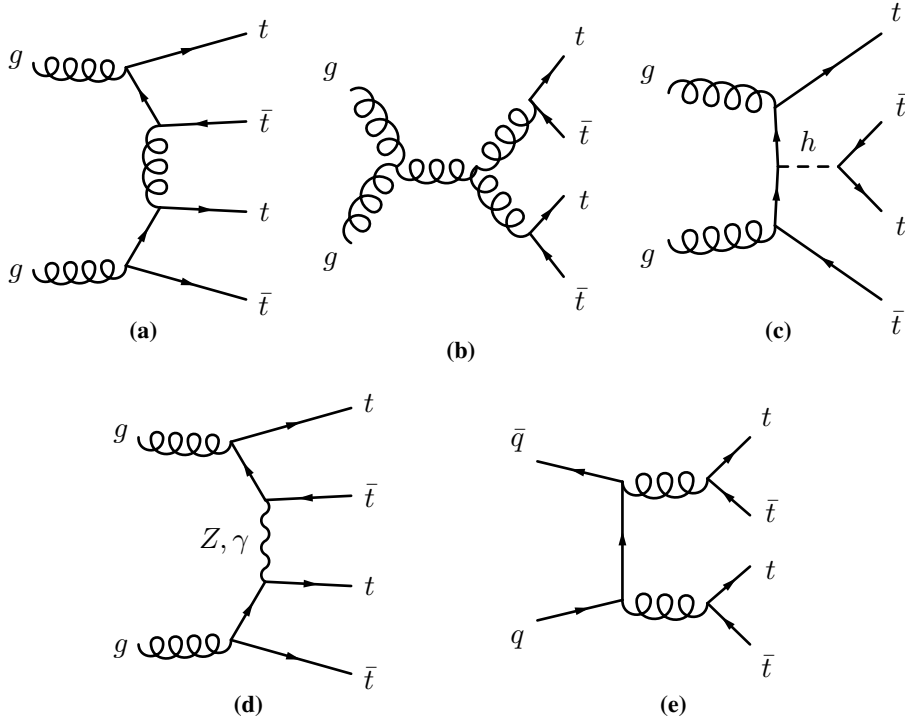
Figure 3.7: Representative Feynman diagrams for the subprocesses (a-d) $gg \to t\bar{t}t\bar{t}$ and the (e) $q\bar{q} \to t\bar{t}t\bar{t}$ at LO in the SM.

Each of the top-pair in the four-top process can decay similarly as shown in Fig. 3.6a. Once the top quarks decay, the final state contains several jets originating from the showering and hadronization of light and b-quarks and, depending on the decays of the W bosons, might contain leptons plus missing energy. Moreover, τ leptons coming possibly from any of the W bosons decay also into a lighter lepton or a jet with additional neutrinos. Due to the low level of the backgrounds, the experimental searches focused on collision events producing two leptons with the same charge (two same-sign) and the three or more leptons (multi-leptons) final states [107–109]. This considers $W \to \ell\nu$ with $\ell = e, \mu$ including leptonic decays of τ leptons. The corresponding branching ratios are

$$\mathrm{BR(two\ same-sign)} \approx 0.07, \quad \mathrm{BR(multi-leptons)} \approx 0.05. \quad (3.10)$$

The main background processes with similar final states of the four-top production are the top-pair productions in association with other particles such as the Higgs ($t\bar{t}h$+jets), W and Z bosons ($t\bar{t}W$+jets and $t\bar{t}Z$+jets). Other processes with smaller cross-sections are multi-boson production, $t\bar{t}WW$, single-

top and $t\bar{t}t$ processes. The possibility of assigning the wrong charge to the detected leptons and misidentified jets as leptons also contribute significantly to the background.

Chapter 4

The SMEFT as a consistent QFT

In chapter 2 we presented general aspects concerning EFTs and their phenomenological applications. When pursuing precision in our predictions, theoretical aspects of effective theories at one-loop need to be discussed. The present chapter is dedicated to this task. We start by presenting the renormalization procedure of an effective Lagrangian and the renormalization scale dependence. The matching to the UV completion at one-loop is also presented, as a consequence we show that the effective theory captures the low energy behaviour of the full theory. This is then followed by the introduction of evanescent operators and their scheme dependence. We finish with a discussion of anomalies in the SMEFT.

Section 4.1 about the renormalization procedure in the SMEFT serves as an introduction to the procedure of dealing with divergent contributions in the chapter 6 when we discuss the double Higgs production in the SMEFT. Part of our work leading to the results in chapter 5 consisted of the validation of the SMEFT implementation at one-loop in MadGraph5_aMC@NLO [110]. Such validation was twofold: the analytical computation of the one-loop contribution to the $t\bar{t}$ production at the LHC of a subset of four-fermion operators involving the top quark and the testing of a consistent scheme to treat anomalies.

4.1   Renormalization

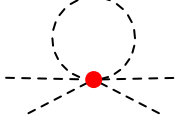The renormalization of a model requires selecting a regularization scheme of loop integrals. In general, cutoff regularization leads to complications [111]. The cutoff scale Λ_c has to be chosen at the same order of the EFT's cutoff scale Λ. The cutoff regularization introduces terms with powers of Λ in the numerator of the amplitudes. For example, let us consider the case of a theory

for the scalar φ with the effective interaction

$$\mathcal{L}_{\text{Scalar}} = \mathcal{L}_{\text{Kin}} + \frac{1}{6!}\frac{c_6}{\Lambda^2}\varphi^6 \tag{4.1}$$

where, with cutoff regularization, the $\varphi\varphi \to \varphi\varphi$ scattering receives the contribution

 $= -\frac{c_6}{2\Lambda^2}\int\frac{d^4k}{(2\pi)^4}\frac{1}{k^2-m_\varphi^2} \xrightarrow{m_\varphi \ll \Lambda_c} -\frac{c_6}{2\Lambda^2}\frac{\Lambda_c^2}{16\pi^2}. \tag{4.2}$

In order to maintain the validity of the EFT, the cutoff scale Λ_c is smaller than Λ in Eq. (4.2). Additionally, the quantity m_φ has been neglected since the scalar φ is considered to be a light particle in the effective theory, *i.e.* $m_\varphi \ll \Lambda_c$. Similarly, higher dimensional operators with derivatives lead to higher powers of the cutoff in the numerator. Such analytical contributions in $\Lambda_c \equiv \Lambda$ lead to the breakdown of the EFT expansion in powers $1/\Lambda$. This can be seen from the the violation of the power counting formula in Eq. (2.28). The breakdown of the EFT expansion can be avoided by choosing a Λ_c that is in between Λ and the typical energies of the experiments where the EFT is intended to be used. However such a regulator is often artificial and not very practical in the implementation of EFTs. Pauli-Villars regulators lead to a similar situation.

On the other hand, numerators in dimensional regularization preserve the power counting since no powers of Λ are introduced. This type of regularization is preferred in EFT computations since it provides a non-analytic dependence on the cutoff without any spurious analytic contributions at low energies. Thus, in amplitudes with effective interactions only additional powers of $1/\Lambda$ are introduced, which satisfies the power counting formula in Eq. (2.28). Moreover, if we do not consider gauge anomalies, dimensional regularization has the advantage of preserving gauge symmetry.

As discussed previously, EFTs are not renormalizable theories in the traditional sense as they require an infinite number of counterterms. In order to obtain predictions from an EFT a truncation at a given order in $1/\Lambda$ must be performed. This leads to require a finite number of counterterms and all of the infinities can be reabsorbed at such order in the effective expansion. Hence, EFTs are order-by-order renormalizable in the power counting.

In what follows we study a toy model that serves as an example of the renormalization of an EFT. Additionally we will see that the behaviour of the

EFT and the full theory matches at low energies at one-loop. Let us consider the model with a massless fermion with electric charge eQ interacting with heavy scalar:

$$\mathcal{L}_{\text{Toy}}^{\text{Full}} = -\frac{1}{4}(F_{\mu\nu})^2 + i\bar{\psi}\slashed{D}\psi + \frac{1}{2}(\partial_\mu\varphi)^2 - \frac{1}{2}M^2\varphi^2 + \lambda\varphi\bar{\psi}\psi. \quad (4.3)$$

In the regime of low energies compared to the mass of the scalar, $E^2 \ll M^2$, we can integrate this field out. The effective Lagrangian corresponding to the model above is

$$\mathcal{L}_{\text{Toy}}^{\text{EFT}} = -\frac{1}{4}(F_{\mu\nu})^2 + i\bar{\psi}_0\slashed{D}\psi_0 + \frac{c_6^0}{2\Lambda^2}\bar{\psi}_0\psi_0\bar{\psi}_0\psi_0 + \frac{c_8^0}{\Lambda^4}\bar{\psi}_0\psi_0(\partial_\mu\bar{\psi}_0\partial^\mu\psi_0) + \ldots \quad (4.4)$$

where the null index indicates bare quantities. Analyzing the case of a massless fermion will make manifest the IR behaviour of the full and effective theories. We focus on the renormalization of the terms involving the ψ_0 field as it is enough to highlight the points we want to discuss. This is achieved by rescaling the fermion field as

$$\psi_0 = Z_\psi^{1/2}\psi. \quad (4.5)$$

By inserting this in the effective Lagrangian we see that

$$\begin{aligned}\mathcal{L}_{\text{Toy}}^{\text{EFT}} \supset {}& i\bar{\psi}\slashed{D}\psi + \frac{c_6}{2\Lambda^2}\bar{\psi}\psi\bar{\psi}\psi + \frac{c_8}{\Lambda^4}\bar{\psi}\psi(\partial_\mu\bar{\psi}\partial^\mu\psi) \\ &+ i\delta Z_\psi\bar{\psi}\slashed{\partial}\psi + \frac{\delta c_6}{2\Lambda^2}\bar{\psi}\psi\bar{\psi}\psi + \frac{\delta c_8}{\Lambda^4}\bar{\psi}\psi(\partial_\mu\bar{\psi}\partial^\mu\psi)\end{aligned} \quad (4.6)$$

The first line in Eq. (4.6) is the Lagrangian written in terms of the physical quantities. The terms in second line of Eq. (4.6) are the counterterms which absorb the divergences defined as

$$\delta Z_\psi = Z_\psi - 1, \qquad \delta c_6 = c_6^0 Z_\psi^2 - c_6, \qquad \delta c_8 = c_8^0 Z_\psi^2 - c_8. \quad (4.7)$$

The counterterm associated to the wavefunction absorbs the divergence of the self-energies of the ψ-field. There are quantum corrections from the c_6 coupling and from QED to the self-energy. The corrections from the effective

$\psi(p_1)$ $\psi(p_3)$

$\psi(p_2)$ **(a)** $\psi(p_4)$ **(b)** **(c)**

(d) **(e)** **(f)**
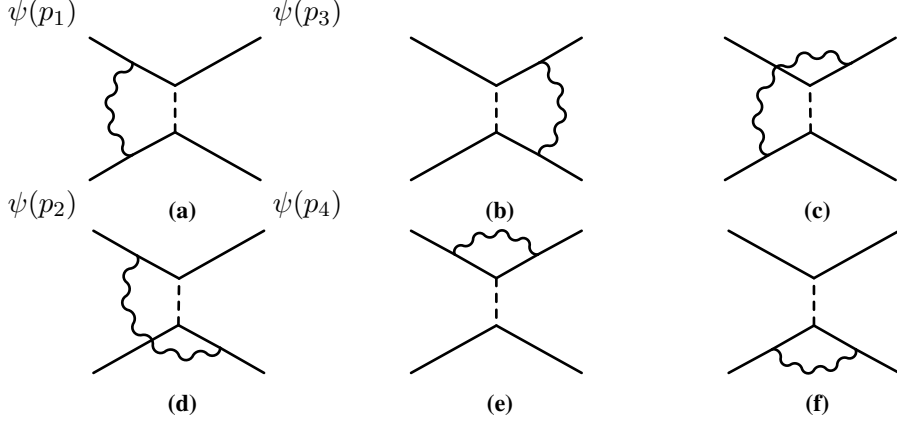
Figure 4.1: Feynman diagrams of the process $\psi\psi \to \psi\psi$ in the full theory.

interaction is computed to be

$$= -i\frac{c_6}{\Lambda^2} \int \frac{d^4k}{(2\pi)^4} \frac{i\slashed{k}}{k^2 - \mu_{\mathrm{IR}}^2} = \frac{-i}{(4\pi)^2} \frac{c_6}{\Lambda^2} \mu_{\mathrm{IR}}^3 \left(\frac{1}{\epsilon} - \log\frac{\mu_{\mathrm{IR}}^2}{\mu^2} + 1\right),$$

(4.8)

with μ_{IR} being the IR cutoff that make manifests the IR behaviour of the theory, and μ is the renormalization scale. Since the result above does not depend on the external momentum of the fermion as $\slashed{p}$, then the dimension-6 operator does not contribute to the wavefunction counterterm δZ_ψ.

The underlying theory and the EFT should match at every perturbation order. At tree-level the matching can be obtained by computing the process $\psi\psi \to \psi\psi$ in the two theories. In the computation of the amplitude in the full theory the propagator of the heavy scalar is expanded. From this we can fix the Wilson coefficients in terms of parameters in the Lagrangian in Eq. (4.3). Explicitly, from keeping the first term of the expansion of the φ-propagator we find that $\Lambda^2 = M^2$ and $c_6 = \lambda^2$. The next term in the expansion of the φ-propagator leads to the identification $c_8 = \lambda^2$. The Wilson coefficients appear as independent on the renormalization scale at tree-level, but at the end of this section it will become clear that in reality the matching at tree-level stands as $c_6(\mu = M) = \lambda^2$, $c_8(\mu = M) = \lambda^2$.

The matching above can be improved by considering loop corrections. In the following we compute the QED corrections to the process $\psi\psi \to \psi\psi$.

Since we are interested in the matching we set $p_i = 0$ in the propagators when possible, which is allowed since the matching holds for any particular values of the external momenta as far as the limit $p_i^2/M^2 \to 0$ is hold. The Feynman diagrams in the underlying theory are shown in Fig. 4.1, from which the amplitude of the first diagram is

$$
\begin{aligned}
\mathcal{M}^{\text{Full}}_{(a)} &= \int \frac{d^4k}{(2\pi)^4} \bar{u}(p_3)(-i\lambda)\frac{i\slashed{k}}{k^2 - \mu_{\text{IR}}^2}(ieQ\gamma^\mu)u(p_1)\frac{-ig_{\mu\nu}}{k^2 - \mu_{\text{IR}}^2}\frac{i}{k^2 - M^2} \\
&\qquad\qquad \bar{u}(p_4)(-i\lambda)\frac{i\slashed{k}}{k^2 - \mu_{\text{IR}}^2}(ieQ\gamma^\nu)u(p_2) \\
&= (eQ\lambda)^2 \bar{u}(p_3)\gamma^\rho\gamma_\mu u(p_1)\bar{u}(p_4)\gamma^\sigma\gamma^\mu u(p_2) \\
&\qquad\qquad \int \frac{d^4k}{(2\pi)^4}\frac{k_\rho k_\sigma}{(k^2 - \mu_{\text{IR}}^2)^3(k^2 - M^2)}.
\end{aligned}
$$

(4.9)

Analogous expressions are obtained for the diagrams 4.1b-4.1d with the difference being the legs to which the photon is being attached. At the amplitude level, this translates into the order of the γ-matrices in Eq. (4.9). The sum of the four diagrams leads to

$$
\mathcal{M}^{\text{Full}}_{(abcd)} = -i\frac{\alpha Q^2}{4\pi^2}\frac{\lambda^2}{M^2}\Big(\log\frac{\mu_{\text{IR}}^2}{M^2} + 1\Big)\mathcal{U}_T,
$$

(4.10)

with

$$
\mathcal{U}_T = \bar{u}(p_3)\sigma_{\mu\nu}u(p_1) \cdot \bar{u}(p_4)\sigma^{\mu\nu}u(p_2)
$$

(4.11)

and we remember the definition $\sigma^{\mu\nu} = \frac{i}{2}[\gamma^\mu, \gamma^\nu]$. The amplitude of this process presents UV divergences coming from the diagrams 4.1e and 4.1f. The contribution of the former can be written as

$$
\mathcal{M}^{\text{Full}}_{(e)} = (eQ\lambda)^2\bar{u}(p_3)\gamma^\rho\gamma^\sigma u(p_1)\bar{u}(p_4)u(p_2)\int\frac{d^4k}{(2\pi)^4}\frac{k_\rho k_\sigma}{(k^2 - \mu_{\text{IR}}^2)^3(q^2 - M^2)}.
$$

(4.12)

The amplitude for the diagram in Fig. 4.1f is computed analogously to the one in Eq. (4.12), and by adding those two diagrams, we obtain

$$
\mathcal{M}^{\text{Full}}_{(ef)} = (eQ\lambda)^2\Big(\frac{2}{\epsilon} - 2\log\frac{\mu_{\text{IR}}^2}{M^2} - 1\Big)\mathcal{U}_S,
$$

(4.13)
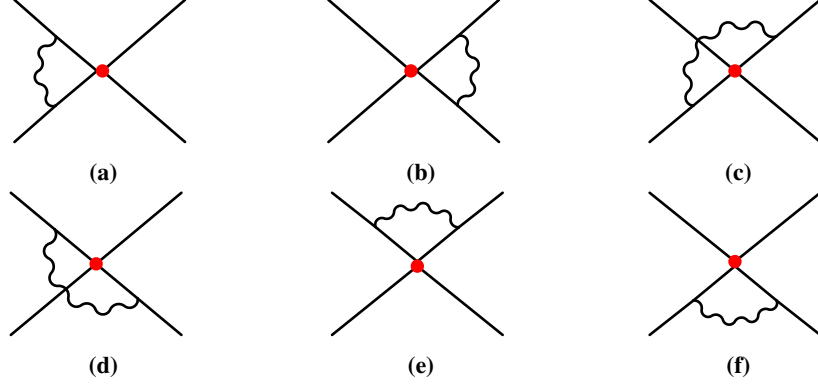
Figure 4.2: Feynman diagrams of the process $\psi\psi \to \psi\psi$ in the EFT.

where the loop integral has been performed and we define

$$\mathcal{U}_S = \bar{u}(p_3)u(p_1) \cdot \bar{u}(p_4)u(p_2). \tag{4.14}$$

The total amplitude of the process is thus obtained by including the tree-level result amplitude (proportional to $\mathcal{U}_S$), joining the results from Eq. (4.10) and (4.13), and including the cross-diagrams obtained from exchanging $p_3 \leftrightarrow p_4$. Therefore, the total result in the full theory reads

$$\mathcal{M}_{\text{Total}}^{\text{Full}} = \frac{i\lambda^2}{M^2} \left(1 + \frac{\alpha Q^2}{\pi}\left(\frac{2}{\epsilon} - 2\log\frac{\mu_{\text{IR}}^2}{M^2} - 1\right)\right)\mathcal{U}_S$$
$$- \frac{i\lambda^2}{M^2}\frac{\alpha Q^2}{8\pi}\left(2\log\frac{\mu_{\text{IR}}^2}{M^2} + 2\right)\mathcal{U}_T - \{3 \leftrightarrow 4\}. \tag{4.15}$$

The computation in the EFT follows similar steps. In this case the Feynman diagrams are as shown in Fig. 4.2. For the first diagram we obtain the amplitude

$$\mathcal{M}_{\text{(a)}}^{\text{EFT}} = i\frac{c_6}{\Lambda^2}\int\frac{d^4k}{(2\pi)^4}\bar{u}(p_3)\frac{i\slashed{k}}{k^2 - \mu_{\text{IR}}}(ieQ\gamma^\mu)u(p_1)\frac{-ig_{\mu\nu}}{k^2 - \mu_{\text{IR}}^2}$$
$$\bar{u}(p_4)\frac{i\slashed{k}}{k^2 - \mu_{\text{IR}}}(ieQ\gamma^\nu)u(p_2)$$
$$= -e^2Q^2\frac{c_6}{\Lambda^2}\bar{u}(p_3)\gamma^\rho\gamma_\mu u(p_1)\cdot\bar{u}(p_4)\gamma^\sigma\gamma^\mu u(p_2)\int\frac{d^4k}{(2\pi)^4}\frac{k_\rho k_\sigma}{(k^2 - \mu_{\text{IR}}^2)^3}$$
$$\tag{4.16}$$

Once again, the difference between the first four diagrams in 4.2 is the insertion of the photons onto the external legs. By summing those diagrams we find the result

$$\mathcal{M}^{\text{EFT}}_{(\text{abcd})} = i \frac{\alpha Q^2}{4\pi} \frac{c_6}{\Lambda^2} \left(\frac{1}{\epsilon} + \log \frac{\mu^2_{\text{IR}}}{\mu^2_{\text{UV}}} - \frac{1}{2} \right) \mathcal{U}_T \tag{4.17}$$

The Lorentz structure of the loop corrections above cannot be obtained at tree-level from the original EFT Lagrangian in Eq. (4.4). In particular, we have an UV divergence that cannot be absorbed by any of the interactions in the original Lagrangian. This requires the inclusion of the term

$$\mathcal{L}^{\text{EFT}}_{\text{Toy}} = \cdots + \frac{c_T}{2\Lambda^2} (\bar{\psi} \sigma_{\mu\nu} \psi)(\bar{\psi} \sigma^{\mu\nu} \psi). \tag{4.18}$$

Finally, the diagrams in Fig. 4.2f and 4.2e lead to the amplitude

$$\mathcal{M}^{\text{EFT}}_{(\text{ef})} = i \frac{\alpha Q^2}{\pi} \frac{c_6}{\Lambda^2} \left(\frac{2}{\epsilon} - 2 \log \frac{\mu^2_{\text{IR}}}{\mu^2_{\text{UV}}} - 1 \right) \mathcal{U}_S \tag{4.19}$$

Hence, by collecting the results above, the cross-diagrams contributions and the tree-level amplitudes we obtain the total result in the EFT

$$\begin{aligned} \mathcal{M}^{\text{EFT}}_{\text{Total}} = {} & i \frac{c_6}{\Lambda^2} \left(1 + \frac{\alpha Q^2}{\pi} \left(\frac{2}{\epsilon} - 2 \log \frac{\mu^2_{\text{IR}}}{\mu^2_{\text{UV}}} - 1 \right) \right) \mathcal{U}_S \\ & + \left(i \frac{c_T}{\Lambda^2} + i \frac{c_6}{\Lambda^2} \frac{\alpha Q^2}{8\pi} \left(\frac{2}{\epsilon} - 2 \log \frac{\mu^2_{\text{IR}}}{\mu^2_{\text{UV}}} + 1 \right) \right) \mathcal{U}_T - \{3 \leftrightarrow 4\}. \end{aligned} \tag{4.20}$$

By comparison of Eq. (4.15) and (4.20) we notice that the two amplitudes have the same behaviour at low energies captured by the parameter μ_{IR}. On the other hand, the UV poles do not match. From the renormalization scheme used to absorb the divergences in the EFT we have

$$\log \frac{\mu^2_{\text{IR}}}{M^2} \neq \log \frac{\mu^2_{\text{IR}}}{\mu^2_{\text{UV}}}. \tag{4.21}$$

The parameter μ_{UV} is a non-physical quantity which can be set to $\mu^2_{\text{UV}} = M^2$. In this situation it is said that the matching is performed at the energy scale of M. Thus, the QED corrections at one-loop yield the relations

$$c_6(\mu^2_{\text{UV}} = M^2) = \lambda^2 + \mathcal{O}(\alpha^2), \tag{4.22}$$

$$c_T(\mu^2_{\text{UV}} = M^2) = -\frac{3\alpha Q^2}{8\pi} \lambda^2 + \mathcal{O}(\alpha^2). \tag{4.23}$$

The coefficient c_6 does not receive one-loop QED corrections, while the coefficient c_T is generated purely from quantum corrections. Regarding the counterterms, we obtain the expressions

$$\delta c_6 = -\frac{3\alpha Q^2}{2\pi} c_6 \cdot \frac{1}{\epsilon} \tag{4.24}$$

$$\delta c_T = -\frac{\alpha Q^2}{4\pi} c_6 \cdot \frac{1}{\epsilon}. \tag{4.25}$$

Both of these counterterms are proportional to the Wilson coefficient c_6, so that c_6 and c_T renormalize each other. In terms of the running of the Wilson coefficients the result above implies that the two operators mix. The running and mixing is dictated by

$$\frac{d}{d\log\mu} c_i = \gamma_{ij} c_j, \tag{4.26}$$

with γ being the anomalous dimension matrix

$$\gamma = \frac{2\alpha Q^2}{\pi} \begin{pmatrix} -\frac{3}{2} & -\frac{1}{2} \\ -\frac{1}{2} & \frac{1}{2} \end{pmatrix}. \tag{4.27}$$

The entries in the second column are obtained via other scattering processes.

4.2 Evanescent operators

In the previous section we studied the situation in which a four-fermion operator could mix through quantum correction into another operator that was not included originally in the Lagrangian. In this section we will discuss the possibility of Wilson operators mixing into non-physical operators which can nevertheless have an effect in our observables. Such effects are manifest through the rational part of amplitudes.

We remember that any one-loop amplitude can be written as

$$\mathcal{M}^{\text{One−loop}} = \int \frac{d^d\ell}{(2\pi)^d} \frac{N(\ell)}{d_0 d_1 \ldots d_{m-1}} \tag{4.28}$$

$$= \sum_i d_i D_0^i + \sum_i c_i C_0^i + \sum_i b_i B_0^i + \sum_i a_i A_0^i + \mathcal{R}, \tag{4.29}$$

where the box (D_0), triangle (C_0), bubble (B_0) and tadpole (A_0) scalar integrals are known and can be expressed in terms of logarithm and dilogarithm functions, and $\mathcal{R}$ is the rational term. Following the nomenclature of 't Hooft

and Veltman [112], the scalar integrals are defined as

$$A_0(m_0^2) = \int \frac{d^d\ell}{(2\pi)^d} \frac{1}{d_0}, \qquad (4.30)$$

$$B_0(p_1^2; m_0^2, m_1^2) = \int \frac{d^d\ell}{(2\pi)^d} \frac{1}{d_0 d_1}, \qquad (4.31)$$

$$C_0(p_1^2, p_2^2, s_{12}; m_0^2, m_1^2, m_2^2) = \int \frac{d^d\ell}{(2\pi)^d} \frac{1}{d_0 d_1 d_2}, \qquad (4.32)$$

$$D_0(p_1^2, p_2^2, p_3^2, p_4^2, s_{12}, s_{23}; m_0^2, m_1^2, m_2^2, m_3^2) = \int \frac{d^d\ell}{(2\pi)^d} \frac{1}{d_0 d_1 d_2 d_3}, \qquad (4.33)$$

where $s_{12} = (p_1 + p_2)^2$, $s_{23} = (p_2 + p_3)^2$, $d_i = (\ell + q_i)^2 - m_i^2 + i\epsilon$ and $q_i = \sum_{j=1}^i p_i$. Additionally, rational terms are finite contributions generated by the part of the integrand linear in $d-4$. The computation of the rational part is organized into the $\mathcal{R}_1$, arising from the $d-4$ component in the denominator of the integrand, and $\mathcal{R}_2$, corresponding to the finite part coming from the $d-4$ component of the numerator. The $\mathcal{R}_1$ terms can be obtained using the so-called OPP method [113], while $\mathcal{R}_2$ terms are obtained by

$$\mathcal{R}_2 = \lim_{\epsilon \to 0} \int d^d\ell \frac{\tilde{N}(\ell, \epsilon)}{d_0 d_1 \dots d_{m-1}}, \qquad (4.34)$$

where $\tilde{N}$ stands as the $d-4$ component of the numerator in Eq. (4.28). In this section, we focus on the evanescent operators, which are known to contribute to the amplitudes through $\mathcal{R}_2$ terms. We start by discussing a particular case where evanescent structures arise and then we extend the discussion into a more general approach.

The Fermi interactions in the section 2.1 were obtained through the integration of the W-boson. From the top-down approach in the SM, we know that four-fermion interactions between different quark flavours are generated when the W-boson is integrated out. Let us discuss the case of the nonleptonic weak interaction

$$\mathcal{L} = \frac{c_6}{\Lambda^2} (\bar{d}\gamma_\mu P_L u)(\bar{u}\gamma^\mu P_L s). \qquad (4.35)$$

Similar operators such as $(\bar{s}\gamma_\mu P_L d)(\bar{s}\gamma^\mu P_L d)$ and $(\bar{s}\gamma_\mu P_L d)(\bar{u}\gamma^\mu P_L c)$, appearing either in χPT or HEQT, induce nonleptonic transitions resulting in mesons oscillations like the $K^0 - \bar{K}^0$ mixing [114–116]. In this context, QCD corrections to nonleptonic weak transitions of K-, D- and B-mesons play an important role. The Feynman diagrams of those QCD corrections to operators

of the HQET are as displayed in Fig. 4.2, where the photon propagator should now be replaced by the gluon propagator. Large efforts were done in the past to compute those corrections in a consistent manner, with Ref. [117] being the first analysis of evanescent operators in the context of RG improved QCD corrections to electroweak transitions.

The determination of the QCD contributions to the running of the operator in (4.35) requires the evaluation of the diagrams in fig 4.2 for the process $s(p_1)\bar{u}(p_2) \to d(p_3)\bar{u}(p_4)$. Let us focus on the diagram 4.2c, with the corresponding amplitude

$$
\begin{aligned}
\mathcal{M}_{(c)} &= (ig)^2 \int \frac{d^d k}{(2\pi)^4} \frac{-i}{k^2} \bar{u}(p_3)\gamma_\nu T^A \frac{i\not{k}}{k^2}\gamma_\mu P_L v(p_4)\bar{v}(p_2)\gamma^\mu P_L T^A \frac{i\not{k}}{k^2}\gamma^\nu u(p_1) \\
&= \frac{g^2}{4}\frac{\Gamma(2-d/2)}{(4\pi)^2}\bar{u}(p_3)\gamma_\nu\gamma_\lambda\gamma_\mu P_L T^A v(p_4)\bar{v}(p_2)\gamma^\mu P_L \gamma^\lambda\gamma^\nu T^A u(p_1),
\end{aligned}
$$
(4.36)

where we set external momenta to zero because we are interested in the divergent contribution. The γ_5 matrix is treated in the naive-dimensional regularization scheme (NDR)[1], so that $\{\gamma_5, \gamma_\mu\} = 0$ in all dimensions. Therefore, with $d = 4 - 2\epsilon$ and expanding around $\epsilon = 0$ we obtain

$$
\mathcal{M}_{(c)} = \frac{g^2}{4}\frac{1}{(4\pi)^2}\frac{1}{\epsilon}\bar{u}(p_3)\gamma_\nu\gamma_\lambda\gamma_\mu P_L T^A v(p_4)\bar{v}(p_2)\gamma^\mu\gamma^\lambda\gamma^\nu P_L T^A u(p_1).
$$
(4.37)

We observe that in terms of two-components spinors

$$
\begin{aligned}
\bar{u}_L(p_3)&\bar{\sigma}^\nu\bar{\sigma}^\lambda\bar{\sigma}^\mu v_L(p_4)\bar{v}_L(p_2)\bar{\sigma}_\mu\bar{\sigma}_\lambda\bar{\sigma}_\nu u_L(p_1) \\
&= \big(\bar{u}_L(p_3)\bar{\sigma}^\nu\bar{\sigma}^\lambda\big)_a\big(\bar{\sigma}^\mu\big)_{ab}\big(v_L(p_4)\big)_b\big(\bar{v}_L(p_2)\big)_c\big(\bar{\sigma}_\mu\big)_{cd}\big(\bar{\sigma}_\lambda\bar{\sigma}_\nu u(p_1)\big)_d \\
&= 2\epsilon_{ac}\epsilon_{bd}(\bar{u}_L(p_3)\bar{\sigma}^\nu\bar{\sigma}^\lambda)_a\big(v_L(p_4)\big)_b\big(\bar{v}_L(p_2)\big)_c(\bar{\sigma}_\lambda\bar{\sigma}_\nu u_L(p_1))_d \\
&= -2\epsilon_{ac}\epsilon_{bd}(\bar{u}_L(p_3)\bar{\sigma}^\nu\bar{\sigma}^\lambda)_a\big(v_L(p_4)\big)_d\big(\bar{v}_L(p_2)\big)_c(\bar{\sigma}_\lambda\bar{\sigma}_\nu u_L(p_1))_b \\
&= -\bar{u}_L(p_3)\bar{\sigma}^\nu\bar{\sigma}^\lambda\bar{\sigma}^\mu\bar{\sigma}_\lambda\bar{\sigma}_\nu u_L(p_1)\bar{v}_L(p_2)\bar{\sigma}_\mu v_L(p_4),
\end{aligned}
$$
(4.38)

where we used the identity $\big(\bar{\sigma}^\mu\big)_{ab}\big(\bar{\sigma}_\mu\big)_{cd} = 2\epsilon_{ac}\epsilon_{bd}$ to obtain the first and fourth equalities. Thus, the Dirac structure in eq. (4.37) can be written in a

---

[1]Technical difficulties arise when extending the definition of γ_5 to $d = 4 - 2\epsilon$ dimensions. The algebra satisfied by γ_5 defines different schemes [118].

different way by using Fierz identities as

$$
\begin{aligned}
\bar{u}(p_3)&\gamma^\nu\gamma^\lambda\gamma^\mu P_L v(p_4)\bar{v}(p_2)\gamma_\mu\gamma_\lambda\gamma_\nu P_L u(p_1) \\
&= \bar{u}(p_3)\gamma^\nu\gamma^\lambda\gamma^\mu\gamma_\lambda\gamma_\nu P_L u(p_1)\bar{v}(p_2)\gamma_\mu P_L v(p_4) \\
&= (2-d)^2\bar{u}(p_3)\gamma^\mu P_L v(p_4)\bar{v}(p_2)\gamma_\mu P_L u(p_1) \\
&= (4-8\epsilon)\bar{u}(p_3)\gamma^\mu P_L v(p_4)\bar{v}(p_2)\gamma_\mu P_L u(p_1) + \mathcal{O}(\epsilon^2), \quad (4.39)
\end{aligned}
$$

where we have used the algebra of the γ-matrices in d-dimensions. The derivation in Eq. (4.39) relies on the Fierz identities. Computations in effective theories involving four-fermion operators often make use of the Fierz identities discussed in section 2.7. These identities are valid in $d=4$ since the Lorentz algebra is no longer closed in $d=4-2\epsilon$ dimensions, which brings complications in loop level computations that require dimensional regularization.

In exactly the same way, in the SMEFT at dimension-6, the evanescent operators appear from the fact that the Dirac algebra is infinite dimensional for non-integer d. More generally, the evanescent operators are defined as the difference between operators and their transformed versions using identities held in $d=4$. Under this definition, we can consider the case of flavour-changing four-quark operators. In particular, among the operators responsible for the K^0-$\bar{K}^0$ mixing with $\Delta F = 2$ there is

$$
\mathcal{O}_{sd} = (\bar{s}\gamma_\mu P_L d)(\bar{s}\gamma^\mu P_L d) \tag{4.40}
$$

which at one-loop receives corrections through virtual gluons exchanges, yielding the evanescent operator [115]

$$
\mathcal{E}_{sd} = (\bar{s}\gamma_\mu\gamma_\nu\gamma_\rho P_L d)(\bar{s}\gamma^\mu\gamma^\nu\gamma^\rho P_L d) - (16-4\epsilon)\mathcal{O}_{sd}. \tag{4.41}
$$

Examples of evanescent structures different from the current-current interactions are dimension-10 operators composed of field strength $F_{\mu\nu}$ and their covariant derivatives in Yang-Mills theories [119].

In general, the application of Fierz identities and the loop integration operation do not commute. To address this issue, the introduction of the so-called evanescent operators is required. At tree-level an operator $\mathcal{O}$ and its Fierz-transformed version $\mathcal{F}\mathcal{O}$ are trivially related as

$$
\mathcal{O} = \mathcal{F}\mathcal{O}, \tag{4.42}
$$

while at one-loop

$$\mathcal{O} = \mathcal{F}\mathcal{O} + E. \tag{4.43}$$

The evanescent operators can be extracted from this relationship as the difference between $\mathcal{O}$ and $\mathcal{F}\mathcal{O}$. Now, let us consider the more general case of physical four-fermion operators

$$\mathcal{O}_k = \bar{\psi} q_k \psi \cdot \bar{\psi} \tilde{q}_k \psi, \tag{4.44}$$

with $k = 1, 2, 3, \cdots$ and q_k a representing the Dirac structure of the operator. The matrix elements of $\mathcal{O}_k$ are of the form

$$\Gamma_{ij} \cdot [Q_k]_{ijrs} \cdot \Gamma'_{rs} = \bar{u}_i (\gamma_\mu \gamma_\nu \cdots (1 - \gamma_5))_{ij} u_j \cdot \bar{u}_r (\gamma^\mu \gamma^\nu \cdots (1 - \gamma_5))_{rs} u_s, \tag{4.45}$$

where u_i is a generic spinor. The Dirac structure $[Q]_{ijrs}$ are more conveniently written as

$$Q_k = q_k \otimes \tilde{q}_k. \tag{4.46}$$

Generalizing the discussion in the section 4.1, the matrix elements of four-fermion operators present a perturbative expansion in the coupling g of the form

$$Z_\psi^2 \langle \mathcal{O}_k^{\text{Bare}} \rangle = \sum_{j \geq 0} \left(\frac{g^2}{16\pi^2} \right)^j \langle \mathcal{O}_k^{\text{Bare}} \rangle^{(j)}, \tag{4.47}$$

with the angle brackets indicating the matrix elements. Following the result of Eq. (4.36), the insertion at one-loop of the operator corresponding in the Lagrangian in Eq. (4.35)

$$Q = \gamma_\mu (1 - \gamma_5) \otimes \gamma^\mu (1 - \gamma_5), \tag{4.48}$$

leads to the linear combination with the Dirac structure

$$Q' = [\gamma_\nu \gamma_\lambda \otimes \mathbb{1}] Q [\mathbb{1} \otimes \gamma^\lambda \gamma^\nu]. \tag{4.49}$$

When more operators are included in the Lagrangian the one-loop matrix elements of the operator $\mathcal{O}_k$ are computed to be

$$\langle \mathcal{O}_k^{\text{Bare}} \rangle^{(1)} = d_{kl}^{(1)} \langle \mathcal{O}_l \rangle^{(0)} + d_{k,Q'_k}^{(1)} \langle \mathcal{O}'_k \rangle^{(0)}, \tag{4.50}$$

where, on the left-hand, side we have tree-level matrix elements. The coefficients $d^{(1)}$ have a finite part and a term proportional to $1/\epsilon$. The operator $\mathcal{O}'_k$ can be decomposed into a linear combination of the $\mathcal{O}_l$ and evanescent operators

$$\mathcal{O}'^{\text{Bare}}_k = (f_{kl} + a_{kl}\epsilon)\mathcal{O}^{\text{Bare}}_l + \mathcal{E}_1[\mathcal{O}_k] + \mathcal{O}(\epsilon^2), \qquad (4.51)$$

The coefficients f_{kl} are uniquely determined by the decomposition into the Dirac basis in $d = 4$. However, the coefficients a_{kl} are arbitrary since a priori one can add to evanescent operators entering the amplitude any multiple of ϵ times a given physical operator. In the literature there are different definitions of the a_{kl} leading to different corresponding evanescent operators. In Ref. [117] the a_{kl} are computed by choosing a basis

$$\mathcal{B} = \{\gamma^{(1)} \otimes \tilde{\gamma}^{(1)}, \cdots, \gamma^{(10)} \otimes \tilde{\gamma}^{(10)}\} \qquad (4.52)$$

so that any Dirac structures in $d = 4$ can be written in terms of the elements of $\mathcal{B}$ and the coefficients f_{kl} and a_{kl} satisfying

$$\text{tr}(\gamma^{(m)} q'_k \tilde{\gamma}^{(m)} \tilde{q}'_k) = (f_{kl} + a_{kl}\epsilon) \, \text{tr}(\gamma^{(m)} q_l \tilde{\gamma}^{(m)} \tilde{q}_l) + \mathcal{O}(\epsilon^2), \qquad (4.53)$$

with $m = 1, \cdots, 10$. We can see the Eq. (4.53) as the contraction of the operators $\mathcal{O}'_k$ and $\mathcal{O}_l$ onto the elements of the basis $\mathcal{B}$. In our example in Eq. (4.39) we used implicitly the basis

$$\mathcal{B}_1 = \{\mathbb{1} \otimes \mathbb{1}, \mathbb{1} \otimes \gamma_5, \gamma_5 \otimes \mathbb{1}, \gamma_5 \otimes \gamma_5, \gamma_\mu \otimes \gamma^\mu, \gamma_\mu \otimes \gamma^\mu \gamma_5, \gamma_5 \gamma_\mu \otimes \gamma^\mu,$$
$$\gamma_\mu \gamma_5 \otimes \gamma^\mu \gamma_5, \sigma_{\mu\nu} \otimes \sigma^{\mu\nu}, \gamma_5 \sigma_{\mu\nu} \otimes \sigma^{\mu\nu}\}. \qquad (4.54)$$

Then, for the Dirac structure in (4.48) we obtained from the Eq. (4.39) in the basis $\mathcal{B}_1$

$$Q' = \gamma_\rho \gamma_\sigma \gamma_\mu (1 - \gamma_5) \otimes \gamma^\mu \gamma^\sigma \gamma^\rho (1 - \gamma_5)$$
$$= (4 - 8\epsilon)Q + E_1[Q] + \mathcal{O}(\epsilon^2). \qquad (4.55)$$

This result can also be obtained from Eq. (4.53). To see this, we take the contraction of the operator Q' above with the fifth element of $\mathcal{B}_1$:

$$\text{tr}(\gamma_\alpha q' \gamma^\alpha \tilde{q}') = \text{tr}(\gamma^\alpha \gamma^\rho \gamma^\sigma \gamma^\mu (1 - \gamma_5)\gamma_\alpha \gamma_\mu \gamma_\sigma \gamma_\rho (1 - \gamma_5))$$
$$= 8d(2 - d)^3 \qquad (4.56)$$

and the contraction of the operator Q with the same basis element

$$(f^{\mathrm{b1}} + a^{\mathrm{b1}}\epsilon)\mathrm{tr}(\gamma_\alpha q\gamma^\alpha \tilde{q}) = (f^{\mathrm{b1}} + a^{\mathrm{b1}}\epsilon)\mathrm{tr}(\gamma^\alpha \gamma^\mu(1-\gamma 5)\gamma_\alpha \gamma_\mu(1-\gamma 5))$$
$$= 8d(2-d)(f^{\mathrm{b1}} + a^{\mathrm{b1}}\epsilon). \qquad (4.57)$$

Therefore, the matching of Eq. (4.56) and (4.57) yields the values for the coefficients

$$(f^{\mathrm{b1}} + a^{\mathrm{b1}}\epsilon) = (2-d)^2 = 4 - 8\epsilon \mathcal{O}(\epsilon^2). \qquad (4.58)$$

A different basis generates the same f_{kl} but different a_{kl}. For example, let us consider a basis with the same elements of $\mathcal{B}_1$ except for the sixth and eigth elements:

$$\mathcal{B}_2 = \{\mathbb{1} \otimes \mathbb{1}, \mathbb{1} \otimes \gamma_5, \gamma_5 \otimes \mathbb{1}, \gamma_5 \otimes \gamma_5, \gamma_\mu \otimes \gamma^\mu, \gamma_\mu\gamma_\nu\gamma_\rho \otimes \gamma^\mu\gamma^\nu\gamma^\rho, \gamma_5\gamma_\mu \otimes \gamma^\mu,$$
$$\gamma_5\gamma_\mu\gamma_\nu\gamma_\rho \otimes \gamma^\mu\gamma^\nu\gamma^\rho, \sigma_{\mu\nu} \otimes \sigma^{\mu\nu}, \gamma_5\sigma_{\mu\nu} \otimes \sigma^{\mu\nu}\}. \qquad (4.59)$$

When we project the operator Q' over the elements of $\mathcal{B}_2$ there are two non-trivial possible results. When Q' is contracted with the fifth element of the basis we obtain

$$\mathrm{tr}(\gamma^\alpha q'\gamma_\alpha\tilde{q}') = \mathrm{tr}(\gamma^\alpha\gamma^\rho\gamma^\sigma\gamma^\mu(1-\gamma_5)\gamma_\alpha\gamma_\mu\gamma_\sigma\gamma_\rho(1-\gamma_5))$$
$$= -8(d-2)^3 d, \qquad (4.60)$$

while when contracted with the eighth element

$$\mathrm{tr}(\gamma^5\gamma^\alpha\gamma^\beta\gamma^\delta q'\gamma_\alpha\gamma_\beta\gamma_\delta\tilde{q}')$$
$$= \mathrm{tr}(\gamma^5\gamma^\alpha\gamma^\beta\gamma^\delta\gamma^\rho\gamma^\sigma\gamma^\mu(1-\gamma_5)\gamma_\alpha\gamma_\beta\gamma_\delta\gamma_\mu\gamma_\sigma\gamma_\rho(1-\gamma_5))$$
$$= -8(d-2)d(d(d((d-22)d+140)-344)+224). \qquad (4.61)$$

This hints that we need two operators to write down the evanescent operator in the second basis. The chosen operators are $Q_1 = Q$ and $Q_2 = (1+\gamma_5) \otimes (1-\gamma_5)$. Thus, we compute the analogous projections

$$(f_l^{\mathrm{b2}} + a_l^{\mathrm{b2}}\epsilon)\mathrm{tr}(\gamma_\alpha q_l\gamma^\alpha\tilde{q}_l)$$
$$= (f_1^{\mathrm{b2}} + a_1^{\mathrm{b2}}\epsilon)\mathrm{tr}(\gamma^\alpha\gamma^\mu(1-\gamma 5)\gamma_\alpha\gamma_\mu(1-\gamma 5))$$
$$+ (f_2^{\mathrm{b2}} + a_2^{\mathrm{b2}}\epsilon)\mathrm{tr}(\gamma^\alpha(1+\gamma 5)\gamma_\alpha(1-\gamma 5))$$
$$= 8d(2-d)(f_1^{\mathrm{b2}} + a_1^{\mathrm{b2}}\epsilon) + 8d(f_2^{\mathrm{b2}} + a_2^{\mathrm{b2}}\epsilon), \qquad (4.62)$$

and

$$
\begin{aligned}
(f_l^{\mathrm{b2}} + a_l^{\mathrm{b2}}\epsilon)&\mathrm{tr}(\gamma^\alpha\gamma^\beta\gamma^\delta q_l\gamma_\alpha\gamma_\beta\gamma_\delta\tilde{q}_l) \\
&= (f_1^{\mathrm{b2}} + a_1^{\mathrm{b2}}\epsilon)\mathrm{tr}(\gamma^5\gamma^\alpha\gamma^\beta\gamma^\delta\gamma^\mu(1-\gamma5)\gamma_\alpha\gamma_\beta\gamma_\delta\gamma_\mu(1-\gamma5)) \\
&\qquad + (f_2^{\mathrm{b2}} + a_2^{\mathrm{b2}}\epsilon)\mathrm{tr}(\gamma^5\gamma^\alpha\gamma^\beta\gamma^\delta(1+\gamma5)\gamma_\alpha\gamma_\beta\gamma_\delta(1-\gamma5)) \\
&= -8d(f_1^{\mathrm{b2}} + a_1^{\mathrm{b2}}\epsilon)(d-2)((d-10)d+8) \\
&\qquad + 8d(f_2^{\mathrm{b2}} + a_2^{\mathrm{b2}}\epsilon)((d-6)d+4).
\end{aligned}
\tag{4.63}
$$

Matching Eq. (4.60) and (4.61) to Eq. (4.62) and (4.63), respectively, and expanding around $\epsilon = 0$ yields the two equations from the terms of order $\mathcal{O}(\epsilon^0)$

$$
8f_1^{\mathrm{b2}} - f_2^{\mathrm{b2}} = 32, \qquad 32f_1^{\mathrm{b2}} - f_2^{\mathrm{b2}} = 128,
\tag{4.64}
$$

with solutions $f_1^{\mathrm{b2}} = 4$ and $f_2^{\mathrm{b2}} = 0$. From the terms of order $\mathcal{O}(\epsilon)$ we get the equations

$$
8a_1^{\mathrm{b2}} + 16 = a_2^{\mathrm{b2}}, \qquad 2a_1^{\mathrm{b2}} + 16 = a_2^{\mathrm{b2}},
\tag{4.65}
$$

with solutions $a_1^{\mathrm{b2}} = 0$ and $a_2^{\mathrm{b2}} = 16$. Thus, we write

$$
Q' = 4Q + 16\epsilon(1+\gamma_5) \otimes (1-\gamma_5) + E_1'[Q] + \mathcal{O}(\epsilon^2).
\tag{4.66}
$$

Hence, we obtain a different evanescent operator. In the case of using a different scheme for γ_5 in d dimensions the Eq. (4.55) and (4.66) are modified and the evanescent operators present more complicated structures. Moreover, there is an arbitrariness in the definition of the evanescent operators, as all of the information that we have available is that they vanish in $d = 4$ but there is a freedom associated to the way they vanish. An alternative way to define the evanescent operators is to choose the coefficients a_{kl} first and then add the corresponding combinations of the evanescent structures to the elements of the basis $\mathcal{B}$.

From the examples above we can see that when the evanescent operators are inserted in divergent diagrams the factors of order $\mathcal{O}(\epsilon)$ lead to finite contributions. It is then referred that the evanescent operators contribute to the rational terms. In the end, we are interested in those finite contributions. Some recent proposals have appeared in the literature where the they are obtained through different approaches such as generalizing the Fierz identities to the one-loop

level [120] and through the direct computations of the current-current and penguin diagrams in two different effective operator basis [121].

It is important to emphasize that when performing computations at one-loop in effective theories two points should be clear:

- Physical and evanescent operators provide counterterms to each other and so they mix at one-loop and beyond. A change of the definition of the evanescent operators, *i.e.* the a_{kl} coefficients, leads to modifications in the physical components of the anomalous dimension matrix. In other words, different choice of a_{kl} coefficients corresponds to a different renormalization scheme on the physical operators. Therefore, the presentation of a given anomalous dimension matrix should include the definition of the evanescent operators used in the calculation. Consequently, if the definition follows Eq. (4.53) then it should be clear which basis $\mathcal{B}$ was implemented.

- When presenting results in the SMEFT it is required to state explicitly the implemented basis of the effective operators. Two different basis related through Fierz identities will lead to different matrix elements at one-loop. This is important specially in the automation of computations like MadGraph5_aMC@NLO, since it might happen that the reported basis differs by Fierz identities from the one implemented in the programs.

Finally, the renormalization of the evanescent operators can be done in such a way that they do not affect the physics at the matching scale with the full renormalizable theory [122, 123]. In practical terms, the contributions from the evanescent operators are subtracted in the matching process. Thus, even though one-loop SMEFT results depend on the definitions of the evanescent structures, employing the same operator basis in the one-loop matching to a specific full theory and the inclusion of two-loop anomalous dimensions would lead to the cancellation of such an arbitrary dependence. Complete lectures on this topic can be found in [124].

4.3   The anomaly free nature of the SMEFT

Classical symmetries might not survive the quantization process of a theory, thus generating the so called anomalies. Such anomalies in a QFT can arise from global or gauge symmetries. In the former case, the anomaly gives important information about the phenomenology of the still consistent theory. In the

latter, the case of an anomaly of a gauge symmetry leads to the non-unitarity of the S-matrix.

The SM is an anomaly-free theory. When considering EFTs extensions of the SM, such as the SMEFT, we realise that new axial couplings between SM fields are introduced through effective operators. Thus, it is natural to ask if the anomalies in the SMEFT depend on the Wilson coefficients c_i. In the hypothetical scenario in which such dependence on the c_i happens, we could require anomaly cancellation and so the Wilson coefficients would have to satisfy sets of relations, providing theoretical constraints on the SMEFT parameters. Even more, experimental signs showing the violation of these relations would indicate the existence of new sectors coupling to the SM at the electroweak scale. Although appealing, this is not the case of the SMEFT, where constraints cannot be imposed on the Wilson coefficients, as we will discuss during this section.

In Ref. [125] the authors brought attention to the topic by finding theoretical constraints arising on the Wilson coefficients $\{c_{\varphi e}, c_{\varphi u}, c_{\varphi d}, c_{\varphi l}^{(1)}, c_{\varphi q}^{(1)}, c_{\varphi l}^{(3)}, c_{\varphi q}^{(3)}\}$ by studying operators of the form

$$
\mathcal{O}_{\varphi \psi_R} = \left(\varphi^\dagger i \overleftrightarrow{D}_\mu \varphi\right) \bar{\psi}_R \gamma^\mu \psi_R, \qquad \mathcal{O}_{\varphi \psi_L}^{(1)} = \left(\varphi^\dagger i \overleftrightarrow{D}_\mu \varphi\right) \bar{\psi}_L \gamma^\mu \psi_L,
$$
$$
\mathcal{O}_{\varphi \psi_L}^{(3)} = \left(\varphi^\dagger i \overleftrightarrow{D}_\mu^a \varphi\right) \bar{\psi}_L \tau^a \gamma^\mu \psi_L. \tag{4.67}
$$

In the broken phase these operators shift the gauge couplings of fermions of the SM. Then, by requiring the cancellation of anomalies order by order in the $1/\Lambda$ expansion, the authors find summation rules among some dimension-6 Wilson coefficients. Later, in Ref. [126] an improved computation of the anomalies coming from the operators in Eq. (4.67) was presented, where they include the (would-be) Goldstone bosons in the expression of the gauge current. The inclusion of those extra contributions to the anomaly leads to the conclusion that a combination between c_i is not needed to cancel the anomaly. In addition the authors present two anomaly-free UV models that can be matched to the SMEFT in which the relations found in [125] can be violated.

These results on anomalies in the SMEFT can be understood with an heuristic argument. A given anomaly depends on the transformations of the fermions under the gauge group, meaning the charges and the group generators, and not on the other parameters in the Lagrangian. When we extend the SM to include higher dimensional operators, we are not changing the gauge symmetry, then it is expected that anomalies do not appear when moving into the non-renormalizable case.
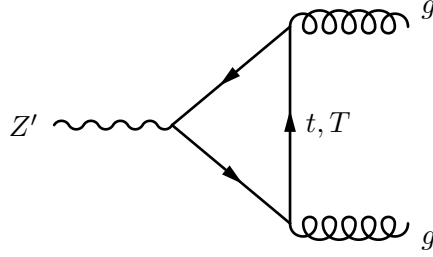
Figure 4.3: Top-philic scenario.

Anomalies in non-renormalizable theories are treated in a more general fashion in Ref. [127]. By analysing the process of quantization at the level of the regularized effective action, $W_r\left[A_\mu, \varphi, \varphi^\dagger\right]$, we can see that the anomalies can depend on the c_i but also they can be removed by fixing the renormalization scheme. Choosing a renormalization scheme means adding to W_r the space-integral of local polynomials (P_c) in the bosonic fields, gauge and scalars. The theory is anomaly-free if we can find such polynomial satisfying

$$L\left(x\right)\left(W_r + \int d^4 y P_c\left(y\right)\right) = 0, \tag{4.68}$$

where the operator $L\left(x\right)$ performs a gauge variation. In this case we can define $W = W_r + \int d^4 y P_c\left(y\right)$. Under this light, dependencies of the anomaly on the Wilson coefficients are not physical. This can be seen in the practice, when it is noticed that such dependence can be different if we change the regularization scheme or if we change the starting vertex in the computation of loop diagrams [128]. Under this light, the results in Ref. [126] are incomplete in the sense that a dependence of the anomaly on the parameters c_i can be reintroduced when we consider the full bosonic background of the theory.

In what follows we will briefly see the case of a specific scenario that will serve as an example of the implications of anomalies in the low-energy regime of EFTs. Then we show an example of how anomalies contribute to one-loop amplitudes through $\mathcal{R}_2$ contributions in the SMEFT.

4.3.1 The case of the top-philic scenarios

The discussion in this section follows the work in Ref. [128]. We start by considering the effective Lagrangian that includes the Z' boson as

$$
\begin{aligned}
\mathcal{L}_{\text{EFT}} =& \mathcal{L}_{\text{SM}} - \frac{1}{4} Z'_{\mu\nu} Z'^{\mu\nu} + \frac{1}{2} M_{Z'}^2 Z'_\mu Z'^\mu + Z'_\mu \bar{t} \gamma^\mu (c_{t_L} P_L + c_{t_R} P_R) t \\
&+ Z'_\mu \bar{\ell}_i \gamma^\mu (c_{\ell_L}^i P_L + c_{\ell_R}^i P_R) \ell_i,
\end{aligned}
\tag{4.69}
$$

where $\ell = e, \mu, \tau$. This model is of interest in the context of dark matter, in which the Z' could couple to light dark force mediators. The Z' boson is associated to an additional $U(1)'$ gauge group, and by adding an extra gauge group we might introduce anomalies associated to it. As it stands, the Lagrangian in Eq. (4.69), valid at electroweak scales and below, leads to gauge anomalies except for the particular case of equal left- and right-handed couplings, $c_L = c_R$. The anomaly associated to the $U(1)'$ symmetry is cancelled at very high energies in the UV model by unknown heavy particles often referred as 'spectator' fermions. In the UV theory the gauge symmetry is restored by choosing appropriately the $U(1)'$ charges of the spectator fermions. At low energies, the non-conservation of the $U(1)'$ current is not necessarily a pathology, because the EFT in Eq. (4.69) can still be quantized by introducing a cutoff.

The Z' boson can couple to two gluons via quantum corrections. At one-loop this happens via the triangle contributions with the top running in the loop, as represented by the diagram in Fig. 4.3, and the corresponding cross-diagram. Each of these diagrams are divergent but a finite result can be obtained by adding them up. However, a regularization scheme and loop momentum routing scheme are required in order to properly define the amplitude. For the case in which the Z' boson couples to anomalous currents, no regulator exists that could preserve simultaneously the conservation of the currents of the three bosons involved in the loop. Regarding the loop momentum routing scheme, there are two popular choices, which in the case of $Z'(k_1, \mu) \to g(k_2, \nu, A) g(k_3, \rho, B)$ can be phrased as:

- **Covariant Anomaly Scheme** (CVA) consists of starting the loop trace from the vertex of the massive gauge boson (Z) and manifestly respects the $SU(3)_c$ gauge invariance by satisfying

$$
k_3^\rho \mathcal{M}_{\mu\rho\nu}^{AB} = k_2^\nu \mathcal{M}_{\mu\rho\nu}^{AB} = 0.
\tag{4.70}
$$
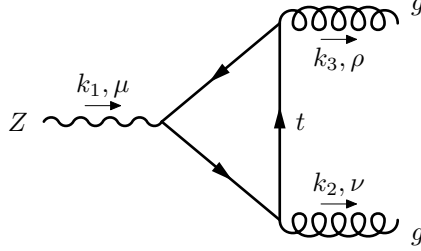
Figure 4.4: Feynman diagram of the $Z \to gg$ process.

- **Consistent Anomaly Scheme** (CNA) symmetrizes with respect to all three external momenta by computing the traces starting from each of the vertices in the loop and then averaging, such that

$$-k_1^\mu \mathcal{M}_{\mu\rho\nu}^{AB} = k_3^\mu \mathcal{M}_{\rho\mu\nu}^{AB} = k_2^\mu \mathcal{M}_{\rho\nu\mu}^{AB} \neq 0, \qquad (4.71)$$

  i.e. $SU(3)_c$ gauge invariance is lost. This is compensated by adding the Wess-Zumino term to the effective Lagrangian

$$\mathcal{L}_{\text{EFT}} \supset c_{\text{WZ}} g_X g_s^2 \epsilon^{\mu\nu\rho\sigma} Z'_\mu \Big(G_\nu^A \partial_\rho G_\sigma^A + \frac{1}{3} g_s \epsilon^{ABC} G_\nu^A G_\rho^B G_\sigma^C \Big), \qquad (4.72)$$

  where c_{WZ} is the coefficient of the Wess-Zumino term fixed by requiring that the total amplitude $\mathcal{M}_{\text{Tot}} = \mathcal{M} + \mathcal{M}_{WZ}$ satisfies the $SU(3)_c$ gauge invariance given by Eq. (4.70).

We notice that the Wess-Zumino term is not required in the CVA, and it is set c_{WZ}. In the top-down approach, the Wess-Zumino term is interpreted as arising from integrating out the spectator fermion (T). Finally, we emphasize that the two loop momentum routing schemes lead to the same anomaly of the $U(1)'$ current, which in the limit of massless fermion running in the loop takes the expression

$$-k_1^\mu \mathcal{M}_{\mu\nu\rho}^{AB} = (c_{T_L} - c_{T_R}) \frac{g_X g_s^2}{4\pi^2} \text{Tr}(T^A T^B) \epsilon_{\nu\rho\lambda\sigma} k_3^\lambda k_2^\sigma, \qquad (4.73)$$

where c_{T_L} and c_{T_R} are the chiral couplings associated to the spectator fermion.

4.3.2   A case of study: the ggZ amplitude

In what follows we are concerned with the computation of the amplitude for the process $Z(k_1, \mu) \to g(k_2, \nu) g(k_3, \rho)$ as shown in the Fig. 4.4. We show

the results for this amplitude in the CVA and CNA schemes. We compute the amplitude by starting the loop trace from the Z-vertex, which we will see that corresponds to the CVA to the end of this computation. With g_Z indicating the coupling of the Z boson to the fermion ψ with mass m, we have that the amplitude can be written as:

$$
\begin{aligned}
\mathcal{M}_1^{\text{CVA}} = &-\text{Tr}(T^A T^B)\,(ig_s)^2\,(ig_Z)\,i^3\epsilon_1^\mu\epsilon_2^\nu\epsilon_3^\rho \\
&\int \frac{d^d q}{(2\pi)^d}\frac{\text{tr}\left(\gamma_\mu P_L\left(\slashed{q}+\slashed{k}_2+m\right)\gamma_\nu\left(\slashed{q}+m\right)\gamma_\rho\left(\slashed{q}-\slashed{k}_3+m\right)\right)}{\left((q+k_2)^2-m^2\right)(q^2-m^2)\left((q-k_3)^2-m^2\right)} \\
= &-\frac{1}{2}g_Z g_s^2\text{Tr}(T^A T^B)\epsilon_1^\mu\epsilon_2^\nu\epsilon_3^\rho \\
&\int \frac{d^d q}{(2\pi)^d}\frac{N_{\mu\nu\rho}}{\left((q+k_2)^2-m^2\right)(q^2-m^2)\left((q-k_3)^2-m^2\right)} \\
= &-\frac{1}{2\,(2\pi)^4}g_Z g_s^2\text{Tr}(T^A T^B)\epsilon_1^\mu\epsilon_2^\nu\epsilon_3^\rho\,\mathcal{I}_{\mu\nu\rho}, \quad\quad (4.74)
\end{aligned}
$$

where the trace in the numerator is

$$
N_{\mu\nu\rho} = \text{tr}\left(\gamma_\mu\gamma^5\left(\slashed{q}+\slashed{k}_2+m\right)\gamma_\nu\left(\slashed{q}+m\right)\gamma_\rho\left(\slashed{q}-\slashed{k}_3+m\right)\right), \quad\quad (4.75)
$$

and the loop integral that we have to solve is

$$
\mathcal{I}_{\mu\nu\rho} = \int d^d q\frac{N_{\mu\nu\rho}}{\left((q+k_2)^2-m^2\right)(q^2-m^2)\left((q-k_3)^2-m^2\right)}. \quad\quad (4.76)
$$

We have also replaced $P_L \to (1-\gamma_5)/2$. In the results above, the vectorial part of the amplitude was dropped as it should be zero since it is forbidden by the Landau-Yang theorem. We work the Dirac algebra in $d=4$ and use the Passarino-Veltman reduction method in what follows, and at the end we take care of the rational term in an indirect way. The numerator can be simplified into

$$
\begin{aligned}
N_{\mu\nu\rho} = &\text{tr}\left(\gamma_\mu\gamma^5\left(\slashed{q}+\slashed{k}_2\right)\gamma_\nu\slashed{q}\gamma_\rho\left(\slashed{q}-\slashed{k}_3\right)\right) + m^2\left(\text{tr}\left(\gamma_\mu\gamma^5\left(\slashed{q}+\slashed{k}_2\right)\gamma_\nu\gamma_\rho\right)\right. \\
&\left. +\text{tr}\left(\gamma_\mu\gamma^5\gamma_\nu\slashed{q}\gamma_\rho\right) + \text{tr}\left(\gamma_\mu\gamma^5\gamma_\nu\gamma_\rho\left(\slashed{q}-\slashed{k}_3\right)\right)\right) \\
= &-\text{tr}\left(\gamma_\mu\left(\slashed{q}+\slashed{k}_2\right)\gamma_\nu\slashed{q}\gamma_\rho\left(\slashed{q}-\slashed{k}_3\right)\gamma^5\right) + 4im^2\epsilon_{\mu\nu\rho\sigma}\left(q+k_2-k_3\right)^\sigma.
\end{aligned}
$$
$$(4.77)$$

The trace in the last line can be computed to be

$$
\begin{aligned}
t_{\mu\nu\rho} &= \operatorname{tr}\left(\gamma_\mu\left(\slashed{q}+\slashed{k}_2\right)\gamma_\nu\slashed{q}\gamma_\rho\left(\slashed{q}-\slashed{k}_3\right)\gamma^5\right) \\
&= -4i\Big(g_{\nu\rho}\epsilon_{\mu\sigma\alpha\beta}k_2^\sigma k_3^\alpha q^\beta + \epsilon_{\mu\nu\rho\sigma}\left(\left(q^2+k_2\cdot k_3\right)q^\sigma + \left(q^2-q\cdot k_3\right)k_2^\sigma\right. \\
&\quad\left. -\left(q^2+q\cdot k_2\right)k_3^\sigma\right) + \epsilon_{\mu\nu\sigma\alpha}\left(2q_\rho q^\alpha k_2^\sigma - q^\alpha k_{2\rho}k_3^\sigma - q_\rho k_2^\sigma k_3^\alpha\right) \\
&\quad + \epsilon_{\mu\rho\sigma\alpha}\left(2q_\nu q^\alpha k_3^\sigma + q^\alpha k_{3\nu}k_2^\sigma - q_\nu k_2^\sigma k_3^\alpha\right)\Big).
\end{aligned}
\tag{4.78}
$$

the first term above vanishes as the result of the integral associated to it is either proportional to $k_2^\sigma k_2^\beta$ or $k_3^\alpha k_3^\beta$, which are terms that vanish when are contracted with the levi-Civita. Thus we have,

$$
\begin{aligned}
N_{\mu\nu\rho} &= -4i(\epsilon_{\mu\nu\rho\sigma}((q^2-m^2+k_2\cdot k_3)q^\sigma + (q^2-m^2-q\cdot k_3)k_2^\sigma \\
&\quad -(q^2-m^2+q\cdot k_2)k_3^\sigma) + \epsilon_{\mu\nu\sigma\alpha}(2q_\rho q^\alpha k_2^\sigma - q^\alpha k_{2\rho}k_3^\sigma - q_\rho k_2^\sigma k_3^\alpha) \\
&\quad + \epsilon_{\mu\rho\sigma\alpha}(2q_\nu q^\alpha k_3^\sigma + q^\alpha k_{3\nu}k_2^\sigma - q_\nu k_2^\sigma k_3^\alpha)).
\end{aligned}
\tag{4.79}
$$

We notice that in the numerator we keep the terms $s = q^2$ as the virtuality of the Z boson. In the results below we omit the dependence of the triangle integrals as it is the same all along the computation, hence we use the abbreviation $C_{ij} = C_{ij}\left(0,0,0;m^2,m^2,m^2\right)$ In this numerator we can see three different Lorentz structures, thus we divide the loop integral into $\mathcal{I}_{\mu\nu\rho} \equiv \mathcal{I}_{\mu\nu\rho}^{(1)} + \mathcal{I}_{\mu\nu\rho}^{(2)} + \mathcal{I}_{\mu\nu\rho}^{(3)}$. The first of these integrals can be computed as

$$
\begin{aligned}
\mathcal{I}_{\mu\nu\rho}^{(1)} &= -4i\epsilon_{\mu\nu\rho\sigma}\int d^d q \frac{1}{\left((q+k_2)^2-m^2\right)(q^2-m^2)\left((q-k_3)^2-m^2\right)} \\
&\quad \left(\left(q^2-m^2+k_2\cdot k_3\right)q^\sigma + \left(q^2-m^2-q\cdot k_3\right)k_2^\sigma\right. \\
&\quad\left. -\left(q^2-m^2+q\cdot k_2\right)k_3^\sigma\right) \\
&= 2\epsilon_{\mu\nu\rho\sigma}\left(k_2^\sigma\left(-B_0\left(s,m\right)-2B_1\left(s,m\right)+B_0\left(0,m\right)+2k_2\cdot k_3 C_1\right)\right. \\
&\quad\left. -k_3^\sigma\left(B_0\left(s,m\right)+2B_1\left(s,m\right)+B_0\left(0,m\right)+2k_2\cdot k_3 C_2\right)\right) \\
&= 2\epsilon_{\mu\nu\rho\sigma}\left(k_2^\sigma\left(-2B_1\left(s,m\right)\right)-k_3^\sigma\left(2B_0\left(s,m\right)+2B_1\left(s,m\right)\right)\right) \\
&= 2\epsilon_{\mu\nu\rho\sigma}\left(k_2-k_3\right)^\sigma B_0\left(s,m\right).
\end{aligned}
\tag{4.80}
$$

Next, the second integral is obtained as

$$
\begin{aligned}
\mathcal{I}_{\mu\nu\rho}^{(2)} &= -4i\epsilon_{\mu\nu\sigma\alpha} \int d^d q \frac{2q_\rho q^\alpha k_2^\sigma - q^\alpha k_{2\rho} k_3^\sigma - q_\rho k_2^\sigma k_3^\alpha}{\left((q+k_2)^2 - m^2\right)(q^2 - m^2)\left((q-k_3)^2 - m^2\right)} \\
&= 4\epsilon_{\mu\nu\sigma\alpha}\left(k_{2\rho}k_3^\sigma\left(k_3^\alpha C_2 - k_2^\alpha C_1\right) + k_2^\sigma\left(-k_3^\alpha k_{2\rho}\left(2C_{12} + C_1\right)\right.\right.\\
&\qquad\qquad \left.\left. +2k_2^\alpha k_{2\rho}C_{11} + 2g_\rho^\alpha C_{00}\right)\right) \\
&\to -4\epsilon_{\mu\nu\rho\sigma}\left(2\left(\epsilon_3 \cdot k_2\right)\epsilon_1^\mu\epsilon_2^\nu k_2^\rho k_3^\sigma \cdot \frac{m^2}{s}C_0 + \epsilon_1^\mu\epsilon_2^\nu\epsilon_3^\rho k_2^\sigma\left(\frac{1}{2}B_0\left(s,m\right) + m^2 C_0\right)\right),
\end{aligned}
\tag{4.81}
$$

where in the last line we have contracted the integral with the polarization vectors in order to further simplify the result. Finally, the third integral is found to be

$$
\begin{aligned}
\mathcal{I}_{\mu\nu\rho}^{(3)} &= -4i\epsilon_{\mu\rho\sigma\alpha} \int d^d q \frac{2q_\nu q^\alpha k_3^\sigma + q^\alpha k_{3\nu} k_2^\sigma - q_\nu k_2^\sigma k_3^\alpha}{\left((q+k_2)^2 - m^2\right)(q^2 - m^2)\left((q-k_3)^2 - m^2\right)} \\
&= 4\epsilon_{\mu\rho\sigma\alpha}\left(k_3^\sigma\left(-2k_2^\alpha k_{3\nu}C_{12} + 2g_\nu^\alpha C_{00}\right)\right) \\
&\to 4\epsilon_{\mu\nu\rho\sigma}\left(2\frac{m^2}{s}\left(\epsilon_2 \cdot k_3\right)\epsilon_1^\mu\epsilon_3^\nu k_2^\rho k_3^\sigma C_0 + \epsilon_1^\mu\epsilon_2^\nu\epsilon_3^\rho k_3^\sigma\left(\frac{1}{2}B_0\left(s,m\right) + m^2 C_0\right)\right),
\end{aligned}
\tag{4.82}
$$

where once again we have multiplied in the last line by the polarization vectors. Therefore, when adding up the results for the integrals in Eq. (4.80), (4.81) and (4.82), we see that the total integral contracted with the polarization vectors is

$$
\begin{aligned}
\mathcal{I}_{\epsilon_1\epsilon_2\epsilon_3} &= 4\epsilon_{\mu\nu\rho\sigma}\left(\frac{1}{2}\epsilon_1^\mu\epsilon_2^\nu\epsilon_3^\rho\left(k_2 - k_3\right)^\sigma B_0\left(s,m\right) - 2\left(\epsilon_3 \cdot k_2\right)\epsilon_1^\mu\epsilon_2^\nu k_2^\rho k_3^\sigma \cdot \frac{m^2}{s}C_0\right. \\
&\qquad\qquad \left. -\epsilon_1^\mu\epsilon_2^\nu\epsilon_3^\rho k_2^\sigma\left(\frac{1}{2}B_0\left(s,m\right) + m^2 C_0\right) + 2\left(\epsilon_2 \cdot k_3\right)\epsilon_1^\mu\epsilon_3^\nu k_2^\rho k_3^\sigma \cdot \frac{m^2}{s}C_0\right. \\
&\qquad\qquad \left. +\epsilon_1^\mu\epsilon_2^\nu\epsilon_3^\rho k_3^\sigma\left(\frac{1}{2}B_0\left(s,m\right) + m^2 C_0\right)\right) \\
&= -\frac{2}{s}\left(2m^2 C_0\right)\epsilon_{\mu\nu\rho\sigma}(s\epsilon_1^\mu\epsilon_2^\nu\epsilon_3^\rho\left(k_2^\sigma - k_3^\sigma\right) - 2\left(\epsilon_2 \cdot k_3\right)\epsilon_1^\mu\epsilon_3^\nu k_2^\rho k_3^\sigma \\
&\qquad\qquad + 2\left(\epsilon_3 \cdot k_2\right)\epsilon_1^\mu\epsilon_2^\nu k_2^\rho k_3^\sigma).
\end{aligned}
\tag{4.83}
$$

Finally, we substitute this result in the amplitude in Eq. (4.74) to get

$$
\mathcal{M}_1^{\text{CVA}} = \frac{1}{16\pi^2} g_Z g_s^2 \text{Tr}(T^A T^B) \cdot \frac{1}{s} \left(2m^2 C_0\right) \epsilon_{\mu\nu\rho\sigma} \cdot
$$
$$
\left(s\epsilon_1^\mu \epsilon_2^\nu \epsilon_3^\rho \left(k_2^\sigma - k_3^\sigma\right) - 2\left(\epsilon_2 \cdot k_3\right) \epsilon_1^\mu \epsilon_3^\nu k_2^\rho k_3^\sigma + 2\left(\epsilon_3 \cdot k_2\right) \epsilon_1^\mu \epsilon_2^\nu k_2^\rho k_3^\sigma\right)
$$
$$(4.84)$$

In addition, there is a cross diagram that leads to the same result, so that the result above gets multiplied by a factor of two. To obtain the rational part such contributions can be computed as the negative of the large fermion mass limit of the non-rational amplitude. This method to compute the rational term works because the amplitude turns out to be finite. Moreover, we also remember that the asymptotic behavior for large m^2 of some of the triangle integrals is

$$
C_{12}\left(0,0,0; m^2, m^2, m^2\right) \sim -\frac{1}{24m^2}, \qquad C_1\left(0,0,0; m^2, m^2, m^2\right) \sim \frac{1}{6m^2}
$$
$$
C_0\left(0,0,0; m^2, m^2, m^2\right) \sim -\frac{1}{2m^2}. \qquad (4.85)
$$

With this we get the final result:

$$
\mathcal{M}^{\text{CVA}} = \frac{g_Z g_s^2}{16\pi^2} \delta^{AB} \frac{1}{s} \left(2m^2 C_0 + 1\right) \epsilon_{\mu\nu\rho\sigma} \cdot
$$
$$
\left(s\epsilon_1^\mu \epsilon_2^\nu \epsilon_3^\rho \left(k_2^\sigma - k_3^\sigma\right) - 2\left(\epsilon_2 \cdot k_3\right) \epsilon_1^\mu \epsilon_3^\nu k_2^\rho k_3^\sigma + 2\left(\epsilon_3 \cdot k_2\right) \epsilon_1^\mu \epsilon_2^\nu k_2^\rho k_3^\sigma\right).
$$
$$(4.86)$$

It is important to notice that the coupling of the Z boson with two gluons is allowed off-shell, in which case it is imperative to incorporate the width of the Z boson. From Eq. (4.86) it is possible to check by replacing $\epsilon_2 \to k_2$ and $\epsilon_3 \to k_3$ that the $SU(3)_c$ gauge symmetry is preserved. The analogous amplitude in the consistent scheme takes the form

$$
\mathcal{M}^{\text{CNA}} = \frac{g_Z g_s^2}{16\pi^2} \delta^{AB} \frac{1}{s} \epsilon_{\mu\nu\rho\sigma} \Big((2m^2 C_0 + \frac{1}{3}) \epsilon_1^\mu \epsilon_2^\nu \epsilon_3^\rho (k_2^\sigma - k_3^\sigma)
$$
$$
- 2(2m^2 C_0 + 1)(\epsilon_2 \cdot k_3)\epsilon_1^\mu \epsilon_3^\nu k_2^\rho k_3^\sigma + 2(2m^2 C_0 + 1)(\epsilon_3 \cdot k_2)\epsilon_1^\mu \epsilon_2^\nu k_2^\rho k_3^\sigma \Big).
$$
$$(4.87)$$

In this scheme it is required to add the Wess-Zumino term to recover the gauge invariance over the currents associated to the gluon. The Wess-Zumino term contributes to the amplitude as

$$
\mathcal{M}_{\text{WZ}}^{\text{CNA}} = c_{\text{WZ}} g_Z g_s^2 \delta^{AB} \epsilon_{\mu\nu\rho\sigma} \epsilon_1^\mu \epsilon_2^\nu \epsilon_3^\rho (k_2^\sigma - k_3^\sigma), \qquad (4.88)
$$

where by requiring gauge invariance we identify

$$c_{\text{WZ}} = \frac{1}{24\pi^2}. \tag{4.89}$$

We also observe from Eq. (4.86) that in the covariant scheme the rational term is

$$\mathcal{M}_{R_2}^{\text{CVA}} = \frac{g_Z g_s^2}{24\pi^2} \delta^{AB} \epsilon_{\mu\nu\rho\sigma} \epsilon_1^\mu \epsilon_2^\nu \epsilon_3^\rho (k_2^\sigma - k_3^\sigma). \tag{4.90}$$

On the other hand, in the consistent scheme, the R_2 term is different from the result in Eq. (4.90), for which the rational terms vanish. This analysis can easily be extended to SMEFT operators that modify chiral interactions in the SM. For example, let us consider the modifications to the electroweak couplings of the top quark. In particular, for the $t\bar{t}Z$ coupling we get the effective modifications proportional to

$$-i\frac{v^2}{\Lambda^2}((c_{\varphi Q}^1 - c_{\varphi Q}^3)\gamma^\mu P_L + c_{\varphi t}\gamma^\mu P_R), \tag{4.91}$$

from which we make the identification

$$g_Z \to -\frac{e}{2s_W c_W}\frac{v^2}{\Lambda^2}(c_{\varphi Q}^1 - c_{\varphi t}). \tag{4.92}$$

This g_Z can be substituted in all of the results obtained in this subsection.

We conclude by emphasizing that the computation of one-loop diagrams involving chiral couplings might lead to the emergence of anomalous terms, that, although they do not bare any physical content as they do not appear in the UV completion, they can affect our results. In this cases, it is necessary to define a loop momentum routing scheme. In the predictions obtained from the implementation of the SMEFT@NLO in MadGraph5_aMC@NLO the covariant anomaly scheme is implemented in order to preserve the $SU(3)_c$ gauge invariance [110]. Thus, gauge invariance provides a check of the results in the following chapter.

Chapter 5

Phenomenology of top-pair production at NLO

When considering the different sectors of the SMEFT, the top sector is presented as a good prospect in the search for BSM physics. The largest coupling of the Higgs boson is the Yukawa interaction with the top quark, hence it is expected that the properties of the SSB can be further studied through the top, one of the least constrained quarks. As it has already been mentioned, the leading top quark production mechanisms at hadron colliders are the $t\bar{t}$ pair and single top production processes. The $t\bar{t}$ production has been extensively studied in the SMEFT framework, this due mainly to the fact that it is one of the most precisely known process to date. Bounds to different type of operators have been found from top-pair production [129–132], and in general from the top sector of the SMEFT at LO ref. [133–136]. Although such studies are quite robust, a better understanding of the contribution of four-fermion operators at NLO in this process is missing.

In addition, the treatment of effective operators in one-loop processes requires a high level of consistency. First, the running Wilson coefficients associated with the renormalization scheme should be included to achieve full NLO accuracy. Second, these operators might introduce spurious gauge-anomalous contributions, which have to be treated in a consistent scheme. Third, evanescent operators might change our results depending on the basis used to write down the four-fermion operators in the Lagrangian.

Once these subtleties are solved, studies on the phenomenology of the effective operators can be done. The four-fermion operators entering the $t\bar{t}$ production can be organized in three groups:

- color singlet operators presenting quarks from the 3rd generation and light quarks.

- color octet operators presenting quarks from the 3rd generation and light quarks.

- color singlet and octet operators with purely 3rd generation quarks.

These three groups of operators can also be constrained at tree-level in the four-top production process. Bounds for these operators are shown in [137]. Since the four-top production has been recently measured by ATLAS and CMS [107–109], its relevance in global fits has grown. The invariant-mass distribution for the final product presents a peak around 1.3 TeV and falls gradually ranging along some few TeV's (see Fig. 5.7b).

In this chapter we present a comparison between the sensitivity of top-pair and four-top production to four-fermion operators involving purely the 3rd generation of quarks. Recently, it has been suggested that the contribution of these operators to electroweak precision observables (EWPO) through loop corrections lead to sensitive effects [138], arising the question of whether a thorough study in the top-pair production could provide more information about the NLO effects from such effective operators. Additionally, this analysis is motivated by the fact that both theoretical and experimental uncertainties are better controlled in top-pair production. As a matter of fact, the top-pair cross-section is known at NNLO while four-top predictions are known at NLO. Furthermore, the relative uncertainties both at LO and at NLO are larger for four-top than top-pair production, suggesting that even if NNLO four-top predictions would become available they would not be as accurate as the predictions for top-pair production. At the experimental level, the much larger cross-section of top-pair production gives access to better statistics and to more differential distributions. We show that with the current level of precision the top-pair production is more sensitive to the linear terms in the effective expansion, while the four-top process is more sensitive to the quadratic. Thus, questions arise regarding the validity of the dimension-6 truncation in the four-top process. In this vein, the bounds obtained from the $t\bar{t}$ production are under better theoretical control, at least until a full description regarding dimension-8 contributions to four-top is obtained. In addition, we revisit the subtleties that arise in the study of the process $pp \to t\bar{t}$ at one-loop in the SMEFT.

Finally, four-heavy-quark operators mainly contribute at one-loop in the top-pair process, i.e. through the interference between the tree-level SM and their one-loop amplitude. The other contributions are through bottom induced subprocesses which are heavily suppressed by PDFs. It is therefore the perfect place to have a full validation, i.e. a comparison between a full analytical

computation and the numerical results from MadGraph5_aMC@NLO, of the one-loop treatment of four-fermions operators as only the four-fermion loops need to be computed and real emissions are highly suppressed.

5.1 Effective operators

In general, the SMEFT Lagrangian can be written as

$$\mathcal{L}_{\text{SMEFT}} = \mathcal{L}_{\text{SM}} + \sum_i \frac{c_i^{(d)}(\mu)}{\Lambda^{d-4}} \mathcal{O}_i^{(d)} + \dots \tag{5.1}$$

where the coefficients c_i are the Wilson coefficients of the dimension-d operators and Λ the energy scale at which we expect to find direct new physic effects. The gauge invariant $\mathcal{O}_i$ are the effective operators built of SM fields. The dots indicate higher-dimensional operators. The predictions obtained from this model at NLO are renormalized in a fixed scale renormalization scheme which introduces a new scale μ_{EFT} in the counterterms of the Wilson coefficients but ensures that they are not running such that full NLO accuraccy can be reached without an implementation of the running in MadGraph5_aMC@NLO. This scheme is similar to the on-shell renormalization of the top quark and has therefore similar properties. Namely, large logarithm only appear when the scales probed in the processes are far from μ_{EFT} which is not the cases for the processes we are considering here. In practice, the scheme is achieved by putting not only the pole but also a log in the UV-counterterms. To go from the $\overline{\text{MS}}$ to our fixed scale scheme, the pole of the EFT operators related to the renormalization of their coefficients are replaced by

$$\frac{1}{\bar{\epsilon}} \rightarrow \frac{1}{\bar{\epsilon}} - \log\frac{\mu_{\text{EFT}}^2}{\mu_r^2} \tag{5.2}$$

in the UV counter-terms. As a result, the $\overline{\text{MS}}$ predictions are recovered when $\mu_{\text{EFT}} = \mu_r$ but the errors are not necessarily the same as they are obtained by varying the renormalization scale μ_r and not μ_{EFT} as this would correspond to changing the renormalization scheme. Hence, along this chapter we set $\mu_{\text{EFT}} = m_t$. The Lagrangian above can be interpreted as an expansion around the SM theory, with the c_i constituting a basis that parametrizes possible devi-

ations from the SM in the observable O_n as

$$\Delta O_n = O_n^{\text{EXP}} - O_n^{\text{SM}}$$
$$= \sum_i \frac{a_{n,i}^{(6)}(\mu)c_i^{(6)}(\mu)}{\Lambda^2} + \sum_{ij} \frac{b_{n,ij}^{(6)}(\mu)c_i^{(6)}(\mu)c_j^{(6)}(\mu)}{\Lambda^4}$$
$$+ \sum_i \frac{a_{n,i}^{(8)}(\mu)c_i^{(8)}(\mu)}{\Lambda^4} + \dots, \tag{5.3}$$

with the coefficients a_i and b_{ij} determining the size of the effects of the operators $\mathcal{O}_i$ are obtained by the computations of each observable[1]. In this approach, if we want trustful predictions for the new physics effects, the experiments and the theoretical computations from the SM should be performed at a high accuracy. In addition, the parametrization of such deviations must be also accurate and consistent. This is the advantage of using the SMEFT: it is a self-consistent quantum field theory that is gauge invariant and renormalizable order by order in $1/\Lambda$. Hence, to enhance our sensitivity to new physics we can improve the predictions from the SMEFT by going at NLO.

In this work, only dimension-six operators are considered ($d \leq 6$). The Warsaw basis is implemented, following the notation in ref. [40]. When regarding the top production in the LHC via strong interactions, there are several classes of operators that should be considered. Bounds found in the literature on several of the interactions that we discussed in this section are collected in Table 5.1. In a first class of effective operators we have the coupling of a top-quark current with bosons (2FB). In a second class are the purely bosonic operators (B). These two classes of effective interactions that involve gluons, the top and the Higgs are relevant in gluon initiated processes:

$$\mathcal{O}_{t\varphi} = (\varphi^\dagger \varphi)(\bar{Q} t_R \widetilde{\varphi}),$$
$$\mathcal{O}_{tG} = (\bar{Q} \sigma_{\mu\nu} T^A t)\tilde{\varphi} G_\mu^{A\mu\nu},$$
$$\mathcal{O}_{\varphi G} = \varphi^\dagger \varphi G_{\mu\nu}^A G^{A\mu\nu},$$
$$\mathcal{O}_G = f^{ABC} G_\mu^{A\nu} G_\nu^{B\rho} G_\rho^{C\mu},$$
$$\mathcal{O}_{\tilde{G}} = f^{ABC} \tilde{G}_\mu^{A\nu} G_\nu^{B\rho} G_\rho^{C\mu},$$
$$\mathcal{O}_{\varphi\tilde{G}} = \varphi^\dagger \varphi \tilde{G}_{\mu\nu}^A G^{A\mu\nu} \tag{5.4}$$

---

[1]The coefficients a_i and b_{ij} contributing to our results are obtained with Mad-Graph5_aMC@NLO.

The first three operators in Eq. (5.4) receive constraints from the Higgs sector and have been studied at LO in [139] and at NLO in the gluon-fusion Higgs production [140]. The chromomagnetic operator $\mathcal{O}_{tG}$, with effects at tree-level in the $t\bar{t}$ production, flips the chirality of the top lines, which introduces an overall factor of m_t^2 in the cross-section. As a consequence, this operator is suppressed in the $t\bar{t}$ production for which the interference goes as m_t^2/Λ^2 at high-energies, instead of growing with energy. Corrections of order QCD-NLO on this operator lead to increments to the $t\bar{t}$ up to 50% compared to the LO at the LHC [132]. The operator $\mathcal{O}_{t\varphi}$ enters through loop corrections in the sub-process $gg \to t\bar{t}$. The operator $\mathcal{O}_G$ has been extensively studied in global fits using $t\bar{t}$ and $t\bar{t}V$ data and dedicated multijet studies [141]. Finally, the interactions in Eq. (5.4) involving the dual field strength $\tilde{G}_{\mu\nu}$ do not contribute at the order $\mathcal{O}(1/\Lambda^2)$ when studying unpolarized cross-sections [134], given their CP-violating nature. We decide therefore to ignore them. Hence, even though all those operators are relevant in the $t\bar{t}$ process, their implications are well known and we do not consider them in the analysis below (see Table 5.1).

As a third class of operators, there are the four-fermion interactions involving two light and two heavy quarks (2L2H):

$$
\begin{aligned}
\mathcal{O}_{Qq}^{(8,3)} &= (\bar{Q}_L\gamma_\mu T^A\tau^i Q_L)(\bar{q}_L\gamma^\mu T^A\tau^i q_L), & \mathcal{O}_{Qq}^{(1,3)} &= (\bar{Q}_L\gamma_\mu \tau^i Q_L)(\bar{q}_L\gamma^\mu \tau^i q_L), \\
\mathcal{O}_{Qq}^{(8,1)} &= (\bar{Q}_L\gamma_\mu T^A Q_L)(\bar{q}_L\gamma^\mu T^A q_L), & \mathcal{O}_{Qq}^{(1,1)} &= (\bar{Q}_L\gamma_\mu Q_L)(\bar{q}_L\gamma^\mu q_L), \\
\mathcal{O}_{td}^{(8)} &= (\bar{t}_R\gamma_\mu T^A t_R)(\bar{d}_R\gamma^\mu T^A d_R), & \mathcal{O}_{td}^{(1)} &= (\bar{t}_R\gamma_\mu t_R)(\bar{d}_R\gamma^\mu d_R), \\
\mathcal{O}_{tu}^{(8)} &= (\bar{t}_R\gamma_\mu T^A t_R)(\bar{u}_R\gamma^\mu T^A u_R), & \mathcal{O}_{tu}^{(1)} &= (\bar{t}_R\gamma_\mu t_R)(\bar{u}_R\gamma^\mu u_R), \\
\mathcal{O}_{tq}^{(8)} &= (\bar{t}_R\gamma_\mu T^A t_R)(\bar{q}_L\gamma^\mu T^A q_L), & \mathcal{O}_{tq}^{(1)} &= (\bar{t}_R\gamma_\mu t_R)(\bar{q}_L\gamma^\mu q_L), \\
\mathcal{O}_{Qd}^{(8)} &= (\bar{Q}_L\gamma_\mu T^A Q_L)(\bar{d}_R\gamma^\mu T^A d_R), & \mathcal{O}_{Qd}^{(1)} &= (\bar{Q}_L\gamma_\mu Q_L)(\bar{d}_R\gamma^\mu d_R), \\
\mathcal{O}_{Qu}^{(8)} &= (\bar{Q}_L\gamma_\mu T^A Q_L)(\bar{u}_R\gamma^\mu T^A u_R), & \mathcal{O}_{Qu}^{(1)} &= (\bar{Q}_L\gamma_\mu Q_L)(\bar{u}_R\gamma^\mu u_R),
\end{aligned}
\tag{5.5}
$$

Operators to the left of Eq. (5.5) are composed by color-octet heavy quark currents, while the ones on the right are composed by color-singlet currents. Hence, the upper indices in parenthesis in the names given to the operators in Eq. (5.5) indicate the type of currents composing the effective operator, explicitly $\blacklozenge^{(8)}$ stands for color-octet, $\blacklozenge^{(3)}$ stands for $SU(2)_L$ triplet and $\blacklozenge^{(1)}$ stands for color-singlet operators. Because of the color structure, when we consider the $t\bar{t}$ process at tree-level, color-octet operators generate diagrams that interfere with the QCD-SM, while the color-singlet ones only interfere

with the EW-SM. Therefore, the contributions of the order $\mathcal{O}\left(\Lambda^{-2}\right)$ for the color singlets are obtained only from the interference with the EW-SM and consequently are smaller. This class of operators can also be constrained via the single top, top-pair in association with jets and four-top processes [142].

As a fourth class of operators, we have the four-heavy-quark operators (4H) defined as follows

$$\mathcal{O}_{Qt}^{(1)} = \left(\bar{Q}_L\gamma_\mu Q_L\right)\left(\bar{t}_R\gamma^\mu t_R\right), \qquad \mathcal{O}_{Qt}^{(8)} = \left(\bar{Q}_L\gamma_\mu T^A Q_L\right)\left(\bar{t}_R\gamma^\mu T^A t_R\right),$$
$$\mathcal{O}_{QQ}^{(1)} = \frac{1}{2}\left(\bar{Q}_L\gamma_\mu Q_L\right)\left(\bar{Q}_L\gamma^\mu Q_L\right), \quad \mathcal{O}_{QQ}^{(8)} = \frac{1}{2}\left(\bar{Q}_L\gamma_\mu T^A Q_L\right)\left(\bar{Q}_L\gamma^\mu T^A Q_L\right),$$
$$\mathcal{O}_{tt}^{(1)} = \left(\bar{t}_R\gamma_\mu t_R\right)\left(\bar{t}_R\gamma^\mu t_R\right). \tag{5.6}$$

The color-octet operator involving only right-handed top quarks absent above as it is equivalent to $\mathcal{O}_{tt}^{(1)}$ after using Fierz identities (see Eq. (2.46)). The five operators in Eq. (5.6) constitute a maximal set of possible operators that can be written consisting of the third generation of quarks . The Wilson coefficients corresponding to these four-heavy-quark operators must be non-zero if the NP couples to the top quark, hence their importance. Four-heavy-quark operators appear in several BSM scenarios, among these we find two-Higgs-doublet models [143] and composite models of the top quark [144, 145]. In composite models the four-top effective operators have coefficients larger than those corresponding to other operators. Top-philic scenarios where vector or scalar resonances mainly couple to the top quarks, but interact weakly with the rest of the SM fermions, are easily relatable to the these effective operators [146–148]. Other four-heavy-quark operators are

$$\mathcal{O}_{QtQb}^{(1)} = \epsilon_{jk}(\bar{Q}^j t)(\bar{Q}^k b), \qquad \mathcal{O}_{QtQb}^{(8)} = \epsilon_{jk}(\bar{Q}^j T^A t)(\bar{Q}^k T^A b), \tag{5.7}$$

which can contribute to the top production, but their interferences with SM amplitudes are suppressed by factors of the bottom mass arising from the flip in chirality of the bottom quark. Hence, we do not consider them in our analysis.

A global fit of the top sector in the SMEFT should include all of the operators aforementioned (see [151] for early attempts to achieve this). In this chapter, we are interested in the sensitivity to the four-heavy-quark operators in Eq. (5.6), as this has not been put under strain before in the literature. As a result of the check procedure, the running of these operators have been computed and compared to the results in [152,153]. Additionally, the contributions

Class	c_i	Ref.	Individual		Marginalized	
			$\mathcal{O}(\Lambda^{-2})$	$\mathcal{O}(\Lambda^{-4})$	$\mathcal{O}(\Lambda^{-2})$	$\mathcal{O}(\Lambda^{-4})$
4H	c_{QQ}^1	[142]	$[-6.13, 23.3]$	$[-2.23, 2.02]$	$[-190, 189]$	$[-2.99, 3.71]$
		[138]	$[-1.61, 2.68]$	-	-	-
		[149]	-	$[-2.2, 3]$	-	-
	c_{QQ}^8	[142]	$[-26.5, 57.8]$	$[-6.81, 5.83]$	$[-190, 170]$	$[-11.2, 8.17]$
		[138]	$[-15.23, 25.41]$	-	-	-
		[149]	-	$[-6.75, 9]$	-	-
	c_{Qt}^1	[142]	$[-195, 159]$	$[-1.83, 1.86]$	$[-190, 189]$	$[-1.39, 1.25]$
		[138]	$[-2.24, 1.35]$	-	-	-
		[149]	-	$[-2.6, 2]$	-	-
	c_{Qt}^8	[142]	$[-5.72, 20.1]$	$[-4.21, 3.35]$	$[-190, 162]$	$[-3.04, 2.20]$
		[149]	-	$[-4.2, 5.3]$	-	-
	c_{tt}^1	[142]	$[-2.78, 12.1]$	$[-1.15, 1.02]$	$[-115, 153]$	$[-0.79, 0.71]$
		[149]	-	$[-1.2, 1.4]$	-	-
2L2H	$c_{Qq}^{8,1}$	[142]	$[-0.273, 0.509]$	$[-0.373, 0.309]$	$[-2.26, 4.82]$	$[-0.555, 0.236]$
	$c_{Qq}^{1,1}$	[142]	$[-3.60, 0.307]$	$[-0.303, 0.225]$	$[-8.05, 9.40]$	$[-0.354, 0.249]$
	$c_{Qq}^{8,3}$	[142]	$[-1.81, 0.625]$	$[-0.470, 0.439]$	$[-3.01, 7.36]$	$[-0.462, 0.497]$
	$c_{Qq}^{1,3}$	[142]	$[-0.099, 0.155]$	$[-0.088, 0.166]$	$[-0.163, 0.296]$	$[-0.167, 0.197]$
	c_{tq}^8	[142]	$[-0.396, 0.612]$	$[-0.483, 0.393]$	$[-4.03, 4.39]$	$[-0.687, 0.186]$
	c_{tq}^1	[142]	$[-0.784, 2.77]$	$[-0.205, 0.271]$	$[-12.4, 6.63]$	$[-0.222, 0.226]$
	c_{tu}^8	[142]	$[-0.774, 0.607]$	$[-0.911, 0.347]$	$[-16.9, 0.368]$	$[-1.12, 0.260]$
	c_{tu}^1	[142]	$[-6.05, 0.424]$	$[-0.380, 0.293]$	$[-15.6, 15.4]$	$[-0.383, 0.331]$
	c_{Qu}^8	[142]	$[-1.50, 1.02]$	$[-1.007, 0.521]$	$[-12.7, 13.8]$	$[-1.00, 0.312]$
	c_{Qu}^1	[142]	$[-0.938, 2.46]$	$[-0.281, 0.371]$	$[-17.0, 1.07]$	$[-0.207, 0.339]$
	c_{td}^8	[142]	$[-1.46, 1.36]$	$[-1.31, 0.638]$	$[-5.49, 25.4]$	$[-1.33, 0.643]$
	c_{td}^1	[142]	$[-9.50, -0.086]$	$[-0.449, 0.371]$	$[-27.7, 11.4]$	$[-0.474, 0.347]$
	c_{Qd}^8	[142]	$[-2.39, 2.04]$	$[-1.61, 0.888]$	$[-24.5, 11.2]$	$[-1.26, 0.715]$
	c_{Qd}^1	[142]	$[-0.889, 6.46]$	$[-0.332, 0.436]$	$[-3.24, 34.6t]$	$[-0.370, 0.384]$
2FB	$c_{t\varphi}$	[142]	$[-1.33, 0.355]$	$[-1.29, 0.348]$	$[-5.74, 3.43]$	$[-2.32, 2.80]$
	c_{tG}	[142]	$[0.007, 0.111]$	$[0.006, 0.107]$	$[-0.127, 0.403]$	$[0.062, 0.243]$
		[132]	$[-0.42, 0.30]$	-	-	-
		[134]	-	$[-0.300, 0.650]$	-	$[-1.32, 1.22]$
	c_{tW}	[142]	$[-0.093, 0.026]$	$[-0.084, 0.029]$	$[-0.313, 0.123]$	$[-0.241, 0.086]$
		[134]	-	$[1.32, 1.82]$	-	$[-4.03, 3.43]$
	c_{tZ}	[142]	$[-0.039, 0.099]$	$[-0.044, 0.094]$	$[-15.9, 5.64]$	$[-1.13, 0.856]$
	$c_{\varphi Q}^-$	[142]	$[-0.998, 1.44]$	$[-1.15, 1.58]$	$[-1.69, 11.6]$	$[-2.25, 2.85]$
	$c_{\varphi t}$	[142]	$[-2.09, 2.46]$	$[-3.03, 2.19]$	$[-3.27, 18.3]$	$[-13.3, 3.95]$
B	c_G	[129, 150]	-	$[-0.04, 0.04]$	-	-
		[134]	-	$[-0.300, 0.450]$	-	$[-1.62, 1.42]$
	$c_{\varphi G}$	[142]	$[-0.002, 0.005]$	$[-0.002, 0.005]$	$[-0.043, 0.012]$	$[-0.019, 0.003]$

Table 5.1: Compendium from the literature of 95% confidence level bounds (assuming $\Lambda = 1$ TeV) for CP-even Wilson coefficients relevant for the top-sector. Individual bounds correspond to results obtained from allowing only one coefficient to vary and marginalized indicates results from allowing several coefficients to be non-zero.

to top-quark pair production, at linear and quadratic levels, LO and NLO, are recomputed in the latest version of MadGraph5_aMC@NLO.

For completeness, we would like to mention that anomalous electroweak couplings have been studied at NLO in the $t\bar{t}$ production, imposing constraints on effective operators that modify SM-like vertices [130]. The operators to consider in this case are are classified in the second class and in the Warsaw basis they are given by

$$
\begin{aligned}
\mathcal{O}_{\varphi t} &= (\varphi^\dagger i \overset{\leftrightarrow}{D}_\mu \varphi)(\bar{t}\gamma^\mu t), \\
\mathcal{O}_{\varphi Q}^{(1)} &= (\varphi^\dagger i \overset{\leftrightarrow}{D}_\mu \varphi)(\bar{Q}\gamma^\mu Q), \\
\mathcal{O}_{\varphi Q}^{(3)} &= (\varphi^\dagger i \overset{\leftrightarrow}{D}_\mu \tau^I \varphi)(\bar{Q}\gamma^\mu \tau^I Q),
\end{aligned}
\tag{5.8}
$$

The Wilson coefficients corresponding to the last two operators normally receive bounds in the combination $c_{\varphi Q}^- = c_{\varphi Q}^1 - c_{\varphi Q}^3$. Bounds on the operators in Eq. (5.8) from measurements of the top and W boson masses have been recently reported [154]. Other operators modifying the electroweak interactions of the top are

$$
\mathcal{O}_{tW} = i(\bar{Q}\sigma^{\mu\nu}\tau^I t)\tilde{\varphi}W_{\mu\nu}^I, \qquad \mathcal{O}_{tB} = i(\bar{Q}\sigma^{\mu\nu}t)\tilde{\varphi}B_{\mu\nu},
\tag{5.9}
$$

where the latter is often constrained through the combination $c_{tZ} = -\sin\theta_W\, c_{tB} + \cos\theta_W\, c_{tW}$. The neutral couplings of the top at NLO have been constrained in [131]. More recently, it has been shown that neural networks can improve the sensitivity to NP from operators that modify the electroweak couplings of the top [155].

5.2   Top-pair production in the SMEFT

In this section, we review the current status of the pure top-quark production in the SMEFT relevant for our analysis. In addition, we present the analytic results of the differential cross-sections of the $t\bar{t}$ process at the partonic level for the interference between SM and SMEFT contributions from four top operators in Eq. (5.6). These analytic results serve as probes of the implementation of the four-fermion operators in the Monte-Carlo-generated predictions used in our analysis of section 5.4. The simulations of the pp-collisions are obtained from MadGraph5_aMC@NLO[2] [156] using the SMEFT@NLO model [110].

---

[2]In particular, the MadGraph5_aMC@NLO version 3.4.1 is known to correctly handle the rational terms. Previous versions suffer from a bug in the indexing of the lists of rational terms.

Unless specified, renormalization and factorization scales are set to the half of
the sum of the masses in the final state. Scale uncertainties are obtained by
variation of renormalization scales by a factor of 2 above and below the cen-
tral value. The NLO sets of NNPDF3.0 for the parton distribution function
are used, which for $\alpha_s(M_Z) = 0.118$ are tagged as NNPDF30_nlo_as_0118.
We consider 5 massless flavors in the proton, including the bottom quark. In
addition, we consider $m_t = 172.5$ GeV, $m_h = 125$ GeV, $m_Z = 91.1876$ GeV,
$m_W = 80.41$ GeV and $G_F = 1.16637 \cdot 10^{-5}$ GeV^{-2}.

The QCD corrections for some of the SMEFT operators have been con-
sidered in previous works. In particular, the effects of four-fermion operators
at NLO have been studied in the Tevatron setup [152]. In this case, the two-
light-two-heavy operators defined in Eq. (5.5) are of relevance since they en-
ter at tree-level in the quark-initiated sub-processes, which are the main con-
tributors to the total $t\bar{t}$-production. The running of those operators has been
computed providing two inequivalent results in ref. [152] and [153]. Those re-
sults can be compared to the information provided by SMEFT@NLO [110],
which is an automation of one-loop computations in the SMEFT covering
bosonic, two- and four-fermion operators. The running of the Wilson coef-
ficients, although not implemented, is encoded in the counter-terms contained
in SMEFT@NLO. The latter differs from the running reported in [152] by an
overall factor of 4. The analytical expressions of the one-loop contributions of
the four-heavy-quark operators in Eq. (5.6) to the top-pair process in a similar
basis can be found in the literature for the gluon initiated process [157]. Our
calculations are in agreement with the results in Ref. [157] and with [152] with
the exception of the running.

In our computations the γ_5 matrix is treated in the naive-dimensional reg-
ularization scheme (NDR), *i.e.* anti-commutes with the Dirac matrices in
d-dimensions. This implies that the cyclic property of the Dirac matrices
is abandoned. The results in the next sub-sections have been validated us-
ing FEYNARTS [158] - FORMCALC[3] [159] supplemented with LOOPTOOLS
[160]. The renormalization of the operator coefficients is performed in the
$\overline{\text{MS}}$ scheme, in which the counter-terms are provided by other four-fermion
operators and SM parameters. From the poles, we can obtain the running of
the coefficients. In this section we show how our results depend on the renor-
malization of our computations. Now, let us proceed to study the different
channels that contribute to the cross-section of the process $pp \to t\bar{t}$.

---

[3]We use the FormCalc v8.4, version known to treat correctly four-fermion interactions.
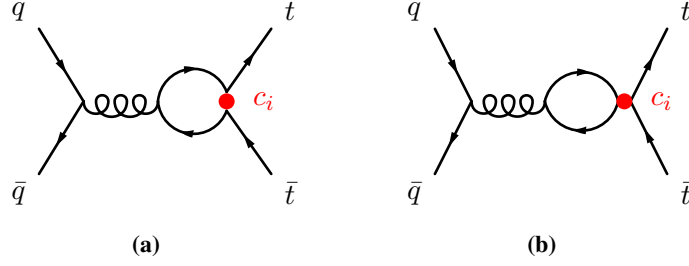
Figure 5.1: EFT one-loop diagrams for the partonic process $qq \to t\bar{t}$.

5.2.1   Quark channel

In what follows, we omit any color factors at first for simplicity. In general, there are two types of loop structures arising from 4-fermion operators. We can have

- Structure 1: Diagrams in which fermion flow goes from one of the external spinors to another, *i.e.* the two fermion currents from the effective operator are involved in the loop. This corresponds to the diagram in Fig. 5.1a.

- Structure 2: Diagrams in which the spinor indices contract in such a way that a trace over the Lorentz structures emerges in the numerator, *i.e.* only one of the fermion currents from the effective operator is involved in the loop. This corresponds to the diagram in Fig. 5.1b.

When we consider the operators listed in Eq. (5.6), there are amplitudes with chirality structure $\bar{L}L\bar{L}L$, $\bar{L}L\bar{R}R$ and $\bar{R}R\bar{R}R$ for each of the structures above. The last chirality structure can be obtained from the first one by parity transformations. Thus, in total there are four possible structures to be computed, which we proceed to discuss.

The amplitude for the structure 1 with $\bar{L}L\bar{L}L$ can be written as

$$\mathcal{M}_{\text{NP}}^{(1)} = \mathcal{C}_i \frac{g^2}{\hat{s}} \frac{c_i}{\Lambda^2} \bar{u}\left(p_4\right) \Gamma_\mu^{\text{LL}} v\left(p_3\right) \cdot \bar{v}\left(p_2\right) \gamma^\mu u\left(p_1\right), \qquad (5.10)$$

with $\mathcal{C}_i$ standing for the color structure of the amplitude with an insertion of the effective operator $\mathcal{O}_i$. The vertex function Γ_μ^{LL} is simplified to have the form

$$\Gamma_\mu^{\text{LL}} = -\frac{i}{4\pi^2} \left(\hat{s}\gamma_\mu - q_\mu \slashed{q}\right) P_R F_1\left(\hat{s}, m\right), \qquad (5.11)$$

with $q = p_1 + p_2$, m the mass of the fermion in the loop and F_1 defined as

$$
F_1\left(\hat{s}, m\right) \equiv -\frac{1}{6\hat{s}} \mathrm{Re}\left[\left(2m^2 + \hat{s}\right) B_0\left(\hat{s}, m^2\right) - 2A_0\left(m^2\right) + 2m^2 - \frac{4}{3}\hat{s}\right]
$$
$$
\xrightarrow{\text{Finite}} \frac{1}{6\hat{s}} \mathrm{Re}\left[\left(2m^2 + \hat{s}\right)\left(\beta_t \log\frac{\beta_t + 1}{\beta_t - 1} - 2\right) - \hat{s}\log\frac{\mu^2}{m^2} + \frac{4}{3}\hat{s}\right].
$$

$$(5.12)$$

We expand around $D = 4 - 2\epsilon$ to obtain the second line of Eq. (5.12) and the divergence is subtracted in the $\overline{\mathrm{MS}}$ scheme with the counter-term provided by the $gt\bar{t}$-vertex. Similarly, the amplitude for the structure 2 with $\bar{L}L\bar{L}L$ can be written as

$$
\mathcal{M}_{\mathrm{NP}}^{(2)} = \mathcal{C}_i \frac{g^2}{\hat{s}} \frac{c_i}{\Lambda^2} \bar{u}\left(p_4\right) \bar{\gamma}_\rho P_L v\left(p_3\right) \cdot \bar{v}\left(p_2\right) \bar{\gamma}^\mu u\left(p_1\right) \cdot \mathcal{I}_{\rho\mu}, \tag{5.13}
$$

where the tensor carrying the information about the loop effects is simplified to

$$
\mathcal{I}_{\rho\mu} = -\frac{i}{4\pi^2}\left(\hat{s}g_{\mu\rho} - q_\mu q_\rho\right) F_2\left(\hat{s}, m\right). \tag{5.14}
$$

The factor F_2 is defined as

$$
F_2\left(\hat{s}, m\right) \equiv -\frac{1}{6\hat{s}} \mathrm{Re}\left[\left(2m^2 + \hat{s}\right) B_0\left(\hat{s}, m^2\right) - 2A_0\left(m^2\right) + 2m^2 - \frac{\hat{s}}{3}\right]
$$
$$
\xrightarrow{\text{Finite}} \frac{1}{6\hat{s}} \mathrm{Re}\left[\left(2m^2 + \hat{s}\right)\left(\beta_t \log\frac{\beta_t + 1}{\beta_t - 1} - 2\right) - \hat{s}\log\frac{\mu^2}{m^2} + \frac{\hat{s}}{3}\right].
$$

$$(5.15)$$

We notice that the axial part of the amplitudes in Eq. (5.10)-(5.13) do not contribute when the interference with the SM tree-level amplitudes is performed. Hence, the results above stand also for the operators with chirality $\bar{R}R\bar{R}R$. The result for the structure 2 with $\bar{L}L\bar{R}R$ is given by the same quantity $\mathcal{I}_{\rho\mu}$ in Eq. (5.14). This is a consequence of the fact that the amplitudes for the $\bar{L}L\bar{L}L$ and $\bar{L}L\bar{R}R$ cases only differ in the sign of the terms with Levi-Civita tensors, but such terms vanish in the final result.

Finally, we consider the structure 1 with $\bar{L}L\bar{R}R$, where the right-handed fermions in the effective vertex are taken to be the top quarks in the final state. For this case, the amplitude is given by Eq. (5.10) with the replacement $\Gamma_\mu^{\mathrm{LL}} \rightarrow$

Γ_μ^{LR}, where the vertex factor now has the form

$$\Gamma_\mu^{\mathrm{LR}} = -\frac{i}{16\pi^2}\left(D-4\right)m\left(\gamma_\mu \slashed{q} - q_\mu\right)B_0\left(\hat{s}, m^2\right)P_R \qquad (5.16)$$

$$\xrightarrow{\text{Finite}} -\frac{i}{4\pi^2}\cdot 2m\left(\gamma_\mu \slashed{q} - q_\mu\right)P_R. \qquad (5.17)$$

The factor $\left(D-4\right)$ in Eq. (5.16) implies that the finite amplitude for this case is given purely by rational terms[4]. By computing the appropriate color factors and with the results above, we can find the partonic differential cross-section for the interference between tree-level SM and the SMEFT at one-loop in the quark channel:

$$\frac{d\hat{\sigma}}{d\Omega}\bigg|_{\mathcal{O}_{tt}^{(1)}}^{\mathrm{Int}} = \frac{\alpha_s^2}{18\pi^2}\frac{c_{tt}^1}{\Lambda^2}\frac{\beta_t}{\hat{s}^2}\left(2m_t^2\hat{s} + \left(\hat{t}-m_t^2\right)^2 + \left(\hat{u}-m_t^2\right)^2\right)F_1\left(\hat{s}, m_t\right),$$
$$(5.18)$$

$$\frac{d\hat{\sigma}}{d\Omega}\bigg|_{\mathcal{O}_{QQ}^{(1)}}^{\mathrm{Int}} = \frac{\alpha_s^2}{36\pi^2}\frac{c_{QQ}^1}{\Lambda^2}\frac{\beta_t}{\hat{s}^2}\left(2m_t^2\hat{s} + \left(\hat{t}-m_t^2\right)^2 + \left(\hat{u}-m_t^2\right)^2\right)F_1\left(\hat{s}, m_t\right),$$
$$(5.19)$$

$$\frac{d\hat{\sigma}}{d\Omega}\bigg|_{\mathcal{O}_{QQ}^{(8)}}^{\mathrm{Int}} = \frac{\alpha_s^2}{216\pi^2}\frac{c_{QQ}^8}{\Lambda^2}\frac{\beta_t}{\hat{s}^2}\left(2m_t^2\hat{s} + \left(\hat{t}-m_t^2\right)^2 + \left(\hat{u}-m_t^2\right)^2\right)$$
$$\left(3\left(F_2\left(\hat{s}, m_b\right) + F_2\left(\hat{s}, m_t\right)\right) - F_1\left(\hat{s}, m_t\right)\right), \quad (5.20)$$

$$\frac{d\hat{\sigma}}{d\Omega}\bigg|_{\mathcal{O}_{Qt}^{(1)}}^{\mathrm{Int}} = -\frac{\alpha_s^2}{18\pi^2}\frac{c_{Qt}^1}{\Lambda^2}\frac{m_t^2\beta_t}{\hat{s}}, \qquad (5.21)$$

$$\frac{d\hat{\sigma}}{d\Omega}\bigg|_{\mathcal{O}_{Qt}^{(8)}}^{\mathrm{Int}} = \frac{\alpha_s^2}{216\pi}\frac{c_{Qt}^8}{\Lambda^2}\frac{\beta_t}{\hat{s}^2}\bigg(3\left(2m_t^2\hat{s} + \left(\hat{t}-m_t^2\right)^2 + \left(\hat{u}-m_t^2\right)^2\right)\left(F_2\left(\hat{s}, m_b\right)\right.$$
$$\left. +2F_2\left(\hat{s}, m_t\right)\right) + 2m_t^2\hat{s}\bigg). \qquad (5.22)$$

The formulas for the c_{QQ}^8 and c_{Qt}^8 operators stand only for channels where the bottom quark is not included in the initial state since this channel has IR divergences that would need to be considered simultaneously with real radiations. These differential rates can be compared to the SM differential cross-section in Eq. (3.8), from which we notice that, with exception of the result for $\mathcal{O}_{Qt}^{(1)}$, the results above are radiative corrections in the form of overall factors multi-

---

[4]Rational terms appear in the implementation of the Passarino-Veltman reduction of one-loop amplitudes as the finite product of poles of order $\mathcal{O}(\epsilon^{-1})$ and terms in the numerator of order $\mathcal{O}(\epsilon)$. The rational part of a one-loop amplitude can be identified as the terms that do not involve logarithms or dilogarithms at order $\mathcal{O}(\epsilon^0)$.
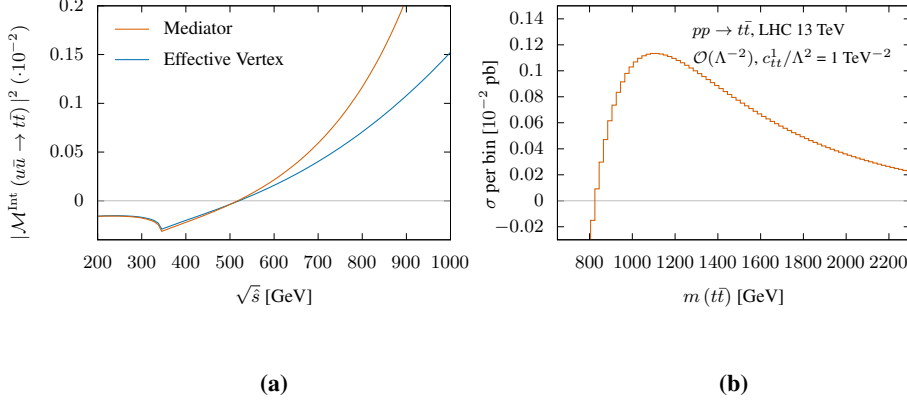
Figure 5.2: Analytical results in the $pp \rightarrow t\bar{t}$: a) Comparison between computations with an auxiliary mediator and with four-fermion operators, with $c_{QQ}^8/\Lambda^2 = 1\,\mathrm{TeV}^{-2}$ and the matching condition $c_{QQ}^8/\Lambda^2 = -g_X^2/2M_X^2$ with $g_X = 1$ and $M_X \simeq 1.4\,\mathrm{TeV}$; b) Tail of the invariant-mass distribution for the operator $\mathcal{O}_{tt}^{(1)}$.

plying the SM result. These interference rates present sign flips given by the factors containing combinations of $F_1(\hat{s}, m)$ and $F_2(\hat{s}, m)$.

The formulas in Eq. (5.18)-(5.22) have been contrasted to a toy model with vector bosons (X_μ) as mediators that could generate the four-heavy-quark operators once the heavy states are integrated out. In the case of the color-octet operators, the mediator must bear the corresponding color structure. In particular, in Fig. 5.2a we show the comparison between the results for the squared-amplitude of the interference contributions arising from the operator $\mathcal{O}_{QQ}^{(8)}$ and from the analogous contribution with the mediator boson X_μ and coupling strength g_X. We notice a good agreement for energies below the mass of the heavy states, $\sqrt{\hat{s}} \ll m_X$.

It should be noted that the operator $\mathcal{O}_{QQ}^{(8)}$ can be written in terms of a color-singlet operator by means of Fierz transformations as

$$c_{QQ}^8 = 8[C_{qq}^{(3)}]^{3333}, \qquad \mathcal{O}_{qq}^{(3)} = (\bar{Q}_L \gamma_\mu \tau^i Q_L)(\bar{Q}_L \gamma^\mu \tau^i Q_L). \qquad (5.23)$$

The differential cross-section starting from the definition in Eq. (5.23) can be computed to yield as a result the formula (5.20) with the replacement $F_2(\hat{s}, m) \rightarrow F_1(\hat{s}, m)$. By inspection of the Eq. (5.12) and (5.15), we notice that the difference of the two results arises from the rational part. This implies that, even though the two definitions of the operator $\mathcal{O}_{QQ}^{(8)}$ are equivalent at tree-level, the amplitudes at one-loop are not. The inclusion of evanescent operators
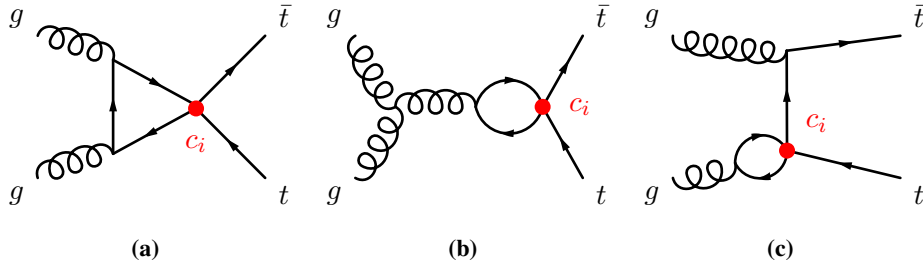
Figure 5.3: EFT one-loop diagrams for the partonic process $gg \to t\bar{t}$.

is required to find an equivalence between these results. The SMEFT@NLO, on which rely the simulations performed in MadGraph5_aMC@NLO, works with the definition in Eq. (5.23), hence the effects of evanescent operators must be taken into account when we compare at the amplitude level the analytical results above and the computations obtained via MadGraph5_aMC@NLO. By doing so, all of our different results agree.

The effects of using a different EFT bases on the contributions from evanescent operators have been studied in the literature [121]. Such effects can be obtained from the diagrams displayed in Fig. 5.1, which are computed in both bases, then compared so that the extra pieces give the contribution arising from evanescent operators involved in the use of Fierz transformations. With this, relating the matching between different bases is achieved.

As a last comment on our analytical results, we discuss the growth with energy of the amplitudes. Let us consider the amplitude corresponding to the operator $\mathcal{O}_{tt}^{(1)}$, for which we take the limit $\hat{s} \gg m_t^2$. Also, we choose $\mu_r = m_t$. From the results of this section it is possible to find

$$\overline{|\mathcal{M}^{\mathrm{Int}}|^2}\,(\hat{s}, \cos\theta) \simeq -\frac{8\alpha_s^2}{81}\frac{c_{tt}^1}{\Lambda^2} \cdot \hat{s}\left(1 + \cos^2\theta\right)\left(2 + 3\log\frac{m_t^2}{\hat{s}}\right), \quad (5.24)$$

where θ is the angle between the incoming light quark and the outgoing top. Hence, the amplitude square grows with energy. In Fig. 5.2b the high energy behaviour of the invariant-mass distribution at the interference level of the operator $\mathcal{O}_{tt}^{(1)}$ is presented.

5.2.2 Gluon Channel

The LO contribution of the the four-heavy-quark operators to the gluon-initiated process is at one-loop through the diagrams shown in Fig. 5.3. The diagrams of the type shown in Fig. 5.3c vanish for the operators $\mathcal{O}_{tt}^{(1)}$, $\mathcal{O}_{QQ}^{(1)}$ and $\mathcal{O}_{QQ}^{(8)}$,

while in the cases of $\mathcal{O}_{Qt}^{(1)}$ and $\mathcal{O}_{Qt}^{8}$ they contribute with a constant factor at the amplitude level coming purely from rational terms. In addition to the diagrams in Fig. 5.3c, there are diagrams that contribute to the self-energy of the top quark in the form of tadpole contributions, which come solely from four-fermion operators mixing helicities: $\mathcal{O}_{Qt}^{(1)}$ and $\mathcal{O}_{Qt}^{(8)}$. These tadpoles turn out to be non-physical as they can be absorbed by the mass counter-term of the top quark.

For convenience, in the results below the Passarino-Veltman integrals are written as $A_0 = A_0(m_t^2)$, $B_0 = B_0(\hat{s}; m_t^2, m_t^2)$, $B_0^0 = B_0(\hat{s}; 0, 0)$ and $C_0 = C_0(0, \hat{s}, 0; m_t^2, m_t^2, m_t^2)$. The partonic differential cross-section for the interference between SM at tree-level and SMEFT at one-loop in the gluon channel are given by the expressions

$$\frac{d\hat{\sigma}}{d\Omega}\Big|_{\mathcal{O}_{tt}^{(1)}}^{\text{Int}} = \frac{1}{16\pi^2}\frac{c_{tt}^1}{\Lambda^2}\frac{\alpha_s^2 m_t^2 \beta_t}{96\hat{s}^2}\frac{1}{(\hat{t}-m_t^2)(\hat{u}-m_t^2)}$$
$$\left(2m_t^2\hat{s}(9\left(\hat{t}-\hat{u}\right)^2 - 13\hat{s}^2)C_0 + 36(\hat{t}-\hat{u})^2(m_t^2 B_0 - A_0)\right.$$
$$\left. + 3(\hat{s}+12m_t^2)\left(\hat{t}-\hat{u}\right)^2 - 13\hat{s}^3\right) \quad (5.25)$$

$$\frac{d\hat{\sigma}}{d\Omega}\Big|_{\mathcal{O}_{QQ}^{(1)}}^{\text{Int}} = \frac{1}{16\pi^2}\frac{c_{QQ}^1}{\Lambda^2}\frac{\alpha_s^2 m_t^2 \beta_t}{96\hat{s}^2}\frac{1}{(\hat{t}-m_t^2)(\hat{u}-m_t^2)}$$
$$\left(2m_t^2\hat{s}(9\left(\hat{t}-\hat{u}\right)^2 - 13\hat{s}^2)C_0 + 36(\hat{t}-\hat{u})^2(m_t^2 B_0 - A_0)\right.$$
$$\left. + 3(\hat{s}+12m_t^2)\left(\hat{t}-\hat{u}\right)^2 - 19\hat{s}^3\right) \quad (5.26)$$

$$\frac{d\hat{\sigma}}{d\Omega}\Big|_{\mathcal{O}_{QQ}^{(8)}}^{\text{Int}} = \frac{1}{16\pi^2}\frac{c_{QQ}^8}{\Lambda^2}\frac{\alpha_s^2 m_t^2 \beta_t}{288\hat{s}^2}\frac{1}{(\hat{t}-m_t^2)(\hat{u}-m_t^2)}$$
$$\left(4m_t^2\hat{s}(9\left(\hat{t}-\hat{u}\right)^2 - 13\hat{s}^2)C_0 + 72(\hat{t}-\hat{u})^2(m_t^2 B_0 - A_0)\right.$$
$$\left. + 3(5\hat{s}+24m_t^2)\left(\hat{t}-\hat{u}\right)^2 - 41\hat{s}^3\right)$$
$$(5.27)$$

$$\frac{d\hat{\sigma}}{d\Omega}\Big|_{\mathcal{O}_{Qt}^{(1)}}^{\text{Int}} = \frac{1}{16\pi^2}\frac{c_{Qt}^1}{\Lambda^2}\frac{\alpha_s^2 m_t^2 \beta_t}{192\hat{s}^2}\frac{(\hat{s}+\hat{t}-\hat{u})(\hat{s}-\hat{t}+\hat{u})}{(\hat{t}-m_t^2)^2(\hat{u}-m_t^2)^2}$$
$$\left(2\hat{s}(7\hat{s}^2 - 22m_t^2\hat{s} + 56m_t^4)C_0 + \hat{s}(56m_t^2 - 19\hat{s}) - 18\left(\hat{t}-\hat{u}\right)^2\right)$$
$$(5.28)$$

$$\frac{d\hat{\sigma}}{d\Omega}\Big|_{\mathcal{O}_{Qt}^{(8)}}^{\text{Int}} = \frac{1}{16\pi^2}\frac{c_{Qt}^8}{\Lambda^2}\frac{(\hat{s}+\hat{t}-\hat{u})(\hat{s}-\hat{t}+\hat{u})}{(\hat{t}-m_t^2)^2(\hat{u}-m_t^2)^2}\left(28s\left(4m_t^2 s - s^2 + 2\left(t+u\right)^2\right)C_0\right.$$
$$\left. + 28s^2 + 56s\left(t+u\right) + 9\left(t-u\right)^2\right) \quad (5.29)$$

The differential cross-sections corresponding to the the operators $\mathcal{O}_{QQ}^{(1)}$ and $\mathcal{O}_{tt}^{(1)}$ are different only in the rational term. This is due to the contribution of

a diagram of the type 5.3a with the bottom quark running in the loop. Such diagram is given purely as a rational contribution.

In Fig. 5.4 we compare the square of the amplitudes corresponding to the cross-sections in Eq. (5.25)-(5.29) with the standalone results from Mad-Graph5_aMC@NLO for the fixed value $\cos\theta = 0$ by taking the ratio shown in the inset at the bottom of the figure. We observe a satisfactory agreement between both results except for points where the amplitude vanishes. The curves obtained from MadGraph5_aMC@NLO come from an interpolation of ten output points, leading to large numerical uncertainties around the zeros of the amplitudes. This is the reason for the present of spikes in the ratios.

### 5.2.3 Differential distributions and validation

We now compute the interference of the four-heavy-quark operators with leading QCD contributions in the SM at the LHC. In Fig. 5.5 we present the invariant-mass distribution for the interference and quadratic contributions on the operators. In the inset at the bottom the K-factors[5] are displayed for the effective operators that contribute at tree-level. The operators $\mathcal{O}_{QQ}^{(8)}$ and $\mathcal{O}_{Qt}^{(8)}$ can interfere with the SM at tree-level through the bottom channel due to their color structure. The K-factor corresponding to the coefficient $c_{QQ}^{(8)}$ shows that the loop corrections are comparable to the tree-level contributions. This means that, even though it is suppressed by PDFs, the bottom channel presents a sizable cross-section except for the near-threshold region where the loop induced gluon channel contributions can be almost three times bigger. Similarly occurs with the $\mathcal{O}_{Qt}^{(8)}$ operator, with a more drastic K-factor in the near threshold region favoring the gluon channel.

The one-loop interference with SM amplitudes of operators that do not have a tree-level bottom channel are quite small, but when we consider the differential distributions, as presented in Fig. 5.5a, we notice that there are portions of the phase-space that are favored. Fortunately, differential distributions have been measured for the top-pair production and we can exploit this to get a better sensitivity to the four-heavy-quark operators than just considering total rates. In particular, the distributions in Fig. 5.5a show that the coefficient c_{Qt}^1 leads to contributions one order of magnitude bigger than the other coefficients, also because they only change sign at high energy, i.e. in between 1

---

[5]The K-factors in this document are defined as the ratio $\sigma_{\mathrm{NLO}}/\sigma_{\mathrm{LO}}$. When considering K-factors of new physics we take into consideration purely NLO and LO SMEFT contributions.
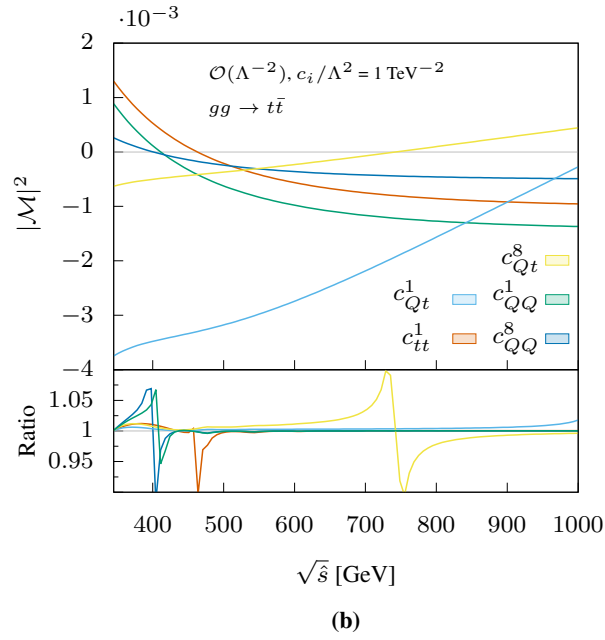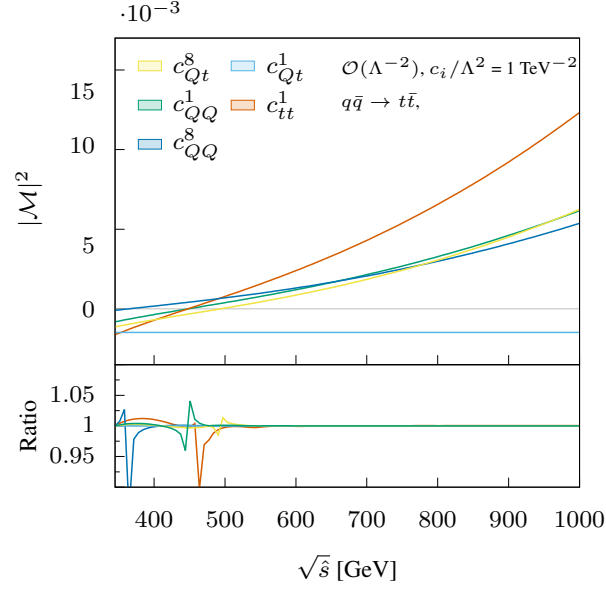
Figure 5.4: Comparison of the amplitude-square linear in the c_i leading to the formulas in Eq. (5.25)-(5.29) with the standalone outputs from MadGraph5_aMC@NLO for $\cos\theta = 0$. In the plot at the top, the curves corresponding to each of the computations are on top of each other for all of the coefficients.
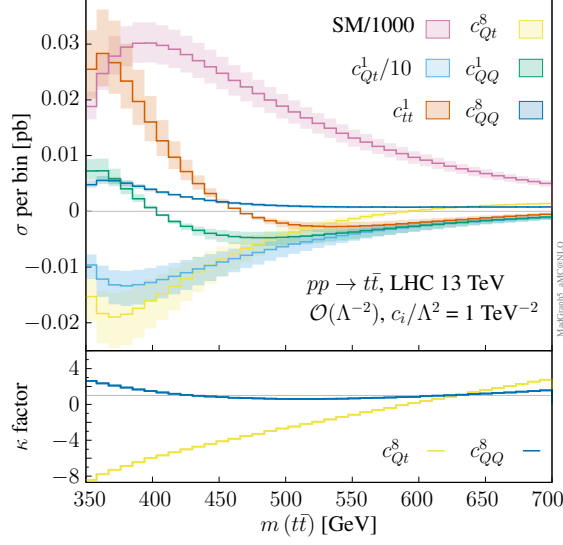
(a)
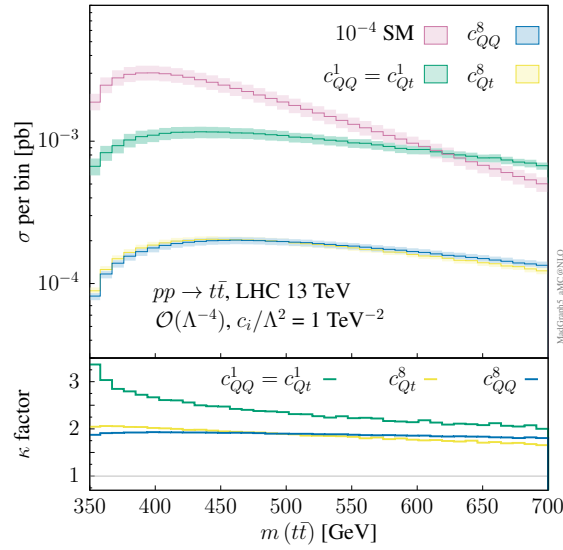
(b)

Figure 5.5: invariant-mass distribution of the top-pair production at NLO of the (a) interference between four-heavy-quark operators and the SM [110] and (b) new physics square. The Wilson coefficients are set to $c_i/\Lambda^2 = 1\,\text{TeV}^{-2}$. Include Table for K factor and uncertainties.

- 1.5 TeV. On the contrary, for the coefficients c_{QQ}^1 and c_{tt}^1 such flip of sign happens at around 400 GeV and 460 GeV, respectively. Finally, the operator c_{Qt}^8 presents a change in sign at an invariant-mass of ~ 600 GeV. As discussed previously in our analytical computations, this change in signs is present at the partonic level in each of the channels, although at different energies. In the end, when we weight the results with PDFs we have cancellations in some regions of the phase-space, but in the end the origin of the negative interference is traced back to the partonic amplitudes.

The quadratic contributions showed in Fig. 5.5b are computed for operators that appear at tree-level in any of the quark channels because quadratic contributions originating from the square of one-loop amplitudes in the gluon-channel are suppressed. This is also the reason for the absent of a distribution for the $\mathcal{O}_{tt}^{(1)}$ operator in Fig. 5.5b.

5.3 Four-top production

In this section, we revisit the main features of the $pp \rightarrow t\bar{t}t\bar{t}$ process and the contributions of the four-heavy-quark operators to it in comparison to the $pp \rightarrow t\bar{t}$. Just like in the case of the top-pair production, strong efforts have been done in understanding the four-top production. In the SM, the $t\bar{t}t\bar{t}$ production cross-section is dominated by the gluon channel. The Born amplitudes receive contributions of the order $\mathcal{O}(\alpha_s^2)$ and $\mathcal{O}(\alpha_s\alpha)$, with α indicating couplings of electroweak origin. The theoretical prediction for the production rate is $\sigma(pp \rightarrow t\bar{t}t\bar{t}) = 11.97^{+18\%}_{-21\%}$ fb at NLO considering QCD+EW corrections [106], where the errors come from scale uncertainties as specified in the beginning of section 5.2.

All the five operators in Eq. (5.6) contribute at tree-level to both gluon and quark induced four-top production by connecting the initial state with one or two gluons to their four-top vertex. The Feynman diagrams of this process with insertions of four-fermion operators are shown in the Fig. 5.6. Their contributions are also largely dominated by gluon fusion. In addition, the operators $\mathcal{O}_{Qt}^{(1)}$, $\mathcal{O}_{QQ}^{(1)}$, $\mathcal{O}_{Qt}^{(8)}$ and $\mathcal{O}_{QQ}^{(8)}$ enter at tree-level in the four-top production through the bottom initiated sub-process where the bottom quarks originate from the vertices with two bottom and two top. As mentioned in the previous section, they affect also top-pair production at the tree-level through that same vertex and in the same production sub-channel. However, suppression from PDFs to the bottom channel reduce the sensitivity to these effects and therefore the four-heavy-quark operators at tree-level are better studied in the LHC
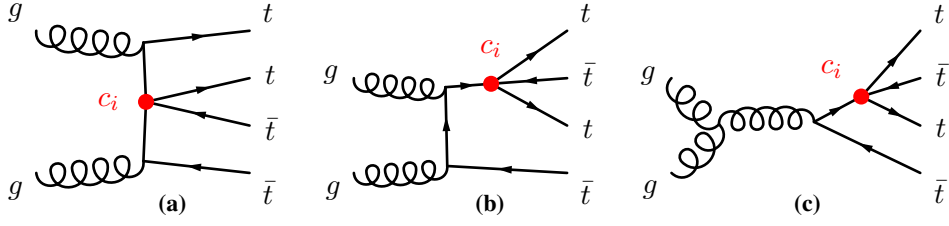
Figure 5.6: EFT tree-level diagrams for $gg \to t\bar{t}t\bar{t}$.

via the four-top quark production. As a result, the four-top quark production is understood to be complementary to the top-pair production. Moreover, the color-singlet operators between two light and two heavy quarks interfere at tree-level with the SM amplitude of the $t\bar{t}t\bar{t}$, unlike the $t\bar{t}$ production. Another alternative to study those operators is the top-pair production in association with a bottom pair. While their effects are large [161], the QCD background makes this process very challenging.

The typical cross-section for the four-top production is of some few fb, thus naively, its constraining power is expected to be limited. In reality, this is compensated by the high sensitivity of the $t\bar{t}t\bar{t}$ process to four-quark operators. Furthermore, such sensitivity is enhanced by the behaviour of the partonic cross-sections at high-energies in the quadratic contribution due to the energy scaling of the four-fermion operators. The increasing cross-section at high energies hints however that there might be EFT validity issues. In ref. [137] a complete discussion about the validity of the SMEFT implementation for this process is presented, where it is shown that for $c_i/\Lambda^2 < 1$ TeV^{-2} the EFT expansion is under control. However, the strongest constraints to the new-physics scale obtained from four-top production set $c_i/\Lambda^2 \approx 10$ TeV$^{-2} \approx 1/(400 \text{ GeV})^2$ from the quadratic contribution and from high-energy bins in the differential distributions. Special care has to be taken when considering contributions of the order $\mathcal{O}(\Lambda^{-4})$ that come from the square of single insertion of effective operators. Even more, for $c_i/\Lambda^2 \geq 1$ TeV^{-2}, the square of double-insertion diagrams (of order $\mathcal{O}(\Lambda^{-8})$) become the leading contribution when considering contributions from dimension-6 operators. For predictions considering Wilson coefficients $c_i/\Lambda^2 \geq 1$ TeV^{-2}, a consistent computation should include contributions coming from the interference between double insertion of NP couplings and the SM, as well as contributions coming from dimension-8 operators and possible contributions when considering EOM at the order $\mathcal{O}(\Lambda^{-4})$.

The inclusive cross-section of the four-top process is computed with single insertions of dimension-6 operators as

$$\sigma_{t\bar{t}t\bar{t}}(c_i) = \sigma_{t\bar{t}t\bar{t}}^{\mathrm{SM}} + \sigma_{t\bar{t}t\bar{t}}^{\mathrm{Int.}} \frac{c_i}{\Lambda^2} + \sigma_{t\bar{t}t\bar{t}}^{\mathrm{Quad.}} \frac{c_i c_j}{\Lambda^4}, \tag{5.30}$$

with

$$\sigma_{t\bar{t}t\bar{t}}^{\mathrm{Int.}} = \alpha_s^3 \sigma_{t\bar{t}t\bar{t}}^{\mathrm{Int.1}} + \alpha_s^2 \alpha\, \sigma_{t\bar{t}t\bar{t}}^{\mathrm{Int.2}}, \tag{5.31}$$

where in principle terms of order $\mathcal{O}(\alpha_s \alpha^2)$ and $\mathcal{O}(\alpha^3)$ also should be present, but such terms are negligible as they arise from the quark channels and then are suppressed by the PDFs. Hence, linear terms arise mostly as new physics interfering with gluon-initiated SM amplitudes. In Table 5.2 we present the tree-level contributions at linear and quadratic order in the effective theory expansion following the conventions of Eq. (5.30) (corresponding QCD-NLO corrections have been computed in [110]). It is noteworthy to point out the drastic change in the interference pattern due to the inclusion of electroweak contributions [146,149]. At order $\mathcal{O}(\Lambda^{-4})$ only diagonal contributions proportional to the square of each operator coefficient are listed. These contributions are dominated by terms of the order α_s^2 as the gluon initiated channels are the largest sub-processes. The interference from four-heavy-operators suffer from large cancellations. In particular, the QCD interference (order $\mathcal{O}(\alpha_s^3 \Lambda^{-2})$ in Table 5.2) is suppressed by about a factor 3 for all operators but $\mathcal{O}_{Qt}^{(1)}$, for which the interference almost vanishes [162]. Furthermore the QCD and QED interference also have opposite sign. The scale uncertainties are also large (50-70%) such that only leading effects can meaningfully be constrained and not small variations as we will see later.

Let us focus on the interference of the new-physics with SM-EW contribution to the four-top production. At a first glance, the electroweak contributions to this process may be expected to be sub-leading. Actually, the LO contributions of the order $\mathcal{O}(\alpha_s^2 \alpha^2)$ are around +30-45% of the pure QCD contributions and terms of the order $\mathcal{O}(\alpha_s^3 \alpha)$ are around −25-30%. When we consider radiative corrections, these two contributions cancel out, giving a total contribution of around ±1-2% [106]. However, this cancellation is not present in the region of the phase-space close to threshold. The origin of the cancellation pattern between different orders of EW corrections is not well understood in the SM, and it is not known whether or not this pattern holds when four-fermion operators are present. The electroweak contributions benefit from the large Yukawa coupling between the Higgs and the top in the scattering $t\bar{t} \to t\bar{t}$. The $t\bar{t}t\bar{t}$

(a)   **(b)**
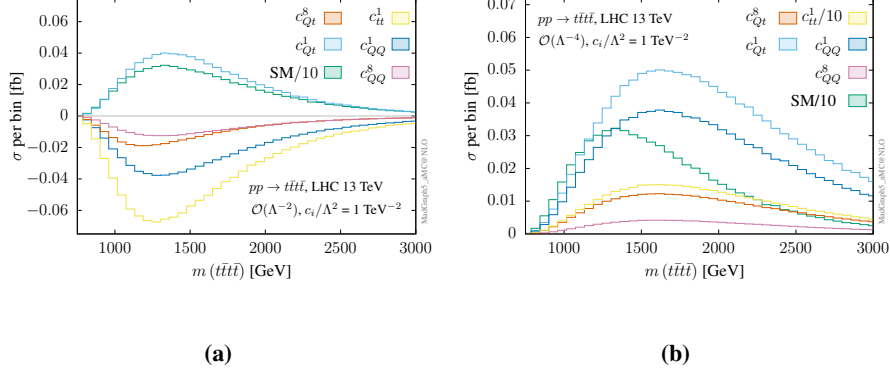
Figure 5.7: Four-top invariant-mass distribution at tree-level of the (a) interference between four-heavy-quark operators and the QCD+EW SM and (b) new physics square. The Wilson coefficients are set to $c_i/\Lambda^2 = 1 \, \text{TeV}^{-2}$. Renormalization and factorization scales are set to $\mu_r = \mu_f = 2m_t = 345$ GeV and $\mu_{\text{EFT}} = m_t$.

process can be used to probe the Yukawa coupling in the SM, y_t, thanks to its high sensitivity to this parameter.

In Fig. 5.7, we present the tree-level contributions from the SM and from the new physics to invariant-mass distribution of the four-top final. The SM amplitudes has terms of the order $\mathcal{O}(\alpha_s^2)$ and $\mathcal{O}(\alpha_s\alpha)$, which interfere with the new physic amplitudes to generate the linear contributions presented in Fig. 5.7a. For the quadratic contributions, only diagonal terms of $c_i c_j$ (with $i = j$) are plotted in Fig. 5.7b. Following the conventions described at the beginning of section 5.2, the renormalization and factorization scales are set as $\mu_r = \mu_f = 2m_t = 345$ GeV. From the invariant-mass distributions linear in the c_i we notice that the sensitivity on 4-heavy-quark operators comes from the region around ~ 1.3 TeV. On the other hand, the square contributions tend to dominate in the high-energy regime. As presented in Fig. 5.7b, the peak tends to be at around 1.7 TeV and falls off gradually, slower than the corresponding linear counterparts. This further indicates that the constrains are valid only for $\Lambda \gtrsim 2$ TeV.

We notice that when we restrict our studies to the pure-four-top component of the operators $\mathcal{O}_{QQ}^{(8)}$ and $\mathcal{O}_{QQ}^{(1)}$, a degeneracy arises from the tree-level relation

$$\mathcal{O}_{QQ}^{(8)} \stackrel{tttt-\text{only}}{=} \frac{1}{3}\mathcal{O}_{QQ}^{(1)}, \tag{5.32}$$

which can be proven by means of the Fierz identities. The biggest tree-level contribution that could resolve such redundancy in the four-top process is the

c_i	$\mathcal{O}(\Lambda^{-2})$			$\mathcal{O}(\Lambda^{-4})$
	$\mathcal{O}(\alpha_s^3\Lambda^{-2})$	$\mathcal{O}(\alpha_s^2\alpha\,\Lambda^{-2})$	Total $\mathcal{O}(\Lambda^{-2})$	
c_{tt}^1	$0.552^{+71\%}_{-39\%}$	$-1.74^{+42\%}_{-27\%}$	$-1.24^{+36\%}_{-25\%}$	$4.25^{+73\%}_{-39\%}$
c_{QQ}^1	$0.272^{+71\%}_{-39\%}$	$-0.991^{+42\%}_{-27\%}$	$-0.737^{+38\%}_{-25\%}$	$1.06^{+73\%}_{-39\%}$
c_{QQ}^8	$0.0889^{+71\%}_{-39\%}$	$-0.329^{+43\%}_{-27\%}$	$-0.245^{+38\%}_{-25\%}$	$0.118^{+73\%}_{-39\%}$
c_{Qt}^1	$-0.0392^{+71\%}_{-39\%}$	$0.747^{+42\%}_{-26\%}$	$0.745^{+42\%}_{-27\%}$	$1.44^{+73\%}_{-39\%}$
c_{Qt}^8	$0.282^{+70\%}_{-39\%}$	$-0.605^{+42\%}_{-27\%}$	$-0.322^{+30\%}_{-22\%}$	$0.349^{+73\%}_{-39\%}$

Table 5.2: Tree-level contributions (in fb.) of the four-fermion operators involving quarks of third-generation to the four-top production at the LHC $\sqrt{s} = 13$ TeV and $c_i/\Lambda^2 = 1$ TeV^{-2} organized according to Eq. (5.30). The SM at NLO considering QCD+EW corrections is $\sigma_{t\bar{t}t\bar{t}}^{SM} = 11.97^{+18\%}_{-21\%}$ fb [102]. Uncertainties are obtained by variation of renormalization scales by a factor of 2 above and below the central value.

bottom production channel, but this effect is negligible due to the PDFs suppression of the bottom quark. By inspection of Table 5.2, we observe that the rows corresponding to the Wilson coefficients c_{QQ}^8 and c_{QQ}^1 are related by roughly a factor of 3 in the interference terms and of 9 in the quadratic terms. In the case of the top-pair production, this degeneracy does not appear as the bottom quark can run in the loop lines. The same happens for the NLO computation of the four-top process.

Contributions with double insertions have been shown recently to be negligible for four-quark operators involving two light quarks [149]. An even stronger suppression is expected in the case of the four-heavy-quark operators as double insertion can only affect bottom induced production. Moreover, dimension-eight operators, equally suppressed by the new scale, are expected to have a much larger effect as they can enter in gluon fusion and have no reason to be then discarded.

The invariant-mass distributions for the top-pair in this section can be compared to the ones for the four-top process in Fig. 5.7. The quadratic terms are smaller in the case of $t\bar{t}$ when contrasted to the interference than in the case of $t\bar{t}t\bar{t}$. This can be an indication that the SMEFT expansion is more under theoretical control in the $t\bar{t}$. However, the largest (or at least expected to be largest) of their quadratic contribution is not included in top-pair as it corresponds to two-loop contributions to gluon and quark production channels. Besides, the bulk of the distribution in the case of four tops is above 1 TeV, in contrast to the

Proc.	Tag	$\sqrt{s}, \mathcal{L}$	Final state	Observable	N_{data}	Ref.
$t\bar{t}$	CMS$_{tt}$-1	13 TeV, 2.3 fb^{-1}	lepton+jets	$d\sigma/dm_{t\bar{t}}$	8	[163]
	CMS$_{tt}$-2	13 TeV, 35.8 fb^{-1}	lepton+jets	$d\sigma/dm_{t\bar{t}}$	10	[164]
	CMS$_{tt}$-3	13 TeV, 2.1 fb^{-1}	dilepton	$d\sigma/dm_{t\bar{t}}$	6	[165]
	CMS$_{tt}$-4	13 TeV, 35.9 fb^{-1}	dilepton	$d\sigma/dm_{t\bar{t}}$	7	[166]
	ATLAS$_{tt}$	13 TeV, 36.1 fb^{-1}	lepton+jets	$d\sigma/dm_{t\bar{t}}$	9	[167]
	HL-LHC	13 TeV, 3 ab^{-1}	Total	$d\sigma/dm_{t\bar{t}}$	23	
$t\bar{t}t\bar{t}$	CMS$_{4t}$-1	13 TeV, 35.9 fb^{-1}	Two same-sign or multi-leptons	$\sigma_{\text{Tot}}(t\bar{t}t\bar{t})$	1	[107]
	CMS$_{4t}$-2	13 TeV, 137 fb^{-1}	Two same-sign or multi-leptons	$\sigma_{\text{Tot}}(t\bar{t}t\bar{t})$	1	[108]
	ATLAS$_{4t}$	13 TeV, 139 fb^{-1}	Two same-sign or multi-leptons	$\sigma_{\text{Tot}}(t\bar{t}t\bar{t})$	1	[109]
	HL-LHC	13 TeV, 3 ab^{-1}	Total	$d\sigma/dm_{t\bar{t}t\bar{t}}$	5	

Table 5.3: Experimental measurements of top-pair (top block of the Table) and four-top production (Bottom block of the Table) at the LHC considered in the analysis of section 5.4. The first column shows the label used to present the results obtained from the corresponding dataset.

top-pair, for which we have that the peaks are close to threshold energy. These facts are expected to have an impact in our sensitivity analysis and validity discussion presented in the next section.

5.4   Analysis and Results

In this section, we present the analysis of the constraining power of the processes $pp \to t\bar{t}$ and $pp \to t\bar{t}t\bar{t}$ on the four-heavy-quark operators. The theoretical predictions are computed with the setup presented in the beginning of the section 5.2.

Our sensitivity study is based on the fit of the χ^2-distribution. The 95% confidence level (CL) bounds on the effective operators couplings are obtained by using the data sets listed in Table 5.3. We construct the χ^2-distribution depending on the set of Wilson coefficients $c_i = \{c_{tt}^1, c_{QQ}^1, c_{QQ}^8, c_{Qt}^1, c_{Qt}^8\}$ as

$$\chi^2\left(\frac{c_i}{\Lambda^2}\right) = \frac{\left(\text{O}_{\text{SMEFT}}\left(\frac{c_i}{\Lambda^2}\right) - \text{O}_{\text{Exp}}\right)^2}{(\delta\text{O})^2}, \qquad (5.33)$$

where the observable O can be the invariant-mass differential distribution or the total cross-section of the $t\bar{t}$ or the $t\bar{t}t\bar{t}$ processes. The theoretical errors are
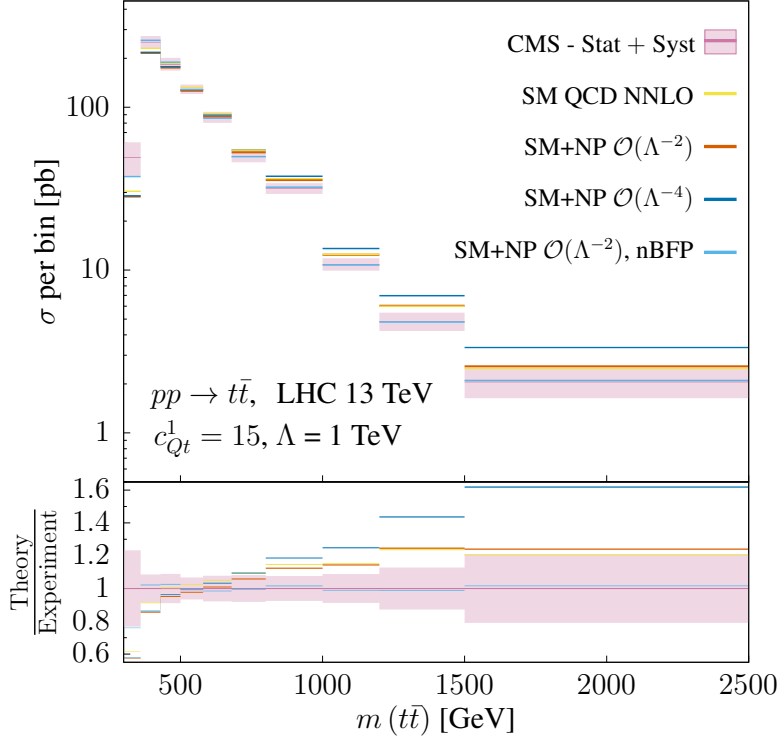
Figure 5.8: Invariant-mass distribution of the top-pair production for new physics parametrized by the $\mathcal{O}_{Qt}^{(1)}$ operator, with the exception of the light blue histogram, for which the coefficients are set near to the Best Fit Point (nBFP). The experimental data corresponds to measurements with 35.8 fb^{-1} of integrated luminosity at CMS (CMS$_{t\bar{t}}$-2 in Table 5.3). The ratio between the different theoretical predictions and the CMS value is displayed in the inset at the bottom.

not considered in the total uncertainties entering the χ^2-distribution , thus the uncertainties are given fully by the reported uncertainties from the experiments ($\delta O = \delta O_{\text{Exp}}$) which are much larger than the theoretical errors. In the case of the ATLAS results for the top-pair production we disregard non-Gaussian uncertainties as they are sub-leading. The measured total cross-sections of the four-top production are reported with non-Gaussian uncertainties, thus we shift the cross-section in such a way that the error bands are symmetric, which is sufficient for the goals of our analysis. Finally, we assume that all uncertainties are not correlated.

The theoretical computation of the observable $\mathrm{O}_{\mathrm{SMEFT}}$ in Eq. (5.33) is organized as follows

$$\mathrm{O}_{\mathrm{SMEFT}}\left(\frac{c_i}{\Lambda^2}\right) = \mathrm{O}_{\mathrm{SM}} + \sum_i a_i \frac{c_i}{\Lambda^2} + \sum_{ij} b_{ij} \frac{c_i c_j}{\Lambda^4}, \qquad (5.34)$$

so that the bounds at the interference order ($\mathcal{O}(\Lambda^{-2})$) in the tables below refer to numbers obtained from a truncation up to the second term in the right-hand side of the Eq. (5.34), while bounds at the quadratic order ($\mathcal{O}(\Lambda^{-4})$) consider all the terms including off-diagonal elements b_{ij} arising from multiplying diagrams with insertions at tree-level of effective operators $\mathcal{O}_i$, and diagrams having insertions at tree-level with diagrams having insertions at one-loop.

5.4.1   Fits to the measurements of the top-pair production

To obtain the theoretical prediction of the SM to the top-pair production, $d\sigma_{\mathrm{SM}}/dm_{t\bar{t}}$, we perform the computations in MadGraph5_aMC@NLO at QCD-NLO and use K-factors at a differential level extracted from ref. [100, 101] to account for NNLO effects. The SM prediction obtained by this procedure is in agreement (at the order of 3-4%) within the error bands of the results from [102], which contain the invariant-mass distributions with the same bin size of the experimental results of the dataset CMS$_{tt}$-4. Since the analysis of ref. [102] includes EW-NLO corrections in the SM, we use their predictions in the fit of the dataset CMS$_{tt}$-4.

To illustrate the sizable NLO contributions to the top-pair process, in Fig. 5.8 we show the invariant-mass distribution in the LHC 13 TeV. We consider the experimental results of the dataset CMS$_{tt}$-2 (in pink), which has the largest number of bins, and compare them to the effects of the effective operators at linear (in red) and quadratic orders (in dark blue). We present the case of the Wilson coefficient $c_{Qt}^1 = 15$, for which the $t\bar{t}$ process is the most sensitive. In the region between 1-1.5 TeV the interference and the SM bins are on top of each other, which is a consequence of the flip in the sign for the c_{Qt}^1 contributions in this phase-space region. The differential distribution obtained from near the best fit point (nBFP) with only interference terms is also shown in Fig. 5.8 (in light blue), where the BFP is found at

$$c_{tt}^1 = 116, \qquad c_{Qt}^1 = -64.9, \qquad c_{QQ}^1 = 484\,(150),$$
$$c_{Qt}^8 = 164\,(150), \qquad c_{QQ}^8 = -1113\,(-150), \qquad (5.35)$$

with $\Lambda = 1$ TeV. By near the BFP, we mean that when the coefficients take too large values, we set them to $c_i = \pm 150$, presented in round brackets in Eq (5.35). Finally, the SM prediction at QCD-NNLO order is also included (in yellow), which seems to present a different shape from the one measured by CMS. In particular, strong deviations are observed in the first bin. The issue of the first bin has been addressed in ref. [141], where the effects of the $\mathcal{O}_G$ operator are discussed, which can bring the theoretical predictions closer to the measured value without spoiling the tail behaviour. However, more stringent bounds on c_G are found from multijet data [150,168,169] (at the order $\mathcal{O}(\Lambda^{-4})$), suggesting that this operator cannot fully parametrize this apparent deviation near threshold. A global fit should shed more light on this issue.

A final note regarding the datasets: the reported values from the measurement CMS$_{tt}$-4 do not agree at 95% CL with our best prediction of the SM. For the latter we use the results from [102], where predictions at NNLO-QCD and NLO-EW are provided with the same bin size as the used in the CMS analysis. We notice that the tension resides on the first bin. A first possible explanation is that the theoretical predictions do not include resummation of threshold logarithms and small-mass logarithms. However, this option seems to be discarded as resummation effects are not large enough [170].

The individual 95% CL bounds on the Wilson coefficients of the four-heavy-quark operators obtained from the $t\bar{t}$ datasets of Table 5.3 are given in Table 5.4. The last column stands for the bounds obtained from considering only the datasets CMS$_{tt}$-2, CMS$_{tt}$-4 and ATLAS$_{tt}$, since they have the best statistics, moreover they are extracted from a different final state and collaboration, thus avoiding any complicated correlations between the samples used in our fits. The bounds typically range from $\mathcal{O}(1\,\text{TeV}^{-2})$ to over $\mathcal{O}(100\,\text{TeV}^{-2})$. Only the coefficient c_{Qt}^1 presents tighter bounds at the interference level. The coefficient c_{tt}^1 is poorly constrained even when quadratic contributions are included since they are negligible because the $\mathcal{O}_{tt}^{(1)}$ operator does not enter at tree-level, which explains the reason for the corresponding entries for $\mathcal{O}(\Lambda^{-2})$ and $\mathcal{O}(\Lambda^{-4})$ being the same. For the other Wilson coefficients, the quadratic fit yields more competitive bounds. The bounds from these differential measurements are expected to be in general more stringent than the bounds obtained from the inclusive measurements because of the increasing sensitivity in the high $m_{t\bar{t}}$ region. The marginalized bounds on the Wilson coefficients are also presented in Table 5.4, for which we allow all the c_i to vary at the

			CMS$_{tt}$-1	CMS$_{tt}$-2	CMS$_{tt}$-3	CMS$_{tt}$-4	ATLAS$_{tt}$	Combined
c_{tt}^1	Ind.	$\mathcal{O}(\Lambda^{-2})$	[−148, 64.4]	[−58.9, 0.99]	[−129, 332]	[−56.4, −0.81]	[−26.4, 52.2]	[−28.1, 7.16]
		$\mathcal{O}(\Lambda^{-4})$	[−148, 64.4]	[−58.9, 0.99]	[−129, 332]	[−56.4, −0.81]	[−26.4, 52.2]	[−28.1, 7.16]
	Marg.	$\mathcal{O}(\Lambda^{-4})$	[−122, 3.22]	[−50.8, −10.8] ∪ [4.55, 255]	-	-	[−232, 129]	[−48.0, 2.83]
c_{QQ}^1	Ind.	$\mathcal{O}(\Lambda^{-2})$	[−292, 139]	[−107, 2.17]	[−335, 462]	[−109, −1.66]	[94.3, −51.3]	[−51.7, 14.9]
		$\mathcal{O}(\Lambda^{-4})$	[−18.2, 16.2]	[−3.04, 1.27]	[−21.4, 21.1]	-	[−19.7, 18.1]	[−5.72, 4.29]
	Marg.	$\mathcal{O}(\Lambda^{-4})$	[−12.7, 13.1]	[−15.3, 12.1]	-	-	[−26.5, 24.0]	[−8.05, 4.95]
c_{QQ}^8	Ind.	$\mathcal{O}(\Lambda^{-2})$	[−323, 126]	[−157, 1.74]	[−575, 334]	[−119, −2.53]	[−60.1, 105]	[−66.9, 15.0]
		$\mathcal{O}(\Lambda^{-4})$	[−43.0, 32.1]	[−11.9, 1.52]	[−48.9, 43.1]	-	[−40.2, 29.2]	[−16.1, 7.90]
	Marg.	$\mathcal{O}(\Lambda^{-4})$	[−31.5, 26.7]	[−316, 163]	-	-	[−75.2, 68.8]	[−18.7, 14.8]
c_{Qt}^1	Ind.	$\mathcal{O}(\Lambda^{-2})$	[−53.7, 78.8]	[−3.23, 11.4]	[−451, 28.0]	-	[−33.2, 29.0]	[−11.4, 12.7]
		$\mathcal{O}(\Lambda^{-4})$	[−15.9, 17.7]	[−1.52, 2.32]	[−30.4, 14.8]	-	[−20.7, 12.3]	[−4.94, 4.80]
	Marg.	$\mathcal{O}(\Lambda^{-4})$	[−6.79, 18.2]	[−50.3, 30.2]	-	-	[−43.8, 24.7]	[−6.33, 7.24]
c_{Qt}^8	Ind.	$\mathcal{O}(\Lambda^{-2})$	[−177, 69.5]	[−100, 0.88]	[−322, 64.3]	[−95.8, −0.77]	[−32.3, 44.9]	[−44.6, 5.92]
		$\mathcal{O}(\Lambda^{-4})$	[−55.5, 31.1]	[−26.0, 0.85]	[−72.8, 34.2]	[−27.3, −0.79]	[−59.7, 25.7]	[−31.4, 5.02]
	Marg.	$\mathcal{O}(\Lambda^{-4})$	[−35.6, 25.2]	[−142, −6.50] ∪ [2.21, 82.5]	-	-	[−100, 58.2]	[−23.7, 1.77]

Table 5.4: The 95% CL bounds (assuming $\Lambda = 1$ TeV) for the coefficients of the four-heavy-quark operators in the process $pp \to t\bar{t}$ individual and marginalized. The intervals are presented for the different datasets introduced in Table 5.3.

same time. The allowed volumes in the parameter space of the Wilson coefficients are found by acceptance and rejection methods. In general, the results from the marginalized fit do not change drastically the individual bounds at the quadratic level, just widening slightly the allowed intervals. Finally, the missing entries marked with a dash line are configurations for which the χ^2-distribution is not small enough to provide meaningful bounds, due to a bad fit to the SM prediction.

	CMS$_{tt}$-1	CMS$_{tt}$-2	CMS$_{tt}$-3	CMS$_{tt}$-4	ATLAS$_{tt}$	Combined
c_1	[−48.1, 60.7]	[−8.96, 49.9]	[−40.7, 1.92]	[−0.27, 44.1]	[8.39, 30.5]	[−28.4, −4.90]
c_2	[−24.1, 90.4]	[−47.8, 21.1]	[−86.7, 160]	[−26.6, 33.3]	[−44.6, 1.53]	[−17.2, 19.1]
c_3	[−282, 526]	[−8.97, 425]	[−4.72, 460]	[−321, −1.91]	[−144, 227]	[−261, 5.60]
$c_4(\cdot 10^3)$	[−17.1, 17.8]	[−4.58, 4.09]	[−12.5, 19.3]	[−0.35, 0.078]	[−35.0, 53.3]	[−0.14, 0.38]
$c_5(\cdot 10^4)$	[−31.0, 23.1]	[−32.6, 32.3]	[−21.7, 15.4]	[−23.5, 23.5]	[−30.1, 29.8]	[−0.048, 0.46]

Table 5.5: The 95% CL bounds (assuming $\Lambda = 1$ TeV) for the coefficients of the four-heavy operators in the diagonal basis in the process $pp \to t\bar{t}$. The marginalized intervals are presented for the different datasets introduced in Table 5.3

The intervals for a marginalized fit at the linear expansion can also be obtained. These fits present strong flat directions, nevertheless stringent bounds can be obtained in some directions. In Table 5.5 the 95% CL bounds are listed for the combinations c_i with $i = 1, ..., 5$ given by the change of basis

$$\mathbf{c}' = \mathcal{R} \cdot \mathbf{c} \tag{5.36}$$

with

$$\mathbf{c}^T = \begin{bmatrix} c_{Qt}^1, c_{tt}^1, c_{Qt}^8, c_{QQ}^1, c_{QQ}^8 \end{bmatrix} \quad \text{and} \quad \mathbf{c}'^T = [c_1, c_2, c_3, c_4, c_5]. \tag{5.37}$$

Given the fact that the χ^2-distribution is a quadratic polynomial in the c_i at the interference level, the rotation matrix is obtained by finding the eigenvectors of the matrix of coefficients of the quadratic terms. Hence, the $\mathcal{R}$ matrix is different for each dataset. In particular, for the combination of datasets the rotation matrix has the form

$$\mathcal{R}_{\text{Combined}}^{t\bar{t}} = \begin{bmatrix} -0.99 & -0.012 & -0.12 & -0.062 & 0.0024 \\ 0.097 & -0.70 & -0.55 & -0.33 & -0.31 \\ -0.072 & -0.51 & 0.79 & -0.32 & 0.073 \\ 0.039 & -0.19 & -0.24 & -0.068 & 0.95 \\ -0.057 & -0.46 & 0.053 & 0.88 & -0.016 \end{bmatrix}. \tag{5.38}$$

From this we observe that the most constrained direction c_1 is close to the c_{Qt}^1 axis. In the diagonal basis the BFP can be found at

$$c_1 = 20.5, \quad c_2 = -13.4, \quad c_3 = 208, \quad c_4 = -241 \quad c_5 = -1190. \tag{5.39}$$

The rotational matrices for each of the datasets (listed in the appendix A) show that in most of the cases the two best constrained directions are close to the c_{Qt}^1 and c_{tt}^1 axis. The marginalized analysis for the datasets CMS$_{tt}$-3 and ATLAS$_{tt}$ is especial since the values reported by the experimental collaborations are given as normalized distributions. The χ^2-distribution for normalized distributions has an involved dependence on the Wilson coefficients, which can appear in the denominator. In this situations, the diagonalization approach described above is no longer valid. We solve this issue by multiplying overall the normalized differential distributions by the total cross-section reported in ref. [102].

		CMS$_{4t}$-1	CMS$_{4t}$-2	ATLAS$_{4t}$	Combined
c_{tt}^1	$\mathcal{O}(\Lambda^{-2})$	$[-24.9, 15.0]$	$[-9.44, 7.94]$	$[-20.4, 0.17]$	$[-9.42, 0.12]$
	$\mathcal{O}(\Lambda^{-4})$	$[-2.55, 2.84]$	$[-1.52, 1.81]$	$[-2.30, 2.59]$	$[-1.52, 1.81]$
c_{QQ}^1	$\mathcal{O}(\Lambda^{-2})$	$[-41.8, 25.2]$	$[-15.9, 13.4]$	$[-34.3, 0.28]$	$[-15.9, 0.20]$
	$\mathcal{O}(\Lambda^{-4})$	$[-5.06, 5.75]$	$[-2.99, 3.69]$	$[-4.55, 5.24]$	$[-2.99, 3.67]$
c_{QQ}^8	$\mathcal{O}(\Lambda^{-2})$	$[-126, 75.8]$	$[-47.8, 40.2]$	$[-103, 0.87]$	$[-47.7, 0.60]$
	$\mathcal{O}(\Lambda^{-4})$	$[-15.2, 17.2]$	$[-8.97, 11.0]$	$[-13.6, 15.7]$	$[-8.97, 11.0]$
c_{Qt}^1	$\mathcal{O}(\Lambda^{-2})$	$[-24.9, 41.4]$	$[-13.2, 15.7]$	$[-0.28, 33.9]$	$[-0.20, 15.7]$
	$\mathcal{O}(\Lambda^{-4})$	$[-4.89, 4.37]$	$[-3.12, 2.60]$	$[-4.46, 3.94]$	$[-3.12, 2.60]$
c_{Qt}^8	$\mathcal{O}(\Lambda^{-2})$	$[-95.7, 57.7]$	$[-36.4, 30.6]$	$[-78.5, 0.65]$	$[-36.3, 0.45]$
	$\mathcal{O}(\Lambda^{-4})$	$[-8.95, 9.87]$	$[-5.35, 6.27]$	$[-8.06, 8.98]$	$[-5.34, 6.27]$

Table 5.6: Same as Table 5.4, now in the $pp \to t\bar{t}t\bar{t}$ process. Only individual bounds are presented in this case.

5.4.2   Fits to the measurements of the four-top production

As indicated in Table 5.3, measurements of the $pp \to t\bar{t}t\bar{t}$ only embody inclusive cross-sections. Hence, following Eq. (5.34), we consider as theoretical prediction from the SM and the SMEFT the values presented in Table 5.2.

The individual 95% CL bounds on the Wilson coefficients of the four-heavy-quark operators obtained from the $t\bar{t}t\bar{t}$ datasets are given in Table 5.6. The last column stands for the bounds obtained from considering only datasets from a different final state and collaboration, *i.e.* the results registered in CMS$_{4t}$-2 and ATLAS$_{4t}$, where the former is chosen because it presents better statistics. The bounds are in a similar range as those from the $t\bar{t}$ process although slightly tighter, since the intervals barely overpass $c_i \sim 100 \, \text{TeV}^{-2}$ in the $t\bar{t}t\bar{t}$ case. In general, it can be said that in the $t\bar{t}t\bar{t}$ case the bounds range from $\mathcal{O}(1 \, \text{TeV}^{-2})$ to over $\mathcal{O}(100 \, \text{TeV}^{-2})$. Additionally, from Table 5.6 a clear improvement in the bounds is observed when considering quadratic contributions.

A marginalized analysis, allowing the five Wilson coefficients being non-zero at the time, is not possible in the four-top production. Given the uncorrelated measurements from ATLAS and CMS combined, we are fitting two data points $N_{\text{data}} = 2$ from the same observable (total cross-section) with five parameters. In essence, the two data points are sensitive to the same combination of parameters given by the contributions of the effective operators given in the

fourth column of Table 5.2. From this, the χ^2-distribution can only yield meaningful bounds along one direction in the parameter space. The marginalized bounds with one degree of freedom, $N_{\mathrm{dof}} = 1$, are

$$c_1 \in [-6.98, 0.087] \qquad (5.40)$$

with

$$c_1 = 0.74\, c_{tt}^1 + 0.44\, c_{QQ}^1 + 0.15\, c_{QQ}^8 - 0.44\, c_{Qt}^1 + 0.19\, c_{Qt}^8. \qquad (5.41)$$

### 5.4.3 2D comparison between top-pair and four-top processes

In Fig. 5.9 and 5.10 the results of considering two effective operators at the time are shown. The exclusion regions are obtained at 95% CL, so that points outside the coloured boundaries are excluded. At the interference level, the regions corresponding to the top-pair production are represented by ellipses, while for the four-top production they are represented by planes bounded only along one axis as a consequence of only having two data points in the fit of the two Wilson coefficients. For the purpose of clarity, only the sector of the interference bound regions that are comparable to the results from including the quadratic terms are shown in the plots. The inclusion of the quadratic contributions reduce drastically the allowed region of the Wilson coefficients.

In general, the results in Fig. 5.9 indicate that the top-pair production can render limits on the Wilson coefficients comparable to those extracted from four-top production. Specifically, the regions from considering the quadratic contributions in the plane c_{QQ}^1-c_{Qt}^1 are about same size. In the interest of performing a global fit in the top sector, the results at the interference level suggest that the two processes are complementary in most of the cases, *i.e.* each of these processes constraint the Wilson coefficients along different directions. This will be even more clear in the next subsection with the projected bounds for the HL-LHC.

By inspection of Fig. 5.10, we can infer that at the interference level the two processes are complementary and that at the quadratic level the best sensitivity is provided by the four-top production. Notoriously from Fig. 5.10, strong bounds along the c_{tt}^1 coefficient are found, which in the end is expected as the contributions of the corresponding operator are the largest at the linear and quadratic orders (see Table 5.2).
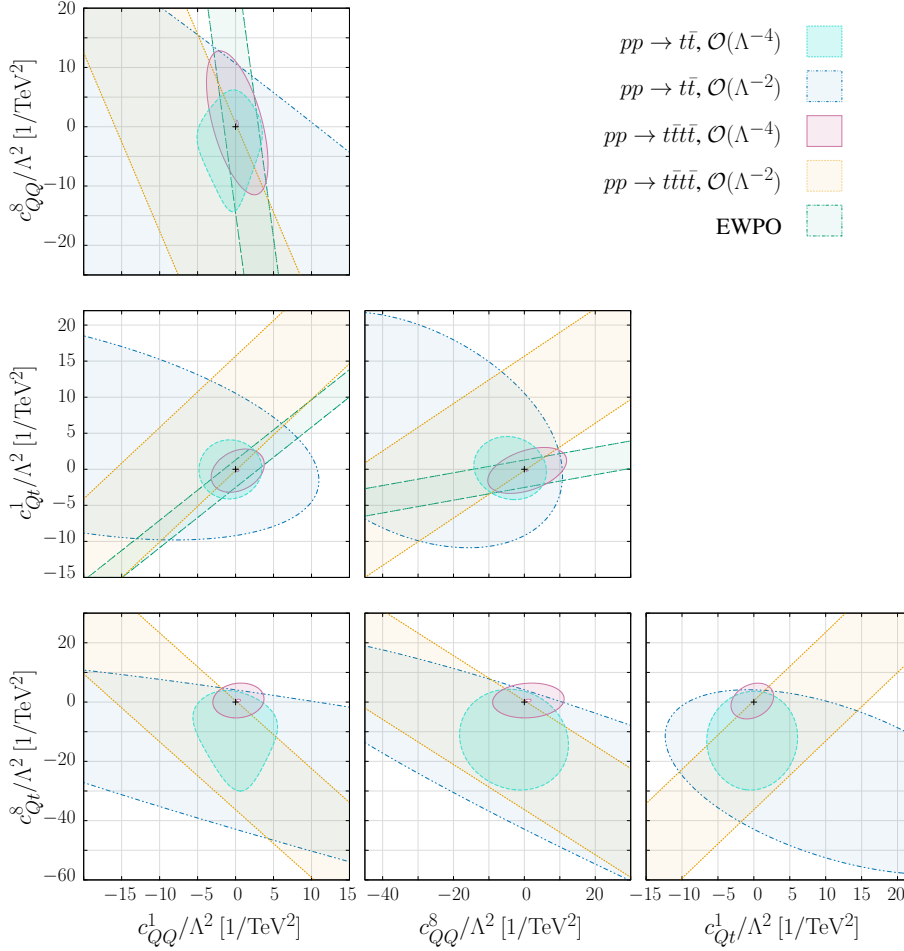
Figure 5.9: Exclusion regions in the (c_i, c_j)-plane obtained from measurements at the LHC with datasets listed in Table 5.3 for $t\bar{t}$ and $t\bar{t}t\bar{t}$ production processes. Bounds obtained from observables with a linear dependence on the Wilson coefficient are indicated with dashed border lines and mild colors, while bounds obtained from quadratic dependencies are shown with solid border lines and stronger colors. Bounds from EWPO at linear order in c_i/Λ^2 extracted from [138] are also shown. The black cross stands for the SM case. Points that lie outside the ellipses are excluded at 95% CL.
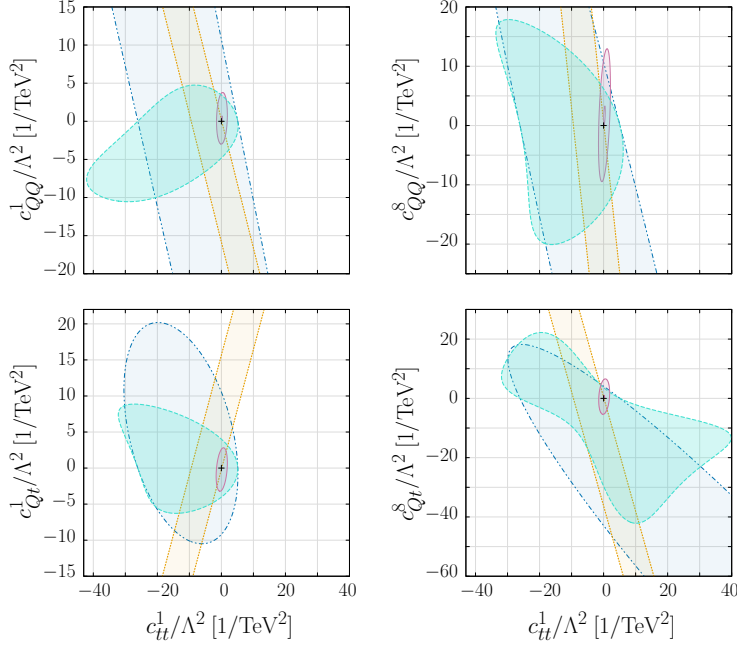
Figure 5.10: Same as Fig. 5.9 for planes along the c_{tt}^1 direction. Labels are given in Fig. 5.9.

Finally, our results can be compared to the sensitivity of EWPO to four-heavy-quark operators [138]. The operators $\mathcal{O}_{QQ}^{(1)}$, $\mathcal{O}_{QQ}^{(8)}$ and $\mathcal{O}_{Qt}^{(1)}$ enter through loop corrections in the observables

$$\Gamma_Z,\ \sigma_{\mathrm{h}},\ R_l,\ R_b,\ R_c,\ A_b,\ A_{b,\mathrm{FB}}, \tag{5.42}$$

where σ_h corresponds to the cross-section of the process $e^+e^- \to$ hadrons. The corresponding experimental measurements of these quantities are found in [171]. In Fig. 5.9 the 95% CL exclusion regions are presented in the planes of the three operators aforementioned at the linear order in c_i/Λ^2. Only experimental uncertainties were considered to get these regions. Theoretical errors do not change substantially the bounds presented here, just widening slightly the region bands. The individual bounds from EWPO are

$$c_{QQ}^1 \in [-1.61, 2.68], \tag{5.43}$$

$$c_{QQ}^8 \in [-15.23, 25.41], \tag{5.44}$$

$$c_{Qt}^1 \in [-2.24, 1.35], \tag{5.45}$$

which seem to be competitive when compared to the ones obtained from the $t\bar{t}$ process up to interference contributions.

c_i	$\mathcal{O}(\Lambda^{-2})$			$\mathcal{O}(\Lambda^{-4})$
	$\mathcal{O}(\alpha_s^3\Lambda^{-2})$	$\mathcal{O}(\alpha_s^2\alpha\,\Lambda^{-2})$	Total $\mathcal{O}(\Lambda^{-2})$	
c_{tt}^1	$0.679^{+69\%}_{-55\%}$	$-2.33^{+41\%}_{-27\%}$	$-1.67^{+34\%}_{-25\%}$	$6.62^{+75\%}_{-64\%}$
c_{QQ}^1	$0.338^{+69\%}_{-55\%}$	$-1.33^{+42\%}_{-27\%}$	$-0.996^{+37\%}_{-25\%}$	$1.66^{+74\%}_{-64\%}$
c_{QQ}^8	$0.114^{+68\%}_{-55\%}$	$-0.445^{+41\%}_{-27\%}$	$-0.331^{+37\%}_{-25\%}$	$0.184^{+75\%}_{-64\%}$
c_{Qt}^1	$0.00184^{+486\%}_{-3300\%}$	$1.0^{+40\%}_{-26\%}$	$0.999^{+41\%}_{-27\%}$	$2.25^{+75\%}_{-64\%}$
c_{Qt}^8	$0.380^{+68\%}_{-57\%}$	$-0.812^{+42\%}_{-27\%}$	$-0.431^{+29\%}_{-22\%}$	$0.541^{+74\%}_{-64\%}$

Table 5.7: Contributions (in fb.) of the four-fermion operators involving quarks of third-generation to the four-top production at the LHC with $\sqrt{s} = 14$ TeV organized according to the (5.30).

5.5   Sensitivity projection at HL-LHC

In this section we focus on the projections of the processes at the HL-LHC with $\sqrt{s} = 14$ TeV. In Table 5.7 we present the contributions of the four-heavy-quark operators to the four-top process at the HL-LHC. This can be compared to the situation with $\sqrt{s} = 13$ TeV shown in Table 5.2, from which it is remarkable the increment of the quadratic contribution of around 56% for the five operators. In the case of the interference with the QCD terms, the HL-LHC contributions are around 24% larger, except for the $\mathcal{O}_{Qt}^{(1)}$ operator, due to the phase-space cancellations, and $\mathcal{O}_{Qt}^{(1)}$ for which the increment is of around 35%.

We study the constraining power of the top-pair and four-top processes at the HL-LHC considering the measurement of the invariant-mass distribution of the final state in each production process. For this we assume the measured observables O_n to coincide with the SM predictions. Valid for a counting observable, the uncertainties are constructed as

$$\delta O_n = \sqrt{(\delta O_n)^2_{\text{stat}} + (\delta O_n)^2_{\text{syst}}} = \sqrt{\frac{\sigma_n^{\text{SM}}}{\mathcal{L}} + \alpha^2(\sigma_n^{\text{SM}})^2}, \qquad (5.46)$$

so that the statistical uncertainty is taken to be $(\delta O_n)_{\text{stat}} = \sqrt{\sigma_n^{\text{SM}}/\mathcal{L}}$, where $\mathcal{L}$ is the integrated luminosity and σ_n^{SM} is the cross-section in the bin n of the invariant-mass distribution. The systematic uncertainty has been parametrized by $\delta(O_n)_{\text{syst}} = \alpha\,\sigma_n^{\text{SM}}$, following the study performed in ref. [172], where α

c_i	Cut	$pp \to t\bar{t}$ Individual $\mathcal{O}(\Lambda^{-2})$	$\mathcal{O}(\Lambda^{-4})$	Marginalized $\mathcal{O}(\Lambda^{-4})$	$pp \to t\bar{t}t\bar{t}$ Individual $\mathcal{O}(\Lambda^{-2})$	$\mathcal{O}(\Lambda^{-4})$	$t\bar{t}+t\bar{t}t\bar{t}$ Marginalized $\mathcal{O}(\Lambda^{-4})$
c_{tt}^1	$m_{\text{Tot.}} < 5\,\text{TeV}$	$[-0.51, 0.51]$	$[-0.51, 0.51]$	$[-11.3, 10.6]$	$[-2.64, 2.64]$	$[-0.43, 0.48]$	$[-0.59, 0.62]$
	$m_{\text{Tot.}} < 3\,\text{TeV}$	$[-2.58, 2.58]$	$[-2.58, 2.58]$	$[-38.1, 13.2]$	$[-2.49, 2.49]$	$[-0.69, 0.88]$	$[-1.10, 1.20]$
c_{QQ}^1	$m_{\text{Tot.}} < 5\,\text{TeV}$	$[-1.02, 1.02]$	$[-1.11, 0.96]$	$[-5.82, 5.38]$	$[-4.10, 4.10]$	$[-0.83, 0.98]$	$[-2.13, 3.05]$
	$m_{\text{Tot.}} < 3\,\text{TeV}$	$[-5.0, 5.0]$	$[-7.71, 3.07]$	$[-10.3, 11.4]$	$[-4.23, 4.23]$	$[-1.33, 1.80]$	$[-3.62, 5.59]$
c_{QQ}^8	$m_{\text{Tot.}} < 5\,\text{TeV}$	$[-1.21, 1.21]$	$[-1.24, 1.18]$	$[-13.1, 12.7]$	$[-12.4, 12.4]$	$[-2.50, 2.95]$	$[-7.45, 4.67]$
	$m_{\text{Tot.}} < 3\,\text{TeV}$	$[-6.01, 6.01]$	$[-21.1, 4.74]$	$[-26.3, 28.7]$	$[-12.7, 12.7]$	$[-3.99, 5.40]$	$[-16.6, 8.09]$
c_{Qt}^1	$m_{\text{Tot.}} < 5\,\text{TeV}$	$[-9.03, 9.03]$	$[-4.24, 2.92]$	$[-6.45, 5.39]$	$[-4.75, 4.75]$	$[-0.79, 0.72]$	$[-1.08, 1.01]$
	$m_{\text{Tot.}} < 3\,\text{TeV}$	$[-17.7, 17.7]$	$[-5.44, 4.31]$	$[-10.8, 10.2]$	$[-4.23, 4.23]$	$[-1.51, 1.17]$	$[-2.17, 1.90]$
c_{Qt}^8	$m_{\text{Tot.}} < 5\,\text{TeV}$	$[-0.82, 0.82]$	$[-0.82, -0.82]$	$[-16.4, 12.0]$	$[-9.65, 9.65]$	$[-1.49, 1.66]$	$[-2.04, 2.07]$
	$m_{\text{Tot.}} < 3\,\text{TeV}$	$[-3.86, 3.86]$	$[-4.21, 3.61]$	$[-27.7, 20.8]$	$[-9.08, 9.08]$	$[-2.45, 3.03]$	$[-3.76, 3.69]$

Table 5.8: The 95% confidence level bounds (assuming $\Lambda = 1$ TeV) for the coefficients of the four-heavy-quark operators in the processeses $pp \to t\bar{t}$ and $pp \to t\bar{t}t\bar{t}$ at the HL-LHC with $\sqrt{s} = 14$ TeV. The intervals are presented for the two different cuts in the invariant-mass distribution.

is a dimensionless coefficient that represents the magnitude of the systematic error in relation to the SM cross-section. For the top-pair process we choose a value of $\alpha_{tt} = 0.05$ corresponding to a 5% of systematic errors, while for the four-top process we expect systematic errors to be of around 20%, $\alpha_{4t} = 0.2$, given the large scale uncertainties and the fact that computations at NNLO for the four-top final state seem to be out of reach in the near future.

The luminosity for the HL-LHC is expected to be of the order $\mathcal{L} = 3$ ab^{-1}. Thus, for the typical values of the cross-sections of the two top production processes, the total uncertainties tend to be systematics dominated. Because of this, the binning of our projections for the invariant-mass distribution is chosen in such a way that the systematics are comparable to the statistical uncertainties.

The individual 95% CL bounds on the Wilson coefficients of the four-heavy-quark operators obtained from the top-pair and four-top production processes are given in Table 5.8. The last column stands for the bounds obtained from combining the theoretical predictions from both processes. Marginalized limits are also tabulated for predictions including quadratic terms. Considering the individual bounds, we observe that the two processes tend to be more sensitive to the c_{tt}^1 coefficient. (Probably because of an enhanced sensitivity

c_i	Cut	$pp \to t\bar{t}$	$pp \to t\bar{t}t\bar{t}$	$t\bar{t} + t\bar{t}t\bar{t}$
c_1	$m_{\text{Tot.}} < 5\,\text{TeV}$	$[-0.35, 0.35]$	$[-1.24, 1.24]$	$[-0.38, 0.38]$
	$m_{\text{Tot.}} < 3\,\text{TeV}$	$[-1.71, 1.71]$	$[-1.48, 1.48]$	$[-1.72, 1.72]$
c_2	$m_{\text{Tot.}} < 5\,\text{TeV}$	$[-17.6, 17.6]$	$[-15.7, 15.7]$	$[-6.96, 6.96]$
	$m_{\text{Tot.}} < 3\,\text{TeV}$	$[-29.8, 29.8]$	$[-25.0, 25.0]$	$[-7.29, 7.29]$
c_3	$m_{\text{Tot.}} < 5\,\text{TeV}$	$[-39.6, 39.6]$	$[-24.4, 24.4]$	$[-23.0, 23.0]$
	$m_{\text{Tot.}} < 3\,\text{TeV}$	$[-85.5, 85.5]$	$[-89.8, 89.8]$	$[-63.7, 63.7]$
c_4	$m_{\text{Tot.}} < 5\,\text{TeV}$	$[-62.1, 62.1]$	$[-953, 953]$	$[-67.6, 67.6]$
	$m_{\text{Tot.}} < 3\,\text{TeV}$	$[-289, 289]$	$[-1.23 \cdot 10^9, 1.23 \cdot 10^9]$	$[-105, 105]$
c_5	$m_{\text{Tot.}} < 5\,\text{TeV}$	$[-403, 403]$	$[-4983, 4983]$	$[-88.8, 88.8]$
	$m_{\text{Tot.}} < 3\,\text{TeV}$	$[-727, 727]$	$-$	$[-259, 259]$

Table 5.9: Marginalized 95% confidence level bounds (assuming $\Lambda = 1$ TeV) for the interference given by the coefficients of the four-heavy-quark operators in the diagonal basis of the processes $pp \to t\bar{t}$ and $pp \to t\bar{t}t\bar{t}$. The intervals are presented for the two different cuts in the invariant-mass distribution.

from the tails) In some particular entries, like those for c_{Qt}^1, the four-top is more sensitive than the top-pair process, but in others, like those for c_{QQ}^8 and c_{Qt}^8, the situation is inverted. This suggests that the two processes are sensitive to different directions in the parameter space, and consequently are complementary. Finally, by comparing the results for the two cuts, we can infer that high-energy effects from the tails of the distribution are important, specially for the c_{QQ}^8 operator the difference is drastic, rising questions about validity of including those high-energy bins. Also, the cut at $m_{\text{Tot.}} < 3$ TeV does not impact strongly the limits from the four-top process.

Marginalized bounds for the predictions truncated at the interference order are presented in Table 5.9 for the diagonal directions. The rotation procedure is done as in the section 5.4, with rotation matrices for the cut $m_{\text{Tot.}} < 5$ TeV

given by

$$
\mathcal{R}_{\mathrm{HL}}^{t\bar{t}} = \begin{bmatrix}
-0.038 & -0.74 & -0.46 & -0.37 & -0.31 \\
0.86 & -0.24 & 0.16 & 0.37 & -0.19 \\
-0.36 & -0.018 & -0.36 & 0.80 & -0.32 \\
-0.36 & -0.52 & 0.76 & 0.16 & -0.015 \\
0.032 & -0.34 & -0.25 & 0.25 & 0.87
\end{bmatrix}, \qquad (5.47)
$$

$$
\mathcal{R}_{\mathrm{HL}}^{4t} = \begin{bmatrix}
0.41 & -0.74 & -0.20 & -0.47 & -0.16 \\
0.74 & -0.057 & 0.067 & 0.63 & 0.20 \\
-0.45 & -0.44 & -0.57 & 0.50 & 0.16 \\
-0.27 & -0.48 & 0.75 & 0.088 & 0.34 \\
0.093 & 0.15 & -0.24 & -0.35 & 0.89
\end{bmatrix}, \qquad (5.48)
$$

$$
\mathcal{R}_{\mathrm{HL}}^{\mathrm{Comb.}} = \begin{bmatrix}
-0.034 & -0.74 & -0.46 & -0.37 & -0.31 \\
-0.86 & 0.21 & -0.35 & 0.26 & -0.18 \\
0.35 & -0.17 & -0.18 & 0.83 & -0.36 \\
0.37 & 0.51 & -0.75 & -0.19 & 0.056 \\
-0.069 & -0.33 & -0.26 & 0.28 & 0.86
\end{bmatrix}. \qquad (5.49)
$$

The limits from the four-top process obtained for the cut $m_{t\bar{t}t\bar{t}} < 3$ TeV account for deviations in three bins, leading to constraining only three directions in the parameter space, which is reflected in Table 5.9, where no meaningful value was obtained along the corresponding c_5. Similarly happens for the cut $m_{t\bar{t}t\bar{t}} < 5$ TeV where the c_5 is loosely constrained. The last column of Table 5.9 shows the significance of the bounds obtained from the top-pair production, as the constraints tend to be similar to those of the third column. In the directions of the c_2 and c_5 coefficients the complementary features in between the two processes is the strongest. Finally, we can see that the cut removing high-energy bins does not have a big impact in most of the limits presented.

We also notice that choosing a value of $\alpha_{4t} = 0.05$, *i.e.* a value four times smaller than the used to obtain Table 5.8, to parametrize the systematic errors of the four-top process leads to more stringent constraint bands by a factor of roughly 4 on each extreme at the order $\mathcal{O}(\Lambda^{-2})$. This is a consequence of the uncertainties being systematics dominated. At the order $\mathcal{O}(\Lambda^{-4})$ the bounds get more stringent by a factor of ~ 4 on each extreme. A scenario with such small uncertainties seems rather optimistic considering the big scale uncertainties in the four-top process (see Table 5.7).

We also explore the consequences of the four-top process being measured only through some of its decaying channels. Most likely, differential distribu-

tions for this process will be measured through the decay channels with two
leptons with the same electric, and channels with three isolated leptons, corre-
sponding in total to a branching ratio of

$$\text{BR}_{t\bar{t}t\bar{t}}(\text{semi} - \text{leptonic} + \text{multi} - \text{leptons}) \approx 0.12. \qquad (5.50)$$

By considering this branching ratio in the analysis leading to the individual
bounds obtained from the differential distributions with five bins, we obtained
wider limits of around 6-16% of the ones displayed in Table 5.8. Considering
the size of branching ratio, it seems the change in the limits is not big, this
is due to the fact that the uncertainties are systematic dominated, leading to
the effect of the branching ratio cancelling out among the numerator and the
denominator of the χ^2-distribution. The measurement of invariant-mass distri-
butions with five bins is also optimistic given the statistical uncertainties for a
measurement in the decay channels discussed above. We notice that the limits
do not get affected by analysing the more plausible situation with distribu-
tions composed by two bins. The invariant-mass distribution might not be the
best observable to look for deviations in the four-top process. Although other
differential distributions could be more suitable, we use the invariant-mass dis-
tribution as a first estimate.

In Fig. 5.11 we present the invariant-mass distribution of the top-pair pro-
cess used in our projections, while in Fig. 5.12 the four-top process case is
presented. In total 24 bins in the top-pair process are considered and, due to
the uncertainties, no more than 5 bins are suitable for the four-top process.
Details on the binning can be found in the appendix A. Comparing those two
figures, a better behaviour is observed in the tail of the four-top production for
the interference as its ratio with the SM tends to smaller values in the high-
energy bins, while for the top-pair production the ratio approaches 1. Finally,
we also notice that in the top-pair production the histograms in Fig. 5.11 aris-
ing from the effective operators are almost on top of each other in the high
energy regime, with the exception of the c_{Qt}^1 case. Hence, it might be diffi-
cult to distinguish the contributions of this effective operators at high energies.
The biggest difference between the histograms is observed at energies below
1.5 TeV.
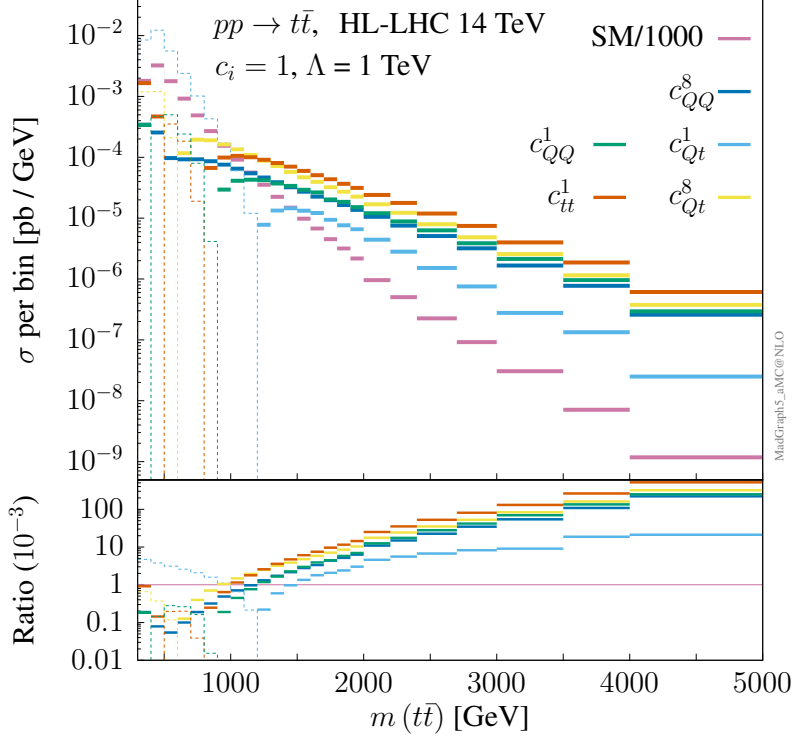
Figure 5.11: Invariant-mass distribution of the top-pair production at one-loop for the interference between four-heavy-quark operators and the SM at the HL-LHC. The Wilson coefficients are set to $c_i/\Lambda^2 = 1\,\text{TeV}^{-2}$. The bins of the interference distributions with negative weights are represented by dashed lines.

5.6 Discussion

The top-pair production at hadron colliders offers the possibility to probe dimension-6 operators involving the third generation of quarks that enter through loop corrections, with exception of contributions via the bottom channel. Not only are the constraints competitive when compared to the sensitivity from other processes, like the four-top production, but they are complementary, yielding limits over different directions in Wilson coefficients space. This is promising when we look towards a global statistical analysis. We also observe that the effective expansion seems to be under better theoretical control in the case of the top-pair production than in the four-top process.

Additionally, we present compact analytical results computed for the first time for the top-pair production partonic cross-sections at $\mathcal{O}(\Lambda^{-2})$ from the
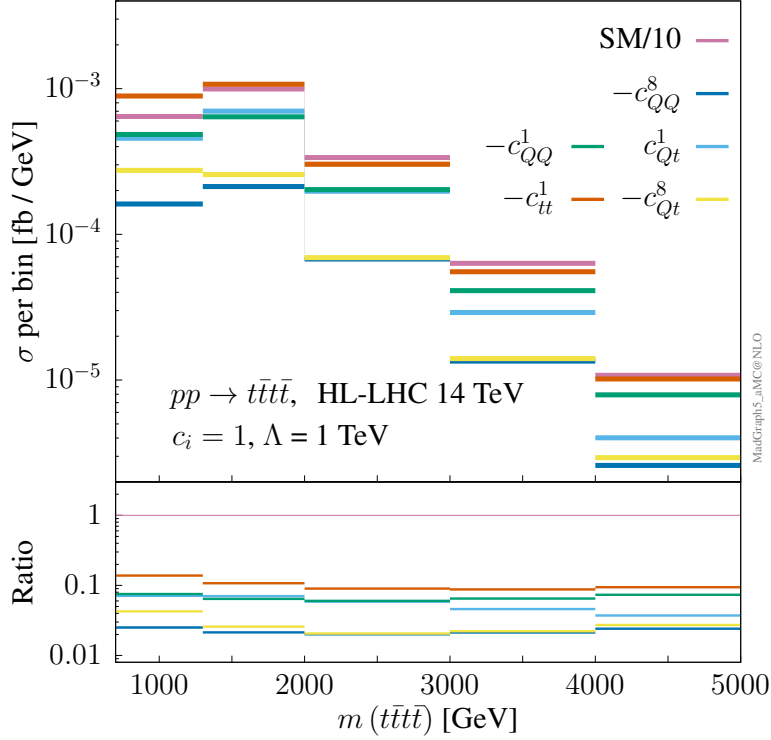
Figure 5.12: Same is in Fig. 5.11 but for the four-top production at tree-level.

interference of four-heavy-quark operators and the SM in the quark-initiated production channels. The insertion in loop diagrams of four-fermion operators composed by chiral currents leads to delicate computations, involving an adequate scheme definition to treat possible anomalous contributions and a clear definition of the evanescent operators (see chapter 4). These subtleties were taken care of by our computations leading to the analytical formulas in Eq. (5.18)-(5.22) and Eq. (5.25)-(5.29), which served to validate the one-loop computations performed by MadGraph5_aMC@NLO, leading to the identification of a coding *logic error* consisting of the wrong selection of rational terms corresponding to a given one-loop amplitude. With this, the implementation of four-fermion operators in MadGraph5_aMC@NLO has been taken to one step further in validation.

The sensitivity projections for the HL-LHC were also explored. We observed an enhancement in sensitivity in all of the four-heavy-quark operators with respect to the sensitivity found from the current measurements at the

LHC. Hence, we find that in the best scenario, the operators can probe scales $c_i/\Lambda^2 \approx 0.5 \text{ TeV}^{-2} \approx 1/(1.5 \text{ TeV})^2$. This bound puts the EFT validity into question when we consider that the chosen cuts in the invariant-mass are at 3 and 5 TeV.

Chapter 6

Double Higgs production at future e^+e^- colliders

The possibility of the quark coupling to new physics can also be studied in processes where the top does not make part of the final state. The Higgs sector is a potential place to look for new physics interacting with the top when we consider that its largest coupling measured to date is the Yukawa coupling to the Higgs. In the previous chapter we focus on the effective four-heavy-quark interactions that arise in BSM scenarios where heavy states couple to the top. In this chapter we study effective interactions arising from scenarios where the heavy states also couple to the Higgs boson.

Since the discovery of the Higgs boson during the Run I of the LHC [14,15] a great effort has been made by the experimental collaborations in the attempt to define the properties of this new particle, namely its mass, spin, parity and coupling to itself and the other particles of the SM, mainly through global fits in the so-called kappa framework [173, 174].

These analyses are crucial to pin down the Higgs boson properties and to understand the nature of electroweak symmetry breaking (EWSB). These studies will play a fundamental role especially during the high-luminosity run of the LHC (HL-LHC) as well as for the future hadron and lepton colliders. Any deviations from SM predictions would unravel the presence of new physics.

As the second run of the LHC is coming to an end, no clear signs of new physics have been found yet. This fact points to a scenario in which new physics is most probably out of the reach of the LHC and in this case the best way to search for it is through indirect effects via precision measurements.

Precision studies of the properties of the Higgs boson and the nature of the electroweak symmetry breaking strongly motivate the construction of a lepton collider which benefits from a cleaner environment with respect to hadron colliders. There have been several proposals for a future electron-positron collider, such as the Compact Linear Collider (CLIC) [175], the International Lin-

ear Collider (ILC) [176], the Circular Electron Positron Collider (CPEC) [177] and the Future Circular Collider with e^+e^- (FCC-ee) at CERN, previously known as TLEP [178].

The main production mechanism of the Higgs boson at e^+e^- colliders is the Higgsstrahlung process $e^+e^- \rightarrow hZ$. At a center-of-mass energies of 240-250 GeV, close to the maximum of the Higgsstrahlung cross section, this process will allow to determine Higgs couplings to gauge bosons with unprecedented precision. In addition there are also weak boson fusion production processes $e^+e^- \rightarrow W^*W^*/Z^*Z^* \rightarrow h\nu\bar{\nu}/he^+e^-$ which provide an increasingly powerful handle at higher center-of-mass energies. Finally, also the process $e^+e^- \rightarrow t\bar{t}h$ benefits from high energies and represent an important measurement to directly constrain the top Yukawa coupling. A comprehensive sensitivity study about the effect of new physics, parametrized by higher-dimensional operators, affecting these production mechanisms for the different proposed e^+e^- machines have been performed in [172, 179, 180].

Some of the Higgs boson couplings can also be tested in higher order processes involving for instance Higgs pair production. In this case, the Higgs self coupling and the couplings to gauge bosons can be measured in the so-called double Higgsstrahlung ($e^+e^- \rightarrow hhZ$) and vector boson fusion ($e^+e^- \rightarrow e^+e^-(\nu\bar{\nu})hh$) processes [181–183]. The top Yukawa can be measured in double Higgs production in association with top quarks ($e^+e^- \rightarrow hht\bar{t}$). These processes are tree-level dominated processes but compared to the previous ones they are characterized by higher orders in the coupling constants.

On the other hand, the process $e^+e^- \rightarrow hh$, where only two Higgs bosons are actually produced in the final state, is completely dominated by the contribution of one-loop diagrams and therefore one can test higher order effects in a clean way because they are not masked by tree diagram contributions. For instance, it can be useful to discriminate between the Higgs sector of the Standard Model from the more complicated scalar sectors belonging to possible extensions, *e.g.* two Higgs doublet model [184, 185].

At hadron colliders, double Higgs production via gluon fusion at LHC has been exhaustively studied as a probe of physics beyond the SM [186–190]. The sensitivity to new physics is enhanced due to a cancellation between triangle and box contributions in the gluon fusion process in the SM [191]. It is well known that Higgs pair production at hadron colliders is sensitive to new physics effects parametrized by higher-dimensional operators [192, 193]. On the other hand, an enhancement in the cross section can also arise from the presence of an hidden sector, as studied in [194]. Double Higgs produc-

tion has also been studied as probe for Higgs anomalous couplings at future electron-proton colliders [195].

The SM cross section for double Higgs production at the LHC is not very large (approximately 37 fb at 14 TeV at NNLO) and the background can be challenging even for HL-LHC. Therefore, the cleaner environment of an electron-positron collider could be very helpful to find deviations from the SM or to improve bounds on new physics.

In this study we will proceed in that direction and focus on the process $e^+e^- \rightarrow hh$ at future lepton colliders as a probe of new physics which we take to be parametrized by the presence of dimension-six effective operators of the SM effective field theory (SMEFT). This chapter is based on the work published in Ref. [1]

6.1   SM double Higgs production at e^+e^- colliders

The process $e^+e^- \rightarrow hh$ is an interesting one from the theoretical point of view because SM tree level diagrams (see Fig. 6.1) give a negligible contribution to the cross section since they are proportional to m_e/v, where m_e is the electron mass and $v = 246$ GeV is the Higgs vacuum expectation value (VEV). This fact has been recognized long ago and as a consequence the cross section is quite small both in the SM and MSSM extensions [184, 196, 197].
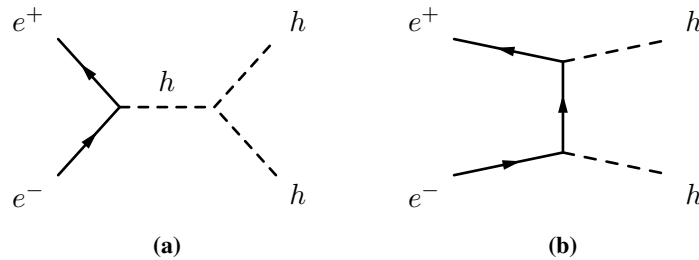

Figure 6.1: SM tree level diagrams for $e^+e^- \rightarrow hh$.

Non-negligible contributions to $e^+e^- \rightarrow hh$ can therefore only come from one-loop diagrams. In the SM, all one-loop diagrams involving the $\bar{e}eh$ vertex must give zero contributions in the chiral limit $m_e = 0$, to all orders in perturbation theory. Furthermore, because of CP invariance, the diagrams containing intermediate γ and Z boson which give rise to two Higgs bosons, also vanish

(see Fig. 6.2 (b)). Additional contributions from triangle diagrams involving the quartic $W^+W^-hh/ZZhh$ and triple hhh couplings are also related to the renormalization of the $\bar{e}eh$ vertex (when one Higgs is taken to its vev) and hence negligible (see Fig. 6.2 (a) and (c)).
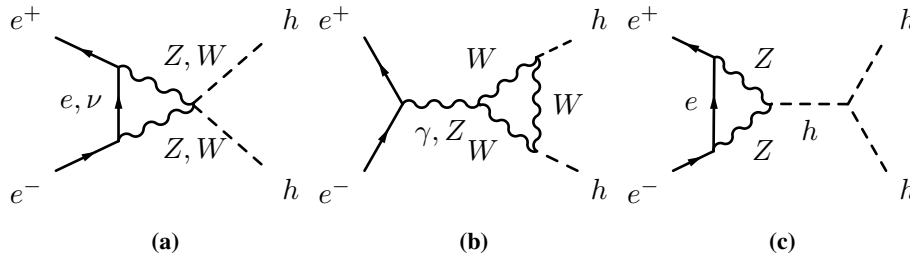

Figure 6.2: SM 1-loop triangle diagrams for $e^+e^- \to hh$.

Therefore, the only contribution to Higgs pair production in the SM comes from W and Z box diagrams of Fig. 6.3. Notice that, contrary to double Higgs production in gluon fusion $gg \to hh$, there is no such feature as the cancellation between triangle and box diagrams because the triangle ones are subleading and vanish in the $m_e = 0$ limit. Moreover, the dependence of the SM cross section on the triple Higgs coupling λ is also negligible because it enters only in diagrams that vanish in the $m_e = 0$ limit (see Fig. 6.2 (c)) where the triangle loop is related to the renormalization of the $\bar{e}eh$ coupling.
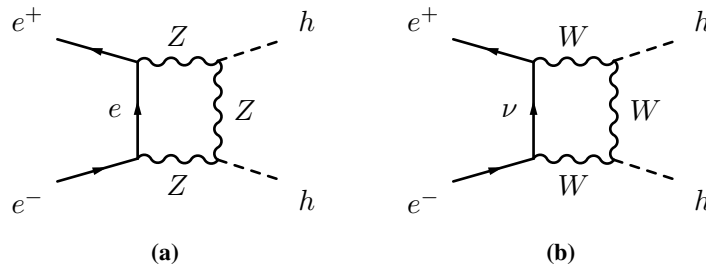
Figure 6.3: SM 1-loop loop box diagrams for $e^+e^- \to hh$.

The energy dependence of the leading order SM cross section for $e^+e^- \to hh$ is shown in Fig. 6.4. The cross section acquires its maximum value of approximately 0.015 fb at around $\sqrt{s} = 500$ GeV.
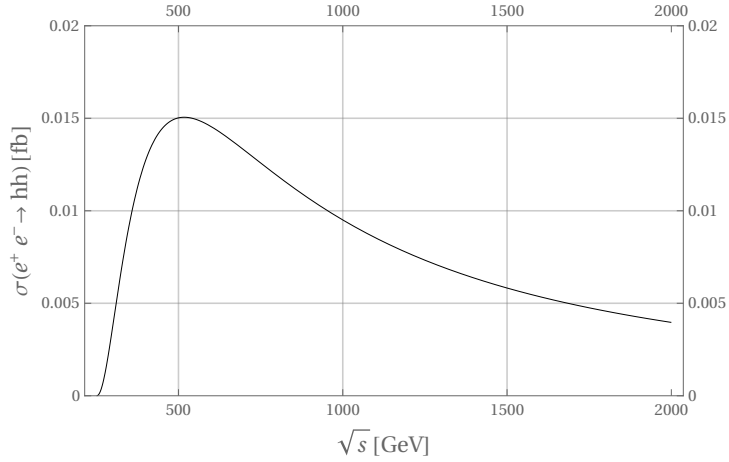
Figure 6.4: SM cross section for $e^+e^- \rightarrow hh$ as function of the center of mass energy $\sqrt{s}$ for unpolarized beams.

6.2 EFT contributions to $e^+e^- \rightarrow hh$

Double Higgs production at e^+e^- colliders in the SM has been shown to have a tiny cross section of the order of fraction of femtobarns (see Fig. 6.4) as discussed in the previous section. However, with large luminosities expected at future e^+e^- colliders, a few hundred events might eventually be collected in the course of a few years, allowing for the experimental study of this final state. On the other hand, cross sections can be enhanced by contributions coming from physics beyond the SM and in this chapter we want to entertain this possibility. In particular we will consider effects of new physics parametrized by the presence of higher dimensional operators in the SMEFT framework.

In this work we focus on the contributions of dimension-six operators of the SMEFT because they give the leading contributions in the systematic expansion E/Λ, where E is the typical energy of the process (the unique dimension-five operator does not contribute to the process $e^+e^- \rightarrow hh$). In this work we use the parametrization of [40]. In principle, all dimension-six operators that are relevant for the electron and Higgs sector should be considered. However, several of these operators are already constrained from other observables and therefore will not be taken into account in this study. In particular, dimension-six operators that modify the $\bar{e}eZ$, $e\nu W$, hZZ and hWW vertices are already (strongly) constrained by electroweak precision data and LHC Higgs measurements [198–204] and we will safely ignore their effects. We are then left with two classes of effective operators that can give sizable contributions: operators

that induce an effective $\bar{e}ehh$ coupling and operators that generate an effective $\bar{e}e\bar{t}t$ coupling. The first class enters at tree-level while the second class operators only contribute at one-loop.

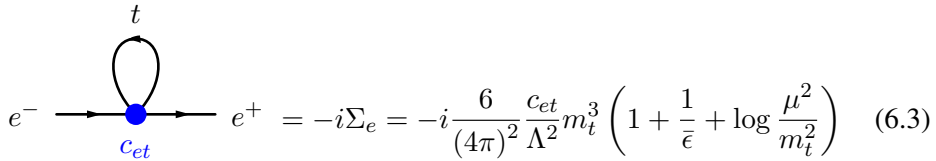There is a unique operator belonging to the first class

$$\frac{c_{e\varphi}}{\Lambda^2}(\varphi^\dagger\varphi - \frac{\upsilon^2}{2})\bar{l}_L\varphi e_R + \text{h.c.} \tag{6.1}$$

On the other hand there are seven four-fermion operators belonging to the second class, however six of them give zero contribution because of their chirality structure and in the end we are left with just one four-fermion operator

$$\frac{c_{et}}{\Lambda^2}\epsilon_{ij}\bar{l}_L^i e_R \bar{q}_L^j t_R + \text{h.c.} \tag{6.2}$$

In the equations above $c_{e\varphi}$ and c_{et} are dimensionless coefficients, Λ is the scale of new physics, $l = (\nu\ e)$, $q = (t\ b)$, φ is the Higgs doublet and ϵ_{ij} is the total antisymmetric tensor of rank 2.

The operator in Eq. (6.1) has been written with the constant piece $\upsilon^2/2$ subtracted to the invariant $\varphi^\dagger\varphi$ term in order to formally maintain the tree level relation $m_e = y_e\upsilon/\sqrt{2}$ also in the effective theory. This mass relation is however altered by the potentially sizable loop correction to the electron mass coming from the top-quark loop induced by the effective operator in Eq. (6.2). The contribution of this effective operator to the electron self energy in dimensional regularization is given by

$$e^- \xrightarrow{\hspace{1.5cm}} e^+ \;=\; -i\Sigma_e = -i\frac{6}{(4\pi)^2}\frac{c_{et}}{\Lambda^2}m_t^3\left(1 + \frac{1}{\bar{\epsilon}} + \log\frac{\mu^2}{m_t^2}\right) \tag{6.3}$$

where $1/\bar{\epsilon} = 1/\epsilon - \gamma + \log 4\pi$. Thus the inverse electron propagator reads

$$\not{p} - y_e\frac{\upsilon}{\sqrt{2}} - \delta y_e\frac{\upsilon}{\sqrt{2}} - \Sigma_e \tag{6.4}$$

In $\overline{\text{MS}}$ the Yukawa counterterm is chosen to be

$$\delta y_e = -\frac{6}{(4\pi)^2}\frac{\sqrt{2}}{\upsilon}\frac{c_{et}}{\Lambda^2}m_t^3\frac{1}{\bar{\epsilon}} \tag{6.5}$$

such that the physical electron mass is given by

$$m_e = y_e \frac{v}{\sqrt{2}} + \frac{6}{(4\pi)^2} \frac{c_{et}}{\Lambda^2} m_t^3 \left(1 + \log \frac{\mu^2}{m_t^2} \right) \tag{6.6}$$

From the theoretical point of view this mass correction may introduce a fine tuning problem and in order to avoid it one must require that $|\delta m_e| \lesssim m_e$. In this case we have that

$$\left| \frac{c_{et}}{\Lambda^2} \right| \lesssim \frac{8\pi^2}{3} \frac{m_e}{m_t^3} \simeq 2 \times 10^{-3} \text{TeV}^{-2} \tag{6.7}$$

The electron mass formula in Eq. (6.6) introduces a dependence between the Yukawa coupling and the c_{et} coefficient that can be rewritten as follows

$$y_e(\mu) = \frac{\sqrt{2}}{v} m_e - \frac{6}{(4\pi)^2} \frac{\sqrt{2}}{v} \frac{c_{et}}{\Lambda^2} m_t^3 \left(1 + \log \frac{\mu^2}{m_t^2} \right) \tag{6.8}$$

Therefore, thanks to this relation, tree level diagrams of Fig. 6.1 proportional to y_e are not negligible anymore if $c_{et} \neq 0$. Notice from Eq. (6.8) that, contrary to the SM case, the limit of vanishing electron mass does not imply a vanishing Yukawa coupling. The scale μ entering in Eq. (6.8) will be set equal to $2m_h$ in the computation of $e^+e^- \to hh$.

The effective operators in Eq. (6.1) and (6.2) modify the $\bar{e}eh$ coupling with respect to the SM case as follows

$$-\frac{m_e}{v} \to -\frac{m_e}{v} + \frac{c_{e\varphi}(\mu)v^2}{\Lambda^2\sqrt{2}} - \frac{3}{(4\pi)^2} \frac{y_t}{\sqrt{2}} \frac{c_{et}}{\Lambda^2} (4m_t^2 - q^2) \left[f(q^2, m_t^2) + \log \frac{\mu^2}{m_t^2} \right] \tag{6.9}$$

where q is the Higgs momentum and

$$f(q^2, m_t^2) = 2 + \sqrt{1 - \frac{4m_t^2}{q^2}} \log \frac{2m_t^2 - q^2 + \sqrt{q^2(q^2 - 4m_t^2)}}{2m_t^2} \tag{6.10}$$

Eq. (6.9) has been obtained by taking into account the tree level contribution to the $\bar{e}eh$ vertex coming from the $c_{e\varphi}$ operator, the redefinition of the Yukawa coupling in Eq. (6.8), the top-loop diagram induced by the c_{et} operator and the proper counterterms.

The operator in Eq. (6.1) introduces a tree level coupling of the electron to the Higgs given by

$$g_{\bar{e}eh} = \frac{c_{e\varphi}v^2}{\Lambda^2\sqrt{2}} \tag{6.11}$$

After taking into account all contributions to the $\bar{e}eh$ vertex, it is possible to consider the Higgs decay to electrons [205] to extract a direct bound on our effective operator coefficients. We have

$$\left| -\frac{m_e}{v} + \frac{c_{e\varphi}(\mu)v^2}{\Lambda^2\sqrt{2}} - \frac{3}{(4\pi)^2}\frac{y_t}{\sqrt{2}}\frac{c_{et}}{\Lambda^2}(4m_t^2 - m_h^2)\left[f(m_h^2, m_t^2) + \log\frac{\mu^2}{m_t^2}\right]\right| \lesssim \kappa_e\frac{m_e}{v} \tag{6.12}$$

where the explicit form of $f(m_h^2, m_t^2)$ is given in Eq. (6.10). Recent LHC measurements provide a coefficient $\kappa_e^{\text{LHC}} \simeq 600$. This upper bound is expected to be improved at future lepton colliders by roughly two orders of magnitude ($\kappa_e = 10$), as shown in [205]. The operator in Eq. (6.1), besides modifying the $\bar{e}eh$ vertex, induces also an effective $\bar{e}ehh$ coupling given by

$$g_{\bar{e}ehh} = \frac{3c_{e\varphi}v}{2\Lambda^2\sqrt{2}} \tag{6.13}$$

which is not present in the SM. This operator contributes at tree level to $e^+e^- \to hh$, as shown in Fig. 6.5.
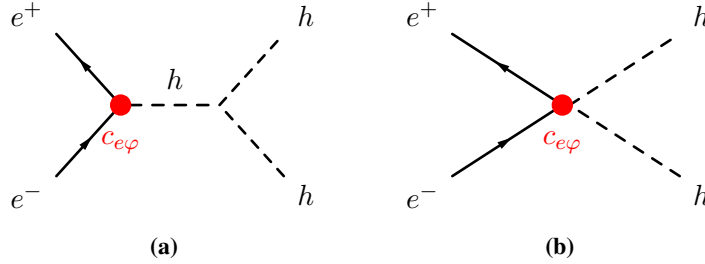
Figure 6.5: Tree level contribution to $e^+e^- \to hh$ coming from Eq. (6.1).

On the other hand, the operator in Eq. (6.2) contributes to $e^+e^- \to hh$ through the counterterm related to the redefinition of the Yukawa coupling of Eq. (6.8) and it also enters directly at one loop, as shown by the diagrams of Fig. 6.6.

Notice that the operator in Eq. (6.1) plays also the role of the counterterm needed to absorb the divergence produced by the one-loop insertion of the operator in Eq. (6.2) and its coefficient $c_{e\varphi}$ has to be formally taken as function of the renormalization scale μ. For the explicit derivation of the counterterm see the section 6.3 Therefore, in the process we are studying the coefficients $c_{e\varphi}$ and c_{et} are both formally evaluated at the scale $\mu = 2m_h$.

In our computation we consider just the leading contributions of the operator of Eq. (6.1) which arise at tree level while the contributions of the oper-
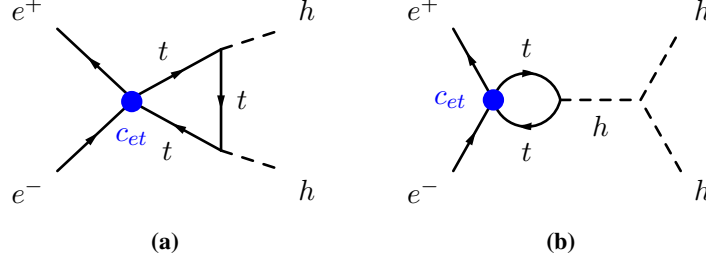
Figure 6.6: Loop level contributions $e^+e^- \to hh$ coming from Eq. (6.2)

ator of Eq. (6.2) comes at one loop. The total cross section turns out to be a pure quadratic function of the coefficients $c_{e\varphi}$, c_{et}, namely the only sizable new physics contributions are of order $c_{e\varphi}^2$, c_{et}^2 and $c_{e\varphi}c_{et}$ because linear terms coming from the interference between SM diagrams, which are helicity conserving, and new physics diagrams, which are helicity flipping, turns out to be proportional to m_e/v and therefore negligible. Helicity selection rules and non-interference effects in the context of dimension-six operators have been studied in [206]. Notice that the EFT expansion is under control because possible interference terms expected from dimension-eight operators which would give comparable contribution in term of the $1/\Lambda^4$ expansion are proportional to m_e/v as well.

6.3 Divergent $e^+e^- \to hh$ diagrams and counterterms

The one-loop diagrams (a) and (b) of Fig. 6.6 are proportional to c_{et} and UV divergent. The computation in dimensional regularization of the divergent part of these diagrams gives

$$
\begin{aligned}
\mathcal{M}^{(a)div} + \mathcal{M}^{(b)div} &= \frac{9}{(4\pi)^2}c_{et}2m_t\left(y_t^2 - \lambda\right)\left(1 + \frac{m_h^2}{s - m_h^2}\right)\frac{1}{\bar{\epsilon}}\bar{v}_e(p_2)u_e(p_1) \\
&+ \frac{9}{(4\pi)^2}c_{et}2m_t\lambda y_t^2\frac{v^2}{s - m_h^2}\frac{1}{\bar{\epsilon}}\bar{v}_e(p_2)u_e(p_1) \quad (6.14)
\end{aligned}
$$

where y_t is the top Yukawa, λ the Higgs self-coupling, u_e and v_e are the electron and positron Dirac spinors and $1/\bar{\epsilon} = 1/\epsilon - \gamma + \log 4\pi$. Let us now consider the counterterm diagrams proportional to $\delta c_{e\varphi}$ and δy_e needed to cancel

this divergence, as shown in diagrams (c), (d) and (e) of Fig. 6.7. We have that

$$
\begin{aligned}
\mathcal{M}^{(c)ct} + \mathcal{M}^{(d)ct} + \mathcal{M}^{(e)ct} &= -\frac{3\delta c_{e\varphi}}{\sqrt{2}}\upsilon \left(1 + \frac{m_h^2}{s - m_h^2}\right) \bar{v}_e(p_2)u_e(p_1) \\
&\quad + \frac{3\delta y_e}{\sqrt{2}\upsilon}\frac{m_h^2}{s - m_h^2}\bar{v}_e(p_2)u_e(p_1) \quad (6.15)
\end{aligned}
$$

By comparing Eq. (6.14) and (6.15) we obtain the explicit form of the counterterms in $\overline{\mathrm{MS}}$
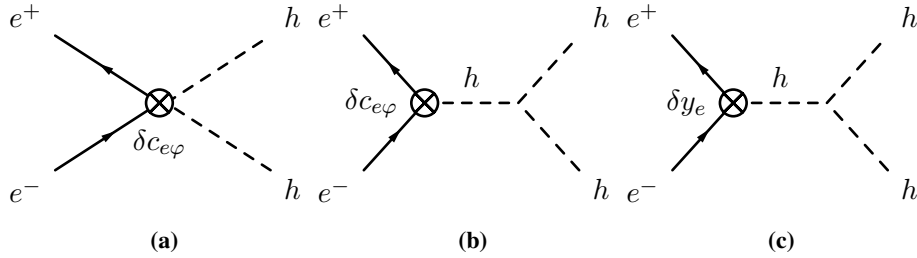
$$
\delta c_{e\varphi} = \frac{6}{(4\pi)^2}c_{et}y_t\left(y_t^2 - \lambda\right)\frac{1}{\bar{\epsilon}} \quad (6.16)
$$

$$
\delta y_e = -\frac{3}{(4\pi)^2}c_{et}\frac{\upsilon^2}{\Lambda^2}y_t^3\frac{1}{\bar{\epsilon}} \quad (6.17)
$$

where we have used $m_t = y_t\upsilon/\sqrt{2}$ and $m_h^2 = 2\lambda\upsilon^2$. From the explicit form of the counterterm $\delta c_{e\varphi}$ we can read off the contribution of c_{et} to the RG equation of $c_{e\varphi}$

$$
\mu\frac{\partial c_{e\varphi}}{\partial\mu} = \frac{12}{(4\pi)^2}c_{et}y_t\left(y_t^2 - \lambda\right) \quad (6.18)
$$

which agrees with [207] and [208].

Figure 6.7: Counterterm diagrams for $e^+e^- \to hh$.

6.4   Analysis and results

We compute the $e^+e^- \to hh$ cross section $\sigma = \sigma(\frac{c_{e\varphi}}{\Lambda^2}, \frac{c_{et}}{\Lambda^2})$ as function of the effective couplings as discussed in the previous section. In order to perform this calculation, we first implemented the effective lagrangian in FEYN-

RULES [209] and generate the corresponding FEYNARTS model output. We used FEYNARTS 3.10 [158] and FORMCALC 8.4 [159] to compute the tree and one-loop amplitudes relevant for the process in the chiral limit ($m_e = 0$). Finally, we use LOOPTOOLS [160] to compute numerically the cross section as a function of the center of mass energy and effective couplings. We further checked the cross section computation by means of the development version of NLOCT [210] and MadGraph5_aMC@NLO [156].

In order to extract the expected 95% CL limits on the effective operators couplings we assume the measured cross section to coincide with the SM predictions and we construct the following χ^2 function

$$\chi^2 = \chi^2\left(\frac{c_{e\varphi}}{\Lambda^2}, \frac{c_{et}}{\Lambda^2}\right) = \frac{\left[\sigma\left(\frac{c_{e\varphi}}{\Lambda^2}, \frac{c_{et}}{\Lambda^2}\right) - \sigma_{\text{SM}}\right]^2}{\delta\sigma^2} \tag{6.19}$$

where $\sigma_{\text{SM}} = \sigma(0,0)$. The total cross section uncertainty $\delta\sigma$ that enters in the χ^2 computation is given by the combination of the expected experimental $\delta\sigma_{\text{exp}}$ and theoretical uncertainties $\delta\sigma_{\text{th}}$. In our analysis we assume the theoretical uncertainty to be negligible such that the total uncertainty coincides with the expected experimental one, namely $\delta\sigma = \delta\sigma_{\text{exp}}$, which is given by the sum in quadrature of statistic $\delta\sigma_{\text{stat}}$ and systematic uncertainties $\delta\sigma_{\text{sys}}$

$$\delta\sigma = \sqrt{\delta\sigma_{\text{stat}}^2 + \delta\sigma_{\text{sys}}^2} = \sqrt{\frac{\sigma_{\text{SM}}}{\mathcal{L}} + \alpha^2 \sigma_{\text{SM}}^2}\,. \tag{6.20}$$

The statistical uncertainty is taken to be $\delta\sigma_{\text{stat}} = \sqrt{\sigma_{\text{SM}}/\mathcal{L}}$, where $\mathcal{L}$ is the integrated luminosity. This way to project the sensitivities follows the same procedure used in 5.5 and in Ref. [172]. Hence, the systematic uncertainty is given by $\delta\sigma_{\text{sys}} = \alpha\,\sigma_{\text{SM}}$. We take a conservative value and we fix $\alpha = 0.1$, which corresponds to a 10% error. However, the impact of the systematic uncertainty will be marginal since our total uncertainty turns out to be statistics dominated due to the expected smallness of the SM cross sections.

We consider different benchmark values of the center of mass energy and luminosity that have been proposed for the future e^+e^- machines (see Table 6.1) and for each configuration we determine 95% CL limits on the operator coefficients. Values of the coefficients for which $\chi^2 > 3.84$ are excluded.

To perform a more realistic investigation we have to consider a set of possible final states that are assumed to be measured at future e^+e^- colliders in order to reconstruct the Higgs particle through its decay channels. Once a set of final states $(f\bar{f})$ and the corresponding branching ratio $\text{BR}(h \to f\bar{f})$ have been identified, then we need to properly rescale the cross section and

uncertainty that enter in the chi-squared function of Eq. (6.19) by a factor $k = \text{BR}(h \to f_1 \bar{f}_1) \times \text{BR}(h \to f_2 \bar{f}_2)$. For instance, if we assume that each Higgs particle is going to be reconstructed only through its decay to $b\bar{b}$ then $k \sim 0.35$.

B	Exp.	$\sqrt{s}$ (GeV)	$\mathcal{L}$ (ab^{-1})	$\|c_{e\varphi}/\Lambda^2\|$(TeV^{-2})	$\|c_{et}/\Lambda^2\|$(TeV^{-2})
1	FCC-ee	350	2.6	< 0.003 (< 0.004)	< 0.116 (< 0.146)
2	CLIC	380	0.5	< 0.004 (< 0.006)	< 0.143 (< 0.184)
3	ILC	500	4	< 0.003 (< 0.004)	< 0.068 (< 0.083)
4	CLIC	1500	1.5	< 0.003 (< 0.003)	< 0.027 (< 0.035)
5	CLIC	3000	3.0	< 0.002 (< 0.002)	< 0.012 (< 0.015)

Table 6.1: Table of the different benchmark scenarios (B) considered in our analysis. Each benchmark consists of a specific value of the center of mass energy ($\sqrt{s}$) and luminosity ($\mathcal{L}$) that has been proposed for the future e^+e^- colliders. The last two columns represent the 95 % CL intervals for each operator coefficient taken individually in the analysis with $k = 1$ ($k = 0.35$).

The results for $k = 1$ ($k = 0.35$) in which each operator is considered individually are reported in the last two columns of Table 6.1. The table shows that all benchmark configurations considered in our study provide the same order of magnitude bound for the coefficient $c_{e\varphi}/\Lambda^2$, which is $|c_{e\varphi}/\Lambda^2| \lesssim 3 \times 10^{-3}$ TeV^{-2} for $k = 1$. This behaviour is expected since the contribution to the total cross section of the operator in Eq. (6.1) is almost insensitive to the energy in the process. Assuming an order one coefficient for $c_{e\varphi}$ implies a quite strong bound on the new physics scale of the order $\Lambda \gtrsim 18$ TeV. It is important to notice that this scale changes if other assumptions about the UV theory responsible for this kind of NP are made. For instance, in the context of minimal flavor violation models one expects $c_{e\varphi}$ to be naturally suppressed by the small electron Yukawa, namely $c_{e\varphi} = \tilde{c}_{e\varphi} y_e$ with $\tilde{c}_{e\varphi} \sim \mathcal{O}(1)$. In this case the bound on the new physics scale reduces to $\Lambda \gtrsim 30$ GeV, which is clearly outside the validity of EFT.

Assuming flavor universality in the dimension-six lepton Yukawa operators, namley $c_{e\varphi} = c_{\mu\varphi} = c_{\tau\varphi}$, it is possible to use recent LHC Higgs measurements to derive a bound on $c_{e\varphi}$ in this more constrained scenario [204]. In
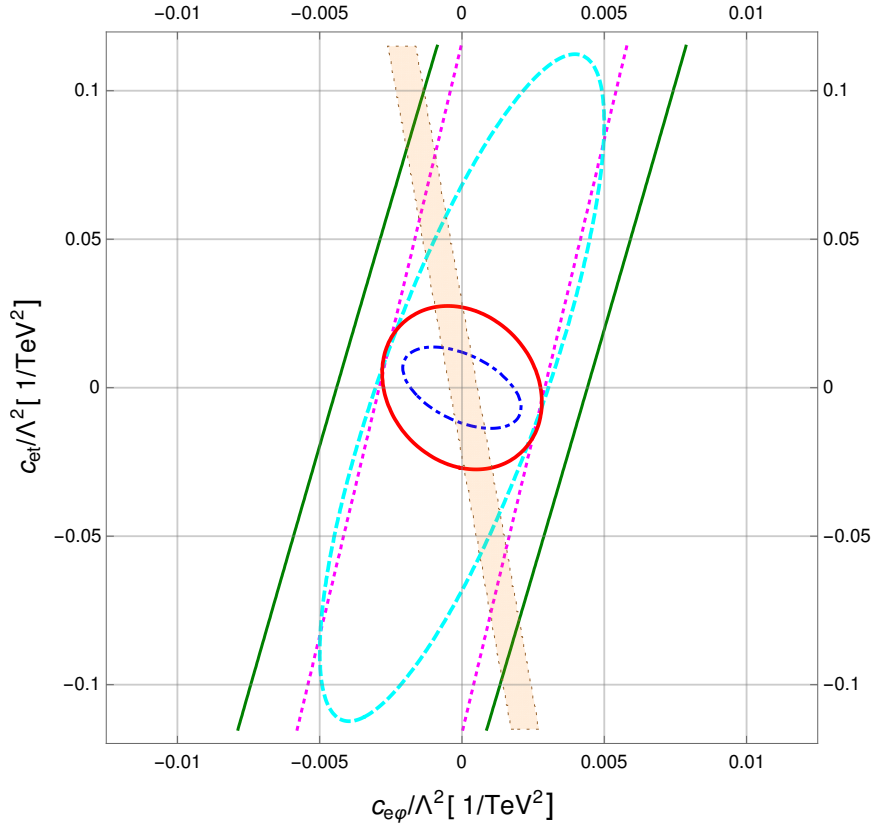
Figure 6.8: Exclusion regions in the $(c_{e\varphi}/\Lambda^2, c_{et}/\Lambda^2)$ plane for the different benchmark configurations of energy and luminosity reported in Table 6.1 in the case $k = 1$. Points that lie outside the ellipses are excluded at 95% CL. The light orange band represents the expected exclusion region obtained from Higgs decay measurements at future lepton colliders. The colors of the limits in the plot are as follows: B1 (magenta), B2 (green), B3 (cyan), B4 (red) and B5 (blue), with the benchmarks described in Table 6.1.

this case we have

$$\left|\frac{c_{e\varphi}}{\Lambda^2}\right| \lesssim 0.06 \text{ TeV}^{-2} \tag{6.21}$$

which is weaker than what we obtained from our analysis.

On the other hand, the bound on the coefficient c_{et}/Λ^2 turns out to be weaker than the bound on $c_{e\varphi}/\Lambda^2$. This is expected since the c_{et}/Λ^2 contribution enters at one-loop compared to $c_{e\varphi}/\Lambda^2$ which enters at tree level. Moreover, the bound depends on the benchmark configuration considered, because the contribution to the total cross section of the operator in Eq. (6.2) turns out to be quite sensitive to the energy of the process. Assuming an order one coefficient for c_{et} and $k = 1$, the weakest bound $|c_{et}/\Lambda^2| \lesssim 0.15 \text{ TeV}^{-2}$ is obtained from one of the benchmark configurations with lowest center of mass energy and luminosity and can be translated into $\Lambda \gtrsim 2.5$ TeV, while the strongest bound $|c_{et}/\Lambda^2| \lesssim 0.01 \text{ TeV}^{-2}$ is obtained from the benchmark configuration with highest center of mass energy and can be translated into $\Lambda \gtrsim 10$ TeV. The case $k = 0.35$ shows modifications of the bounds of the order of 25-50 % with respect to the $k = 1$ case. The fine tuning estimation on c_{et}/Λ^2 in Eq. (6.7) is one order of magnitude stronger than the best expected bound coming from our analysis, however one has to keep in mind that the fine tuning bound is based on theoretical considerations while our bound is based on experimental measurements. Moreover, the actual fine tuning could be milder thanks to cancellations induced by additional operators that we are not considering in our study.

The results for $k = 1$ in which both effective operator coefficients are taken into account are shown in Fig. 6.8. For each benchmark configuration, the exclusion region is represented by an ellipse. Points that lie outside the ellipse are considered excluded at 95% CL. By inspection of Fig. 6.8, we can infer that the best sensitivity is given by benchmark scenario number 5 which is characterized by the highest, among the considered configurations, center of mass energy of 3000 GeV. In Fig 6.8 we show also the expected exclusion region (light orange band) obtained from Higgs decay measurements at future lepton colliders in Eq. (6.12). This contribution is complementary and allows to improve the bounds we obtain just by considering $e^+e^- \to hh$.

The results for $k = 0.35$ are not presented since they differ from the results in Fig. 6.8 by $\sim 30\%$ and the corresponding ellipses do not present significant modifications.

6.5 Discussion

Double Higgs production at future e^+e^- colliders offers the possibility to explore the sensitivity to dimension-6 operators involving electrons that have not been constrained yet. The small SM cross section and the clean environment make this process an ideal laboratory for these studies. In particular, two operators are relevant for this process and are characterized by dimensionless Wilson coefficients $c_{e\varphi}$ and c_{et}. By including their contributions to the double Higgs cross section we derived 95% bounds based on several benchmarks for these future colliders under certain assumptions of final decay channels to be reconstructed and the errors. We found that the bounds on $c_{e\varphi}$ typically probe scales of $\mathcal{O}(10~\text{TeV})$ while the c_{et} operator is less constrained since it enters only at one-loop level. More stringent limits on c_{et}/Λ^2 of $\mathcal{O}(10^{-3})~\text{TeV}^{-2}$ can be obtained by studying top quark pair production at future e^+e^- colliders, as shown in [211], and using that result would give marginalized bounds on $c_{e\varphi}$ of the same order than the ones obtained in Table 6.1. In conclusion, searches for $e^+e^- \rightarrow hh$ should also be pursued in addition to the more traditional double Higgs production in double Higgsstrahlung and vector boson fusion in order to explore these possible new couplings.

Chapter 7

Sommerfeld Enhancement

The methodology in the search of new physics presented in previous chapters focuses on the effects of new particles at the high energy regions of the phase-space. As it has been discussed, the origin of this idea is that the unknown particles are heavier than the reach of our experiments. There is still the possibility of existing light particles which for some reason have escaped our detectors. Light mediators can have strong effects on the other end of the phase-space, in the non-relativistic region, known as Sommerfeld enhancement. This opens a window through which we can find new physics, and understand better possibly spurious deviations from the SM.

The Sommerfeld enhancement [212] in scattering amplitudes can be understood as the result of multiple exchanges of light mediators among either the initial or the final state particles in the process. This is a non-relativistic quantum mechanical effect that can be expressed as a deformation of the initial or final state wavefunctions induced by the interaction of the light mediators with the external states. This modification can be obtained by solving the Schrödinger equation with a potential term that results from the new interaction. Typically, these effects lead to significant enhancements in the cross-sections near the threshold due to non-perturbative effects. These effects can overcome phase space suppression, resulting in a finite cross-section even at the threshold.
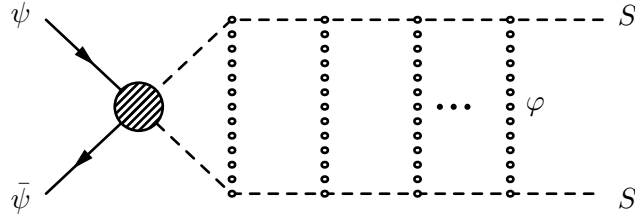
The first computation of the Sommerfeld enhancement due to the Coulomb interaction between final-state leptons was performed in [213]. Examples of Sommerfeld enhancement computations in S-wave dominated processes involving stable particles can be found in studies related to dark matter annihilation [214–217]. General results for arbitrary partial waves have been obtained in [218,219]. Examples of Sommerfeld enhancement computations in S-wave dominated processes involving unstable particles can be found in studies related to W^+W^- production [220]. Other interesting processes have significant P-wave contributions and involve unstable particles (like stop quarks) in

the final states. Sommerfeld enhancement studies for this kind of process have been performed in [221–224].

In addition to the processes aforementioned, the $t\bar{t}$ presents a reach structure in the non-relativistic regime with S-wave and P-wave contributions computed in the literature. In this case, the aspirations is that this regime can be better measured in $e^{+}e^{-}$ colliders where the observations are free of the QCD background. In particular, the FCC-ee proposal with a center of mass energy of $\sqrt{s} = 350$ GeV is appealing as it would run at the $t\bar{t}$ threshold-energy region. The NRQCD is a popular effective theory used to obtain the non-perturbative effects near threshold energy of the $t\bar{t}$. Finally, the double Higgs production in hadron colliders can be enhanced via the S-wave dominated process $gg \rightarrow hh$ [194, 225], while the process $e^{+}e^{-} \rightarrow hh$ studied in the chapter 6 is P-wave dominated.

The computation of the Sommerfeld enhancement for unstable particles in the final state uses Green's functions and the optical theorem. The finite width of unstable particles regulates an infrared divergence by damping the wave functions at large distances. However, it also introduces ultraviolet divergences in the usual procedure to compute the Sommerfeld enhancement for P-waves [221, 223, 226]. The reason is that for the P-wave, the enhancement is calculated from the Laplacian of the Green's function, which is divergent at the origin (short distance). This divergence is real for stable particles and S-wave processes with unstable particles, and hence it does not contribute to the cross-section. When considering unstable particles in P-wave processes, the width introduces a divergence in the imaginary part of the amplitude that contributes to the cross-section through the optical theorem. This ultraviolet divergence introduces a certain degree of arbitrariness in the computation of the Sommerfeld enhancement. This work aims to point to a solution to this problem by showing that this divergence can be absorbed by the usual counterterms in a renormalized quantum field theory, thereby eliminating ambiguities in the computations.

Along this chapter we briefly review the Sommerfeld enhancement effect in a 2-to-2 process due to the exchange of a light mediator in the final state. We consider the annihilation of a fermion-antifermion into two scalars as a concrete example. In section 7.2 we introduce the general formalism for the calculation of the enhancement in the presence of an unstable particle in the final state using the optical theorem. In section 7.3 we present the computation of the enhancement for a specific S-wave dominated process and we propose a procedure to deal with the UV divergences appearing in the calculation.

Figure 7.1: Sommerfeld enhancement in the process $\psi\bar{\psi} \to SS$ due to the mediation of the scalar φ.

In section 7.4 we present the computation of the enhancement for a specific P-wave dominated process. In this case, the divergences are imaginary and by applying our method we show how the renormalization procedure provides a finite unambiguous result. We discuss some of the differences between using our renormalization procedure and a finite cutoff in section 7.5. We summarize our findings in section 7.6. This chapter is based on the work published in Ref. [2].

7.1 Brief Review of Sommerfeld enhancement

The Sommerfeld enhancement for a 2-to-2 scattering process is due to the exchange of a light force carrier between the initial or final state particles and can be computed using two distinct methods. The first method, which is the way the effect was discovered, uses the computation of the wave function of the produced final state [217–219, 227]. The calculation of this wave function at the origin includes the non-perturbative information of the interaction potential and gives the enhancement factor of the scattering process. This approach is straightforward and uses basic quantum mechanics. The second method, instead, takes advantage of the optical theorem to relate the cross-section with the imaginary part of an amplitude where initial and final states are the same [228–230]. In this study, we adopt this second approach to use the full power of quantum field theory and tackle the divergences that arise in the computations.

To demonstrate our methodology, in this chapter we consider the annihilation of two fermionic particles ψ into two massive scalars S with mass m_S and width Γ_S [1]. We will further assume the existence of a light real scalar field φ which interacts exclusively with S in such a way that the cross-section of the process $\psi\bar{\psi} \to SS$ can be enhanced by the multiple exchanges of φ-particles

---

[1] In principle, the field S can be a complex scalar but for simplicity, we take it to be real.
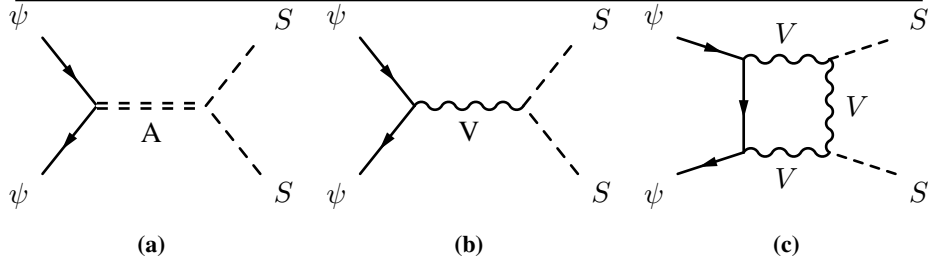
Figure 7.2: Examples of processes that are dominated by a single partial-wave: (a) S-wave dominated, (b) P-wave dominated at tree-level and (c) P-wave dominated at 1-loop.

between the two scalar particles in the final state, as shown in Fig. 7.1. In the non-relativistic limit, the ladder diagrams dominate and we can ignore the cross diagrams. We can define the enhancement of the cross-section in this process as:

$$\sigma(\psi\bar{\psi} \to SS) = \mathcal{S}(E)\,\sigma_0(\psi\bar{\psi} \to SS)\,, \tag{7.1}$$

where $\sigma_0(\psi\bar{\psi} \to SS)$ is the leading order cross-section and $\mathcal{S}(E)$ is the energy-dependent Sommerfeld enhancement factor. The computation of the enhancement factor $\mathcal{S}(E)$ depends on two important elements of the theory. The first one is the form of the φSS interaction vertex. It can be generic, but in this study, we assume a simple form that occurs in a plethora of different models, namely:

$$\mathcal{L}_{\text{int}} = \frac{\kappa}{2}\varphi S^2\,, \tag{7.2}$$

where κ is a dimensionful coupling constant. The second element is the leading order amplitude $\mathcal{M}_0(\psi\bar{\psi} \to SS)$ such that:

$$\sigma_0(\psi\bar{\psi} \to SS) \sim |\mathcal{M}_0(\psi\bar{\psi} \to SS)|^2. \tag{7.3}$$

The most general leading-order (off-shell) amplitude for the process $\psi(q_1)\bar{\psi}(q_2) \to S(p_1)S(p_2)$ can be written as:

$$\mathcal{M}_0(\psi\bar{\psi} \to SS) = \bar{v}(q_2)\Gamma_I u(q_1)F_0^I(q,p)\,, \tag{7.4}$$

where $q = q_1 + q_2 = p_1 + p_2 = \sqrt{s}$ is the center of mass energy and $\Gamma_I = 1, \gamma_\mu, \gamma_5, \gamma_\mu\gamma_5, \sigma_{\mu\nu}$ is an element of the Clifford space basis. By defining $p_1 = q/2 + p$, $p_2 = q/2 - p$ and using momentum conservation, we have that the

leading order form factor F_0^I is a function of three independent momenta: q_1, q and p. For simplicity, we just write $F_0^I(q, p)$.

At this point, we can expand the amplitude in partial waves as follows

$$\mathcal{M}_0 = 16\pi \sum_{l=0}^{\infty} (2l+1) P_l(\cos\theta) \mathcal{M}_0^l(s), \tag{7.5}$$

where s, t, u are the usual Mandelstam variables, $P_l(x)$ is the Legendre polynomial of order l and $\mathcal{M}_0^l$ is the l-th partial wave amplitude. Even though this expansion is not a necessary step for performing the Sommerfeld enhancement computation, it represents a very useful tool that simplifies the study of the enhancement in cases where only one partial wave dominates.

For instance, S-wave ($l = 0$) amplitudes can arise in renormalizable models where the $\psi\bar{\psi} \to SS$ process is mediated by the exchange of a scalar particle A with mass m_A in the s-channel (see Fig. 7.2a) and they can be written as:

$$\mathcal{M}_0^{\text{S-wave}}(\psi\bar{\psi} \to SS) \propto \frac{y_{\psi A}\kappa_{SA}}{q^2 - m_A^2} \bar{v}(q_2)u(q_1), \tag{7.6}$$

where $y_{\psi A}$ is the $\bar{\psi}\psi A$ Yukawa coupling and κ_{SA} is the trilinear ASS scalar coupling. One concrete occurrence of such amplitude is the tree-level Higgs pair production at muon colliders, which is dominated by the s-channel exchange of the Higgs itself and $y_{\psi A}$ is the lepton Yukawa coupling and κ_{SA} is the triple Higgs coupling λ_h.

An example of P-wave ($l = 1$) amplitude can arise in renormalizable models where we have a vector field V_μ with mass m_V which couples to ψ and S [2]. In this case, the $\psi\bar{\psi} \to SS$ process is mediated by the exchange of V_μ in the s-channel (see Fig. 7.2b) and the amplitude can be written as:

$$\mathcal{M}_0^{\text{P-wave}}(\psi\bar{\psi} \to SS) \propto \frac{g_\psi g_S}{q^2 - m_V^2} \bar{v}(q_2)\slashed{p}\, u(q_1), \tag{7.7}$$

where g_ψ and g_S are, respectively, the fermionic and the scalar gauge couplings. One concrete occurrence of such amplitude is the stop pair production at lepton colliders in the MSSM, where there is a photon exchange in the s-channel and g_ψ and g_S are the electromagnetic gauge couplings to leptons and stops [231].

There is also the possibility of having a P-wave-dominated process in models where the structure of the interactions is such that we have contributions to $\psi\bar{\psi} \to SS$ that come from diagrams involving the one-loop exchange of

---

[2] Notice that in this case S is charged and the final state will be $S\bar{S}$

vector bosons. For instance, if we consider a theory where a gauge field V_μ couples minimally to ψ (with vector and axial couplings) while S is a neutral scalar component which has a SVV coupling induced by a symmetry breaking mechanism, then we can write a box diagram (see Fig. 7.2c) which has the following amplitude:

$$\mathcal{M}_0^{\mathrm{P-wave}}(\psi\bar{\psi} \to SS) = F_0(q,p)\bar{v}(q_2)\slashed{p}\,u(q_1) + G_0(q,p)\bar{v}(q_2)\gamma_5\slashed{p}\,u(q_1)\,, \tag{7.8}$$

where F_0 and G_0 are one-loop structure functions. In general, these form factors are given in terms of complicated functions of momenta and masses but assume a simple form in the limit of heavy V_μ. The form of this amplitude is similar to the one obtained by considering the leading box diagrams in Higgs pair production at electron colliders, which involve W and Z bosons in the loop [232]. In general, the F_0 and G_0 form factors have additional p dependence which makes the enhancement calculation more complicated compared with the case of having form factors which are independent of p, as we highlight in the next section.

In this study we calculate the Sommerfeld enhancement for both S-wave and P-wave processes, focusing on two concrete examples where the leading order amplitude is generated by an effective $\psi\bar{\psi}SS$ interaction. More specifically, for the S-wave case, we use as a leading order amplitude the one in Eq. (7.6) computed in the limit of heavy A, while for the P-wave case we use Eq. (7.7) as the leading order amplitude in the limit of heavy V. Examining Eq. (7.6) and Eq. (7.7) we see that the calculation of the enhancement is actually independent of the presence of the mediator propagator in the s-channel and we can safely work in the limit where we integrate out this intermediate particle. The only difference is that using the renormalizable models one would have to consider $A/V \to SS$ as the initial process for the computation of the enhancement, while in the effective field theory limit we are working directly with the $\psi\bar{\psi}SS$ interaction. In general, working with non-renormalizable $\psi\bar{\psi}SS$ interactions can introduce additional problems. For instance, the $\psi\bar{\psi} \to SS$ cross-section could be divergent already when considering one single exchange of the φ particles in the final state, in a way that this quantity is no longer a prediction of the theory [233, 234] and needs to be renormalized by itself. This is not the case for the interactions we are consid-
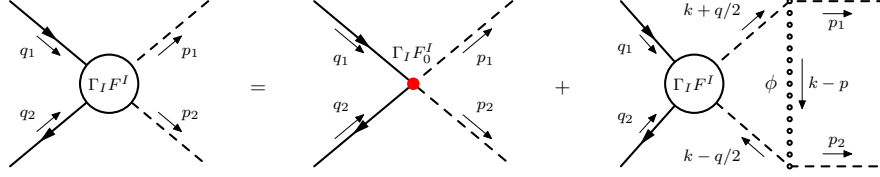
Figure 7.3: Recursion relation for the leading operator in the $\psi\bar{\psi} \to SS$ process. The red dot represents the leading interaction which in general can be momentum dependent.

ering in this chapter since there are no additional factors of momenta in the effective vertex. [3]

7.2   The enhancement factor $\mathcal{S}(E)$

The infinite series of ladder diagrams, representing the exchange of an increasing number of φ particles in the final state, can be re-summed by solving a recursion relation for the non-perturbative form factor $F^I(q, p)$. This recursion relation is shown diagrammatically in Fig. 7.3, and the corresponding equation is given by:

$$
\begin{aligned}
F^I(q,p) = &\, F_0^I(q,p) \\
&+ (i\kappa)^2 \int \frac{\mathrm{d}^4 k}{(2\pi)^4} \frac{i}{(k+\frac{q}{2})^2 - m_S^2 + im_S\Gamma_S} \frac{i}{(k-\frac{q}{2})^2 - m_S^2 + im_S\Gamma_S} \\
&\qquad\qquad\qquad \frac{i}{(k-p)^2 - m_\varphi^2} F^I(q,k) \, .
\end{aligned}
$$
(7.9)

In the non-relativistic limit, we have that

$$
q \to (2m_S + E, \vec{0}) \qquad \text{and} \qquad p \to (0, \vec{p}) \, ,
$$
(7.10)

where E is the non-relativistic energy of the final state system. Using these momenta approximations and performing the k_0 integral, the recursion relation

---

[3]However, there could be a problem when considering a generic effective operator which might introduce higher powers of p momenta in the $\psi\bar{\psi}SS$ vertex. In UV complete models this is not a problem because the renormalization occurs as usual.

in Eq. (7.9) reduces to (see Appendix B.1 for the derivation):

$$F^I(E, \vec{p}) = F_0^I(E, \vec{p}) - \frac{\kappa^2}{4m_S^2} \int \frac{\mathrm{d}^3 k}{(2\pi)^3} \frac{1}{E + i\Gamma_S - \frac{\vec{k}^2}{m_S}} \frac{1}{\left(\vec{k} - \vec{p}\right)^2 + m_\varphi^2} F^I(E, \vec{k}) \,.$$

(7.11)

Let us define the following function:

$$\tilde{G}^I(z, \vec{p}) = -\frac{1}{z - \frac{\vec{p}^2}{m_S}} F^I(E, \vec{p}) \,,$$

(7.12)

where $z = E + i\Gamma_S$. With the above definition, we can write the recursion relation in Eq. (7.11) as:

$$\left(\frac{\vec{p}^2}{m_S} - z \right) \tilde{G}^I(z, \vec{p}) = F_0^I(E, \vec{p}) + \int \frac{\mathrm{d}^3 k}{(2\pi)^3} \tilde{V}(\vec{k} - \vec{p}) \tilde{G}^I(z, \vec{k}) \,.$$

(7.13)

The quantity

$$\tilde{V}(\vec{p}) = -\frac{4\pi\alpha_\varphi}{\vec{p}^2 + m_\varphi^2}$$

(7.14)

is the Fourier transform of the Yukawa potential induced by the exchange of φ

$$V(\vec{r}) = -\alpha_\varphi \frac{e^{-m_\varphi r}}{r} \,,$$

(7.15)

where $r = |\vec{r}|$ and $\alpha_\varphi = \frac{\kappa^2}{16\pi m_S^2}$. At this point it is useful to define the position space representation of $\tilde{G}^I(z, \vec{p})$ as follows:

$$G^I(z, \vec{r}) = \int \frac{\mathrm{d}^3 p}{(2\pi)^3} \tilde{G}^I(z, \vec{p}) \, e^{i\vec{p}\cdot\vec{r}} \,.$$

(7.16)

Now we need to find the connection between $G^I(z, \vec{r})$ defined above and the $\psi\bar{\psi} \to SS$ cross-section. In order to do so, we consider the amplitude of the 2-to-2 scattering process $\psi\bar{\psi} \to \psi\bar{\psi}$, which is shown in Figure 7.4, and compute the total cross-section for $\psi\bar{\psi} \to SS$ by applying the optical theorem. We can write the amplitude $\mathcal{M}(\psi\bar{\psi} \to \psi\bar{\psi})$ as follows:

$$\mathcal{M}(\psi\bar{\psi} \to \psi\bar{\psi}) = \bar{v}(q_2)\Gamma_I u(q_1)\bar{u}(q_1)\Gamma_J v(q_2) I^{IJ}(q) \,,$$

(7.17)
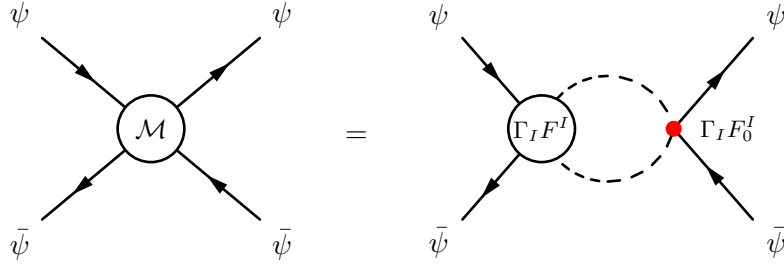
Figure 7.4: Recursion relation for $\bar{\psi}\psi \to \bar{\psi}\psi$ at all orders in the exchange of the light particles (contained in the effective Γ vertex).

where $I^{IJ}(q)$ is given by:

$$I^{IJ}(q) = -i \int \frac{\mathrm{d}^4k}{(2\pi)^4} F^I(q,k) \frac{1}{(k+\frac{q}{2})^2 - m_S^2 + im_S\Gamma_S}$$
$$\frac{1}{(k-\frac{q}{2})^2 - m_S^2 + im_S\Gamma_S} F_0^J(q,k)\,.$$
$$(7.18)$$

In the non-relativistic limit, the quantity $I^{IJ}(q)$ can be written in terms of the leading order form factor F_0^J and the function $\tilde{G}^I(z,\vec{k})$ defined in Eq. (7.12). We have:

$$I^{IJ}(E) = \frac{1}{4m_S^2} \int \frac{\mathrm{d}^3k}{(2\pi)^3} F_0^J(E,\vec{k})\tilde{G}^I(z,\vec{k}) = \frac{1}{4m_S^2}\mathcal{O}^J G^I(z,\vec{r})\bigg|_{\vec{r}=0}\,.$$
$$(7.19)$$

The quantity $I^{IJ}(E)$ is just the Fourier transform of $F_0^J(E,\vec{k})\tilde{G}^I(z,\vec{k})$ evaluated at $\vec{r}=0$. Notice that, after performing the Fourier transform, the form factor $F_0^J(E,\vec{k})$ becomes a differential operator in position space, that we denoted by $\mathcal{O}^J$, which acts on $G^I(z,\vec{r})$. This quantity is in general divergent[4]: the divergences can be real and imaginary. However, only imaginary divergences are problematic for the computation of the enhancement, as we will see in the following.

---

[4]The Fourier transform at $\vec{r} \neq 0$ acts as regulator for the divergent quantity $I^{IJ}(E)$. In this case, the divergences are represented as singular terms for $\vec{r} \to 0$.

Let us compute the total cross section for $\psi\bar{\psi} \to SS$ by applying the optical theorem:

$$
\begin{aligned}
s\sigma(\bar{\psi}\psi \to SS) &= \mathrm{Im} \sum_{\mathrm{spins}} \mathcal{M}(\bar{\psi}\psi \to \bar{\psi}\psi) \\
&= \mathrm{Im} \sum_{\mathrm{spins}} \bar{v}(q_2)\Gamma_I u(q_1)\bar{u}(q_1)\Gamma_J v(q_2) I^{IJ}(q)
\end{aligned}
\tag{7.20}
$$

In the non-relativistic limit, we can write

$$
\sigma^{\mathrm{NR}}(\bar{\psi}\psi \to SS) = \frac{1}{s} g_{IJ} \, \mathrm{Im} \, I^{IJ}(E)
\tag{7.21}
$$

where $g_{IJ} = \mathrm{Tr}\big(\Gamma_I q\!\!\!/_1 \Gamma_J q\!\!\!/_2\big)$ is a real quantity. We should point out that there are subtleties in using the optical theorem with unstable particles in internal lines. We discuss this issue in Appendix B.2, where we show that the usual Cutkosky rules apply with good approximation when the widths are narrow compared to the particle's mass. Using Eq. (7.19) and Eq. (7.21) we can write the Sommerfeld enhancement factor as follows:

$$
\mathcal{S}(E) = \frac{\sigma^{\mathrm{NR}}(\psi\bar{\psi} \to SS)}{\sigma_0^{\mathrm{NR}}(\psi\bar{\psi} \to SS)} = \frac{g_{IJ} \, \mathrm{Im} \, \mathcal{O}^J G^I(z,\vec{r})\big|_{\vec{r}=0}}{g_{IJ} \, \mathrm{Im} \, \mathcal{O}^J G_0^I(z,\vec{r})\big|_{\vec{r}=0}},
\tag{7.22}
$$

where $G_0^I(z,\vec{r})$ is the Fourier transform of the function defined in Eq. (7.12) computed in the free case, namely for $\alpha_\varphi = 0$. The specific form of the enhancement factor defined in Eq. (7.22) is computed in the following sections for different types of interactions (S-wave and P-wave) and depending on the form of the interaction, the quantity $I^{IJ}(E) \sim \mathcal{O}^J G^I(z,\vec{r})\big|_{\vec{r}=0}$ presents imaginary divergences which need to be renormalized to provide a finite result.

7.3   S-wave Sommerfeld enhancement

In this section, we study the enhancement of an S-wave process. In this case, the divergences appearing in the computation of $I^{IJ}(E)$ in Eq. (7.19) are real [228–230] even when the width of S is non-zero (unstable final-state particles). Therefore, the computation of the total cross-section in Eq. (7.21) is unaffected by the presence of divergent terms. Here we will compute those divergences in any case because they will help us understand the origin of

imaginary divergences occurring in the P-wave case that directly affect the enhancement calculation and will be discussed in the next section.

Let us consider an effective dimension-5 operator $(\bar{\psi}\psi SS)$ that gives the following S-wave leading order amplitude for $\psi\bar{\psi} \to SS$:

$$\mathcal{M}_0^{\text{S-wave}} = \lambda_0 \bar{v}(q_2) u(q_1) \,, \tag{7.23}$$

where λ_0 is a real dimensionful coupling constant. The same amplidude [5] can be derived from Eq. (7.6) in the limit of very heavy A and in this case $\lambda_0 = -y_{\psi A}\kappa_{SA}/m_A^2$. By comparing Eq. (7.23) with the most general parametrization of the amplitude in Eq. (7.4) we have that

$$\Gamma_I = \mathbf{1} \qquad \text{and} \qquad F_0^I(q, p) = \lambda_0 \,. \tag{7.24}$$

Using these definitions together with Eq. (7.11), we can write the following recursion relation for the non-perturbative form factor $F(E, \vec{p})$ in the non-relativistic limit:

$$F(E, \vec{p}) = \lambda_0 + \int \frac{\mathrm{d}^3 k}{(2\pi)^3} \tilde{V}(\vec{k} - \vec{p}) F(E, \vec{k}) \frac{1}{z - \frac{\vec{k}^2}{m_S}} \,, \tag{7.25}$$

where $\tilde{V}(\vec{k} - \vec{p})$ has been defined in Eq. (7.14). At this point, it is convenient to define the Green's function in momentum space as follows[6]:

$$\tilde{G}(z, \vec{k}) = -\frac{1}{z - \frac{\vec{k}^2}{m_S}} \frac{F(E, \vec{k})}{\lambda_0} \,, \tag{7.26}$$

such that the Fourier transform of Eq. (7.25) becomes the familiar Schrödinger equation:

$$\left[-\frac{\nabla^2}{m_S} - z + V(\vec{r}) \right] G(z, \vec{r}) = \delta^3(\vec{r}) \,. \tag{7.27}$$

where $V(\vec{r})$ is the Yukawa potential defined in Eq. (7.15). The function $G(z, \vec{r})$ is the Fourier transform of Eq. (7.26) and can be interpreted as the standard Schrödinger Green's function $G(z, \vec{r}, \vec{r}')$, evaluated at $\vec{r}' = 0$. The next step is to use the optical theorem to find the relation between the cross-section and

---

[5] As already said, the Sommerfeld enhancement computed with Eq. (7.23) will be identical to the one computed with Eq. (7.6).

[6] In this case the $F_0^I = \lambda_0$ is constant and we can divide the equation by it to simplify the calculation.

the imaginary part of the Green's function. We can start from Eq. (7.19) and write the integral as:

$$I(E) = \frac{\lambda_0^2}{4m_S^2} \int \frac{\mathrm{d}^3 k}{(2\pi)^3} \tilde{G}(z, \vec{k}) = \frac{\lambda_0^2}{4m_S^2} G(z, \vec{r}) \Big|_{\vec{r}=0}. \tag{7.28}$$

Notice that the integral $I(E)$ is simply given by the Green's function $G(z, \vec{r})$ evaluated at $\vec{r} = 0$. Therefore, the optical theorem in Eq. (7.21) can be written as:

$$\sigma(\bar{\psi}\psi \to SS) = \frac{1}{s} \mathrm{Tr}\left(\not{q}_2 \not{q}_1\right) \mathrm{Im}\, I(E) = \frac{1}{s} \mathrm{Tr}\left(\not{q}_2 \not{q}_1\right) \frac{\lambda_0^2}{4m_S^2} \mathrm{Im}\, G(z, \vec{r}) \Big|_{\vec{r}=0} \tag{7.29}$$

The Sommerfeld enhancement factor in Eq. (7.22) is given by:

$$\mathcal{S}(E) = \frac{\mathrm{Im}\, G(z, \vec{r})|_{\vec{r}=0}}{\mathrm{Im}\, G_0(z, \vec{r})|_{\vec{r}=0}}. \tag{7.30}$$

From now on we will consider the limit $m_\varphi \to 0$. In this limit, the Yukawa potential in Eq. (7.15) becomes the Coulomb potential and Eq. (7.27) admits an analytic solution [235]. To identify the divergent terms of $I(E) \sim G(z, \vec{r}) \Big|_{\vec{r}=0}$ we take the analytic Coulomb Green's function $G(z, \vec{r}, \vec{r}')$ [235] evaluated at $\vec{r}' = 0$ and expand it around $\vec{r} = 0$. Therefore we get:

$$I^{\mathrm{div}}(E) = \frac{\lambda_0^2}{4m_S^2} \left(\frac{m_S}{4\pi r} + \frac{m_S^2 \alpha_\varphi}{4\pi} \log(r) \right) \Bigg|_{\vec{r}=0}. \tag{7.31}$$

We can see that the divergent terms of the Coulomb Green's function at $\vec{r} = 0$ are real and they do not affect the computation of the enhancement factor in Eq. (7.30) which involves only the imaginary part of $G(z, \vec{r})|_{\vec{r}=0}$. Nevertheless, it is very instructive to analyze the origin of these divergences. In order to do this, let us use Eq. (7.25) and Eq. (7.26) to solve Eq. (7.28) by expanding the recursion relation for $F(E, \vec{k})$ in powers of α_φ. We can write

$$I(E) = I_0(E) + I_1(E) + \ldots + I_n(E) + \ldots, \tag{7.32}$$

where $I_n(E) = I_n^{\mathrm{finite}}(E) + I_n^{\mathrm{div}}(E)$ contains terms of order α_φ^n. Here we compute the first two terms of the series in Eq. (7.32) and identify the divergent pieces. These quantities, $I_0(E)$ and $I_1(E)$, represent the non-relativistic limit of the loop integrals shown in Fig. 7.5a and Fig. 7.5b, respectively. The first

(a) (b)
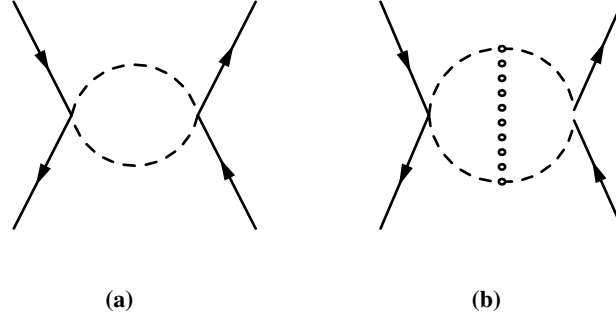
Figure 7.5: Feynman diagrams corresponding to the first two terms in the expansion of $I(E)$ in powers of α_φ.

integral is

$$I_0(E) = \frac{\lambda_0^2}{4m_S^2} \int \frac{\mathrm{d}^3 k}{(2\pi)^3} \frac{1}{\frac{\vec{k}^2}{m_S} - z} = \frac{\lambda_0^2}{4m_S^2} G_0(z, \vec{r}) \bigg|_{\vec{r}=0}, \qquad (7.33)$$

where $G_0(z, \vec{r})$ is the free Green's function which is given by

$$G_0(z, \vec{r}) = \frac{m_S}{4\pi r} e^{i\sqrt{m_S z} r}. \qquad (7.34)$$

Expanding around $\vec{r} = 0$ we identify the following divergent contribution

$$I_0^{\mathrm{div}}(E) = \frac{\lambda_0^2}{4m_S^2} \left(\frac{m_S}{4\pi r}\right) \bigg|_{\vec{r}=0}, \qquad (7.35)$$

which coincides with the first term of Eq. (7.31). The second integral of the expansion is

$$I_1(E) = -\frac{\lambda_0^2}{4m_S^2} \int \frac{\mathrm{d}^3 k}{(2\pi)^3} \frac{1}{\frac{\vec{k}^2}{m_S} - z} \int \frac{\mathrm{d}^3 k'}{(2\pi)^3} \frac{4\pi\alpha_\varphi}{(\vec{k'} - \vec{k})^2} \frac{1}{\frac{\vec{k'}^2}{m_S} - z}. \qquad (7.36)$$

The position space representation can be done by integrating one of the momenta and doing the Fourier transform of what survives in the large momenta region. Expanding around $\vec{r} = 0$ we identify the following divergent contribution (see Appendix B.3):

$$I_1^{\mathrm{div}}(E) = \frac{\lambda_0^2}{4m_S^2} \frac{m_S^2 \alpha_\varphi}{4\pi} \log(r), \qquad (7.37)$$

which coincides with the second term of Eq. (7.31). All the $I_n(E)$ integrals, with $n \geq 2$, are finite. Therefore, in the ladder approximation, we have that the

UV divergences appearing in the computation of $\mathcal{M}(\psi\bar{\psi} \to \psi\bar{\psi})$ in the non-relativistic limit are two-loop exact, namely $I^{\mathrm{div}}(E) = I_0^{\mathrm{div}}(E) + I_1^{\mathrm{div}}(E)$. The $\bar{\psi}\psi \to \bar{\psi}\psi$ amplitude can be simply renormalized by introducing the following counterterm

$$\bar{v}_s(q_2)u_r(q_1)\bar{u}_r(q_1')v_r(q_2')\delta I_{CT} \,, \tag{7.38}$$

with δI_{CT} equal to $-I^{\mathrm{div}}(E)$ given by Eq. (7.31). Notice that this counterterm looks non-renormalizable because we considered a non-renormalizable interaction to start with. On the other hand, in a renormalizable model, where there is another particle in the s-channel that mediates the interaction between ψ and S, the counter term would enter in the renormalization of that particle's self-energy. The counterterm in Eq. (7.38) cancels all the divergences appearing in the non-relativistic limit in the ladder approximation in the $\psi\bar{\psi} \to \psi\bar{\psi}$ process, which are directly related to $G(z, \vec{r})\big|_{\vec{r}=0}$. To compute the Sommerfeld enhancement, one can start directly with the Green's function and remove all the imaginary divergent terms there. In the S-wave case, because these divergences are real, it is safe to ignore them for the computation of the enhancement. The picture changes when considering a P-wave-dominated process, as we will show in the next section.

Notice that we are using a position space regularization scheme, which is not the one usually implemented in standard quantum field theory calculations. If one wants to compute, in addition to the enhancement, other observables of the theory, then the same regularization scheme needs to be implemented. This means that one would need to compute the Green's function in dimensional regularization [236, 237] or use the position space regularization scheme for the computation of the observables.

7.4 P-wave Sommerfeld enhancement

In the previous section, we saw that no imaginary divergences are affecting the computation of the S-wave enhancement. On the other hand, for the P-wave case, the situation is different and imaginary divergences appear. The Sommerfeld enhancement in P-wave dominated processes was studied in [221, 223, 238]. There are different forms of P-wave-dominated amplitudes one can write down but all of them have the property of being proportional to the velocity of the final state system in the region close to the threshold.

In this section we consider an effective dimension-6 operator ($\bar{\psi}\gamma^\mu\psi S\partial_\mu S$) that gives the following P-wave leading order amplitude for $\psi\bar{\psi} \to SS$:

$$\mathcal{M}_0^{\text{P-wave}} = F_0\bar{v}(q_2)\slashed{p}u(q_1)\,, \tag{7.39}$$

where F_0 is a real dimensionful coupling constant. We choose this form of interaction because it is the most simple example of a P-wave process and can occur in different models. For instance, the same amplitude can be derived from Eq. (7.7) in the limit of very heavy V and in this case $F_0 = -g_\psi g_S/m_V^2$. By comparing Eq. (7.39) with the most general parametrization of the amplitude in Eq. (7.4) we have that

$$\Gamma_I = \gamma^\mu \qquad \text{and} \qquad F_0^I(q, p) = p_\mu F_0\,. \tag{7.40}$$

Using these definitions together with Eq. (7.11), we can write the following recursion relation for the non-perturbative form factor $F^i(z, \vec{p})$ [7] in the non-relativistic limit:

$$F^i(z, \vec{p}) = p^i F_0 + \int \frac{\mathrm{d}^3k}{(2\pi)^3} \tilde{V}(\vec{k} - \vec{p})F^i(z, \vec{k})\frac{1}{z - \frac{\vec{k}^2}{m_S}}\,, \tag{7.41}$$

where $\tilde{V}(\vec{k} - \vec{p})$ has been defined in Eq. (7.14). In analogy to the S-wave case, it is convenient to define:

$$\tilde{G}^i(z, \vec{k}) = -\frac{1}{z - \frac{\vec{k}^2}{m_S}}\frac{F^i(z, \vec{k})}{F_0} \equiv k^i\tilde{G}(z, \vec{k})\,, \tag{7.42}$$

where the in the last equality we have used the fact that $F^i(z, \vec{p}) \sim p^i$, since p^i is the only vector we have at our disposal to construct a covariant expression for $F^i(z, \vec{p})$. With this definition, the position space representation of Eq. (7.41) becomes:

$$\left[-\frac{\nabla^2}{m_S} - z + V(\vec{r})\right]\partial_i G(z, \vec{r}) = \partial_i\delta^3(\vec{r})\,, \tag{7.43}$$

where $V(\vec{r})$ is the Yukawa potential defined in Eq. (7.15) and $G(z, \vec{r})$ is the Fourier transform of $\tilde{G}(z, \vec{k})$ defined in Eq. (7.42). Let us show that $G(z, \vec{r})$ can be taken to be the standard Schrödinger Green's function $G(z, \vec{r}, \vec{r}')$ that

---

[7]Because we are using effective interactions, it could be that $F^i(z, \vec{p})$ is also divergent. This divergence would spoil the predictability of the process and is something to be careful of in a general model. In our case, the amplitude is finite and we do not have this specific problem.

solves

$$\left[-\frac{\nabla^2}{m_S} - z + V(r) \right] G(z, \vec{r}, \vec{r}') = \delta^3(\vec{r} - \vec{r}') \,, \tag{7.44}$$

evaluated at $\vec{r}' = 0$. In order to do this, let us take Eq. (7.44) and act with $-\partial_i'$ on both sides:

$$\left[-\frac{\nabla^2}{m_S} - z + V(r) \right] \left(-\partial_i' G(z, \vec{r}, \vec{r}') \right) = -\partial_i' \delta^3(\vec{r} - \vec{r}') \,. \tag{7.45}$$

Using the fact that $\partial_i' G(z, \vec{r}, \vec{r}') = -\partial_i G(z, \vec{r}, \vec{r}')$ and substituting this relation back into Eq. (7.45), it is possible to show that we recover Eq. (7.43) after taking $\vec{r}' \to 0$. Therefore, the Green's function equation we need to solve here is the same as the one we encountered in the S-wave case. The difference appears when expressing the cross-section in terms of the Green's function, using the optical theorem. To show this let us start from Eq. (7.19) and write the integral as

$$I^{ij}(E) = \frac{F_0^2}{4m_S^2} \int \frac{\mathrm{d}^3 k}{(2\pi)^3} k^j \tilde{G}^i(z, \vec{k}) = \frac{F_0^2}{4m_S^2} \int \frac{\mathrm{d}^3 k}{(2\pi)^3} k^i k^j \tilde{G}(z, \vec{k}) \,, \tag{7.46}$$

where in the second equality we used Eq. (7.42). Thanks to the symmetry properties of the integrand, we can replace $k^i k^j \to \delta^{ij} k^2/3$ inside the second integral of Eq. (7.46). In this way we obtain:

$$I^{ij}(E) = \frac{F_0^2}{12m_S^2} \delta^{ij} \int \frac{\mathrm{d}^3 k}{(2\pi)^3} k^2 \tilde{G}(z, \vec{k}) = -\frac{F_0^2}{12m_S^2} \delta^{ij} \nabla^2 G(z, \vec{r}) \Big|_{\vec{r}=0} \,. \tag{7.47}$$

Notice that the integral $I^{ij}(E) = \delta^{ij} I(E)$ is simply given in terms of the Laplacian of the Green's function that solves Eq. (7.44) evaluated at $\vec{r} = \vec{r}' = 0$. The optical theorem in Eq. (7.21) can be written as:

$$\begin{aligned}
\sigma(\bar{\psi}\psi \to SS) &= \frac{1}{s} \mathrm{Tr}\left(\slashed{q}_2 \gamma_i \slashed{q}_1 \gamma_j \right) \delta^{ij} \,\mathrm{Im}\, I(E) \\
&= -\frac{F_0^2}{12m_S^2} \frac{1}{s} \mathrm{Tr}\left(\slashed{q}_2 \gamma_i \slashed{q}_1 \gamma^i \right) \mathrm{Im}\, \nabla^2 G(z, \vec{r}) \Big|_{\vec{r}=0} \,.
\end{aligned} \tag{7.48}$$

In the P-wave enhancement calculation, differently than the S-wave case, the total cross section is given in terms of the Laplacian of $G(z, \vec{r})$ and the Som-

merfeld enhancement factor $\mathcal{S}(E)$ can be written as:

$$S(E) = \frac{\text{Im } \nabla^2 G(z, \vec{r})\big|_{\vec{r}=0}}{\text{Im } \nabla^2 G_0(z, \vec{r})\big|_{\vec{r}=0}}. \quad (7.49)$$

Let us compute $I^{ij}(E) = \delta^{ij} I(E) \sim \delta^{ij} \nabla^2 G(z, \vec{r})\big|_{\vec{r}=0}$ perturbatively in α_φ and identify the divergent terms. In order to do this we use Eq. (7.41) and Eq. (7.42) to solve Eq. (7.46) by expanding the recursion relation for $F^i(z, \vec{k})$ in powers of α_φ. We can write

$$I^{ij}(E) = \delta^{ij} \left(I_0(E) + I_1(E) + \ldots + I_n(E) + \ldots \right), \quad (7.50)$$

where $I_n(E)$ contains terms of order α_φ^n. Let us consider the first two integrals of the expansion, namely $I_0(E)$ and $I_1(E)$. They are UV divergent and represent the non-relativistic limit of the loop integrals shown in Fig. 7.5a and Fig. 7.5b, respectively. The divergences of the Green function are then matched order by order in the perturbative expansion.

The first integral is:

$$I_0(E) = \frac{F_0^2}{12m_S^2} \int \frac{\mathrm{d}^3 k}{(2\pi)^3} \vec{k}^2 \frac{1}{\frac{\vec{k}^2}{m_S} - z} = -\frac{F_0^2}{12m_S^2} \nabla^2 G_0(z, \vec{r})\bigg|_{\vec{r}=0}, \quad (7.51)$$

where $G_0(z, \vec{r})$ is the free Green's function given by Eq. (7.34). Expanding around $\vec{r} = 0$ we identify the following $1/r$ divergent contribution:

$$I_0^{\text{div}}(E) = \frac{F_0^2}{12m_S^2} \frac{m_S^2 z}{4\pi r}\bigg|_{\vec{r}=0}. \quad (7.52)$$

Notice that, in this case, the imaginary part of the $1/r$ divergence is non-zero for finite width, namely for $\Gamma_S \neq 0$. The second integral of the expansion is:

$$I_1 = -\frac{F_0^2 \alpha_\varphi \pi}{3m_S^2} \int \frac{\mathrm{d}^3 k}{(2\pi)^3} \frac{\mathrm{d}^3 l}{(2\pi)^3} (k \cdot l) \frac{1}{z - \frac{\vec{k}^2}{m_S}} \frac{1}{(\vec{k} - \vec{l})^2 + m_\varphi^2} \frac{1}{z - \frac{\vec{l}^2}{m_S}}. \quad (7.53)$$

This integral is UV divergent and it can be regularized by taking the Fourier transforms for a generic $\vec{r} \neq 0$. Then, expanding around $\vec{r} = 0$, it is possible to identify the following divergent contributions (see Appendix B.4):

$$I_1^{\text{div}}(E) = \frac{F_0^2}{12m_S^2} \alpha_\varphi \left(-\frac{m_S^2}{8\pi} \frac{1}{r^2} + \frac{m_S^3 z}{4\pi} \log r \right)\bigg|_{\vec{r}=0} \quad (7.54)$$

Notice that, in this case, we have a new real $1/r^2$ divergence and the imaginary part of the $\log r$ divergence is non-zero for finite width, namely for $\Gamma_S \neq 0$. Contrary to the S-wave case, we have that the UV divergences appearing in the computation of $\mathcal{M}(\psi\bar{\psi} \to \psi\bar{\psi})$ in the non-relativistic limit are not two-loop exact. Indeed, in the P-wave case, additional divergent contributions are coming from higher loops. However, it is possible to show that these divergent terms can only be of the form $1/r^2$, $1/r$ and $\log r$, and no new r dependence appears. To do this, let us consider the $n + 1$-loop expression:

$$I_n(E) = -\frac{F_0^2 \pi^n \alpha_\varphi^n}{3m_S^2} \int \frac{\mathrm{d}^3 k_1}{(2\pi)^3} \frac{\mathrm{d}^3 k_2}{(2\pi)^3} \cdots \frac{\mathrm{d}^3 k_n}{(2\pi)^3} k_1 \cdot k_n \frac{1}{z - \frac{\vec{k}_1^2}{m_S}} \frac{1}{(\vec{k}_1 - \vec{k}_2)^2 + m_\varphi^2}$$

$$\frac{1}{z - \frac{\vec{k}_2^2}{m_S}} \frac{1}{(\vec{k}_2 - \vec{k}_3)^2 + m_\varphi^2} \frac{1}{z - \frac{\vec{k}_3^2}{m_S}} \cdots \frac{1}{(\vec{k}_{n-1} - \vec{k}_n)^2 + m_\varphi^2} \frac{1}{z - \frac{\vec{k}_n^2}{m_S}} .$$

$$(7.55)$$

By inspecting the integrand, one can see that the divergences come from the k_1 and k_n integration, every other integral in between is finite. Therefore, the divergences have the same functional form as the one-loop $I_0(E)$ and two-loop $I_1(E)$ case. We can write

$$I^{\mathrm{div}}(E) = \frac{A}{r^2} + \frac{B}{r} + C \log r \qquad (7.56)$$

where A, B and C are complex coefficients that can be written as a series in α_φ. Since $I(E) \sim \nabla^2 G(z, \vec{r})\big|_{\vec{r}=0}$, the all-order expression of these coefficients can be obtained by considering the Laplacian of the Coulomb Green's function $G(z, \vec{r}, \vec{r}')$ [235] evaluated at $\vec{r}' = 0$ and expand it around $\vec{r} = 0$. The terms in Eq. (7.52) and Eq. (7.54) are recovered by expanding the full result to $\mathcal{O}(\alpha_\varphi)$. The $\bar{\psi}\psi \to \bar{\psi}\psi$ amplitude can be simply renormalized by introducing the following counterterm

$$\bar{v}_s(q_2)\gamma_i u_r(q_1)\bar{u}_r(q_1')\gamma_i v_r(q_2')\delta I_{CT} , \qquad (7.57)$$

with δI_{CT} equal to $-I^{\mathrm{div}}(E)$ given by Eq. (7.56). The counterterm in Eq. (7.57) cancels all the divergences appearing in the non-relativistic limit in the ladder approximation in the $\psi\bar{\psi} \to \psi\bar{\psi}$ process, which are directly related to $\nabla^2 G(z, \vec{r})\big|_{\vec{r}=0}$. In order to compute the Sommerfeld enhancement, one can start directly with the Laplacian of Green's function and remove all the divergent imaginary terms there. In the P-wave case, these divergences have an

imaginary part(proportional to the width Γ_S) and therefore this procedure is crucial to obtaining a finite result.

As an example of the application of this method, we perform the computation of the Sommerfeld enhancement for some specific values of the parameters as a function of the energy E. In Figure 7.6a we show the behavior of the Sommerfeld enhancement factor as function of the energy $E < 0$ (below threshold region), computed for $\alpha_\varphi = 1$, $m_S = 125$ GeV and $\Gamma_S = 0.001$ GeV. In Figure 7.6b we show the same behavior computed for $\alpha_\varphi = 1$, $m_S = 125$ GeV and $\Gamma_S = 1$ GeV. From these two plots, we can see that the finite S width has the effect of smearing out the delta function spikes associated with the energy levels of the SS bound state and this effect is more visible when increasing the width value, Figure 7.6b. Notice that going to larger widths makes the calculation breakdown because of unitarity violations, as discussed in Appendix B.2. In Figure 7.7 we show the behavior of the Sommerfeld enhancement factor as function of the energy $E > 0$ (above threshold region), computed for $\alpha_\varphi = 1$, $m_S = 125$ GeV and two different non-zero values of Γ_S which are taken to be 0.001 and 1 GeV, and we compare it with the $\Gamma_S = 0$ literature result [218]. For $E > 0$, we have that the finite width effects are small compared to $\Gamma_S = 0$ case (less than 10%).

7.5 Discussion

Now that the source of the divergence in the Sommerfeld calculation is clear, it is worth discussing what is the difference between the approach that we propose here and what was used in the literature before. In previous works on the topic, the divergence was noticed for the case where there are unstable particles in P-wave processes. There were different attempts at solving this problem. In [221], it was discussed how the divergence is unavoidable in the non-relativistic limit and an arbitrary cutoff around the scale of the stop mass was adopted. In [223], it was discussed how the uncertainties in choosing the right cutoff for the stop pair production are of the same order of magnitude as higher-order QCD corrections. In this case, there is no clear scale for what the cutoff should be and the reduced mass was used as this sets the scale of the theory. In this approach, the enhancement is acknowledged to be UV sensitive and the physical cutoff shows the dependence on new physics. Near the cutoff, it is expected for order one correction to appear from the new physics con-
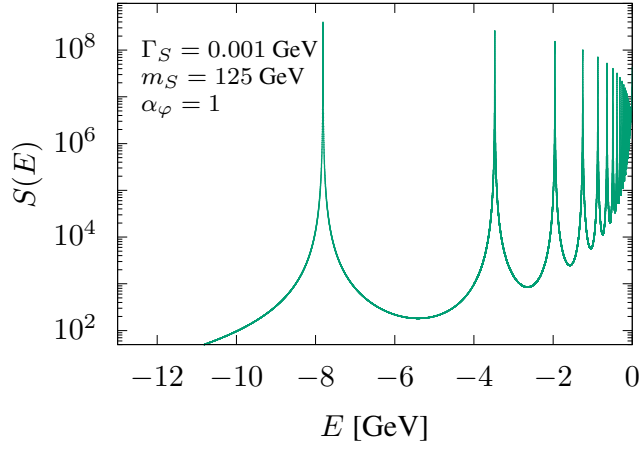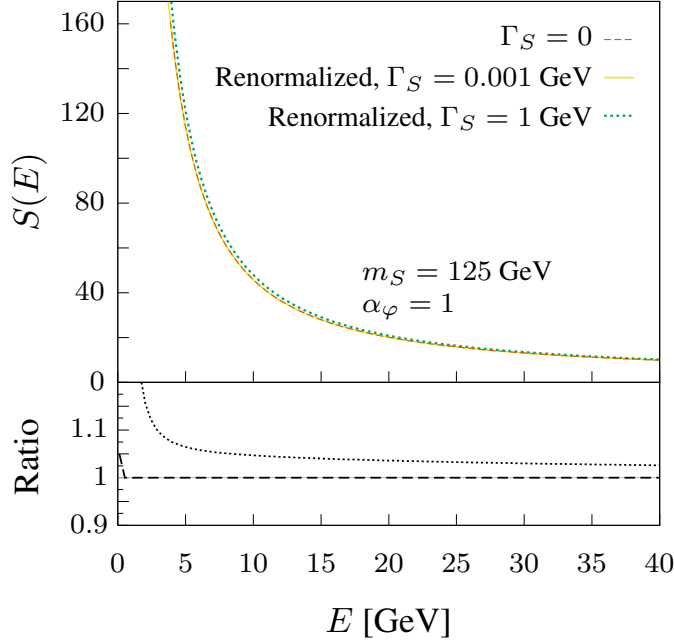
(a)
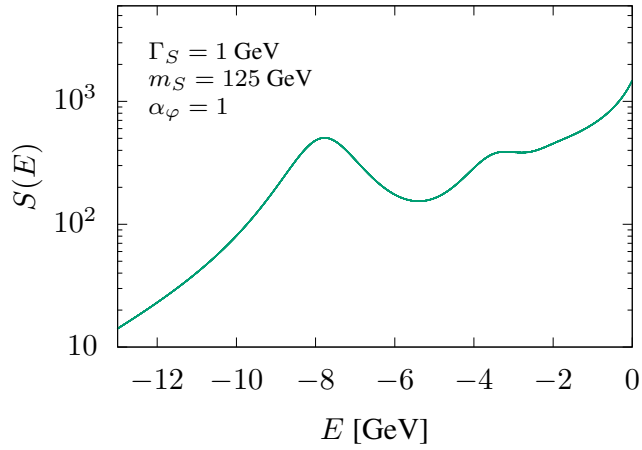
(b)

Figure 7.6: P-wave dominated Sommerfeld enhancement factor $S(E)$ behavior in the below-threshold region, computed using $\alpha_\varphi = 1$, $m_S = 125$ GeV and $\Gamma_S = 0.001$ GeV (a) or $\Gamma_S = 1$ GeV (b).

tribution. This is different from the approach that we introduce in this study.

Figure 7.7: Comparison between the behavior of the Sommerfeld enhancement for the P-wave dominated case in the above threshold region, computed using $\alpha_\varphi = 1$, $m_S = 125$ GeV and two non-zero width values, namely $\Gamma_S = 0.001$ GeV and $\Gamma_S = 1$ GeV, and the literature result [218] obtained with $\Gamma_S = 0$. The inset shows the ratio between the renormalized enhancement and the results from [218] (dashes), and the ratio between the renormalized enhancements for $\Gamma_S = 1$ GeV and $\Gamma_S = 0$ (dots).

By using the quantum field theory renormalization, we are describing all the low-energy physics without having to care about the microscopic description[8]

If we were working in a model where the UV is strongly interacting, then the cutoff can have a better motivated physical meaning as being the dynamical scale itself. In the models that we study here, there is no dynamic scale. This makes it harder to guess what cutoff could give a physical result. In the position space regularization, a cutoff is defined as a minimal distance r_Λ. The only natural cutoff in our case is the scale in which the non-relativistic theory ceases to be a good approximation. In this case, we should expect when the distances probed are smaller than the reduced mass the approxima-

---

[8]There is still some arbitrariness since new physics can contribute to some specific observables, however, the observables in which this occurs are seen as an input for the model instead of a prediction.

tion starts to break down. Because the divergences are of order $1/r^2$, there is a strong sensitivity for the scale. If there were only logarithmic divergences the sensitivity near zero would be softer. In order to show this sensitivity, we choose three different cutoffs and compared with the method proposed here: $r_\Lambda = 10^{-2}$ GeV^{-1}, $r_\Lambda = 10^{-3}$ GeV^{-1} and $r_\Lambda = 10^{-5}$ GeV^{-1}. Since we are using the mass $m_S = 125$GeV we expect that the best cutoff lies around $1/125$GeV^{-1}. We explore these cutoffs in Figure 7.8 for the case where the width is $\Gamma_S = 0.001$. We can see that the cutoff which is closer to the result is the one which is closer to the $1/m_S$ scale.

In the case where the width is larger, we could not find a sensible cutoff, and the behaviour of the enhancement factor breaks down. This regime is unphysical because it was picking too much of the divergent contribution or too much of the finite contribution, and thus the unitarity violation is significant and the approximation ceases to work.
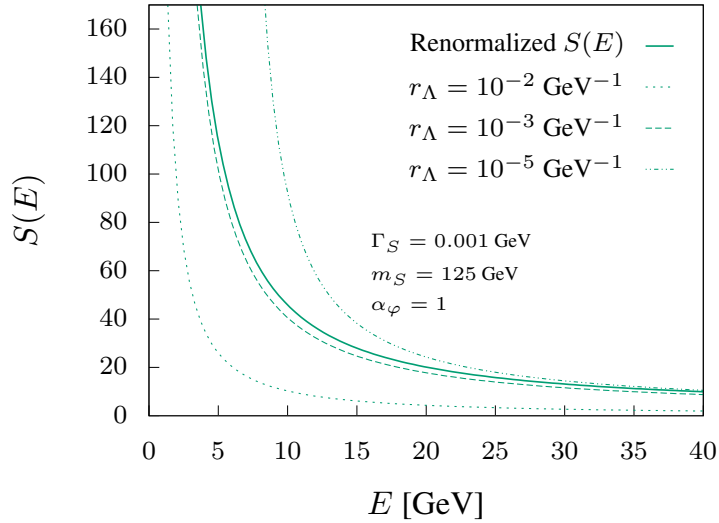
Figure 7.8: Enhancement value ($S(E)$) for the interaction q_3 in the above-threshold regime with $\alpha_\varphi = 1$ and $m_S = 125$ GeV for $\Gamma_S = 0.001$ GeV. The enhancement is presented for positive energies computed using the renormalization approach (Solid curve) and by using different values for a cutoff given by r_Λ for $\Gamma_S = 0.001$ GeV

We can see then that, given a reasonable choice of cutoff, it is possible to reproduce the renormalized result to a good approximation. However, the

sensitivity of the cutoff makes it difficult to choose one, to begin with. In this case, it seems better to approximate the problem to zero width, in which we do not have any divergences than to guess what is the best value for the cutoff. In the approach we propose, we use the consistency of the renormalized quantum field theory to guarantee our result for the Sommerfeld enhancement is sensible and independent of UV physics[9]. This removes the arbitrariness of choosing the cutoff, even if it is physical, and allows us to probe the small, but measurable, finite width effects.

7.6 Summary

In this chapter, we have proposed a method to deal with divergences that arise when computing the Sommerfeld enhancement factor in P-wave dominated processes with unstable particles in the final state. This problem has been recognized in the literature before and previous studies showed that these divergences can be avoided by using a simple cutoff procedure. Contrary to that approach, we showed that these divergences can be dealt with in the same way as the usual UV divergences in quantum field theory. This implies that taking properly into account the standard renormalization procedure in the quantum field theory removes all divergences, and it is not necessary to use any (physical or unphysical) cutoff in the calculation. We also showed that for the specific P-wave process we have studied, the effects of the finite width are small (of the order of 10%) for positive energy.

We have used a specific model to implement our renormalization procedure. However, the procedure that we introduce here can be generalized to any kind of interaction. In approaching a different model, the first step is to verify that the 2-to-2 cross-section, which we want to enhance, is finite (and thus predictable) when considering the loop exchange of the mediator. This check can be done perturbatively and it is always true for renormalizable theories. Then, the next step is to apply the optical theorem, take the non-relativistic limit and identify which operator acts on the Green's function. From that, it is guaranteed that all the divergences are dealt with in the renormalization, and thus one should worry only about picking the finite contribution for the enhancement. A renormalization scheme must be chosen, and if others observables are worked in the same theory, they need to be calculated in the same scheme. In the case where Green's function is only obtained numerically, the subtraction

---

[9]The arbitrariness of the renormalization scheme is the same as in the usual quantum field theory and observables cannot depend on it by construction.

can introduce some additional error since it will be necessary to work out what is the finite contribution of the process. This, unfortunately, is a problem even if the amount to be subtracted is known exactly order by order since numerical noise makes the cancellation not exact.

In the case of Coulomb[10] interaction, the divergences are only a problem for higher partial waves when the particles are unstable. In recent years, the scenario where dark matter has an unstable sector is becoming more popular [239, 240]. This work allows the calculation of enhancement of these kinds of models, provided that the width is small to allow the use of the optical theorem for unstable particles.

---

[10]The analysis for the Yukawa interaction is similar, only that everything becomes numerically and tracking the divergences becomes slightly harder.

Conclusion

In the introduction of this thesis (chapter 1) we presented the main components of the Standard Model, where we also highlighted its incomparable success. Notwithstanding, several phenomena reveal the limitations of the SM, motivating beyond the SM theories. While collider experiments continue to confirm the SM predictions at very high accuracy, they have not been able to provide indications for BSM particles. Given these circumstances, the search for new physics effects is entering a precision era, where the highest accuracy in our predictions is required to match the current and future very-low-uncertainty measurements. Our investigations were directed towards realizing predictions through loop computations in the search for new physics at low and high energies.

Effective Field Theories have become instrumental in the parametrization of deviations from the SM. Hence, chapter 2 was dedicated to the presentation of EFTs, and in particular, of the Standard Model Effective Field Theory, which achieves the aforementioned parametrization by introducing new interactions between the SM fields induced by the unobserved heavy new physics. This is followed by the discussion in chapter 3 about the fundamental concepts needed for making predictions about the top quark physics at hadron colliders, and by chapter 4 which is aimed to provide a review on the subtleties that arise when making predictions at one-loop in EFTs.

By means of the framework introduced in the chapters 2-4, we analyze the top-pair production sensitivity to new physics in the SMEFT via the four-heavy-quark operators, leading to the results presented in chapter 5. These operators are of relevance as they can be obtained from BSM scenarios where the top quark couples to new heavy particles. Our analysis relies on one-loop computations for the four-heavy quark operators and several conclusions arise from this. First, the top-pair production provides bounds on the Wilson coefficients of interest along directions in the parameter space that are complementary to the constraints found currently in the literature. In addition, the analytic computations allowed us to validate the implementation of the SMEFT operators at one-loop in MadGraph5_aMC@NLO according to the consistency require-

ments studied in chapter 4. This lead to the identification of a *logic error* in the coding of MadGraph5_aMC@NLO, consisting of the wrong select of rational terms corresponding to a given one-loop amplitude. After this type of error was corrected, the outputs from MadGraph5_aMC@NLO agreed with our analytical expressions. Finally, we obtained projections of the sensitivity of the $t\bar{t}$ and $t\bar{t}t\bar{t}$ processes at the future HL-LHC. We observed an enhancement in sensitivity in all of the four-heavy-quark operators with respect to the sensitivity found from the current measurements at the LHC. Moreover, by using two different cuts in the invariant-mass distribution, we found that the EFT validity in the two processes should be studied at depth since the obtained bounds are not stringent enough.

In chapter 6, the physics of the double Higgs production at future e^+e^- colliders is discussed. The $e^+e^- \rightarrow hh$ process offers the possibility to look for new physics that can enhance its small cross-section. We use the SMEFT framework to find the sensitivity of the $e^+e^- \rightarrow hh$ to such new physics effects. As a result, bounds on two different operators were found. Namely, the effective operator modifying the Yukawa coupling of the electron, entering at tree-level, and the four-fermion interaction between the electron and top currents, entering at one-loop. The former can probe scales typically of the order $\mathcal{O}(10\,\mathrm{TeV})$. This process presents the advantage of having a clean environment, nevertheless a full study at the detector level is still missing. This might be of interest for future studies, in order to check the full potential of this process in the search for new physics.

We also explored the possibility of low-energy effects from new physics through the Sommerfeld enhancement as a complementary approach to the search of BSM effects via deviations at high energy in the SMEFT. The computation of the Sommerfeld enhancemente to P-wave dominated processes with unstable final particles suffers from divergences. In chapter 7 we showed that the UV divergences can be absorbed within the renormalization of the corresponding quantum field theory. This is an alternative approach to the usual cutoff regularization procedure found in the literature. Moreover, this offers the possibility to reduce uncertainties due to the arbitrary choice of a cutoff. A phenomenological motivation for the study of the Sommerfeld enhancement is the double Higgs production at future lepton colliders, which is a P-wave dominated process. The two Higgs bosons might couple to light dark matter mediators leading to an enhancement in the $e^+e^- \rightarrow hh$ process. The possibility of measuring such a scenario is left for a future analysis.

Numerical inputs and results from chapter 5

Rotation matrices corresponding to the results of the Table 5.5:

$$
\mathcal{R}_{\mathrm{CMS}_{tt}-1} =
\begin{bmatrix}
0.82 & 0.37 & 0.35 & 0.22 & 0.15 \\
0.57 & -0.56 & -0.46 & -0.23 & -0.29 \\
-0.012 & -0.56 & 0.76 & -0.31 & 0.098 \\
0.014 & 0.46 & 0.15 & -0.63 & -0.60 \\
0.068 & 0.16 & -0.24 & -0.63 & 0.72
\end{bmatrix}, \qquad (A.1)
$$

$$
\mathcal{R}_{\mathrm{CMS}_{tt}-2} =
\begin{bmatrix}
-0.30 & -0.65 & -0.53 & -0.34 & -0.29 \\
0.95 & -0.22 & -0.15 & -0.052 & -0.14 \\
0.0032 & -0.52 & 0.78 & -0.32 & 0.11 \\
0.049 & 0.49 & -0.015 & -0.86 & -0.11 \\
0.049 & -0.12 & -0.28 & -0.18 & 0.93
\end{bmatrix}, \qquad (A.2)
$$

$$
\mathcal{R}_{\mathrm{CMS}_{tt}-3} =
\begin{bmatrix}
0.99 & -0.066 & 0.077 & 0.025 & -0.034 \\
0.016 & -0.54 & -0.73 & -0.24 & -0.34 \\
-0.083 & -0.69 & 0.61 & -0.37 & 0.035 \\
-0.0090 & -0.44 & -0.17 & 0.59 & 0.65 \\
-0.069 & -0.19 & 0.23 & 0.67 & -0.68
\end{bmatrix}, \qquad (A.3)
$$

$$
\mathcal{R}_{\mathrm{CMS}_{tt}-4} =
\begin{bmatrix}
-0.20 & -0.69 & -0.54 & -0.35 & -0.24 \\
-0.98 & 0.18 & 0.071 & 0.030 & 0.083 \\
0.050 & 0.22 & -0.71 & 0.18 & 0.64 \\
-0.0034 & -0.48 & 0.44 & -0.23 & 0.72 \\
-0.057 & -0.45 & 0.043 & 0.89 & -0.045
\end{bmatrix}. \qquad (A.4)
$$

$$\mathcal{R}_{\text{ATLAS}_{tt}} = \begin{bmatrix} -0.99 & 0.022 & -0.11 & -0.045 & 0.013 \\ 0.058 & -0.68 & -0.56 & -0.32 & -0.33 \\ -0.081 & -0.54 & 0.77 & -0.32 & 0.10 \\ -0.055 & -0.46 & 0.042 & 0.88 & 0.010 \\ 0.043 & -0.18 & -0.28 & -0.086 & 0.94 \end{bmatrix}. \qquad (A.5)$$

$$\mathcal{R}_{\text{Combined}}^{t\bar{t}} = \begin{bmatrix} -0.99 & -0.012 & -0.12 & -0.062 & 0.0024 \\ 0.097 & -0.70 & -0.55 & -0.33 & -0.31 \\ -0.072 & -0.51 & 0.79 & -0.32 & 0.073 \\ 0.039 & -0.19 & -0.24 & -0.068 & 0.95 \\ -0.057 & -0.46 & 0.053 & 0.88 & -0.016 \end{bmatrix}. \qquad (A.6)$$

The chosen binning of the invariant-mass distribution of the top pair production for the HL-LHC is such that in the range of energies $(300, 2000)$ GeV we have a bin size of 100 GeV, so that in this range there are 17 bins. Then the bin ranges of the other 7 bins in the distribution are

$$\{(2000, 2200), (2200, 2400), (2400, 2700), (2700, 3000),$$
$$(3000, 3500), (3500, 4000), (4000, 500)\}, \qquad (A.7)$$

with units in GeV. Analogously, for the four-top process we have the 5 bins

$$\{(700, 1300), (1300, 2000), (2000, 3000), (3000, 4000), (4000, 5000)\}.$$
$$(A.8)$$

Additional computations of the Sommerfeld enhancement

B.1 Non-relativistic approximation of the recursion relations.

In this appendix, let us work out the non-relativistic approximations of the recursion relations used during the paper. Starting from:

$$
\begin{aligned}
F^I(q, q_1, p_1) = {} & F_0^I(q, q_1, p_1) \\
& + (i\kappa)^2 \int \frac{\mathrm{d}^4 k}{(2\pi)^4} \frac{i}{(k + \frac{q}{2})^2 - m_h^2 + im_h\Gamma_h} \frac{i}{(k - \frac{q}{2})^2 - m_h^2 + im_h\Gamma_h} \\
& \qquad\qquad\qquad \frac{i}{(k - p)^2 - m_\varphi^2} F^I(q, q_1, k) \,,
\end{aligned}
$$

(B.1)

We then consider only contributions linear in the time-like direction inside the integral:

$$
\frac{i}{(k + \frac{q}{2})^2 - m_S^2 + im_S\Gamma_S} \rightarrow \frac{i}{2m_S \left(E/2 + k_0 - \frac{\vec{k}^2}{2m_S} + i\Gamma_S/2 \right)} \,,
$$

(B.2)

$$
\frac{i}{(k - \frac{q}{2})^2 - m_S^2 + im_S\Gamma_S} \rightarrow \frac{i}{2m_S \left(E/2 - k_0 - \frac{\vec{k}^2}{2m_S} + i\Gamma_S/2 \right)} \,,
$$

(B.3)

$$
\frac{i}{(k - p)^2 - m_\varphi^2} \rightarrow \frac{-i}{(\vec{k} - \vec{p})^2 + m_\varphi^2} \,,
$$

(B.4)

The recursion relation ins this limit is then:

$$F^I(E, \vec{p}) = F_0^I(E, \vec{p})$$
$$- \frac{(i\kappa)^2}{4m_S^2} \int \frac{\mathrm{d}^4 k}{(2\pi)^4} \frac{i}{E/2 + i\Gamma_S/2 + k_0 - \frac{\vec{k}^2}{2m_S}} \frac{i}{E/2 + i\Gamma_S/2 - k_0 - \frac{\vec{k}^2}{2m_S}}$$
$$\frac{i}{\left(\vec{k} - \vec{p}\right)^2 + m_\varphi^2} F^I(E, \vec{k}),$$

(B.5)

where we used $q = (2m_S + E, \vec{0})$, with E being the energy above or below the threshold for the production of the S particle pair. In the non-relativistic limit, we have $p^0 = 0$ and thus we can perform the k^0 integral:

$$\int \frac{\mathrm{d}k^0}{2\pi} \frac{i}{2m_S \left(E/2 - k_0 - \frac{\vec{k}^2}{2m_S} + i\Gamma_S/2\right)} \frac{i}{2m_S \left(E/2 + k^0 - \frac{\vec{k}^2}{2m_S} + i\Gamma_S/2\right)}$$
$$= \frac{i}{4m_S^2} \frac{1}{\left(E + i\Gamma_S - \frac{\vec{k}^2}{m_S}\right)}.$$

(B.6)

With this we recover Eq.(7.11):

$$F^I(E, \vec{p}) = F_0^I(E, \vec{p}) - \frac{\kappa^2}{4m_S^2} \int \frac{\mathrm{d}^3 k}{(2\pi)^3} \frac{1}{E + i\Gamma_S - \frac{\vec{k}^2}{m_S}} \frac{1}{\left(\vec{k} - \vec{p}\right)^2 + m_\varphi^2} F^I(E, \vec{k}).$$

(B.7)

B.2 Optical theorem for unstable particles

In the optical theorem approach, it is also possible to treat unstable particles in any internal line. The procedure uses the complex mass scheme [241, 242] where we change the internal propagator to have the decay width:

$$\frac{1}{p^2 - m^2} \to \frac{1}{p^2 - m^2 + im\Gamma}$$

(B.8)

At this point, one should be careful when considering these unstable particles, especially with the unitarity of the theory. The application of Cutkosky rules does not apply directly to unstable particles [241, 243]. However, a general relation (largest time equation) can be obtained, which is valid for both unsta-
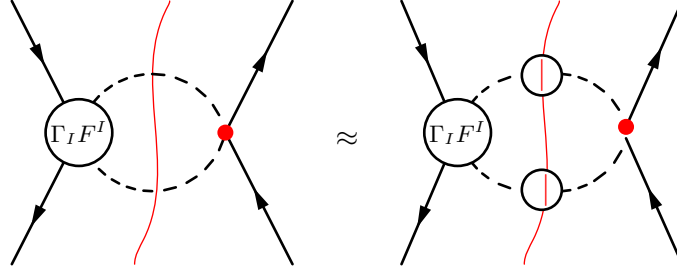
Figure B.1: The cut trough the unstable internal line in the narrow width approximation on the left side of the equation. On the right is the actual cut in the stable states in the case where we have this two-body decay.

ble and stable particles [243]. Using the largest time equation, it is possible to show that any cut with unstable particles does not contribute to the scattering matrix. The physical interpretation is that no final state has those particles. Because of this, we can, in the end, use the Cutkosky rules for both unstable and stable particles, but we do not cut the unstable states [244]. The downside of this approach is that processes that go through the unstable state end up being in higher loop order, as represented in Figure B.1.

The way to simplify such treatment can be achieved when the particle has a narrow width. In this case, we can treat the unstable particles just as stable particles because we separate the production from the decay. The cut generates the imaginary part of the propagator, which in the narrow width approximation has the same delta function form as the stable particle:

$$\text{Im}\left(\frac{1}{p^2 - m^2 + im\Gamma}\right) = -\frac{m\Gamma}{(p^2 - m^2)^2 + m^2\Gamma^2} \approx -\pi\delta(p^2 - m^2) \quad \text{(B.9)}$$

In this case, we can get some effects for the finite width while preserving the optical theorem's simplicity and unitarity. For a more in-depth discussion about this we refer the reader to [241, 244]. With this in mind, we can then use the optical theorem for states with narrow width, which is the main interest of this paper.

B.3 One-loop process(two-loop optical diagram) for the S-wave contact interaction.

The analysis for the one-loop process (two-loop optical diagram) is similar to the leading contribution:

$$i\mathcal{M} = i\bar{v}_s(p_2)u_r(p_1)\bar{u}_r(p_1)v_r(p_2)I_1 \tag{B.10}$$

$$I_1 = -\lambda_0^2\kappa^2 \int \frac{\mathrm{d}^4k}{(2\pi)^4}\frac{\mathrm{d}^4l}{(2\pi)^4} \frac{1}{(k+q/2)^2 - m_S^2 + im_S\Gamma_S} \frac{1}{(k-q/2)^2 - m_S^2 + im_S\Gamma_S}$$
$$\frac{1}{(k-l)^2 - m_\varphi^2} \frac{1}{(l-q/2)^2 - m_S^2 + im_S\Gamma_S} \frac{1}{(l+q/2)^2 - m_S^2 + im_S\Gamma_S} . \tag{B.11}$$

Then, we apply the near-threshold approximation by dropping every quadratic dependence on the energy or the time component of the vectors from the denominator. In this case we drop k_0^2, l_0^2, k_0l_0, k_0E, l_0E and E^2. Using this approximation, the integral in the non-relativistic limit becomes:

$$I_1 = -\lambda_0^2\kappa^2 \int \frac{\mathrm{d}^4k}{(2\pi)^4}\frac{\mathrm{d}^4l}{(2\pi)^4} \frac{1}{2m_S(k_0 + \frac{E+i\Gamma_S}{2} - \frac{\vec{k}^2}{2m_S})} \frac{1}{2m_S(k_0 - \frac{E+i\Gamma_S}{2} - \frac{\vec{k}^2}{2m_S})}$$
$$\frac{-1}{(\vec{k}-\vec{l})^2 + m_\varphi^2} \frac{1}{2m_S(l_0 + \frac{E+i\Gamma_S}{2} - \frac{\vec{l}^2}{2m_S})} \frac{1}{2m_S(l_0 - \frac{E+i\Gamma_S}{2} - \frac{\vec{l}^2}{2m_S})} . \tag{B.12}$$

The integration of k_0 and l_0 is done to give:

$$I_1 = -\frac{\lambda_0^2\kappa^2}{16m_S^4} \int \frac{\mathrm{d}^3k}{(2\pi)^3}\frac{\mathrm{d}^3l}{(2\pi)^3} \frac{1}{E + i\Gamma_S - \frac{\vec{k}^2}{m_S}} \frac{1}{(\vec{k}-\vec{l})^2 + m_\varphi^2} \frac{1}{E + i\Gamma_S - \frac{\vec{l}^2}{m_S}} . \tag{B.13}$$

To write the divergent contribution in position space, we must first perform the following l integral

$$I_1^l = \int \frac{\mathrm{d}^3l}{(2\pi)^3} \frac{1}{(\vec{k}-\vec{l})^2 + m_\varphi^2} \frac{1}{\frac{\vec{l}^2}{m_S} - z} . \tag{B.14}$$

Using the Feynman parametrization, we can rewrite it as:

$$I_1^l = m_S \int_0^1 \mathrm{d}x \int \frac{\mathrm{d}^3l}{(2\pi)^3} \frac{1}{(\vec{l}^2 + \Delta^2)^2} = \frac{m_S}{8\pi} \int_0^1 \mathrm{d}x \frac{1}{\sqrt{\Delta^2}} , \tag{B.15}$$

where $\Delta^2 = (1-x)(\vec{k}^2 + m_\varphi^2) - \vec{k}^2(1-x)^2 - m_S z x$. We can perform the integral in x, which is well behaved in the limit when $m_\varphi \to 0$ and write:

$$I_1 = -\lambda_0^2 \kappa^2 \int \frac{d^3 k}{(2\pi)^3} \frac{\sqrt{-k^2 + m_S z}}{64\pi m_S^2 k (k^2 - m_S z)^{3/2}} \sinh^{-1}\left(\frac{k}{\sqrt{-k^2 + m_S z}}\right).$$

(B.16)

We can expand for large momenta to pick up the most divergent contributions and then perform the Fourier transform:

$$I_1 = -\frac{\lambda_0^2 \kappa_\varphi^2}{16 m_S^4} \frac{m_S}{8\pi} \int \frac{d^3 k}{(2\pi)^3} \left(m_S \pi \frac{1}{|\vec{k}|}^3 + \ldots\right)$$

(B.17)

Now if we perform the Fourier transform using:

$$\mathcal{F}(\frac{1}{k^3}) = -\frac{1}{2\pi^2} \log(r),$$

(B.18)

We can write the one-loop divergent contribution as:

$$I_1^{\text{div}} = -\frac{\lambda_0^2}{4m_S^2} \frac{\kappa_\varphi^2}{4m_S^2} \left(-\frac{m_S^2}{16\pi^2}\right) \log(r) =$$

(B.19)

$$= \frac{\lambda_0^2}{4m_S^2} \alpha_\varphi \left(\frac{m_S^2}{4\pi}\right) \log(r),$$

(B.20)

B.4 One-loop process(two-loop optical diagram) for the P-wave contact interaction.

The next leading order for the P-wave process can be computed as follows:

$$i\mathcal{M} = i\bar{v}_s(p_2)\gamma_\mu u_r(p_1)\bar{u}_r(p_1)\gamma_\nu v_r(p_2) I_1^{\mu\nu}$$

(B.21)

with

$$I_1^{\mu\nu} = -F_0^2 \kappa^2 \int \frac{d^4 k}{(2\pi)^4} \frac{d^4 l}{(2\pi)^4} k^\mu l^\nu \frac{1}{(k+q/2)^2 - m_S^2 + i m_S \Gamma_S} \frac{1}{(k-q/2)^2 - m_S^2 + i m_S \Gamma_S}$$
$$\frac{1}{(k-l)^2 - m_\varphi^2} \frac{1}{(l-q/2)^2 - m_S^2 + i m_S \Gamma_S} \frac{1}{(l+q/2)^2 - m_S^2 + i m_S \Gamma_S}.$$

(B.22)

We can apply the near-threshold approximation by dropping every quadratic dependence on the energy or the time component of the vectors from the de-

nominator and perform the k_0 and l_0 integrals:

$$I_1^{ij} = -\frac{F_0^2 \kappa^2}{16 m_S^4} \int \frac{\mathrm{d}^3 k}{(2\pi)^3} \frac{\mathrm{d}^3 l}{(2\pi)^3} k^i l^j \frac{1}{E + i\Gamma_S - \frac{\vec{k}^2}{m_S}} \frac{1}{(\vec{k}-\vec{l})^2 + m_\varphi^2} \frac{1}{E + i\Gamma_S - \frac{\vec{l}^2}{m_S}} .$$
(B.23)

From this limit we can see that the only tensor structure that can appear is proportional to the Euclidean metric:

$$I_1^{ij} = \delta^{ij} (I_1)_{\mathrm{NR}} ,$$
(B.24)

$$I_1 = -\frac{F_0^2 \kappa^2}{48 m_S^4} \int \frac{\mathrm{d}^3 k}{(2\pi)^3} \frac{\mathrm{d}^3 l}{(2\pi)^3} k.l \frac{1}{\frac{\vec{k}^2}{m_S} - z} \frac{1}{(\vec{k}-\vec{l})^2 + m_\varphi^2} \frac{1}{\frac{\vec{l}^2}{m_S} - z} .$$
(B.25)

To write the divergent contribution in position space we can draw a connection with the S-wave calculation. We can use the Feynman parametrization to write I_1^l as:

$$I_1^l = \int \frac{\mathrm{d}^3 l}{(2\pi)^3} \frac{k.l}{(\vec{k}-\vec{l})^2 + m_\varphi^2} \frac{1}{\frac{\vec{l}^2}{m_S} - z} = m_S \int_0^1 \mathrm{d}x \int \frac{\mathrm{d}^3 l}{(2\pi)^3} \frac{(1-x)k^2}{(\vec{l}^2 + \Delta^2)^2}$$

$$= \frac{m_S}{8\pi} \int_0^1 \mathrm{d}x \frac{(1-x)k^2}{\sqrt{\Delta^2}} ,$$
(B.26)

where Δ is the same as the S-wave. We can perform the x integral to write I_1 as:

$$I_1 = F_0^2 \kappa^2 \int \frac{\mathrm{d}^3 k}{(2\pi)^3} \frac{k\sqrt{-k^2 + m_S z}}{192\pi m_S^2 (k^2 - m_S z)^{3/2}} \sinh^{-1}\left(\frac{k}{\sqrt{-k^2 + m_S z}}\right) .$$
(B.27)

We can then expand in large momenta to perform the Fourier transform of the most divergent contributions:

$$I_1 = \int \frac{\mathrm{d}^3 k}{(2\pi)^3} \left(-F_0^2 \pi \alpha_\varphi \frac{1}{48k} - F_0^2 \pi z \alpha_\varphi \frac{1}{24k^3} + \dots\right)$$
(B.28)

Performing the Fourier transform we have:

$$I_1^{\mathrm{div}} = -\frac{F_0^2}{12 m_S^2} \frac{\kappa_\varphi^2}{4 m_S^2} \left(\frac{m_S^2}{32\pi^2} \frac{1}{r^2} - \frac{m_S^3 z}{16\pi^2} \log(r)\right) =$$
(B.29)

$$= \frac{F_0^2}{12 m_S^2} \alpha_\varphi \left(-\frac{m_S^2}{8\pi} \frac{1}{r^2} + \frac{m_S^3 z}{4\pi} \log(r)\right)$$
(B.30)

Bibliography

[1] Andres Vasquez, Céline Degrande, Alberto Tonero, and Rogerio Rosenfeld, "New physics in double higgs production at future e^+e^--colliders", *Journal of High Energy Physics*, vol. 2019, no. 5, 2019.

[2] Carlos Henrique de Lima, Alberto Tonero, Andres Vasquez, and Rogerio Rosenfeld, "The role of renormalization in sommerfeld enhancement with unstable particles", *arXiv:hep-th/2208.13309*, 2022.

[3] CMS Collaboration, "A portrait of the higgs boson by the cms experiment ten years after the discovery", *Nature*, vol. 607, pp. 60 – 68, 2022.

[4] Sheldon L. Glashow, "Partial-symmetries of weak interactions", *Nuclear Physics*, vol. 22, no. 4, pp. 579–588, 1961.

[5] Steven Weinberg, "A model of leptons", *Phys. Rev. Lett.*, vol. 19, pp. 1264–1266, 1967.

[6] Abdus Salam, "Weak and Electromagnetic Interactions", *Conf. Proc. C*, vol. 680519, pp. 367–377, 1968.

[7] H. Fritzsch, M. Gell-Mann, and H. Leutwyler, "Advantages of the color octet gluon picture", *Physics Letters B*, vol. 47, no. 4, pp. 365–368, 1973.

[8] F. Englert and R. Brout, "Broken symmetry and the mass of gauge vector mesons", *Phys. Rev. Lett.*, vol. 13, pp. 321–323, 1964.

[9] Peter W. Higgs, "Broken symmetries and the masses of gauge bosons", *Phys. Rev. Lett.*, vol. 13, pp. 508–509, 1964.

[10] G. S. Guralnik, C. R. Hagen, and T. W. B. Kibble, "Global conservation laws and massless particles", *Phys. Rev. Lett.*, vol. 13, pp. 585–587, 1964.

[11] David J. Gross and Frank Wilczek, "Ultraviolet behavior of non-abelian gauge theories", *Phys. Rev. Lett.*, vol. 30, pp. 1343–1346, 1973.

[12] H. David Politzer, "Reliable perturbative results for strong interactions?", *Phys. Rev. Lett.*, vol. 30, pp. 1346–1349, 1973.

[13] G. 't Hooft and M. Veltman, "Regularization and renormalization of gauge fields", *Nuclear Physics B*, vol. 44, no. 1, pp. 189–213, 1972.

[14] CMS Collaboration, "Observation of a new boson at a mass of 125 GeV with the CMS experiment at the LHC", *Physics Letters B*, vol. 716, no. 1, pp. 30–61, 2012.

[15] ATLAS Collaboration, "Observation of a new particle in the search for the standard model higgs boson with the ATLAS detector at the LHC", *Physics Letters B*, vol. 716, no. 1, pp. 1–29, 2012.

[16] P Langacker, *The Standard Model and Beyond*, CRC Press; 2nd edition (June 30, 2020), 2017.

[17] STEPHEN P. MARTIN, "A SUPERSYMMETRY PRIMER", in *Perspectives on Supersymmetry*, pp. 1–98. WORLD SCIENTIFIC, 1998.

[18] MATTHEW J. STRASSLER, "AN UNORTHODOX INTRODUCTION TO SUPERSYMMETRIC GAUGE THEORY", in *Strings, Branes and Extra Dimensions*. 2004, WORLD SCIENTIFIC.

[19] Adrian Signer, "ABC of SUSY", *Journal of Physics G: Nuclear and Particle Physics*, vol. 36, no. 7, pp. 073002, 2009.

[20] D CHUNG, L EVERETT, G KANE, S KING, J LYKKEN, and L WANG, "The soft supersymmetry-breaking lagrangian: theory and applications", *Physics Reports*, vol. 407, no. 1-3, pp. 1–203, 2005.

[21] Roberto Contino, Leandro Da Rold, and Alex Pomarol, "Light custodians in natural composite higgs models", *Physical Review D*, vol. 75, no. 5, 2007.

[22] Adrián Carmona, Mikael Chala, and José Santiago, "New higgs production mechanism in composite higgs models", *Journal of High Energy Physics*, vol. 2012, no. 7, 2012.

[23] M. Gillioz, R. Gröber, C. Grojean, M. Mühlleitner, and E. Salvioni, "Higgs low-energy theorem (and its corrections) in composite models", *Journal of High Energy Physics*, vol. 2012, no. 10, 2012.

[24] Kaustubh Agashe, Roberto Contino, and Alex Pomarol, "The minimal composite higgs model", *Nuclear Physics B*, vol. 719, no. 1-2, pp. 165–187, 2005.

[25] Charalampos Anastasiou, Elisabetta Furlan, and José Santiago, "Realistic composite higgs models", *Physical Review D*, vol. 79, no. 7, 2009.

[26] Vernon Barger, Paul Langacker, Mathew McCaskey, Michael Ramsey-Musolf, and Gabe Shaughnessy, "Complex singlet extension of the standard model", *Physical Review D*, vol. 79, no. 1, 2009.

[27] Amine Ahriche and Salah Nasri, "Light dark matter, light higgs boson, and the electroweak phase transition", *Physical Review D*, vol. 85, no. 9, 2012.

[28] G.C. Branco, P.M. Ferreira, L. Lavoura, M.N. Rebelo, Marc Sher, and João P. Silva, "Theory and phenomenology of two-higgs-doublet models", *Physics Reports*, vol. 516, no. 1-2, pp. 1–102, 2012.

[29] Chien-Yi Chen, Sally Dawson, and Marc Sher, "Heavy higgs searches and constraints on two higgs doublet models", *Physical Review D*, vol. 88, no. 1, 2013.

[30] Howard Georgi and Marie Machacek, "Doubly charged higgs bosons", *Nuclear Physics B*, vol. 262, no. 3, pp. 463–477, 1985.

[31] Michael S. Chanowitz and Mitchell Golden, "Higgs Boson Triplets With $M_W = M_Z \cos\theta_W$", *Phys. Lett. B*, vol. 165, pp. 105–108, 1985.

[32] J. Soto, "Overview of non-relativistic QCD", *The European Physical Journal A*, vol. 31, no. 4, pp. 705–710, 2007.

[33] F. Hussain and G. Thompson, "An introduction to the heavy quark effective theory", 1995.

[34] Steven Weinberg, "Pion scattering lengths", *Phys. Rev. Lett.*, vol. 17, pp. 616–621, 1966.

[35] Steven Weinberg, "Dynamical approach to current algebra", *Phys. Rev. Lett.*, vol. 18, pp. 188–191, 1967.

[36] Steven Weinberg, "Precise relations between the spectra of vector and axial-vector mesons", *Phys. Rev. Lett.*, vol. 18, pp. 507–509, 1967.

[37] A Pich, "Chiral perturbation theory", *Reports on Progress in Physics*, vol. 58, no. 6, pp. 563–609, 1995.

[38] Tom Melia and Sridip Pal, "EFT asymptotics: the growth of operator degeneracy", *SciPost Physics*, vol. 10, no. 5, 2021.

[39] W. Buchmuller and D. Wyler, "Effective Lagrangian Analysis of New Interactions and Flavor Conservation", *Nucl. Phys. B*, vol. 268, pp. 621–653, 1986.

[40] B. Grzadkowski, M. Iskrzynski, M. Misiak, and J. Rosiek, "Dimension-Six Terms in the Standard Model Lagrangian", *JHEP*, vol. 10, pp. 085, 2010.

[41] Ilaria Brivio and Michael Trott, "The standard model as an effective field theory", *Physics Reports*, vol. 793, pp. 1–98, Feb 2019.

[42] Adam Falkowski and Riccardo Rattazzi, "Which EFT", *Journal of High Energy Physics*, vol. 2019, no. 10, pp. 255, 2019.

[43] Rodrigo Alonso, Elizabeth E. Jenkins, and Aneesh V. Manohar, "Geometry of the scalar sector", *Journal of High Energy Physics*, vol. 2016, no. 8, pp. 101, 2016.

[44] Timothy Cohen, Nathaniel Craig, Xiaochuan Lu, and Dave Sutherland, "Is SMEFT enough?", *Journal of High Energy Physics*, vol. 2021, no. 3, pp. 237, 2021.

[45] Roberto Contino, Margherita Ghezzi, Christophe Grojean, Margarete Muhlleitner, and Michael Spira, "Effective Lagrangian for a light Higgs-like scalar", *JHEP*, vol. 07, pp. 035, 2013.

[46] Rick S. Gupta, Alex Pomarol, and Francesco Riva, "BSM Primary Effects", 2014.

[47] Eduard Massó, "An effective guide to beyond the standard model physics", *Journal of High Energy Physics*, vol. 2014, no. 10, 2014.

[48] Alex Pomarol, "Higgs physics", *arXiv:hep-ph/1412.4410*, 2014.

[49] Elizabeth E. Jenkins, Aneesh V. Manohar, and Peter Stoffer, "Low-energy effective field theory below the electroweak scale: operators and matching", *Journal of High Energy Physics*, vol. 2018, no. 3, 2018.

[50] Elizabeth E. Jenkins, Aneesh V. Manohar, and Peter Stoffer, "Low-energy effective field theory below the electroweak scale: anomalous dimensions", *Journal of High Energy Physics*, vol. 2018, no. 1, 2018.

[51] Shinya Kanemura and Ryo Nagai, "A new higgs effective field theory and the new no-lose theorem", *Journal of High Energy Physics*, vol. 2022, no. 3, 2022.

[52] LHC Higgs Cross Section Working Group, A. David, A. Denner, M. Duehrssen, M. Grazzini, C. Grojean, G. Passarino, M. Schumacher, M. Spira, G. Weiglein, and M. Zanetti, "LHC HXSWG interim recommendations to explore the coupling structure of a Higgs-like particle", *arXiv:hep-ph/1209.0040*, 2012.

[53] Steven Weinberg, "Baryon and Lepton Nonconserving Processes", *Phys. Rev. Lett.*, vol. 43, pp. 1566–1570, 1979.

[54] Rodrigo Alonso, Elizabeth E. Jenkins, Aneesh V. Manohar, and Michael Trott, "Renormalization Group Evolution of the Standard Model Dimension Six Operators III: Gauge Coupling Dependence and Phenomenology", *JHEP*, vol. 04, pp. 159, 2014.

[55] Landon Lehman, "Extending the standard model effective field theory with the complete set of dimension-7 operators", *Physical Review D*, vol. 90, no. 12, 2014.

[56] Hao-Lin Li, Zhe Ren, Ming-Lei Xiao, Jiang-Hao Yu, and Yu-Hui Zheng, "Complete set of dimension-nine operators in the standard model effective field theory", *Phys. Rev. D*, vol. 104, no. 1, pp. 015025, 2021.

[57] Hao-Lin Li, Zhe Ren, Jing Shu, Ming-Lei Xiao, Jiang-Hao Yu, and Yu-Hui Zheng, "Complete Set of Dimension-8 Operators in the Standard Model Effective Field Theory", *arXiv:hep-ph/2005.00008*, 2020.

[58] Christopher W. Murphy, "Dimension-8 operators in the Standard Model Eective Field Theory", *JHEP*, vol. 10, pp. 174, 2020.

[59] Roberto Trotta, "Bayesian methods in cosmology", *arXiv:hep-ph/1701.01467*, 2017.

[60] Glen Cowan, Kyle Cranmer, Eilam Gross, and Ofer Vitells, "Asymptotic formulae for likelihood-based tests of new physics", *The European Physical Journal C*, vol. 71, no. 2, 2011.

[61] Roger Barlow, "Asymmetric statistical errors", *arXiv:hep-ph/0406120*, 2004.

[62] R.J. Barlow, "Practical statistics for particle physics", *CERN Yellow Reports: School Proceedings*, vol. Vol. 5, pp. 12–25 September 2018, 2020.

[63] Stefan Höche, "Introduction to parton-shower event generators", in *Theoretical Advanced Study Institute in Elementary Particle Physics: Journeys Through the Precision Frontier: Amplitudes for Colliders*, 2015, pp. 235–295.

[64] Richard P. Feynman, *The Behavior of Hadron Collisions at Extreme Energies*, pp. 289–304, Springer Netherlands, Dordrecht, 1988.

[65] John C. Collins, Davison E. Soper, and George Sterman, "Soft gluons and factorization", *Nuclear Physics B*, vol. 308, no. 4, pp. 833–856, 1988.

[66] S. Alioli, S. Badger, J. Bellm, B. Biedermann, F. Boudjema, G. Cullen, A. Denner, H. van Deurzen, S. Dittmaier, R. Frederix, S. Frixione, M.V. Garzelli, S. Gieseke, E.W.N. Glover, N. Greiner, G. Heinrich, V. Hirschi, S. Höche, J. Huston, H. Ita, N. Kauer, F. Krauss, G. Luisoni, D. Maître, F. Maltoni, P. Nason, C. Oleari, R. Pittau, S. Plätzer, S. Pozzorini, L. Reina, C. Reuschle, T. Robens, J. Schlenk, M. Schönherr, F. Siegert, J.F. von Soden-Fraunhofen, F. Tackmann, F. Tramontano, P. Uwer, G. Salam, P. Skands, S. Weinzierl, J. Winter, V. Yundin, G. Zanderighi, and M. Zaro, "Update of the binoth les houches accord for a standard interface between monte carlo tools and one-loop programs", *Computer Physics Communications*, vol. 185, no. 2, pp. 560–571, 2014.

[67] T. Binoth, F. Boudjema, G. Dissertori, A. Lazopoulos, A. Denner, S. Dittmaier, R. Frederix, N. Greiner, S. Höche, W. Giele, P. Skands, J. Winter, T. Gleisberg, J. Archibald, G. Heinrich, F. Krauss, D. Maître, M. Huber, J. Huston, N. Kauer, F. Maltoni, C. Oleari, G. Passarino, R. Pittau, S. Pozzorini, T. Reiter, S. Schumann, and G. Zanderighi, "A

proposal for a standard interface between monte carlo tools and one-loop programs", *Computer Physics Communications*, vol. 181, no. 9, pp. 1612–1622, 2010.

[68] Stefano Carrazza, Celine Degrande, Shayan Iranipour, Juan Rojo, and Maria Ubiali, "Can new physics hide inside the proton?", *Physical Review Letters*, vol. 123, no. 13, 2019.

[69] Admir Greljo, Shayan Iranipour, Zahari Kassabov, Maeve Madigan, James Moore, Juan Rojo, Maria Ubiali, and Cameron Voisey, "Parton distributions in the SMEFT from high-energy drell-yan tails", *Journal of High Energy Physics*, vol. 2021, no. 7, 2021.

[70] Makoto Kobayashi and Toshihide Maskawa, "CP-Violation in the Renormalizable Theory of Weak Interaction", *Progress of Theoretical Physics*, vol. 49, no. 2, pp. 652–657, 1973.

[71] CDF collaboration, "Observation of Top Quark Production $\bar{p}p$ Collisions with the Collider Detector at Fermilab", *Physical Review Letters*, vol. 74, no. 14, pp. 2626–2631, 1995.

[72] D0 collaboration, "Search for High Mass Top Quark Production in $p\bar{p}$ collisions at $\sqrt{s} = 1.8$ TeV", *Physical Review Letters*, vol. 74, no. 13, pp. 2422–2426, 1995.

[73] Particle Data Group, "Review of Particle Physics", *Progress of Theoretical and Experimental Physics*, vol. 2020, no. 8, 2020, 083C01.

[74] ATLAS, CDF, CMS, D0 collaborations, "First combination of Tevatron and LHC measurements of the top-quark mass", *arXiv:1403.4427* , 2014.

[75] CMS collaboration, "A profile likelihood approach to measure the top quark mass in the lepton+jets channel at $\sqrt{s} = 13$ TeV", *CMS-PAS-TOP-20-008*, 2022.

[76] M. Jeżabek and J.H. Kühn, "Lepton spectra from heavy quark decay", *Nuclear Physics B*, vol. 320, no. 1, pp. 20–44, 1989.

[77] W Bernreuther, "Top-quark physics at the LHC", *Journal of Physics G: Nuclear and Particle Physics*, vol. 35, no. 8, pp. 083001, 2008.

[78] Matthew J. Strassler and Michael E. Peskin, "Threshold production of heavy top quarks: Qcd and the higgs boson", *Phys. Rev. D*, vol. 43, pp. 1500–1514, 1991.

[79] Y. Kiyo, Johann H. Kuhn, S. Moch, M. Steinhauser, and P. Uwer, "Top-quark pair production near threshold at LHC", *Eur. Phys. J. C*, vol. 60, pp. 375–386, 2009.

[80] M. Beneke, A. Signer, and Vladimir A. Smirnov, "Top quark production near threshold and the top quark mass", *Phys. Lett. B*, vol. 454, pp. 137–146, 1999.

[81] Nikolaos Kidonakis, "Next-to-next-to-leading-order collinear and soft gluon corrections for t-channel single top quark production", *Phys. Rev. D*, vol. 83, pp. 091503, 2011.

[82] Mathias Brucherseifer, Fabrizio Caola, and Kirill Melnikov, "On the NNLO QCD corrections to single-top production at the LHC", *Physics Letters B*, vol. 736, pp. 58–63, 2014.

[83] Edmond L. Berger, Jun Gao, and Hua Xing Zhu, "Differential distributions for t-channel single top-quark production and decay at next-to-next-to-leading order in QCD", *Journal of High Energy Physics*, vol. 2017, no. 11, 2017.

[84] Nikolaos Kidonakis, "Next-to-next-to-leading logarithm resummation for s-channel single top quark production", *Physical Review D*, vol. 81, no. 5, 2010.

[85] Nikolaos Kidonakis, "Two-loop soft anomalous dimensions for single top quark associated production with a $W-$ or $H-$", *Physical Review D*, vol. 82, no. 5, 2010.

[86] M. Czakon, "Tops from light quarks: Full mass dependence at two-loops in QCD", *Physics Letters B*, vol. 664, no. 4-5, pp. 307–314, 2008.

[87] P. Bärnreuther, M. Czakon, and P. Fiedler, "Virtual amplitudes and threshold behaviour of hadronic top-quark pair-production cross sections", *Journal of High Energy Physics*, vol. 2014, no. 2, 2014.

[88] R Bonciani, A Ferroglia, T Gehrmann, D Maître, and C Studerus, "Two-loop fermionic corrections to heavy-quark pair production: the quark-

antiquark channel", *Journal of High Energy Physics*, vol. 2008, no. 07, pp. 129–129, 2008.

[89] R Bonciani, A Ferroglia, T Gehrmann, and C Studerus, "Two-loop planar corrections to heavy-quark pair production in the quark-antiquark channel", *Journal of High Energy Physics*, vol. 2009, no. 08, pp. 067–067, 2009.

[90] Manoj K. Mandal, Pierpaolo Mastrolia, Jonathan Ronca, and William J. Bobadilla Torres, "Two-loop scattering amplitude for heavy-quark pair production through light-quark annihilation in QCD", *arXiv*, 2022.

[91] R. Bonciani, A. Ferroglia, T. Gehrmann, A. von Manteuffel, and C. Studerus, "Two-loop leading color corrections to heavy-quark pair production in the gluon fusion channel", *Journal of High Energy Physics*, vol. 2011, no. 1, 2011.

[92] Andreas von Manteuffel and Cedric Studerus, "Massive planar and non-planar double box integrals for light nf contributions to $gg \rightarrow t\bar{t}$", *Journal of High Energy Physics*, vol. 2013, no. 10, 2013.

[93] R. Bonciani, A. Ferroglia, T. Gehrmann, A. von Manteuffel, and C. Studerus, "Light-quark two-loop corrections to heavy-quark pair production in the gluon fusion channel", *Journal of High Energy Physics*, vol. 2013, no. 12, 2013.

[94] Simon Badger, Ekta Chaubey, Heribertus Bayu Hartanto, and Robin Marzucca, "Two-loop leading colour QCD helicity amplitudes for top quark pair production in the gluon fusion channel", *Journal of High Energy Physics*, vol. 2021, no. 6, 2021.

[95] ATLAS-collaboration, "Measurement of the $t\bar{t}$ production cross-section and lepton differential distributions in $e\mu$ dilepton events from pp collisions at $\sqrt{s} = 13$ TeV with the ATLAS detector", *The European Physical Journal C*, vol. 80, no. 6, 2020.

[96] ATLAS-collaboration, "Measurement of the $t\bar{t}$ production cross-section using $e\mu$ events with b-tagged jets in pp collisions at $\sqrt{s}$=13 tev with the atlas detector", *Physics Letters B*, vol. 772, pp. 879, 2017.

[97] CMS-collaboration, "Measurement of the $t\bar{t}$ production cross section using events in the $e\mu$ final state in pp collisions at $\sqrt{s} = 13$ TeV", *The European Physical Journal C*, vol. 77, no. 3, Mar 2017.

[98] Peter Bärnreuther, Michał Czakon, and Alexander Mitov, "Percent-Level-Precision Physics at the Tevatron: Next-to-Next-to-Leading Order QCD Corrections to $q\bar{q} \to t\bar{t} + X$", *Physical Review Letters*, vol. 109, no. 13, 2012.

[99] Jun Gao and Andrew S. Papanastasiou, "Top-quark pair-production and decay at high precision", *Physical Review D*, vol. 96, no. 5, Sep 2017.

[100] Michał Czakon, David Heymes, and Alexander Mitov, "Dynamical scales for multi-TeV top-pair production at the LHC", *Journal of High Energy Physics*, vol. 2017, no. 4, 2017.

[101] Michal Czakon, David Heymes, and Alexander Mitov, "High-Precision Differential Predictions for Top-Quark Pairs at the LHC", *Physical Review Letters*, vol. 116, no. 8, Feb 2016.

[102] Michał Czakon, David Heymes, Alexander Mitov, Davide Pagani, Ioannis Tsinikos, and Marco Zaro, "Top-pair production at the LHC through NNLO QCD and NLO EW", *Journal of High Energy Physics*, vol. 2017, no. 10, Oct 2017.

[103] Stefano Catani, Simone Devoto, Massimiliano Grazzini, Stefan Kallweit, Javier Mazzitelli, and Hayk Sargsyan, "Top-quark pair hadroproduction at next-to-next-to-leading order in QCD", *Physical Review D*, vol. 99, no. 5, 2019.

[104] Stefano Catani, Simone Devoto, Massimiliano Grazzini, Stefan Kallweit, and Javier Mazzitelli, "Top-quark pair production at the LHC: fully differential QCD predictions at NNLO", *Journal of High Energy Physics*, vol. 2019, no. 7, 2019.

[105] Nikolaos Kidonakis, "Top-quark double-differential distributions at approximate $\mathrm{N}^3\mathrm{LO}$", *Phys. Rev. D*, vol. 101, pp. 074006, 2020.

[106] Rikkert Frederix, Davide Pagani, and Marco Zaro, "Large NLO corrections in $t\bar{t}W^{\pm}$ and $t\bar{t}t\bar{t}$ hadroproduction from supposedly subleading EW contributions", *Journal of High Energy Physics*, vol. 2018, no. 2, Feb 2018.

[107] CMS-collaboration, "Search for standard model production of four top quarks with same-sign and multilepton final states in proton–proton collisions at $\sqrt{s} = 13\,\mathrm{TeV}$ ", *The European Physical Journal C*, vol. 78, no. 2, Feb 2018.

[108] A. M. Sirunyan and et al., "Search for production of four top quarks in final states with same-sign or multiple leptons in proton–proton collisions at $\sqrt{s} = 13$ TeV", *The European Physical Journal C*, vol. 80, no. 2, Jan 2020.

[109] ATLAS-collaboration, "Evidence for $t\bar{t}t\bar{t}$ production in the multilepton final state in proton-proton collisions at $\sqrt{s} = 13$ tev with the atlas detector", *The European Physical Journal C*, vol. 80, no. 2, 2020.

[110] Céline Degrande, Gauthier Durieux, Fabio Maltoni, Ken Mimasu, Eleni Vryonidou, and Cen Zhang, "Automated one-loop computations in the standard model effective field theory", *Physical Review D*, vol. 103, no. 9, 2021.

[111] Aneesh V. Manohar, "Introduction to effective field theories", 2018.

[112] G. 't Hooft and M. Veltman, "Scalar one-loop integrals", *Nuclear Physics B*, vol. 153, pp. 365–401, 1979.

[113] Giovanni Ossola, Costas G Papadopoulos, and Roberto Pittau, "On the rational terms of the one-loop amplitudes", *Journal of High Energy Physics*, vol. 2008, no. 05, pp. 004–004, 2008.

[114] Gerhard Buchalla, "Heavy quark theory", in *55th Scottish Universities Summer School in Physics: Heavy Flavor Physics (SUSSP 2001)*, 2002, pp. 57–104.

[115] Andrzej J. Buras, Mikołaj Misiak, and Jörg Urban, "Two-loop QCD anomalous dimensions of flavour-changing four-quark operators within and beyond the standard model", *Nuclear Physics B*, vol. 586, no. 1-2, pp. 397–426, 2000.

[116] Robert Fleischer, "Flavour physics and cp violation: Expecting the lhc", *arXiv:hep-ph/0802.2882*, 2008.

[117] A.J. Buras, J. Ellis, M.K. Gaillard, and D.V. Nanopoulos, "Aspects of the grand unification of strong, weak and electromagnetic interactions", *Nuclear Physics B*, vol. 135, no. 1, pp. 66–92, 1978.

[118] K Chetyrkin, "$|\Delta F| = 1$ non-leptonic effective hamiltonian in a simpler scheme", *Nuclear Physics B*, vol. 520, no. 1-2, pp. 279–297, 1998.

[119] Qingjun Jin, Ke Ren, Gang Yang, and Rui Yu, "Gluonic evanescent operators: classification and one-loop renormalization", *Journal of High Energy Physics*, vol. 2022, no. 8, 2022.

[120] Jason Aebischer and Marko Pesut, "One-loop fierz transformations", *arXiv:hep-ph/2208.10513*, 2022.

[121] Jason Aebischer, Andrzej J. Buras, and Jacky Kumar, "Simple Rules for Evanescent Operators in One-Loop Basis Transformations", *arXiv:hep-ph/2202.01225*, 2022.

[122] Michael J. Dugan and Benjamín Grinstein, "On the vanishing of evanescent operators", *Physics Letters B*, vol. 256, no. 2, pp. 239–244, 1991.

[123] Stefan Herrlich and Ulrich Nierste, "Evanescent operators, scheme dependences and double insertions", *Nuclear Physics B*, vol. 455, no. 1-2, pp. 39–58, 1995.

[124] Andrzej J. Buras, "Weak hamiltonian, cp violation and rare decays", 1998.

[125] Oscar Cata, Wolfgang Kilian, and Nils Kreher, "Gauge anomalies in the standard-model effective field theory", 2020.

[126] Quentin Bonnefoy, Luca Di Luzio, Christophe Grojean, Ayan Paul, and Alejo N. Rossia, "Comments on gauge anomalies at dimension-six in the standard model effective field theory", *Journal of High Energy Physics*, vol. 2021, no. 5, 2021.

[127] Ferruccio Feruglio, "A Note on Gauge Anomaly Cancellation in Effective Field Theories", *Journal of High Energy Physics*, vol. 2021, no. 3, Mar 2021.

[128] Patrick J. Fox, Ian Low, and Yue Zhang, "Top-Philic Z' Forces at the LHC", *Journal of High Energy Physics*, vol. 2018, no. 3, Mar 2018.

[129] Nathan P. Hartland, Fabio Maltoni, Emanuele R. Nocera, Juan Rojo, Emma Slade, Eleni Vryonidou, and Cen Zhang, "A Monte Carlo global analysis of the Standard Model Effective Field Theory: the top quark sector", *Journal of High Energy Physics*, vol. 2019, no. 4, 2019.

[130] Till Martini and Markus Schulze, "Electroweak loops as a probe of new physics in $t\bar{t}$ production at the LHC", *Journal of High Energy Physics*, vol. 2020, no. 4, 2020.

[131] Olga Bessidskaia Bylund, Fabio Maltoni, Ioannis Tsinikos, Eleni Vryonidou, and Cen Zhang, "Probing top quark neutral couplings in the Standard Model Effective Field Theory at NLO QCD", 2016.

[132] Diogo Buarque Franzosi and Cen Zhang, "Probing top-quark chromomagnetic dipole moment at next-to-leading order in QCD", 2015.

[133] J. A. Aguilar Saavedra and all, "Interpreting top-quark LHC measurements in the standard-model effective field theory", 2018.

[134] Andy Buckley, Christoph Englert, James Ferrando, David J. Miller, Liam Moore, Michael Russell, and Chris D. White, "Constraining top quark effective theory in the LHC Run II era", *Journal of High Energy Physics*, vol. 2016, no. 4, pp. 1–32, 2016.

[135] Ilaria Brivio, Sebastian Bruggisser, Fabio Maltoni, Rhea Moutafis, Tilman Plehn, Eleni Vryonidou, Susanne Westhoff, and Cen Zhang, "O new physics, where art thou? A global search in the top sector", *Journal of High Energy Physics*, vol. 2020, no. 2, Feb 2020.

[136] Lina Alasfar, Jorge de Blas, and Ramona Gröber, "Higgs probes of top quark contact interactions and their interplay with the Higgs self-coupling", 2022.

[137] Cen Zhang, "Constraining qqtt operators from four-top production: a case for enhanced eft sensitivity", *Chinese Physics C*, vol. 42, no. 2, pp. 023104, Feb 2018.

[138] Sally Dawson and Pier Paolo Giardino, "Flavorful electroweak precision observables in the standard model effective field theory", 2022.

[139] Fabio Maltoni, Eleni Vryonidou, and Cen Zhang, "Higgs production in association with a top-antitop pair in the standard model effective field theory at NLO in QCD", *Journal of High Energy Physics*, vol. 2016, no. 10, 2016.

[140] Nicolas Deutschmann, Claude Duhr, Fabio Maltoni, and Eleni Vryonidou, "Gluon-fusion higgs production in the standard model effective field theory", *Journal of High Energy Physics*, vol. 2017, no. 12, 2017.

[141] John Ellis, Maeve Madigan, Ken Mimasu, Veronica Sanz, and Tevong You, "Top, higgs, diboson and electroweak fit to the standard model effective field theory", *Journal of High Energy Physics*, vol. 2021, no. 4, 2021.

[142] Jacob J. Ethier, Giacomo Magni, Fabio Maltoni, Luca Mantani, Emanuele R. Nocera, Juan Rojo, Emma Slade, Eleni Vryonidou, and Cen Zhang, "Combined SMEFT interpretation of Higgs, diboson, and top quark data from the LHC", 2021.

[143] Nathaniel Craig and Scott Thomas, "Exclusive signals of an extended higgs sector", *Journal of High Energy Physics*, vol. 2012, no. 11, 2012.

[144] Alex Pomarol and Javi Serra, "Top quark compositeness: Feasibility and implications", *Physical Review D*, vol. 78, no. 7, 2008.

[145] Giovanni Banelli, Ennio Salvioni, Javi Serra, Tobias Theil, and Andreas Weiler, "The present and future of four top operators", *Journal of High Energy Physics*, vol. 2021, no. 2, 2021.

[146] Luc Darmé, Benjamin Fuks, and Fabio Maltoni, "Top-philic heavy resonances in four-top final states and their EFT interpretation", *Journal of High Energy Physics*, vol. 2021, no. 9, 2021.

[147] Nicolas Greiner, Kyoungchul Kong, Jong-Chul Park, Seong Chan Park, and Jan-Christopher Winter, "Model-independent production of a top-philic resonance at the LHC", *Journal of High Energy Physics*, vol. 2015, no. 4, 2015.

[148] Jeong Han Kim, Kyoungchul Kong, Seung J. Lee, and Gopolang Mohlabeng, "Probing TeV scale top-philic resonances with boosted top-tagging at the high luminosity LHC", *Physical Review D*, vol. 94, no. 3, 2016.

[149] Rafael Aoude, Hesham El Faham, Fabio Maltoni, and Eleni Vryonidou, "Complete SMEFT predictions for four top quark production at hadron colliders", 2022.

[150] Valentin Hirschi, Fabio Maltoni, Ioannis Tsinikos, and Eleni Vryonidou, "Constraining anomalous gluon self-interactions at the LHC: a reappraisal", *Journal of High Energy Physics*, vol. 2018, no. 7, 2018.

[151] Andy Buckley, Christoph Englert, James Ferrando, David J. Miller, Liam Moore, Michael Russell, and Chris D. White, "Global fit of top quark effective theory to data", *Physical Review D*, vol. 92, no. 9, 2015.

[152] Ding Yu Shao, Chong Sheng Li, Jian Wang, Jun Gao, Hao Zhang, and Hua Xing Zhu, "Model-independent analysis of top quark forward-backward asymmetry at the Tevatron up to $\mathcal{O}(\alpha_s^2/\Lambda^2)$ ", *Physical Review D*, vol. 84, no. 5, Sep 2011.

[153] Rodrigo Alonso, Elizabeth E. Jenkins, Aneesh V. Manohar, and Michael Trott, "Renormalization group evolution of the Standard Model dimension six operators III: gauge coupling dependence and phenomenology", *Journal of High Energy Physics*, vol. 2014, no. 4, 2014.

[154] J. de Blas, M. Pierini, L. Reina, and L. Silvestrini, "Impact of the recent measurements of the top-quark and w-boson masses on electroweak precision fits", 2022.

[155] Oliver Atkinson, Akanksha Bhardwaj, Stephen Brown, Christoph Englert, David J. Miller, and Panagiotis Stylianou, "Improved Constraints on Effective Top Quark Interactions using Edge Convolution Networks", 2021.

[156] J. Alwall, R. Frederix, S. Frixione, V. Hirschi, F. Maltoni, O. Mattelaer, H.-S. Shao, T. Stelzer, P. Torrielli, and M. Zaro, "The automated computation of tree-level and next-to-leading order differential cross sections, and their matching to parton shower simulations", *Journal of High Energy Physics*, vol. 2014, no. 7, 2014.

[157] Christoph Müller, "Top-pair production via gluon fusion in the standard model effective field theory", *Physical Review D*, vol. 104, no. 9, 2021.

[158] Thomas Hahn, "Generating feynman diagrams and amplitudes with feynarts 3", *Computer Physics Communications*, vol. 140, no. 3, pp. 418–431, 2001.

[159] T. Hahn and M. Pérez-Victoria, "Automated one-loop calculations in four and d dimensions", *Computer Physics Communications*, vol. 118, no. 2-3, pp. 153–165, 1999.

[160] T. Hahn and M. Pérez-Victoria, "Automated one-loop calculations in four and d dimensions", *Computer Physics Communications*, vol. 118, no. 2-3, pp. 153–165, 1999.

[161] Celine Degrande, Jean-Marc Gerard, Christophe Grojean, Fabio Maltoni, and Geraldine Servant, "Non-resonant New Physics in Top Pair Production at Hadron Colliders", *JHEP*, vol. 03, pp. 125, 2011.

[162] Celine Degrande and Matteo Maltoni, "Reviving the interference: framework and proof-of-principle for the anomalous gluon self-interaction in the SMEFT", *Phys. Rev. D*, vol. 103, no. 9, pp. 095009, 2021.

[163] CMS-collaboration, "Measurement of differential cross sections for top quark pair production using the lepton+jets final state in proton-proton collisions at 13 TeV", *Physical Review D*, vol. 95, no. 9, 2017.

[164] CMS-collaboration, "Measurement of differential cross sections for the production of top quark pairs and of additional jets in lepton+jets events from pp collisions at $\sqrt{s}$=13 TeV", *Physical Review D*, vol. 97, no. 11, Jun 2018.

[165] CMS-collaboration, "Measurement of normalized differential $t\bar{t}$ cross sections in the dilepton channel from pp collisions at $\sqrt{s} = 13$ TeV", *Journal of High Energy Physics*, vol. 2018, no. 4, 2018.

[166] CMS-collaboration, "Measurements of $t\bar{t}$ differential cross sections in proton-proton collisions at $\sqrt{s} = 13$ TeV using events containing two leptons", *Journal of High Energy Physics*, vol. 2019, no. 2, Feb 2019.

[167] ATLAS-collaboration, "Measurements of top-quark pair differential and double-differential cross-sections in the ℓ+jets channel with pp collisions at $\sqrt{s} = 13$ TeV using the ATLAS detector", *The European Physical Journal C*, vol. 79, no. 12, Dec 2019.

[168] Frank Krauss, Silvan Kuttimalai, and Tilman Plehn, "LHC multijet events as a probe for anomalous dimension-six gluon interactions", *Physical Review D*, vol. 95, no. 3, 2017.

[169] Reza Goldouzian and Michael D. Hildreth, "LHC dijet angular distributions as a probe for the dimension-six triple gluon vertex", *Physics Letters B*, vol. 811, pp. 135889, 2020.

[170] Michal Czakon, Andrea Ferroglia, Alexander Mitov, Davide Pagani, Andrew S. Papanastasiou, Benjamin D. Pecjak, Darren J. Scott, Ioannis Tsinikos, Xing Wang, Li Lin Yang, and Marco Zaro, "Top quark pair

production at complete NLO accuracy with NNLO+NNLL' corrections in QCD", *Chinese Physics C*, vol. 44, no. 8, pp. 083104, 2020.

[171] Sally Dawson and Pier Paolo Giardino, "Electroweak and QCD corrections to Z and W pole observables in the standard model EFT", *Physical Review D*, vol. 101, no. 1, 2020.

[172] Gauthier Durieux, Christophe Grojean, Jiayin Gu, and Kechen Wang, "The leptonic future of the higgs", *Journal of High Energy Physics*, vol. 2017, no. 9, 2017.

[173] ATLAS and CMS collaborations, "Measurements of the higgs boson production and decay rates and constraints on its couplings from a combined ATLAS and CMS analysis of the LHC pp collision data at $\sqrt{s} = 7$ and 8 tev", *Journal of High Energy Physics*, vol. 2016, no. 8, 2016.

[174] ATLAS collaboration, "Measurements of Higgs boson properties in the diphoton decay channel with 36 fb^{-1} of pp collisions data at $\sqrt{s} = 13$ TeV with the ATLAS detector", *Physical Review D*, vol. 98, no. 5, 2018.

[175] CLIC collaboration CLICdp, "Cern yellow reports, vol 4 (2016): Updated baseline for a staged compact linear collider", 2016.

[176] Howard Baer, Tim Barklow, Keisuke Fujii, Yuanning Gao, Andre Hoang, Shinya Kanemura, Jenny List, Heather E. Logan, Andrei Nomerotski, Maxim Perelstein, Michael E. Peskin, Roman Pöschl, Jürgen Reuter, Sabine Riemann, Aurore Savoy-Navarro, Geraldine Servant, Tim M. P. Tait, and Jaehoon Yu, "The international linear collider technical design report - volume 2: Physics", 2013.

[177] CEPC-SPPC Study Group, "CEPC-SPPC Preliminary Conceptual Design Report 1. Physics and Detector (2015)".

[178] M. Bicer et al., "First look at the physics case of TLEP", *Journal of High Energy Physics*, vol. 2014, no. 1, 2014.

[179] John Ellis, Philipp Roloff, Verónica Sanz, and Tevong You, "Dimension-6 operator analysis of the CLIC sensitivity to new physics", *Journal of High Energy Physics*, vol. 2017, no. 5, 2017.

[180] Stefano Di Vita, Gauthier Durieux, Christophe Grojean, Jiayin Gu, Zhen Liu, Giuliano Panico, Marc Riembau, and Thibaud Vantalon, "A

global view on the higgs self-coupling at lepton colliders", *Journal of High Energy Physics*, vol. 2018, no. 2, 2018.

[181] F. Boudjema and E. Chopin, "Double higgs production at the linear colliders and the probing of the higgs self-coupling", *arXiv:9507396*, 1995.

[182] Naoyuki Haba, Kunio Kaneta, Yukihiro Mimura, and Tsedenbaljir Enkhbat, "Higgs pair production at the LHC and ILC from a general potential", *Physical Review D*, vol. 89, no. 1, 2014.

[183] Giuliano Panico, "Prospects for double higgs production", 2015.

[184] A. Djouadi, V. Driesen, and C. Jünger, "Loop-induced higgs boson pair production at e^+e^- colliders", *Physical Review D*, vol. 54, no. 1, pp. 759–769, 1996.

[185] David Ló pez-Val and Joan Solà, "Neutral higgs-pair production at linear colliders within the general two-higgs-doublet model: Quantum effects and triple higgs boson self-interactions", *Physical Review D*, vol. 81, no. 3, 2010.

[186] Claudio O Dib, Rogerio Rosenfeld, and Alfonso Zerwekh, "Double higgs production and quadratic divergence cancellation in little higgs models with t-parity", *Journal of High Energy Physics*, vol. 2006, no. 05, pp. 074–074, 2006.

[187] Roberto Contino, Christophe Grojean, Mauro Moretti, Fulvio Piccinini, and Riccardo Rattazzi, "Strong double higgs production at the LHC", *Journal of High Energy Physics*, vol. 2010, no. 5, 2010.

[188] Roberto Contino, Margherita Ghezzi, Mauro Moretti, Giuliano Panico, Fulvio Piccinini, and Andrea Wulzer, "Anomalous couplings in double higgs production", *Journal of High Energy Physics*, vol. 2012, no. 8, 2012.

[189] Maxime Gouzevitch, Alexandra Oliveira, Juan Rojo, Rogerio Rosenfeld, Gavin P. Salam, and Veronica Sanz, "Scale-invariant resonance tagging in multijet events and new physics in higgs pair production", *Journal of High Energy Physics*, vol. 2013, no. 7, 2013.

[190] Giuliano Panico, "Prospects for double higgs production", 2015.

[191] T. Plehn, M. Spira, and P.M. Zerwas, "Pair production of neutral higgs particles in gluon-gluon collisions", *Nuclear Physics B*, vol. 479, no. 1-2, pp. 46–64, 1996.

[192] Florian Goertz, Andreas Papaefstathiou, Li Lin Yang, and José Zurita, "Higgs boson pair production in the d = 6 extension of the SM", *Journal of High Energy Physics*, vol. 2015, no. 4, 2015.

[193] Aleksandr Azatov, Roberto Contino, Giuliano Panico, and Minho Son, "Effective field theory analysis of double higgs production via gluon fusion", 2015.

[194] A.C.A. Oliveira and R. Rosenfeld, "Hidden sector effects on double higgs production near threshold at the LHC", *Physics Letters B*, vol. 702, no. 4, pp. 201–204, 2011.

[195] Mukesh Kumar, Xifeng Ruan, Rashidul Islam, Alan S. Cornell, Max Klein, Uta Klein, and Bruce Mellado, "Probing anomalous couplings using di-higgs production in electron–proton collisions", *Physics Letters B*, vol. 764, pp. 247–253, 2017.

[196] K. J. F. Gaemers and F. Hoogeveen, "Higgs-boson pair production in $e^{+}e^{-}$ reactions", *Zeitschrift für Physik C Particles and Fields*, vol. 675, no. 3-4, pp. 356–359, 1984.

[197] J.J. Lopez-Villarejo and J.A.M. Vermaseren, "The reaction $e^{+}e^{-} \rightarrow hh$ recomputed", *Physics Letters B*, vol. 675, no. 3-4, pp. 356–359, 2009.

[198] Zhenyu Han and Witold Skiba, "Effective theory analysis of precision electroweak data", *Physical Review D*, vol. 71, no. 7, 2005.

[199] J. de Blas, M. Ciuchini, E. Franco, S. Mishima, M. Pierini, L. Reina, and L. Silvestrini, "Electroweak precision observables and higgs-boson signal strengths in the standard model and beyond: present and future", *Journal of High Energy Physics*, vol. 2016, no. 12, 2016.

[200] Jorge de Blas, Marco Ciuchini, Enrico Franco, Satoshi Mishima, Maurizio Pierini, Laura Reina, and Luca Silvestrini, "The global electroweak and higgs fits in the lhc era", 2017.

[201] John Ellis, Veronica Sanz, and Tevong You, "The Effective Standard Model after LHC Run I", 2014.

[202] Christoph Englert, Roman Kogler, Holger Schulz, and Michael Spannowsky, "Higgs coupling measurements at the LHC", *The European Physical Journal C*, vol. 76, no. 7, 2016.

[203] Anja Butter, Oscar J.P. Éboli, J. Gonzalez-Fraile, M.C. Gonzalez-Garcia, Tilman Plehn, and Michael Rauch, "The gauge-higgs legacy of the LHC run i", *Journal of High Energy Physics*, vol. 2016, no. 7, 2016.

[204] John Ellis, Christopher W. Murphy, Verónica Sanz, and Tevong You, "Updated global SMEFT fit to higgs, diboson and electroweak data", *Journal of High Energy Physics*, vol. 2018, no. 6, 2018.

[205] Wolfgang Altmannshofer, Joachim Brod, and Martin Schmaltz, "Experimental constraints on the coupling of the higgs boson to electrons", *Journal of High Energy Physics*, vol. 2015, no. 5, 2015.

[206] Aleksandr Azatov, Roberto Contino, Camila S. Machado, and Francesco Riva, "Helicity selection rules and noninterference for BSM amplitudes", *Physical Review D*, vol. 95, no. 6, 2017.

[207] Elizabeth E. Jenkins, Aneesh V. Manohar, and Michael Trott, "Renormalization Group Evolution of the Standard Model Dimension Six Operators I: Formalism and lambda Dependence", *JHEP*, vol. 10, pp. 087, 2013.

[208] Elizabeth E. Jenkins, Aneesh V. Manohar, and Michael Trott, "Renormalization Group Evolution of the Standard Model Dimension Six Operators II: Yukawa Dependence", *JHEP*, vol. 01, pp. 035, 2014.

[209] Adam Alloul, Neil D. Christensen, Céline Degrande, Claude Duhr, and Benjamin Fuks, "FeynRules 2.0 — a complete toolbox for tree-level phenomenology", *Computer Physics Communications*, vol. 185, no. 8, pp. 2250–2300, 2014.

[210] Celine Degrande, "Automatic evaluation of UV and R_2 terms for beyond the standard model lagrangians: A proof-of-principle", *Computer Physics Communications*, vol. 197, pp. 239–262, 2015.

[211] Gauthier Durieux, Martín Perelló, Marcel Vos, and Cen Zhang, "Global and optimal probes for the top-quark effective field theory at future lepton colliders", *Journal of High Energy Physics*, vol. 2018, no. 10, 2018.

[212] A. Sommerfeld, "Über die beugung und bremsung der elektronen", *Annalen der Physik*, vol. 403, no. 3, pp. 257–330, 1931.

[213] Andrei D. Sakharov, "Interaction of an Electron and Positron in Pair Production", *Zh. Eksp. Teor. Fiz.*, vol. 18, pp. 631–635, 1948.

[214] Junji Hisano, Shigeki Matsumoto, and Mihoko M. Nojiri, "Explosive dark matter annihilation", *Phys. Rev. Lett.*, vol. 92, pp. 031303, 2004.

[215] Junji Hisano, Shigeki. Matsumoto, Mihoko M. Nojiri, and Osamu Saito, "Non-perturbative effect on dark matter annihilation and gamma ray signature from galactic center", *Phys. Rev. D*, vol. 71, pp. 063528, 2005.

[216] Nima Arkani-Hamed, Douglas P. Finkbeiner, Tracy R. Slatyer, and Neal Weiner, "A theory of dark matter", *Physical Review D*, vol. 79, no. 1, 2009.

[217] Massimiliano Lattanzi and Joseph I. Silk, "Can the WIMP annihilation boost factor be boosted by the Sommerfeld enhancement?", *Phys. Rev. D*, vol. 79, pp. 083523, 2009.

[218] Roberto Iengo, "Sommerfeld enhancement: General results from field theory diagrams", *JHEP*, vol. 05, pp. 024, 2009.

[219] S. Cassel, "Sommerfeld factor for arbitrary partial wave processes", *J. Phys. G*, vol. 37, pp. 105009, 2010.

[220] V. S. Fadin, V. A. Khoze, A. D. Martin, and A. Chapovsky, "Coulomb effects in W^+W^- production", *Physical Review D*, vol. 52, no. 3, pp. 1377–1385, 1995.

[221] I.I Bigi, V.S Fadin, and V Khoze, "Stop near threshold", *Nuclear Physics B*, vol. 377, no. 3, pp. 461 – 479, 1992.

[222] Nicola Fabiano, "Estimates of threshold cross-section for stoponium production at e+ e- colliders", *Eur. Phys. J. C*, vol. 19, pp. 547–551, 2001.

[223] Wolfgang Mödritsch, "On the p-wave contributions to the cross sections of and near threshold", *Nuclear Physics B*, vol. 475, no. 3, pp. 507–521, 1996.

[224] Seyong Kim and M. Laine, "Studies of a thermally averaged p-wave sommerfeld factor", *Physics Letters B*, vol. 795, pp. 469–474, 2019.

[225] Benjamin Grinstein and Michael Trott, "A Higgs-Higgs bound state due to new physics at a TeV", *Phys. Rev. D*, vol. 76, pp. 073002, 2007.

[226] A. A. Penin and A. A. Pivovarov, "Analytical results for e+ e- → t anti-t and gamma gamma → t anti-t observables near the threshold up to the next-to-next-to leading order of NRQCD", *Phys. Atom. Nucl.*, vol. 64, pp. 275–293, 2001.

[227] Brant E. Robertson and Andrew R. Zentner, "Dark matter annihilation rates with velocity-dependent annihilation cross sections", *Phys. Rev. D*, vol. 79, no. 8, pp. 083525, 2009.

[228] Matthew J. Strassler and Michael E. Peskin, "Threshold production of heavy top quarks: QCD and the higgs boson", *Phys. Rev. D*, vol. 43, pp. 1500–1514, 1991.

[229] Y. Sumino, K. Fujii, Kaoru Hagiwara, H. Murayama, and C.K. Ng, "Top quark pair production near threshold", *Phys. Rev. D*, vol. 47, pp. 56–81, 1993.

[230] V. S. Fadin and V. A. Khoze, "Threshold behavior of the cross section for the production of t quarks in e^+e^- annihilation", *Soviet Journal of Experimental and Theoretical Physics Letters*, vol. 46, pp. 525, 1987.

[231] Janusz Rosiek, "Complete set of Feynman rules for the MSSM: Erratum", , 1995.

[232] J.J. Lopez-Villarejo and J.A.M. Vermaseren, "The reaction $e^+e^- \to hh$ recomputed", *Physics Letters B*, vol. 675, no. 3-4, pp. 356–359, 2009.

[233] Gerard 't Hooft and M. J. G. Veltman, "One loop divergencies in the theory of gravitation", *Ann. Inst. H. Poincare Phys. Theor. A*, vol. 20, pp. 69–94, 1974.

[234] Steven Weinberg, "On the Development of Effective Field Theory", *Eur. Phys. J. H*, vol. 46, no. 1, pp. 6, 2021.

[235] Levere Hostler, "Coulomb Green's Functions and the Furry Approximation", *Journal of Mathematical Physics*, vol. 5, no. 5, pp. 591–611, 1964.

[236] L. Chetouani and T. F. Hammann, "Coulomb Green's functions, in an n-dimensional Euclidean space", *Journal of Mathematical Physics*, vol. 27, no. 12, pp. 2944–2948, 1986.

[237] A. A. Penin and A. A. Pivovarov, "Analytical results for $e^+e^- \to t\bar{t}$ and $\gamma\gamma \to t\bar{t}$ observables near the threshold up to the next-to-next-to leading order of NRQCD", *Phys. Atom. Nucl.*, vol. 64, pp. 275–293, 2001.

[238] Hitoshi Murayama and Yukinari Sumino, "Axial-vector-coupling contribution to toponium resonances", *Physical review D: Particles and fields*, vol. 47, pp. 82–92, 1993.

[239] Jonathan Hubert, Aurel Schneider, Doug Potter, Joachim Stadel, and Sambit K. Giri, "Decaying dark matter: simulations and weak-lensing forecast", *JCAP*, vol. 10, pp. 040, 2021.

[240] Emil Brinch Holm, Thomas Tram, and Steen Hannestad, "Decaying warm dark matter revisited", 2022.

[241] Ansgar Denner and Jean-Nicolas Lang, "The Complex-Mass Scheme and Unitarity in perturbative Quantum Field Theory", *Eur. Phys. J. C*, vol. 75, no. 8, pp. 377, 2015.

[242] Ansgar Denner and S. Dittmaier, "The Complex-mass scheme for perturbative calculations with unstable particles", *Nucl. Phys. B Proc. Suppl.*, vol. 160, pp. 22–26, 2006.

[243] M. Veltman, "Unitarity and causality in a renormalizable field theory with unstable particles", *Physica*, vol. 29, no. 3, pp. 186–207, 1963.

[244] John F. Donoghue and Gabriel Menezes, "Unitarity, stability and loops of unstable ghosts", *Phys. Rev. D*, vol. 100, no. 10, pp. 105006, 2019.